



University of Pennsylvania  
**ScholarlyCommons**

---

Publicly Accessible Penn Dissertations


---

2021

## Theoretical And Computational Studies Of Heat Transport Processes In Molecular Systems

Renai Chen  
*University of Pennsylvania*

Follow this and additional works at: <https://repository.upenn.edu/edissertations>

 Part of the [Computational Chemistry Commons](#), [Condensed Matter Physics Commons](#), and the [Physical Chemistry Commons](#)

---

### Recommended Citation

Chen, Renai, "Theoretical And Computational Studies Of Heat Transport Processes In Molecular Systems" (2021). *Publicly Accessible Penn Dissertations*. 4927.  
<https://repository.upenn.edu/edissertations/4927>

This paper is posted at ScholarlyCommons. <https://repository.upenn.edu/edissertations/4927>  
For more information, please contact [repository@pobox.upenn.edu](mailto:repository@pobox.upenn.edu).

---

# Theoretical And Computational Studies Of Heat Transport Processes In Molecular Systems

## Abstract

There has been growing research interest in the field of nanoscale thermal transport over the past two decades due its importance to a variety of fascinating applications, such as waste heat control, improved electronic functionality, and phononics building blocks. Much of this focus has been on solid-state systems for which advanced experimental characterizations and measurements are readily available. Molecule-based systems, which in principle exhibit no less structural richness than solid state systems and may show excellent energy transport capabilities, have been largely ignored until recently. This is mostly because of the difficulties associated with measuring heat transport on the molecular scale. However, a few recent experimental breakthroughs have brought molecular energy transport process into the spotlight, and at the same time established measurement techniques that can be tested, verified, and explained using theoretical tools. This dissertation examines and explores theoretical approaches for modeling heat transport in molecular systems. Specifically, we have developed a stochastic nonequilibrium molecular dynamics (MD) method which mimics the experimental setting of substrate-bridge-substrate structure, i.e., a molecular junction. We incorporate this approach, along with a quantum Landauer's formalism, into the open-source molecular simulation package—GROMACS, so that it can be applied to molecular systems with different topologies and thermal environments. Our simulations of heat conduction in hydrocarbon-based single molecule junctions yield excellent agreement with the recent state-of-the-art experimental data. Within the capacities of the new method, we have also investigated phononic interference effects in the heat conduction characteristics of benzendithiol molecules. Using the methods developed in this dissertation, we have mapped, for the first time, thermal fluxes down to the atomistic level. In the context of phononic energy transport, we develop a simulation method that integrates quantum effects into classical MD. This hybrid method, once fully implemented, will compensate for the disadvantages of classical approaches at low temperatures and for the difficulty in treating anharmonicity in Landauer-type quantum transport calculations. This method will improve the predictive power of classical heat conduction simulations.

The second part of this dissertation explores an intriguing energy transport channel that has been newly discovered termed electron-transfer-induced heat transport (ETIHT), which is distinct from traditional heat transfer mechanisms that rely purely on molecular vibrations. We construct a theoretical model that combines the two energy transport channels (ETIHT and phononic) into one general model and then we show analytically under certain parametric thresholds (e.g. reorganization energies) that ETIHT dominates while other conditions may magnify the phononic contributions. Although the work in this part of the thesis is currently purely theoretical, it may provide useful insights into future organic molecular thermoelectric devices.

## Degree Type

Dissertation

## Degree Name

Doctor of Philosophy (PhD)

## Graduate Group

Chemistry

## First Advisor

Abraham Nitzan

---

**Keywords**

Electron transfer, Energy transfer, Heat transport, Molecular dynamics, Molecular heat conduction, Nanoscale

**Subject Categories**

Computational Chemistry | Condensed Matter Physics | Physical Chemistry

THEORETICAL AND COMPUTATIONAL STUDIES OF HEAT TRANSPORT  
PROCESSES IN MOLECULAR SYSTEMS

Renai Chen

A DISSERTATION

in

Chemistry

Presented to the Faculties of the University of Pennsylvania

in

Partial Fullfillment of the Requirements for the

Degree of Doctor of Philosophy

2021

Supervisor of Dissertation

---

Abraham Nitzan

Donner Professor of Physical Sciences

Graduate Group Chairperson

---

Daniel J. Mindiola

Brush Family Professor of Chemistry

Dissertation Committee

Joseph E. Subotnik, Edmund J. and Louise W. Kahn Endowed Term Professor of  
Chemistry

Marsha I. Lester, Christopher H. Browne Distinguished Professor of Chemistry

Andrew M. Rappe, Blanchard Professor of Chemistry

## DEDICATION

To my parents and my beloved wife

## ACKNOWLEDGMENT

It would be a blatant lie to say that I complete this dissertation all by myself. So many great people have helped me in so many different ways during my Ph.D. journey, without whom this work would not have been possible. First and foremost, I am eternally grateful to have Dr. Abraham Nitzan as my academic advisor. As one of the most distinguished scientists in the field of chemical physics, his scientific expertise and experiences are beyond what I could learn for being a mentee for just five years. Still, his way of deep scientific thinking, sharp physical intuition towards every problem, and meticulous approach to technicality and accuracy, has great influences on my doctorate career and way of doing research. Furthermore, Abe provides me with endless supports and encouragements to my personal and professional development, which forms the foundation of my enjoyable study processes. I feel honored and privileged to be his graduate student.

I would also like to thank all my thesis committee members: Dr. Joseph Subotnik, Dr. Marsha Lester and Dr. Andrew Rappe. It is their precious time investments to my annual meetings each year that give me excellent suggestions and insights into the continuous development and writings of my dissertation. They also helped my career directions towards the end of my staying at Penn.

Big thanks go to all the members of Nitzan's lab. In particular, I cannot thank Dr. Galen Craven enough for his support and help throughout. Starting from my first research project, towards my mid-candidacy, even after he left Penn he has always been one of my main resources for help when I get stuck with my research. I would also like to specifically thank Dr. Inon Sharony who has taught me everything about software development and open source simulation packages. I thank Dr. Maicol

Ochoa for his help with Green's function calculation techniques and job searching. My thanks to Monosij Mondal, Dr. Alexander Semenov, Dr. Henning Kirchberg, and Dr. Hadi Dinpajoo for being great companions in the lab offering numerous help that I couldn't count.

I would also like to thank Dr. Gaohan Miao, Dr. Zuxin Jin, Dr. Tian Qiu, Dr. Nicole Bellonzi, Dr. Wenjun Ouyang, Zeyu Zhou and Dr. Hsing-Ta Chen from Dr. Subotnik's group for helping me through different stages of my career. I want to thank our wonderful graduate coordinator Kristen Simon. She was the first person I got to know in Penn Chemistry, even before I boarded the airplane to the US. Over the years, her resourcefulness and kindness increase my appreciation of Penn Chemistry even more. I want give special thanks to the Family Center and all their staff members there. Their social, emotional, and financial supports has really helped so much to my family. I am grateful for the center that reminds me Penn is not only a place of academic excellence, but also a place that truly care about the people in the community regardless of backgrounds.

lastly, I would like to thank my parents for their unconditional love, my most dearly wife for her love, encouragements and caring, and our lovely kids who fill my life with joy.

## ABSTRACT

### THEORETICAL AND COMPUTATIONAL STUDIES OF HEAT TRANSPORT PROCESSES IN MOLECULAR SYSTEMS

Renai Chen

Abraham Nitzan

There has been growing research interest in the field of nanoscale thermal transport over the past two decades due its importance to a variety of fascinating applications, such as waste heat control, improved electronic functionality, and phononics building blocks. Much of this focus has been on solid-state systems for which advanced experimental characterizations and measurements are readily available. Molecule-based systems, which in principle exhibit no less structural richness than solid-state systems and may show excellent energy transport capabilities, have been largely ignored until recently. This is mostly because of the difficulties associated with measuring heat transport on the molecular scale. However, a few recent experimental breakthroughs have brought molecular energy transport process into the spotlight, and at the same time established measurement techniques that can be tested, verified, and explained using theoretical tools. This dissertation examines and explores theoretical approaches for modeling heat transport in molecular systems. Specifically, we have developed a stochastic nonequilibrium molecular dynamics (MD) method which mimics the experimental setting of substrate-bridge-substrate structure, i.e., a molecular junction. We incorporate this approach, along with a quantum Landauer's formalism, into the open-source molecular simulation package—GROMACS, so that it can be applied to molecular systems with different topologies and thermal environments. Our simulations of heat conduction in hydrocarbon-based single molecule junctions yield excellent agreement with the recent state-of-the-art experimental data. Within the



capacities of the new method, we have also investigated phononic interference effects in the heat conduction characteristics of benzenedithiol molecules. Using the methods developed in this dissertation, we have mapped, for the first time, thermal fluxes down to the atomistic level. In the context of phononic energy transport, we develop a simulation method that integrates quantum effects into classical MD. This hybrid method, once fully implemented, will compensate for the disadvantages of classical approaches at low temperatures and for the difficulty in treating anharmonicities in Landauer-type quantum transport calculations. This method will improve the predictive power of classical heat conduction simulations.

The second part of this dissertation explores an intriguing energy transport channel that has been newly discovered termed electron-transfer-induced heat transport (ETIHT), which is distinct from traditional heat transfer mechanisms that rely purely on molecular vibrations. We construct a theoretical model that combines the two energy transport channels (ETIHT and phononic) into one general model and then we show analytically under certain parametric thresholds (e.g. reorganization energies) that ETIHT dominates while other conditions may magnify the phononic contributions. Although the work in this part of the thesis is currently purely theoretical, it may provide useful insights into future organic molecular thermoelectric devices.

# LIST OF CONTENTS

<b>DEDICATION</b>	<b>ii</b>
<b>ACKNOWLEDGMENT</b>	<b>iii</b>
<b>ABSTRACT</b>	<b>v</b>
<b>LIST OF ILLUSTRATIONS</b>	<b>x</b>
<b>CHAPTER 1 Introduction</b>	<b>1</b>
<b>CHAPTER 2 Phononic energy transport in molecular junctions and its molecular dynamics simulation realization</b>	<b>8</b>
2.1 Introduction . . . . .	8
2.2 Model and Methodology . . . . .	11
2.2.1 Classical simulations . . . . .	11
2.2.2 Quantum calculations in the harmonic approximation . . . . .	18
2.2.3 Quantification of mode localization . . . . .	19
2.3 Results and discussion . . . . .	21
2.4 Conclusion . . . . .	32
2.5 Disorder effect on molecular thermal transport . . . . .	33
2.5.1 Introduction . . . . .	33
2.5.2 Results for this section . . . . .	34
2.5.3 Conclusion . . . . .	45
2.6 Calculation of energy resolved transmission . . . . .	46
<b>CHAPTER 3 Local Atomic Heat Currents and Classical Interference in Single-Molecule Heat Conduction</b>	<b>51</b>
3.1 Introduction . . . . .	51

3.2	Model and methods . . . . .	53
3.2.1	Molecular dynamics simulation . . . . .	53
3.2.2	Landauer-type calculations . . . . .	54
3.3	Results and discussion . . . . .	56
3.4	Conclusion . . . . .	65
<b>CHAPTER 4 Quantum bath augmented classical simulation for heat conduction</b>		<b>67</b>
4.1	Methodology . . . . .	67
4.1.1	Formalism for quantum bath effects in Langevin dynamics . . . . .	67
4.1.2	Specifications of systems with Debye bath signature . . . . .	70
4.2	Numerical tests . . . . .	76
4.2.1	Equilibrium energies obtained after long-time relaxation . . . . .	76
4.2.2	Vibrational relaxation of a diatomic molecule . . . . .	80
4.2.3	Heat conduction through a diatomic molecule . . . . .	82
<b>CHAPTER 5 Electron-transfer-induced and phononic heat transport in molecular environments and energy partitioning in relaxation and activation</b>		<b>88</b>
5.1	Introduction . . . . .	88
5.2	Theory of Multithermal Electron Transfer and Heat Conduction . . . . .	90
5.2.1	System details . . . . .	90
5.2.2	Multithermal electron transfer theory . . . . .	93
5.2.3	Derivation of energy partitioning using master equations . . . . .	97
5.2.4	Electron-transfer-induced heat transport (ETIHT) . . . . .	99
5.2.5	Vibrational heat transfer . . . . .	105
5.3	Results and Discussion . . . . .	106
5.4	Conclusions . . . . .	111

<b>CHAPTER 6</b>	<b>Conclusion and outlook</b>	<b>113</b>
<b>APPENDIX A</b>	<b>Appendix of chapter 2</b>	<b>116</b>
A.1	Setting the substrate . . . . .	116
A.2	Additional details on molecular configuration preparation and MD simulation procedures . . . . .	119
A.3	Derivations of heat currents and end-to-end delocalization . . . . .	121
A.3.1	Atomic local heat fluxes . . . . .	121
A.3.2	Derivation of end-to-end delocalization parameters of energy transfer . . . . .	123
A.4	Supplemental MD simulation results . . . . .	127
A.5	Supplemental Landauer-type results for hydrocarbon heat conduction	127
A.6	Debye Spectrum density generator and diatomic heat conduction . . .	133
A.6.1	Introduction . . . . .	133
A.6.2	Implicit bath density properties . . . . .	135
A.6.3	Center of mass potential equilibrium expansion for exponential repulsive forces . . . . .	136
A.6.4	Bridge the formalism and parameters . . . . .	141
<b>APPENDIX B</b>	<b>Appendix of chapter 3</b>	<b>153</b>
<b>APPENDIX C</b>	<b>Appendix of chapter 4</b>	<b>161</b>
C.1	Explicit Debye bath simulation with two atomic layers . . . . .	161
C.2	Anharmonic potential for the system-bath coupling in the toy model .	161
C.3	Dimensionless units . . . . .	165
<b>BIBLIOGRAPHY</b>		<b>166</b>

## LIST OF ILLUSTRATIONS

2.1	A schematic diagram of the explicit bath model. Region I is the molecular system (including thiol groups); Region II represents the interface and is comprised of explicit layers of metallic materials; Region III are implicit baths representing the infinitely large thermal reservoirs, exerting white noise. . . . .	12
2.2	The steady-state temperature profile for 1,6-hexanedithiol, connecting two gold substrates that are maintained at temperatures 350K and 300K, comparing UFF all-atom and UFF unified-atom force fields. The horizontal axis is labeled by the backbone atoms, Au-S-C-. . . -C-C-S-Au, so that “1” and “10” correspond to the interfacial gold atoms on the two sides. The insert is the illustration of molecular junction structure studied throughout the section (six carbons here). The white noise thermostats are only attached to the layer of gold atoms furthest from the alkane bridge. The error bars represent the standard error. <sup>1,2</sup>	14
2.3	The heat conductance of junctions comprising gold substrates connected by alkane chains and unsaturated alternating single-triple-bond carbon chains for a temperature bias of 300K-350K, obtained from classical MD simulation and displayed as functions of chain lengths. In the legend as well as in the figures below, structures with $-(\text{CH}_2)_n-$ and $-(\text{C})_n-$ denote alkanes and conjugated polyynes respectively. The Standard Error (SE) <sup>1,2</sup> of the computed conductance values shown in the legend is smaller than the size of the square points in the graph.	22
2.4	Heat conductance as function of length of saturated alkane chains (upper panel) and conjugated polyene chains (lower panel), obtained from the classical MD simulations and from Landauer-type quantum calculations (the later done under the harmonic approximation), respectively. The gold substrates temperatures are 350K and 300K. The classical heat conductance is defined as the ratio between the computed steady state heat current and the (50K) temperature bias. . . . .	23

2.5	Temperature profiles for some of the carbon chains shown in Figure 2.3, obtained from the classical MD simulations. In the legend, structures with $\text{CH}_n$ and $\text{C}_n$ denote alkanes and conjugated polyynes respectively. The horizontal axis is labeled according to the index of backbone atoms, starting with the gold atom nearest to the molecules (e.g., atom 1 and 12 for the $(\text{CH}_2)_8$ and $\text{C}_8$ molecules, while atoms 2 and 11 of these molecules are sulfur atoms). The temperatures of the left and right leads are set to 350K and 300K respectively. The error bars represent the $\text{SE}^{1,2}$ of the computed average temperature. . . .	24
2.6	Low temperature heat conductance of alkane chains with temperature bias 25K-75K. Shown are results of from classical MD simulations and quantum Landauer-type calculations. $\text{SE}^{1,2}$ (which are smaller than the square points in the graph) is shown for the classical stochastic simulations. . . . .	26
2.7	Histograms of the normal mode distribution of some representative molecules. The x-axes are the histogram bins (frequencies in wavenumbers), and the y-axes are the count of modes with frequency in the bin. The corresponding molecular topologies are drawn within each panel. Note that the first and last atom in each molecule are sulfurs. The first row shows the normal mode histogram for three- and four-layers gold pyramids (left and right columns, respectively). The following rows depict alkanes (left) and polyynes (right) with 4, 8, and 16 carbon units, respectively. . . . .	28
2.8	Product of participation ratio defined in Equation 2.17 and density of state of the normal modes for different hydrocarbon molecules. (Smoothed as in Eqn. 2.21 with $\Delta\omega = 10\text{cm}^{-1}$ ) This quantity is displayed as function of frequency for 4-carbon chains (upper panels) and 12-carbon chains (lower panels) capped with thiol groups. (The inserts show the same quantities plotted for the $0 - 3000\text{cm}^{-1}$ range with smoothing parameter $\Delta\omega = 50\text{cm}^{-1}$ .) . . . . .	29
2.9	The end-to-end mode delocalization parameter (Eqn.2.20) calculated for different hydrocarbon molecules and displayed as function of frequency for 4-carbon chains (upper panels) and 12-carbon chains (lower panels) capped with thiol groups. (The inserts shows the same quantities plotted for $0 - 3000\text{cm}^{-1}$ range with smoothing parameter $\Delta\omega = 50\text{cm}^{-1}$ .) Unlike Figure 2.7, in which the full force-field has been used, the unified-atom force field (no explicit hydrogens) is used here for the alkanedithiol chains. . . . .	30

2.10	The quantum transmission function, Eqn. 2.13 displayed as function of frequency for different hydrocarbon molecules and shown as function of frequency for 4-carbon chains (upper panels) and 12-carbon chains (lower panels) capped with thiol groups. Smoothing $\Delta\omega = 10\text{cm}^{-1}$ has been applied to this spectrum. The inserts shows the same quantities plotted for the $0 - 3000\text{cm}^{-1}$ range with smoothing parameter $\Delta\omega = 50\text{cm}^{-1}$ . . . . .	31
2.11	Heat current change of a harmonic 1-D chain, with respect to the change of disorder mass, calculated with Landauer-type formalism. The mass of the middle atom on the chain is set to be different (disorder) to the rest of the lattice (in this example, the 6th atom on a lattice of 11 atoms. Force constants are the same throughout). The parameters are: force constant $k=1$ , $\gamma=10$ , $m=10$ (ordered), $T_L=1$ , and $T_R=1.5$ , all of which are given in reduced units with characteristic dimensions: $\tilde{\sigma}=1\text{nm}$ , $\tilde{\tau}=1\text{ps}$ , $\tilde{m}=1m_{amu}$ , $\tilde{k}=10^5(\text{kJ mol}^{-1} \text{nm}^{-2})$ and $\tilde{T}=300\text{K}$ . The curve is scaled by the ordered chain case (i.e. all the masses are equal to $10\tilde{m}$ ) . . . . .	37
2.12	Heat current change of a harmonic 1-D chain, with respect the change of force constant, calculated with Landauer-type formalism. The force in the middle of the chain is set to be different (disorder) to the rest of the lattice (in this example, the 5th $k$ on a lattice of 11 atoms with 10 constants). The parameters are: force constant $k=1$ (ordered), $\gamma=10$ , $m=10$ , $T_L=1$ , and $T_R=1.5$ , all of which are given in reduced units with characteristic dimensions: $\tilde{\sigma}=1\text{nm}$ , $\tilde{\tau}=1\text{ps}$ , $\tilde{m}=1m_{amu}$ , $\tilde{k} = 10^5(\text{kJ mol}^{-1} \text{nm}^{-2})$ and $\tilde{T}=300\text{K}$ . The curve is scaled by the ordered chain case (i.e. all the force constants are equal to $1\tilde{k}$ ) . . . . .	38
2.13	Temperature profile for disordered alkanes of various lengths. The number of backbond atoms in the molecules are 3, 5, 7, 9, 11, 13, 15, 17, 19, respectively, with Si sitting at the middle of every chain and the rest are carbons. The horizontal axis is labeled according to the index of the backbone atoms. The temperatures of the left and right baths are set at 350K and 300K respectively. The error bars are standard errors <sup>1,2</sup> of the temperature measurements. . . . .	41
2.14	Temperature profile for disordered alkanes of 11 backbone atoms with different elements being the 6th atom of each chain, (different elements labeled in the legend) and rest are carbons. The horizontal axis is labeled according to the index of the backbone atoms. The temperatures of the left and right baths are set at 350K and 300K respectively. The error bars are standard errors <sup>1,2</sup> of the temperature measurements. (the computed values of the errors is smaller than the size of the circle points in the graph. So that is why bars cannot be seen for most points except the middle impurity sites) . . . . .	42

2.15	Configurations of molecular structures for the asymmetric interface effects on molecular heat conduction. (a) undecane; (b) pentacene; (c) naphthalene+hexane. . . . .	44
2.16	Temperature profile for three molecular configurations (as labeled in the legend) shown in Figure 2.15 and the insert. The horizontal axis is labeled according to the index of the backbone atom groups. That is, one index is for a single carbon group along the chain or two vertical (normal direction) carbons as (with averaged temperature) one group for the rings circled in red as examples shown in the Figure 2.15. The temperatures of the left and right baths are set at 350K and 300K respectively. The error bars <sup>1,2</sup> are standard errors of the temperature measurements. . . . .	45
2.17	One dimensional damped and driven harmonic chain . . . . .	47
2.18	Frequency resolved energy flux (arbitrary units) generated by driving one sulfur atom the chain molecule and evaluating the heat generation per unit time on the other sulfur taking friction $\gamma = 20 \text{ cm}^{-1}$ to affect the motion along the S-C bond, calculated according to Eqn (2.28). $N$ is the number of backbone carbon atoms, and all molecules are capped with thiol groups. "Saturated" refers to alkanedithiols, while "Unsaturated" refers to conjugated carbon chains with alternating single and triple bond (polyyne)s. The insert in the first figure is a zoom-out of a larger y-scale (0-1) of the same flux. . . . .	49
2.19	The intergarls $I(\omega) = \int_0^\omega J(\omega)$ over the frequency resolved heat fluxes of Figure 2.18, normalized by $I_{N=4,saturated}(3000\text{cm}^{-1})$ and displayed against $\omega$ for the four hydrocarbon species. $N$ is the number of backbone carbon atoms, and all molecules are capped with thiol groups. "Saturated" refers to alkanedithiols, while "Unsaturated" refers to conjugated carbon chains with alternating single and triple bond (polyyne)s.	
	50	
3.1	Schematic diagram of electron transport (a) and vibrational energy transfer (b) in molecular junctions . . . . .	52
3.2	Artist representation of a typical system studied in this work. The unidirectional arrows across left plane ( $P_L$ ) and right plane ( $P_R$ ) denote the direction of heat flows. The double arrows show the connections between the exterior layer of gold lead to the thermal reservoirs, which are characterized with temperature $T_L$ and $T_R$ respectively. . . . .	55



3.3	Thermal conductance of dithiolated-benzene molecules in gold-molecule-gold junctions with different connection (para, meta, and ortho) configurations. Shown are results from classical MD simulations and from the quantum Landauer’s formula. The error bars represent standard errors (= standard deviation / square root of the sample size, which is a statistical uncertainty indicator of the estimated mean value of the conducted measurements. <sup>2</sup> ). The green and black dots represent the conduction calculated using the Landauer formula and classical MD simulations, respectively, for the meta configuration in which heat transport through the site marked X is blocked by taking the mass to be artificially large (100 carbon atom mass). . . . .	57
3.4	Thermal conductance for para-, meta- and ortho- benzenedithiol molecules, calculated from classical MD simulations and from the Landauer expression under different temperatures: a) $T_{hot}=350\text{K}$ and $T_{cold}=300\text{K}$ ; b) $T_{hot}=650$ and $T_{cold}=600\text{K}$ ; c) $T_{hot}=60$ and $T_{cold}=10\text{K}$ . The error bars for MD represent standard errors (as in Figure 3.3). . . . .	59
3.5	Thermal conductance for para- and meta- benzenedithiol molecules, simulated for the configurations with and without replacing one hydrogen with one fluorine at the position indicated in the molecular diagram, for the temperature bias of 300K to 350K. Panel (a) and (b) show results from MD and Landauer calculations, respectively. The error bars in Panel (a) represent standard errors (see caption of Figure 3.3). . . . .	60
3.6	Heat currents maps in junctions comprising benzene molecules connecting in (from left to right) para, meta, and ortho configurations between gold substrates, computed by MD simulations at steady state under temperature bias of 300K and 350K on the two sides of the junction. (a). Molecular structures indicating atom numbering that is used in panel (c). Small light gray balls, bigger dark gray balls, red balls and yellow balls represent hydrogen, carbon, sulfur and gold atoms, respectively. (b) A map of local heat currents calculated at steady state for the three junction configurations. Arrows and thickness correspond to directions and magnitudes of the local currents. (c) two-dimensional map of local currents between atoms arranged according to the numbering shown in panel (a). Current direction is here indicated by sign: positive corresponds to leftward or leftward-tilted flux, or for vertical flow (for example between atom 3 and 6) – to upward flux. Note that the heat current maps shown in (panel c) are symmetric with respect to the white dashed diagonal line. . . . .	62

3.7	Frequency resolved energy flux (arbitrary units) generated by driving one sulfur atom of a benzenedithiol molecule and evaluating the heat generation per unit time on the other sulfur taking friction $\gamma = 20 \text{ cm}^{-1}$ to affect the motion along the S-C bond, calculated according to Eqn. (2.28). . . . .	63
3.8	The integrals $I(\omega) = \int_0^\omega d\omega J(\omega)$ over the frequency resolved heat fluxes of Figure 3.7, normalized by $I_{para}(3000 \text{ cm}^{-1})$ and displayed against $\omega$ for the three benzenedithiol species. . . . .	64
4.1	Schematic drawing of the Debye bath composed of N atoms, attaching a bridge molecule on the left and white bath on the right. . . . .	70
4.2	Schematic drawing of the Debye bath composed of 2 atoms (simplified version of Fig 4.1) . . . . .	74
4.3	Equilibrium energies of a single particle in a Morse potential connected to thermal bath of different characteristic temperatures (T indicated on the x-axis). All dimensionless quantities are scale with respect to the oscillating frequency ( $\omega$ ) of the corresponding harmonic potential with the relation $2D\alpha^2 = m\omega^2$ (see Appendix C.2). Specifically, the unit for T is $\hbar\omega/k_B$ , the unit of inverse length $\alpha$ is $\sqrt{m\omega/\hbar}$ and the energy unit is $\hbar\omega$ . The insert is a zoom-in of the full figure to the T range of 0 to 2. . . . .	79
4.4	Schematic drawing of the diatomic molecule attached to a Debye bath simulated with two harmonically bonded atoms. The molecule is represented as number 0, connected to the bath atoms, which are parameterized according to Eqn. 4.48. . . . .	80
4.5	Examples of energy relaxation rates of the diatomic molecule shown in Fig. 4.4, with classical and quantum (effective temperature method) baths. With internal vibration frequency about 1/4 of Debye and temperature 0.2 ( $\hbar\omega_D/k_B$ ). The x-axis is the evolution time. The slopes of the logarithmic fits of the energy changes (y-axis values) are 0.000209 for the classical and 0.000207 for the quantum, which correspond to their relaxation rates respectively. . . . .	81

4.6	Relaxation rates for the diatomic molecule with respect to different temperatures, under Debye bath composed of two layers of atoms shown in Fig. 4.4. Two sets of internal vibration frequencies of $1.5\omega_D$ and $3\omega_D$ are compared to the frequency of $0.25\omega$ . The force constant ( $k_{01}$ ) is 0.002 in all cases. The comparative data are all labeled in the legend, the numbers(e.g. 1.5, 0.25) denote the internal vibrational frequencies in which the oscillators are simulated (in the anharmonic cases, the potential energies depth and characteristic lengths are chosen to be equal to the harmonic force constants, i.e. $k_{01} = 2\alpha^2 D$ , details in Appendix C.2). The quantum results refer to the “effective temperature (ET) approach”, while classical results is for traditional constant temperature method. . . . .	83
4.7	Comparisons of relaxation rates for the diatomic molecule with different interacting/coupling strengths ( $k_{01}$ in the model, other parameters are the same as in Fig. 4.6). The x-axis is temperature. . . . .	84
4.8	Heat currents for the 1-D diatomic system under three different approaches. The Landauer-type calculations are based on the normal modes in the system, while the other two with error bars (standard deviations) are results from MD simulations. Tconst means classical constant temperature baths while Teff refers to the quantum augmented baths formulated in the method section. X-axis is the temperatures for the left bath, while the right bath is always 50K higher in all the settings. Y-axis are normalized (by Landauer’s current at 2500K) heat currents (MD results are sampled from steady-state inter-atomic heat currents <sup>3,4</sup> ) The units for the system are: 15 a.m.u. for the atomic masses; $292900 \text{ kJmol}^{-1}\text{nm}^{-2}$ for the harmonic bond; $1 \text{ ps}^{-1}$ for the molecule-bath coupling (as in Langevin’s dynamics); and $100 \text{ ps}^{-1}$ for the maximum quantum bath frequency (with 50000 small intervals). . . . .	86
5.1	Schematic of the energetics of heat exchange and energy partitioning between baths during the ascent to the transition state (shown as a circular marker) and the descent to the energy origin of the respective state. The dashed curves represent the energy surfaces $E_A$ and $E_B$ . . . . .	99
5.2	Electron-transfer-induced (solid; black) and phononic (dashed; black) heat currents $\mathcal{J}_Q$ (current direction from left to right) and electron transfer rates $k_{A\rightarrow B}$ (solid; blue) and $k_{B\rightarrow A}$ (solid; red) as functions of the free energy difference $\Delta E_{BA}$ . Units and scale of the heat currents and electron transfer rates are shown on the left and right axes, respectively. The system-bath couplings are $\gamma_a^{(1)} = 1.0 \text{ ps}^{-1}$ , $\gamma_b^{(1)} = 0.1 \text{ ps}^{-1}$ , $\gamma_a^{(2)} = 0.1 \text{ ps}^{-1}$ in both panels, and in (a) $\gamma_b^{(2)} = 1.0 \text{ ps}^{-1}$ and (b) $\gamma_b^{(2)} = 0.05 \text{ ps}^{-1}$ . Other parameters are: $V_{A,B} = 0.01 \text{ eV}$ , $E_{R1} = 0.06 \text{ eV}$ , $E_{R2} = 0.04 \text{ eV}$ , $T_a = 300 \text{ K}$ , and $T_b = 270 \text{ K}$ . . . . .	107

5.3	Electron-transfer-induced and phononic heat currents $\mathcal{J}_Q$ (current direction from left to right) as a function of temperature difference $\Delta T = T_a - T_b$ for various values of the reaction free energy $\Delta E_{BA}$ shown in the legend of (a). The system-bath couplings are: $\gamma_a^{(1)} = 1.0 \text{ ps}^{-1}$ , $\gamma_b^{(1)} = 0.1 \text{ ps}^{-1}$ , $\gamma_a^{(2)} = 0.1 \text{ ps}^{-1}$ in both panels, and in (a) $\gamma_b^{(2)} = 1.0 \text{ ps}^{-1}$ and (b) $\gamma_b^{(2)} = 0.05 \text{ ps}^{-1}$ . Other parameters are: $V_{A,B} = 0.01 \text{ eV}$ , $E_{R1} = 0.06 \text{ eV}$ , $E_{R2} = 0.04 \text{ eV}$ , and $T_b = 270 \text{ K}$ , which is fixed. . . . .	110
A.1	Heat conductance for the molecule $\text{HS}(\text{CH}_2)_6\text{SH}$ connecting surfaces represented by a given numbers $n$ of gold layers interacting at their far ends with white thermal baths characterized by temperatures $T_L = 300\text{K}$ and $T_R = 350\text{K}$ . The bars shown in the Figure are the standard errors (SE) <sup>2</sup> of the calculated conductance. . . . .	118
A.2	Velocity-velocity autocorrelation functions of the only atom in the first layer of each of four different gold clusters. The outermost layers are attached to Markovian thermal reservoirs at temperature of 300K and the clusters are allowed sufficient time (e.g. a few nanoseconds) to relax to the temperature of the bath. Column (a): Velocity time-autocorrelations, $C_{vv}(t)$ , which are normalized to the value at $t = t_1 - t_2 = 0$ ; Column (b): The Fourier transforms of the corresponding correlations, normalized across the whole spectra; Column (c): Artistic representation of the corresponding gold clusters. . . . .	119
A.3	Molecular heat conduction MD simulation procedure and implementation diagram, with Landauer-type quantum calculations included. . .	120
A.4	Total heat conductance for molecular systems with different chain numbers. The molecule unit is hexanedithiol, with number of 1, 2, 4, and 6 chains aligned in parallel and embedded in three layers of Gold substrates in the junction. The temperature bias is set to be 50K. The conductance is calculated by dividing the total heat currents to the temperature difference, and the total currents are calculated as sums of currents in individual chains (intermolecular interaction is not considered here) that go from one side of each chain to the other side. The error bars represent Standard Error <sup>1,2</sup> . . . . .	128
A.5	Heat conductance of saturated carbon-backboned chain molecules with different substitutions to hydrogens. Each species are connected with thiol groups at the two sides of the molecules and further connected to three layers of gold substrates. The temperatures are 300K and 350K on the right and left sides of the junction respectively. The error bars represent Standard Error <sup>1,2</sup> . . . . .	129

A.6	Length-dependent thermal conductance, calculated through the Landauer formula. The exterior-most layers of explicit bulk are coupled to white noise baths. The conductance denotes ratio between heat current and temperature bias, with left and right baths at 300K and 350K respectively. The triangle line has three gold layers, in accordance with the MD simulations. . . . .	130
A.7	Comparison between derivative conductance and finite-bias conductance. For the finite-bias case, bath temperatures of 300K and 350K are taken (i.e. bias of 50K). This is compared with two derivative conductance calculations: Around a temperature of 300K and of 350K.	131
A.8	Temperature dependence of the derivative Landuaer thermal conductance, for butanedithiol ( $\text{HS}(\text{CH}_2)_{10}\text{SH}$ ) adsorbed on a substrate modelled by 3 layers of explicit gold atoms. . . . .	132
A.9	Spectral densities calculated from Eqn. A.28 for different values of n. The dashed line is Debye Spectrum. . . . .	134
A.10	Average decay rate plotted as a function of $\omega$ . The Debye bath is simulated with the accuracy of n=8 in the spectrum function. (Eqn.A.28) The circles are simulated results and the solid line is quadratic fitting of the simulated data. . . . .	135
A.11	Fourier transform of the random position autocorrelation function of $\langle R(t)R(0) \rangle$ for n=8. the circles are numerical implemented data points, and the solid line is plotted according to Eqn. A.28. . . . .	137
A.12	Local temperature of a single impurity calculated from kinetic energy ensemble, when it is put near a Debye bath with temperature of 50K.	138
A.13	Potentials with respect to the particle position. Equilibrium postion is set to be at origin. position is in the unit of width of the rigid body $D$ (The boundaries are $y_l = -3$ and $y_r = 3$ ). Other paramters are: $A = 1, \alpha = 1$ . . . . .	140
A.14	Numerical plot for normalization factor with respect to the value of n	149
A.15	Steady state heat current with regard to the change of relative interaction of diatomic molecule. the blue dot is harmonic link between system and bath, the green dot is expontential link, and the red solid line is for center of mass as a single partcle of the diatomic system. The unit for the heat current is $kcal \cdot mol^{-1} \cdot (48.889fs)^{-1}$ . . . . .	152
B.1	Histogram of normal mode distributions of different substitutions of benzenedithiols. . . . .	154
B.2	Local temperature profiles of the atoms in benzenedithiol molecules with different substitution positions, measured from ensembles of kinetic energies of the atoms at steady states. The unit is in Kelvin. The temperatures of the cold and hot baths are 300K and 350K respectively. The errors represent standard error <sup>1,2</sup> . . . . .	155

B.3	Schematic graph of a ring molecule with only nearest-neighbour harmonic interactions, bridged by two linear chains. The circles are atoms in the molecule, and the dots represent the hidden numbers of atoms that are not shown. The molecule is segregated by four branches: left, top, bottom and right. The incident wave comes from the left (partly reflected), propagates (partially reflected) and leaves the system from the right. . . . .	156
B.4	Transmission probability for different substitutions of benzene-like (six atoms in the backbond) based on the harmonic ring model. (a) The overall transmission from the left side to the right side; If we define total transmission ratio over the period plot here as: The integrations of the corresponding functions divided by the square areas when the probability equals unity, we will have in the overall transmission figure (a) para: 34.8%, meta: 17.8%, ortho: 45.0%. . . . .	158
B.5	Total heat conductance for Benzene-based ring molecules, that is, Benzene, Naphthalene and Anthracene. Simulation details (e.g.substrates, biae and couplings) are described in Chapter 2 and Section A.1. The error bars represent Standard Error <sup>1,2</sup> . . . . .	160
C.1	velocity-velocity autocorrelation function of the atom 0 in Fig. 4.2 . .	162
C.2	Fourier transform of the position of the atom 0 in Fig. 4.2 autocorrelation function $\langle R(t)R(0) \rangle$ . The circles are numerical implemented data points, and the solid line is analytical expression shown in the legend.	163
C.3	Equilibrium energies of a single harmonic oscillator connected to thermal bath of different characteristic temperatures (T indicated on the x-axis). All dimensionless quantities are scale with respect to the oscillating frequency ( $\omega$ ) of the particle. Specifically, the unit for T is $\hbar\omega/k_B$ , and the energy unit is $\hbar\omega$ . The insert is a zoom-in of the full figure to the T range of 0 to 2. . . . .	164

# CHAPTER 1

## Introduction

The idea that energy transport at the molecular level, which often manifests itself as heat transfer, can be controlled and manipulated as we have done to electrical currents in molecular electronics, is intriguing. There are multiple motivations behind this idea, but the primary one is to improve the stability and functionality of nanoscale and molecular electronics.<sup>5,6</sup> Other more ambitious motivations include the potential realization of phononic devices<sup>7</sup> which may form the basic building blocks of thermal computations in the future.

Heat conduction in molecules has become a subject of increasing interest because of its fundamental role in transmitting and dissipating energy on the atomistic scale as well as its technological importance in the performance and stability of molecular nanodevices.<sup>6,8-15</sup> The recent measurement of heat conduction in single-molecule junctions<sup>16</sup> demonstrates the development of state-of-the-art microscopic thermal probing and measuring techniques, and potentially opens the door for unveiling the interplay between molecular structure and thermal transport properties.

Nevertheless, the progress of technological applications using single molecules has been slow because of the lack of understanding of the fundamental mechanisms that govern molecular heat transport, which has been shown to behave differently than its macroscopic counterpart. One example of this is that Fourier's law of heat transfer is typically violated at the atomistic level.<sup>17</sup> Therefore, theoretical and computational work that uncovers the basic principles of thermal transfer processes in molecular systems are needed to advance the field. Ultimately, such studies will enhance our overall abilities to control and harvest energy at the nanoscale when combined with

advanced molecular engineering capacities.<sup>14,18</sup>

In molecular systems, there are mainly two different channels for transporting energy: phononic and electron-transfer-induced. The former has attracted significant research interest for a few decades, with many experimental and computational challenges still waiting to be fully resolved.<sup>6,7,9</sup> The possibility of heat being transported by electron transfer was predicted a few years ago.<sup>19</sup> In an interesting analogue to thermoelectric effect in the metals, the electron-induced heat transport has important implications in molecular systems involving electron transfer (ET) processes.<sup>20,21</sup> In this dissertation, we will discuss research efforts that advance the understanding of both these energy transport channels.

Understanding phononic heat transport processes in molecular junctions is a central issue in the developing field of nanoscale heat conduction and manipulation. In chapter two, we will give an introduction to the basic methodologies we use to study the phononic thermal transport in molecular systems examined in the first half of the thesis. Using a stochastic nonequilibrium molecular dynamics simulation framework, we investigate heat transport processes in molecular junctions in the linear response regime and beyond.

One of the innovations we have introduced is to incorporate molecular dynamics (MD) using full molecular force fields into heat conduction simulations. This innovation has been used to examine heat transport in different substrate-molecule-substrate junction structures. An extended molecular model is used to filter Markovian heat reservoirs through an intermediate substrate region, to provide a realistic and controllable effective bath spectral density. In addition, a quantum Landauer-type formalism is also embedded into the total calculation, so as to provide a insightful comparison as well as comprehensive understanding of the conduction processes.

As one of the initial application examples of the developed numerical tool, hy-



drocarbon chain molecules with different bond saturation (alkanes VS. polyynes) are chosen for our simulations. The results are not only compared to previous theoretical studies from different groups, but also to the most recent state-of-the-art experimental data. The results obtained for alkanedithiol molecules connecting gold substrates agree with previous nonequilibrium Green’s function calculations and match recent experimental thermal conductance measurements of single molecular junctions. For example, our method predicts a thermal conductance of approximately 20 pW/K for alkanedithiols, in strong agreement with experimental measurements. Analyses obtained from different perspectives show anharmonicity, temperature, and localization could all play roles in determining the strength of the heat conduction in the molecules.

In the next section, we probe the effects brought by disordered interfaces (e.g. in the form of molecular impurity) to molecular heat conduction. Simulations show a small amount of disorder in a pure molecule (e.g. silicon replacing carbon in an alkane chain) or structural symmetry changes (e.g. changing the bridge in a junction from a hydrocarbon chain to a ring-chain hybridized molecule) could have significant effects on the heat conduction across the molecules, such as causing ballistic-to-diffusive transition.

In chapter three, we continue our study of molecular heat conduction using ring-based aromatic molecules. An intrinsic, wave-like interference effect in the heat conduction across benzenedithiol single-molecule junctions is uncovered. Previous theoretical descriptions of such effects have relied on the quantum Landauer-type expression for heat transport by harmonic molecules, and such observations are sometimes referred to as “quantum interference”. We demonstrate via classical atomistic simulations of heat conduction in benzenedithiol single-molecule junctions that at room-temperature the interference effect is essentially classical. We also observe a

destructive interference pattern that arises in both classical simulations and quantum calculations, which is interesting especially because there is an analogue to this phenomenon in molecular electronic conduction. At the same time, using the method we described in the previous chapter, we demonstrate the capacity of mapping the total heat current going through a single-molecule junction down to the level of atomic local heat currents. This provides a clearer picture of heat fluxes in the atomic space.

In chapter four, a new computational approach is introduced to merge quantum mechanical calculations with full-force-field classical MD simulations, using some of the advantages of each method in one integrated way. Traditionally, there are two basic theoretical approaches for studying heat conduction in molecular systems, particularly in a molecular junction setting: molecular dynamics (MD) and quantum calculations (QC) based Landauer’s formalism.

Molecular dynamics has been widely used to study the thermal properties of extended systems<sup>22,23,23–32</sup> because of the rich pool of parameterized models that include many-body interactions and its comparatively low computational cost. Quantum calculations are often employed using the harmonic approximations in the form of Landauer transport formula, and although such an approximation may be good at low temperatures, it generally loses applicability at higher temperatures or when anharmonicities or scattering effects are important.<sup>16,18,33–36</sup> As experimental techniques targeting heat transport in single-molecule-junctions (SMJ) develop quickly,<sup>16</sup> there is an urgency for computational scientists to find a way of taking advantages of both MD and QC so that heat conduction in SMJ can be accurately and systematically investigated. In this chapter, we will show such an integration is possible, and how it could be effectively adopted to MD simulations.

The second half of the thesis (chapter five) examines electron-transfer-induced heat transport (ETIHT)<sup>19</sup>. A unified theory of heat transport in environments that sustain

intersite phononic coupling and electron hopping is developed. The heat currents generated by both phononic transport and electron transfer between donor-acceptor sites characterized by different local temperatures are calculated and compared. Using typical molecular parameters, we find that the magnitude of the electron-transfer-induced heat current can be comparable to that of the standard phononic transport for donor-acceptor pairs with efficient bidirectional electron transfer rates (relatively small intersite distance and favorable free-energy difference). In most other situations, phononic transport is the dominant heat transfer mechanism.

Here we describe briefly the theory of electron transfer across a thermal gradient. Let us assume we have a molecular system consisting of two harmonic oscillator modes (that is two parabolas allow the reaction coordinate), in which one mode is in local equilibrium with thermal reservoir of temperature  $T_1$  and the other in local equilibrium with thermal reservoir of temperature  $T_2$  (in general  $T_1 \neq T_2$ ). The two modes do not interact directly, meaning the charge near site 1 only feels the thermal environment of site 1 and the charge near site 2 also only feels the thermal environment of site 2. Under this model setting, the ET rates across the temperature gradient can be evaluated as<sup>37</sup>,

$$k_{a \rightarrow b} \propto \exp \left[ -(\beta_1 E_{R1} + \beta_2 E_{R2}) \left( \frac{\Delta E_{ba} + E_R}{2E_R} \right)^2 \right] \quad (1.1)$$

$$k_{b \rightarrow a} \propto \exp \left[ -(\beta_1 E_{R1} + \beta_2 E_{R2}) \left( \frac{\Delta E_{ba} - E_R}{2E_R} \right)^2 \right]. \quad (1.2)$$

In the above expression, the subscript  $a$  and  $b$  represent the state of the system when the electron stays within the vicinity of site 1 before transfer, and state of the system after the electron hops to site 2, respectively. The characteristic temperatures are represented as  $\beta_j = 1/k_B T_j$  ( $j=1,2$ ).  $E_{R1}$  and  $E_{R2}$  are reorganization energies of harmonic mode 1 and mode 2 alone, while  $E_R$  is the sum of the two.  $\Delta E_{ba}$  denotes

the free energy difference of the two mode parabolas. In the limit of zero thermal gradient ( $T_1 = T_2 = T$ ), the rates above reduce to

$$k_{a \rightarrow b} \propto \exp \left[ -\beta \frac{(\Delta E_{ba} + E_R)^2}{4E_R} \right] \quad (1.3)$$

$$k_{b \rightarrow a} \propto \exp \left[ -\beta \frac{(\Delta E_{ba} - E_R)^2}{4E_R} \right]. \quad (1.4)$$

which agree with the famous Marcus theory<sup>38–40</sup> of ET reaction.

There can be energy transport that arises from electron transfer across a temperature gradient, even when the system is in a nonequilibrium steady state (SS), i.e., when the net charge flux between sites vanishes. Such a heat current is calculated as<sup>37</sup>,

$$J_Q^{(1)} = -J_Q^{(2)} = J_{\text{el}} \frac{2E_{R1}E_{R2}(T_2 - T_1)}{E_{R1}T_1 + E_{R2}T_2}, \quad (1.5)$$

where  $J_Q^{(1)}$  and  $J_Q^{(2)}$  are heat currents flowing out of the thermal reservoirs associated with site 1 and site 2, respectively.  $J_{\text{el}}$  is the unidirectional electronic current at SS. We may see when the two sites have same temperature, the heat current goes to zero, which is in agreement with what would be expected under equilibrium conditions.

The finding of ETIHT in nonequilibrium molecular systems opens a new path for energy manipulation via tuning the ET rate or by controlling chemical reactions using engineering thermal environments. This could have important application in the development of thermoelectric molecular devices. More details on the theory of ETIHT and some recent applications can be found in Ref.<sup>19</sup> and other work<sup>20,21,41,42</sup>. Chapter five examines two the magnitude of ETIHT compares with phononic heat conduction, providing physical insights into both these two different channels in complex molecular systems. This will guide experimental advances toward the measurement of ETIHT.

In summary, this dissertation will, first, give a general survey of the advances in the nanoscale heat transport field, at the molecular level in particular, and, second, show in detail some significant findings from our research using theoretical and computational tools to simulate heat transport at the molecular level.

## CHAPTER 2

### Phononic energy transport in molecular junctions and its molecular dynamics simulation realization

This chapter is partly adapted from *The Journal of Chemical Physics* **153**, 144113 (2020)

#### 2.1 Introduction

Heat conduction in molecular junctions has become a subject of increasing interest because of its fundamental role in transmitting and dissipating energy on the molecular scale as well as its technological importance for heat management in envisioned molecular nanodevices.<sup>6,8,9,11–15,43</sup> Experimentally, such processes were investigated as vibrational energy transfer between molecular moieties that can be vibrationally excited and probed,<sup>13,15,44,45</sup> in adsorbed layers after flash heating a metal substrate,<sup>46–49</sup> along molecular layers connecting two solid substrates<sup>14,30,50–52</sup> and very recently also in single-molecule junctions.<sup>16,53</sup> On the theoretical side, on top of many studies of generic models aimed to examine fundamental aspects concerning the dependence of heat transport in nanoscale systems on dimensionality, disorder and size<sup>12,43,54</sup>, several theoretical and computational studies have investigated specific molecular systems and structures, either by classical molecular dynamics(MD) simulations<sup>30–33,55–60</sup> or by quantum calculations based on the harmonic approximation that enables evaluation of heat conduction by a Landauer-like formula<sup>16,18,34–36</sup>. Such calculations have established, in agreement to experimental observations, the ballistic nature of heat transport through short hydrocarbon and similar chain molecules

(although indications of some diffusive characters are observed in some systems with heavier substituents<sup>15,52,61–63</sup>) as well as sensitivity to molecule-substrate binding and mode-matching.

In the linear response regime, heat transport can be evaluated from equilibrium MD simulations using the Green-Kubo formula<sup>22–26,64–66</sup>. Steady state MD simulations may be done by imposing a temperature difference between the system edges and evaluating the current<sup>22,23,67–69</sup> or, in an inverted fashion, imposing a heat current and evaluating the associated steady state temperature profile.<sup>27–29,70–72</sup> For the present and subsequent numerical studies of the interplay between molecular junctions composition and structure and its heat transport properties, we have developed a numerical tool (described below) that can be readily adapted to different molecules and structures. To make it possible to address non-steady-state situations (such that when the system experiences external driving) we have chosen to use nonequilibrium Langevin dynamics (see, e.g.,<sup>33,73–75</sup>) where each system-bath contact is represented by a stochastic Langevin force and corresponding damping constructed to impose the bath temperature and its spectral properties. Our code is based on the GRONingen MAchine for Chemical Simulations (GROMACS) MD package so that it can readily be applied to many molecular and substrate models and different force fields. Care is taken to address the bath spectral properties, done here by using enough substrate layers as part of the inner system. (Alternatively, this can be achieved by mathematical filtering see, e.g.<sup>76</sup> and also Appendix A.6). A unique feature of our implementation is a model by which we compute heat fluxes between different molecular units, hence obtaining a map of local temperatures and heat currents within the molecular bridge.<sup>3</sup>

Obviously, the computational methodology discussed above is based on classical dynamics which is not generally suitable, at room temperature, for the higher

molecular vibrations. On the other hand, such vibrations are to a good approximation harmonic. In the harmonic approximation a quantum calculation based on a Landauer-type formula (see, e.g.<sup>18,33-36</sup>) can be done. Our code implements this calculation as well, using the molecular normal modes and their couplings to the substrates to calculate the phonon transmission, making it possible to compare quantum and classical results and assess their reliability and relevance. This normal mode analysis can also be used to assess the localization characters of these modes by evaluating their spatial extent and atomic participation ratios,<sup>77</sup> thereby assessing the correlation between these attributes of the molecule and its heat transport behavior.

Here we apply this tool to the study of heat transport in single alkane chains, a system that has been studied numerically<sup>33,34</sup> and experimentally (mostly for alkane layers<sup>50,51,78</sup>, but very recently also for single alkane chains<sup>16</sup>). Our results serve to test our calculations against previous work and compare them to recent experimental results as well as to Landauer based harmonic quantum calculations. Furthermore, we present heat conduction results also for a series of conjugated carbon chains. Such chains are expected to be better electronic conductors<sup>79,80</sup> but are found to be similar to their saturated counterparts in their heat transport behavior.

Section 2.2 provides details on our simulation techniques and our code. Section 2.3 discusses the results of heat conduction properties of different types of hydrocarbon chains within molecular junctions using such approaches, and compare them to the existing theoretical and experimental data. Section 2.4 concludes.



## 2.2 Model and Methodology

### 2.2.1 Classical simulations

While the energy spectrum of molecular vibrations encompasses a relatively large (0 – 0.5 eV) frequency range, high-frequency vibrations tend to be spatially localized, thermally underpopulated and energetically above the cutoff frequency of many solid-state substrates. For these reasons, such modes contribute little to molecular heat transport at room temperature<sup>33</sup>. Molecular heat transport is therefore dominated by lower frequency vibrations, for which classical dynamics provide a reasonable approximation. This behavior is further amplified by the low Debye frequency of the substrate (gold) used in the present study. Available molecular force-fields allow efficient representation of classical, anharmonic molecular potential energy surfaces which are the input to the stochastic nonequilibrium MD studies described below.

In the present work we chose to represent the attributes of the thermal environment using an explicit thermal bath. As shown in Figure 2.1 we extend our molecular system with a few atomic layers of the substrate, which can be seen as the tips of the measuring apparatus and are usually composed of layers of metallic materials (here gold). Such substrates are further connected to infinitely large thermal reservoirs, acting as effective filters of the Markovian white noise.

The system under investigation is a single-molecule junction comprising either alkanedithiols  $HS(CH_2)_nSH$  of different lengths  $n$ , or their conjugated polyyne  $HS(-C \equiv C-)_nSH$  counterparts, connecting gold substrates. Physically, the substrates constitute the thermal baths that drive heat current through the molecular systems, however segments of these substrate (regions II in Figure 2.1) are included in the extended molecule and effectively act as filters for the white noise employed at the interface between regions II and III so as to affect the molecule with the (approximately) cor-

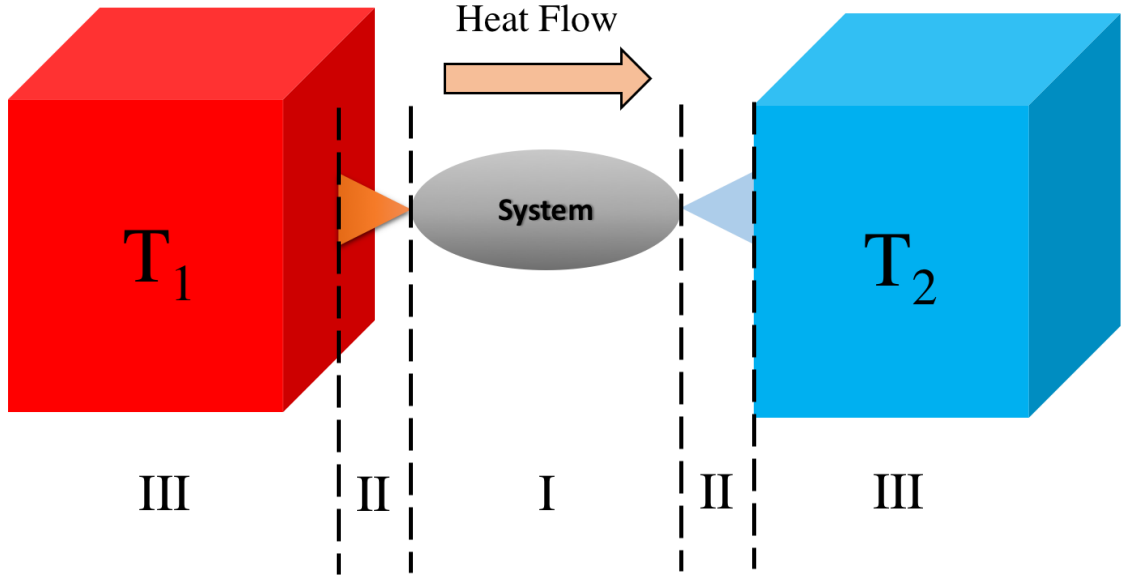


Figure 2.1: A schematic diagram of the explicit bath model. Region I is the molecular system (including thiol groups); Region II represents the interface and is comprised of explicit layers of metallic materials; Region III are implicit baths representing the infinitely large thermal reservoirs, exerting white noise.

rect spectral density of the physical substrate. These segments are taken as pyramids with increasing numbers of atoms per layer (*e.g.* 1, 3, 6, *etc.*, see inserts to Figure 2.2 and A.2) as we go further into the substrate. The atoms in the outermost layer are subjected to white noise and damping related by the imposed temperatures, using standard Langevin dynamics as outlined below. In the simulations presented in Section 5.3 we have used for the extended molecule gold pyramids with 3 gold layers – the smallest number needed to achieve approximate convergence of the heat conduction behavior, see Appendix A.1 for details. Finally, to enforce the junction geometry, the explicit substrate segment is position-restrained by a harmonic force acting on the atoms in the outer layer.

The Universal Force Field (UFF)<sup>81</sup> parameters are chosen throughout the simulations. UFF is one of a few force fields that includes most of the atomic types and bonds across the periodic table, and thus is suitable for organometallic junctions.

As the high frequency carbon-hydrogen bonds often contribute little to the overall vibrational heat conduction, it is reasonable to compare side-by-side the effect of including the hydrogen atoms explicitly appear in the force field (all-atom(aa) UFF ) in comparison to the unified-atom (ua) version of the same force field. Results obtained using these force-fields are compared in Figure 2.2 and Table 2.1 The relative symmetric difference <sup>1</sup> between the calculation results for the two force-fields is 4.89%, and Welch’s t-test<sup>2</sup> is 13%. We therefore conclude that the unified-atom approximation is acceptable for our purposes. To implement the thermal stochastic

	Conductance (pW/K)	SD	SE.
All-Atom	20.73	7.44	0.74
Unified-Atom	21.77	6.40	0.64

Table 2.1: The heat conductance calculated for 1,6-hexanedithiol molecule connecting gold surfaces, using the UFF all-atom and UFF unified-atom force fields. One hundred steady-state trajectories of length 500 ps are taken for each force field. Also shown are the standard deviation (SD) and standard error (SE) associated with this calculation.

boundary conditions, some of the atoms in region II are connected to the external heat baths (region III in Figure 2.1), expressed by standard (constant) friction and (delta-correlated) random fluctuations in their (Markovian Langevin) equations of motion. The Langevin equation of motion for a particle coupled to a Markovian bath is,

$$\ddot{x}_i = -\frac{\partial E(x_i)}{\partial x_i} - \gamma_K \dot{x}_i + R_K^{(i)}(t), \quad (2.1)$$

where  $E(x_i)$  is a mass-weighted energy as a function of the coordinate of the  $i$ th particle  $x_i$ ,  $\gamma_K$  is the friction coupling to the bath  $K$  (in our case  $K \in \{L, R\}$  for the left and right bath), and  $R_K^{(i)}(t)$  is the stochastic noise terms of the respective bath, assumed independent for different connected atoms. The stochastic terms obey the

<sup>1</sup>The relative symmetric difference is  $\delta(x, y) = \frac{|x-y|}{(x+y)/2}$

<sup>2</sup>Welch’s t-test is  $\eta(x, y) = \frac{|\mathbf{E}[x] - \mathbf{E}[y]|}{\sqrt{\sigma_x^2 + \sigma_y^2}}$ , where  $\sigma_x$  is the Standard Deviation in random variable  $x$

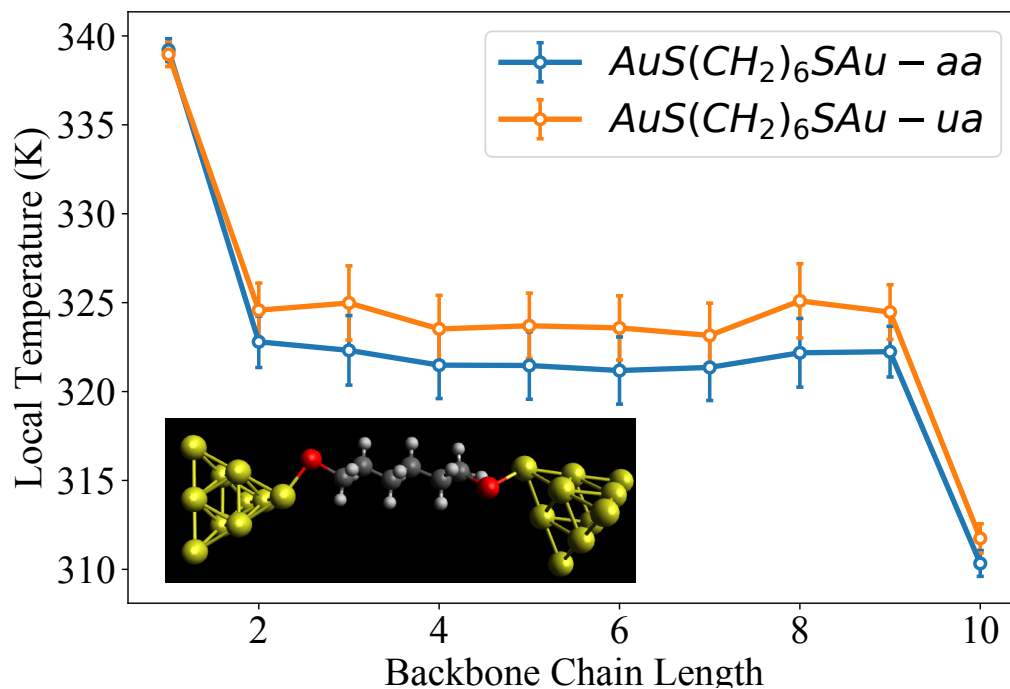


Figure 2.2: The steady-state temperature profile for 1,6-hexanedithiol, connecting two gold substrates that are maintained at temperatures 350K and 300K, comparing UFF all-atom and UFF unified-atom force fields. The horizontal axis is labeled by the backbone atoms, Au-S-C-...-C-C-S-Au, so that “1” and “10” correspond to the interfacial gold atoms on the two sides. The insert is the illustration of molecular junction structure studied throughout the section (six carbons here). The white noise thermostats are only attached to the layer of gold atoms furthest from the alkane bridge. The error bars represent the standard error.<sup>1,2</sup>

usual fluctuation-dissipation relations

$$\left\langle R_K^{(i)}(t)R_K^{(j)}(t') \right\rangle = 2\gamma_K k_B T_K m_i^{-1} \delta(t-t') \delta_{ij}, \quad (2.2)$$

$$\left\langle R_L^{(i)}(t)R_R^{(i)}(t') \right\rangle = 0, \quad (2.3)$$

$$\left\langle R_K^{(i)}(t) \right\rangle = 0, \quad (2.4)$$

where  $i$  and  $j$  are the atoms in the outermost layers in the substrates coupled independently to their respective baths. The underlying simplification provided by this Markovian relaxation dynamics, implemented at the II-III interfaces of Figure 2.1, is amended by the filtering provided by regions II so that the molecule itself is exposed to baths that approximately replicate the actual substrate spectra.

A customized MD package built around GROMACS is developed and utilized to conduct the simulations.<sup>82</sup> The leap-frog algorithm (provided by GROMACS) is used for propagation of the deterministic parts of the system, while Langevin dynamics<sup>83</sup> is used to propagate the stochastic parts of the simulation as described above. Unless otherwise stated, the time step is always 1 fs for all runs and the friction associated with the coupling between the Markovian bath and outermost layer of explicit bulk (region is II) is  $1 \text{ ps}^{-1}$ . Initial conditions are set using different utilities such as *Open Babel*<sup>84</sup>, *Avogadro*<sup>85</sup> and other homemade programs and scripts are used for creating input topologies and indices.

The computed classical trajectories are used to evaluate desired observables that should be averaged over an ensemble of such trajectories obtained from different realizations of the stochastic boundary conditions. To facilitate the calculation of heat currents, the potential energy of the inner system, regions I and II in Figure 2.1, is expressed as a sum of individual interaction terms  $V^{(\tau)}$ , where  $\tau$  refers to different

interaction types, *e.g.*, two-body and three-body interactions, *etc.*, namely

$$E_{pot} = \sum_{\tau} V^{(\tau)}(\{\mathbf{r}_1 \dots \mathbf{r}_{n(\tau)}\}) \quad (2.5)$$

where  $n_{\tau}$  is the number of atoms involved in the interaction  $\tau$ . Note that  $V^{(\tau)}$  itself is a sum of terms in which  $\{\mathbf{r}_1 \dots \mathbf{r}_{n(\tau)}\}$  are the coordinates of any group of  $n(\tau)$  atoms that can be connected by the interaction  $V^{(\tau)}$ . To make it possible to define local energies we assign parts of this interaction to the atomic constituents according to

$$V^{(\tau)}(\{\mathbf{r}_1 \dots \mathbf{r}_{n(\tau)}\}) = \sum_j^{n(\tau)} U_{\tau,j}(\{\mathbf{r}_1 \dots \mathbf{r}_{n(\tau)}\}), \quad U_{\tau,j} = C_{\tau,j} V^{(\tau)}; \quad \sum_j^{n(\tau)} C_{\tau,j} = 1 \quad (2.6)$$

(A similar model has been explored by Torii *et al.*<sup>86</sup>). where the weight factors  $C$  are chosen according to some partition scheme. This choice may reflect some physical intuition about the system and the atoms involved in each interaction type, however in our present calculation we use the simplest symmetric partitioning  $C_{\tau,j} = n(\tau)^{-1}$ . Given the arbitrariness of this choice the resulting scheme should be regarded as informative only on a coarse-grained level, involving molecular localities larger than a single atom or interatomic bond.

With such partitioning defined, the heat flux associated with a given atom  $i$  in the molecular system, is given by (See Appendix A.3.1 for details)

$$J_i \equiv \frac{dE_i}{dt} = \frac{d}{dt} \left( \frac{1}{2} m_i \mathbf{v}_i^2 + \sum_{\tau} U_{\tau,i} \right) = \sum_{\tau} \sum_{j \neq i} J_{\tau,ij}, \quad (2.7)$$

where the heat flux going from atom  $j$  to atom  $i$  which are connected by  $V^{(\tau)}$  is

defined as,

$$J_{\tau,ij} = C_{\tau,j} \mathbf{f}_{\tau,i} \cdot \mathbf{v}_i - C_{\tau,i} \mathbf{f}_{\tau,j} \cdot \mathbf{v}_j. \quad (2.8)$$

where

$$\mathbf{f}_{\tau,k} = -\frac{\partial V^{(\tau)}}{\partial \mathbf{r}_k}; \quad k = i, j \quad (2.9)$$

Eqn. (2.8) and (2.9) can be used to calculate inter-atomic heat currents.

The simulation begins by preparing the desired molecular junction structures (e.g. insert in Figure 2.2) and optimizing their geometries by equilibration to the average temperature of the baths. MD trajectories are generated under the given boundary temperatures (usually 300K and 350K) until steady state is reached (usually about a few nanosecond). With many steady state configurations (often about a thousand steady-state trajectories of 500 ps are taken), interatomic forces and atomic velocities sampled, the overall heat flux  $J_{tot}$  through a plane normal to the heat flow direction is calculated using

$$J_{tot} = \frac{1}{\mathcal{N}} \sum_{s=1}^{\mathcal{N}} \sum_{i \in L, j \in R} \sum_{\tau} J_{\tau,ij}^{(s)}, \quad (2.10)$$

where  $i \in L, j \in R$  implies that atoms  $i$  and  $j$  are on different sides (left and right) of the plane and where  $\mathcal{N}$  is the total steady-state statistical sample number. The average thermal conductance is defined as the ratio between this quantity and the temperature bias between the hot and cold baths,

$$\kappa = \frac{J_{tot}}{T_{hot} - T_{cold}}. \quad (2.11)$$

Furthermore, steady state heat fluxes between individual atom pairs are obtained from Equation(2.8) (see Appendix A.3.1 for more details), which, again, should be

regarded as reflecting exact reality only on a scale larger than individual bond lengths. Note that the latter calculation is not limited to bonded atomic pairs. In addition, the local temperature of each atom in the conducting molecule is calculated from the statistically averaged kinetic energy of the atoms.

## 2.2.2 Quantum calculations in the harmonic approximation

When only the harmonic part of the system-bath interactions is taken into account, the (phononic) heat current can be expressed by the Landauer-like formula<sup>6,33,34,87-90</sup>,

$$J = \frac{\hbar}{2\pi} \int_0^\infty \mathcal{T}(\omega) [f(\omega, T_L) - f(\omega, T_R)] \omega d\omega \quad (2.12)$$

$f(\omega, T) = (e^{\hbar\omega/k_B T} - 1)^{-1}$  is the Bose-Einstein distribution function for a bath of temperature  $T$  and  $\mathcal{T}$  is the transmission probability. The latter can be calculated using the Meir-Wingreen formula<sup>91</sup>

$$\mathcal{T}(\omega) = \text{Tr} [\mathbf{G}_S^r(\omega) \mathbf{\Gamma}_L(\omega) \mathbf{G}_S^a(\omega) \mathbf{\Gamma}_R(\omega)], \quad (2.13)$$

in which  $\mathbf{G}_S^a = [\mathbf{G}_S^r]^\dagger$ , are the advanced and retarded Green's functions of the system and can be written as<sup>87</sup>.

$$\mathbf{G}_S^{r/a}(\omega) = [\omega^2 \mathbf{M} - \mathbf{D} - (\mathbf{\Sigma}_L^{r/a} + \mathbf{\Sigma}_R^{r/a})]^{-1}, \quad (2.14)$$

while

$$\mathbf{\Gamma}_{L/R}(\omega) = i[\mathbf{\Sigma}_{L/R}^r(\omega) - \mathbf{\Sigma}_{L/R}^a(\omega)]. \quad (2.15)$$



In the basis of the atomic coordinates,  $\mathbf{D}$  is the dynamical matrix (or Hessian) whose elements are the second derivatives of the potential energy with respect to the atomic coordinates,  $\mathbf{M}$  is the (diagonal) matrix of atomic masses, and the self-energy matrices  $\Sigma_K^{r/a}$  associated with the K bath ( $K \in L, R$ ) are given by  $[\Sigma_K^r]_{ij} = -i\omega m_i \gamma_K(\omega) \delta_{ij}$ . This simple form expresses our modeling where the outermost gold atoms are taken to interact individually with independent white baths.

To evaluate Eqn.2.13 one needs to obtain the Hessian matrix  $\mathbf{D}$ . The GROMACS software package provides utilities which construct  $\mathbf{D}$  for the given forcefield as well as to obtain the eigenfrequencies and eigenvectors (normal modes) of the system from its diagonalization.

### 2.2.3 Quantification of mode localization

In the harmonic approximation, the contribution of any normal mode to the transmission is reflected by its localization character, which may be quantified by its participation ratio.<sup>33,77</sup> Denote by  $C_{k,\alpha}$  the coefficient for the expansion of the normal mode coordinates  $\{\mu_k\}$  in terms of the atomic ones,  $\{x_\alpha\}$ , *i.e.*

$$\mu_k = \sum_{\alpha} C_{k,\alpha} x_{\alpha}. \quad (2.16)$$

Also define  $p_{k,n} = \sum_{\alpha(n)} |C_{k,\alpha(n)}|^2$  where  $\alpha(n)$  goes over all atomic coordinates (degrees of freedom) associated with a given carbon atom n (all hydrogens attached to this carbon and all spatial directions). Obviously,  $\sum_n p_{k,n} = 1$ . The participation ratio for mode  $k$ , an estimate of the number of carbons strongly associated with this mode, is defined by

$$P_k \equiv \frac{1}{\sum_n p_{k,n}^2}. \quad (2.17)$$

which is 1 if the mode is fully localized on a single atom, and equal to the number of carbon (hydrogens as well if they are present) atoms if it equally delocalized over all of them.

A more stringent measure of the ability of a given normal mode to transfer energy between the two edges of the molecule can be formulated as follows. For simplicity we focus only on the motion along the direction of heat conduction,  $x$ , and denote by  $x_{SL}$  and  $x_{SR}$   $x$ -components of coordinates of substrate (bath) atoms on the left and right sides that connect bilinearly to the nearest molecular bridge atoms,  $x_L$  and  $x_R$ , respectively. Suppose that, and let  $C_{kL}$  and  $C_{kR}$  be the corresponding normal mode expansion coefficients as defined in Eqn.2.16. We show in the Appendix A.3.2 that the response on the left contact to an imposed driving  $x_{SR}(t)$  on the right contact satisfies

$$[\ddot{x}_{SL}]_{L\leftarrow R}(t) \propto \int_0^\infty dt' K(t') x_{SR}(t - t'), \quad (2.18)$$

where

$$K(t) = \sum_k C_{Lk} C_{kR} \frac{1}{\omega_k} \sin[\omega_k t]. \quad (2.19)$$

This suggests that

$$\pi_k \equiv \frac{C_{Lk} C_{kR}}{\omega_k} \quad (2.20)$$

can be used as a measure for the ability of mode  $k$  to transfer energy between the two sides.<sup>92</sup> Below we show the coarse grained versions of  $P_k$  and  $\pi_k$ . For any property

$X_k$  the coarse-grained function is defined by

$$X(\omega) = \frac{1}{\Delta\omega} \sum_{\substack{k \\ \omega_k \in \omega \pm \Delta\omega/2}} X_k \quad (2.21)$$

### 2.3 Results and discussion

Figure 2.3 shows the computed heat conductance of alkanes and polyynes (alternating single and triple bonds), denoted below by  $-(\text{CH}_2)_n-$  and  $-(\text{C})_n-$ , respectively, as function of their lengths. Figure 2.5 shows the corresponding steady state temperature profiles in the different structures. Figure 2.4 compares the results of heat conduction obtained from these classical simulations to those obtained in the harmonic approximation from the Landauer-type expression (Eqn. 3.1).

Qualitative understanding of the observed heat transport behaviors can be achieved by examining the molecular normal modes and their delocalization properties. The normal mode spectra are displayed in Figure 2.7, while their localization properties as expressed by the participation ratios (Eqn. 2.17, coarse grained according to Eqn. 2.21) are shown in Figure 2.8. Figure 2.9 shows the simplified transmission property defined by Eqn. (2.20) and coarse-grained according to Eqn. (2.21). Note that these analyses are presented for bare, not the extended molecules, so these spectral distributions reflect intrinsic molecular properties. The same analyses could of course be done also for the extended molecules. Finally, Figure 2.10 shows the quantum transmission function, Eqn. 2.13, which is a property of the junction, not just the molecular bridge.

The following observations can be made:

(a) The results of alkanedithiol conductance in Figure 2.3 shows a close agreement with the experimental results of Ref.<sup>16</sup> as well as close similarity to the more

sophisticated quantum results obtained in the harmonic approximation<sup>34</sup>.

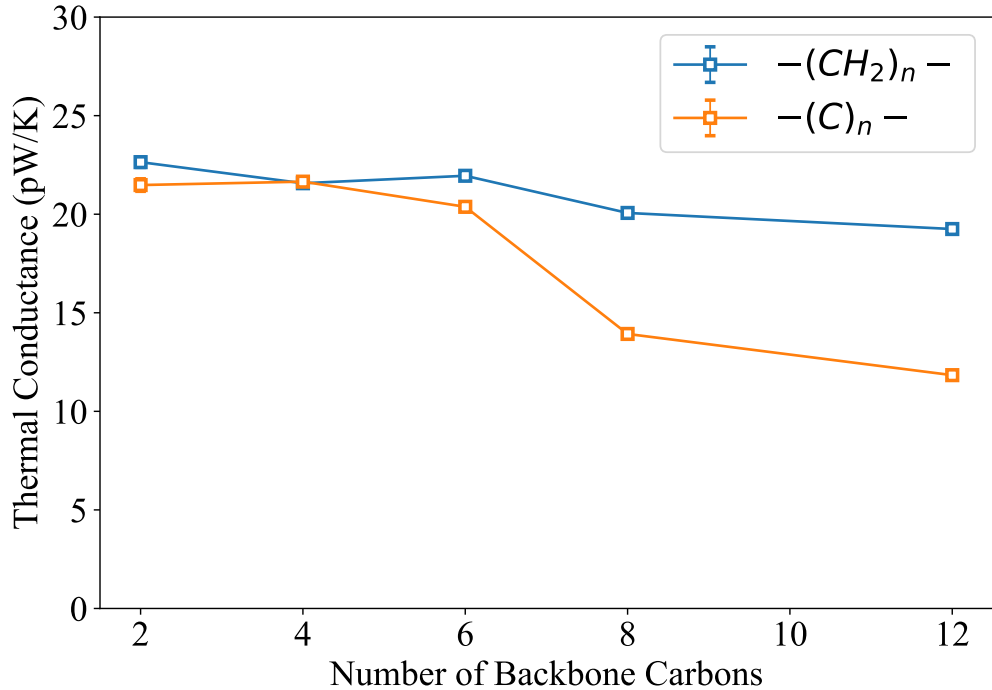


Figure 2.3: The heat conductance of junctions comprising gold substrates connected by alkane chains and unsaturated alternating single-triple-bond carbon chains for a temperature bias of 300K-350K, obtained from classical MD simulation and displayed as functions of chain lengths. In the legend as well as in the figures below, structures with  $-(CH_2)_n-$  and  $-(C)_n-$  denote alkanes and conjugated polyynes respectively. The Standard Error (SE)<sup>1,2</sup> of the computed conductance values shown in the legend is smaller than the size of the square points in the graph.

(b) The bias (300K - 350K) exceeds the regime of validity of linear response, yet is more realistic with respect to existing experimental setups<sup>16,50,51,78</sup>.

(c) The weak dependence of heat conduction on length (Figure 2.3 and 2.4), particularly in the saturated chains, and the flat temperature distribution along the

molecular chains (Figure 2.5) indicate that heat conduction in the molecules studied is mostly ballistic. The flat temperature distribution along the molecular chain is also associated with the observation that the temperature falls take place predominantly at the molecule-substrate interfaces.

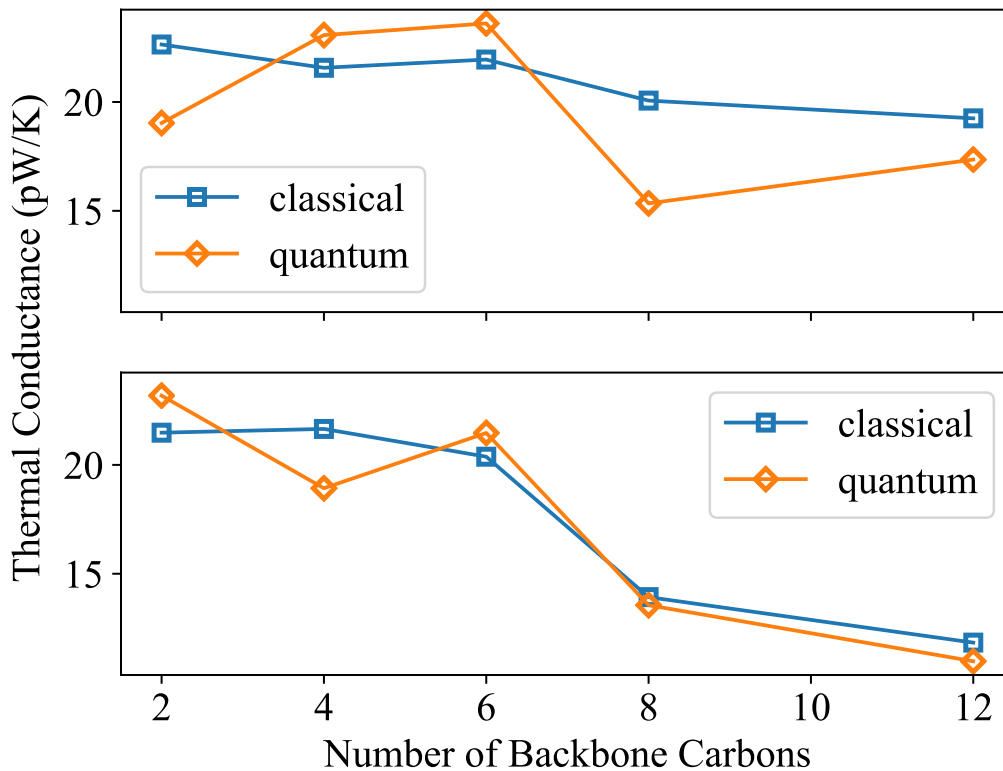


Figure 2.4: Heat conductance as function of length of saturated alkane chains (upper panel) and conjugated polyene chains (lower panel), obtained from the classical MD simulations and from Landauer-type quantum calculations (the later done under the harmonic approximation), respectively. The gold substrates temperatures are 350K and 300K. The classical heat conductance is defined as the ratio between the computed steady state heat current and the (50K) temperature bias.

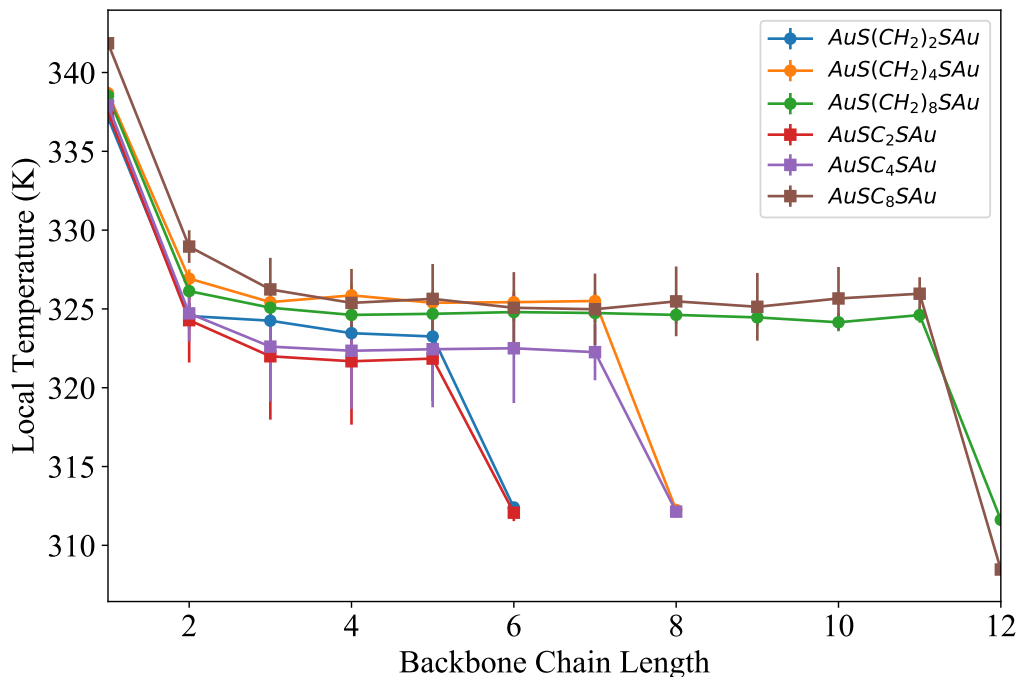


Figure 2.5: Temperature profiles for some of the carbon chains shown in Figure 2.3, obtained from the classical MD simulations. In the legend, structures with  $CH_n$  and  $C_n$  denote alkanes and conjugated polyynes respectively. The horizontal axis is labeled according to the index of backbone atoms, starting with the gold atom nearest to the molecules (e.g., atom 1 and 12 for the  $(CH_2)_8$  and  $C_8$  molecules, while atoms 2 and 11 of these molecules are sulfur atoms). The temperatures of the left and right leads are set to 350K and 300K respectively. The error bars represent the  $SE^{1,2}$  of the computed average temperature.

(d) The fact that the conjugated chain is less conducting than the saturated one stands in contrast to experience from observation of electronic conduction and reflect the fact that the saturated molecules have a higher density of low frequency modes.

(e) The close similarity of the quantum and classical results at room tempera-

ture (Figure 2.4) indicates that classical mechanics dominates heat transport in the molecules investigated. This arises from the fact that near room temperature only low frequency modes can be populated. This is compounded by the low Debye frequency of gold which introduces a natural frequency cutoff in the calculated transmission process. The observed close similarity also indicates that the harmonic part of the molecular forcefield (which is used in the quantum calculation) dominates the heat transfer dynamics in these system. In fact, our classical results agree with the experimental observation somewhat better than the present quantum calculations as well as those of Ref.<sup>34</sup> While it is quite possible this is merely accidental, it may also indicate a possible signature of anharmonic effects. Not surprisingly, at low temperature (Figure 2.6), the classically computed heat conduction deviates strongly from the quantum result.

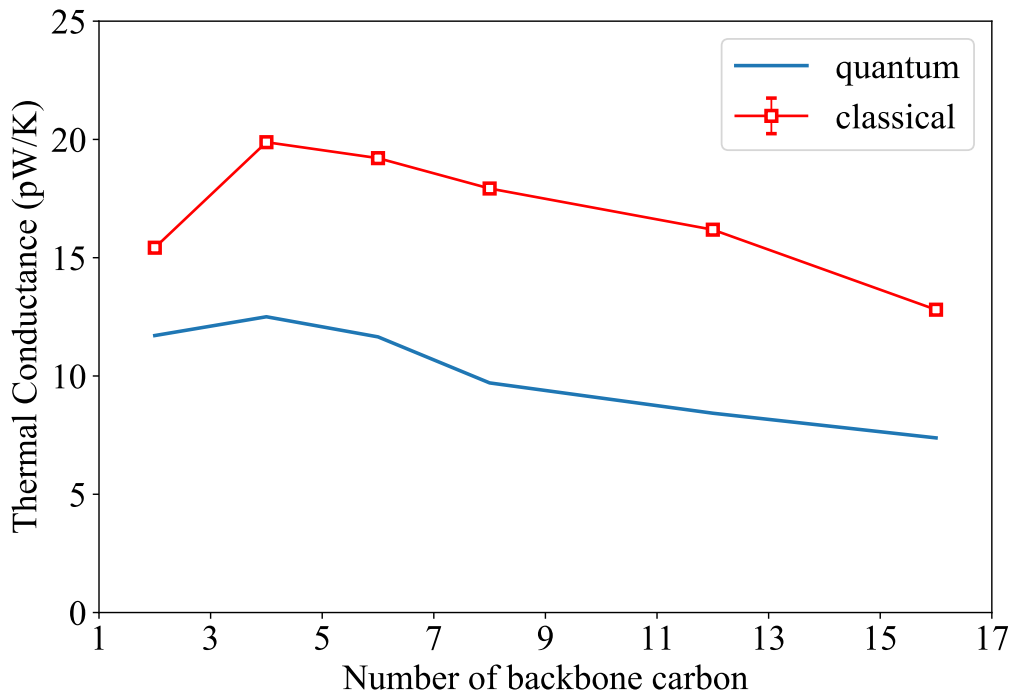


Figure 2.6: Low temperature heat conductance of alkane chains with temperature bias 25K-75K. Shown are results of from classical MD simulations and quantum Landauer-type calculations.  $SE^{1,2}$  (which are smaller than the square points in the graph) is shown for the classical stochastic simulations.

(f) The initial rise with chain length of the low temperature heat conduction of short alkane chains seen in Figure 2.6 is similar to the observations made in Ref.<sup>33</sup>, which was interpreted by the observation that low temperature heat conduction is dominated by very low frequency modes that are more abundant in longer chain molecules. Surprisingly, this trend is considerable less pronounced in the quantum calculation. This issue deserves further study.

(g) While the difference between heat transport behavior of  $-(CH_2)_n-$  and  $-(C)_n-$  chains is evident from Figure 2.7 and 2.8 that show molecular modes and



their localization properties, it should be kept in mind, as emphasized above, that in the particular junctions and the temperature range considered, one should focus on the low frequency mode regime for addressing this comparison, as is directly seen from the energy dependence of the quantum transmission, Figure 2.10. Clearly, the differences between the transmission properties –  $(\text{CH}_2)_n$  – and –  $(\text{C})_n$  – chains seen in Figure 2.10 are strongly correlated with the number and localization properties of the low frequency modes seen in the insets to the different panels of Figure 2.8. Another expression of mode delocalization, Eqn. 2.20, which indicates the extent to which a given mode “sees” both interfaces of the junction is seen (Figure 2.9) to also correlates well with these observations.

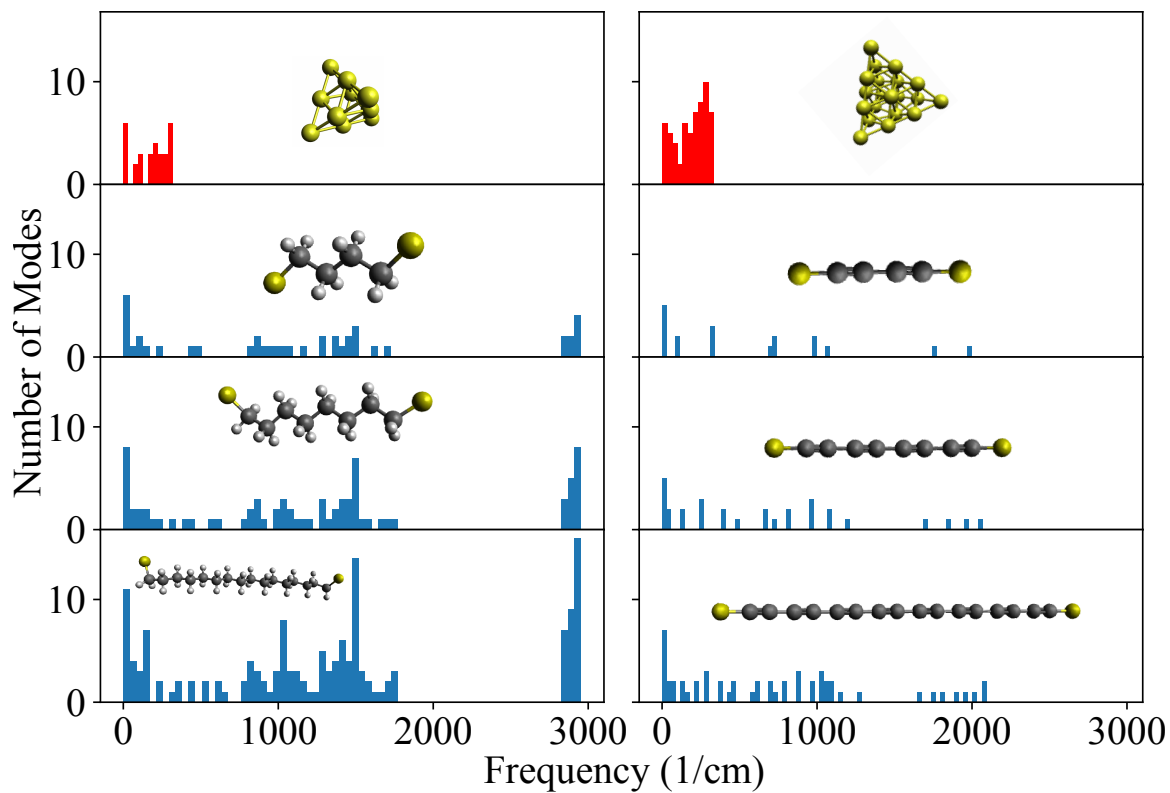


Figure 2.7: Histograms of the normal mode distribution of some representative molecules. The x-axes are the histogram bins (frequencies in wavenumbers), and the y-axes are the count of modes with frequency in the bin. The corresponding molecular topologies are drawn within each panel. Note that the first and last atom in each molecule are sulfurs. The first row shows the normal mode histogram for three- and four-layer gold pyramids (left and right columns, respectively). The following rows depict alkanes (left) and polyynes (right) with 4, 8, and 16 carbon units, respectively.

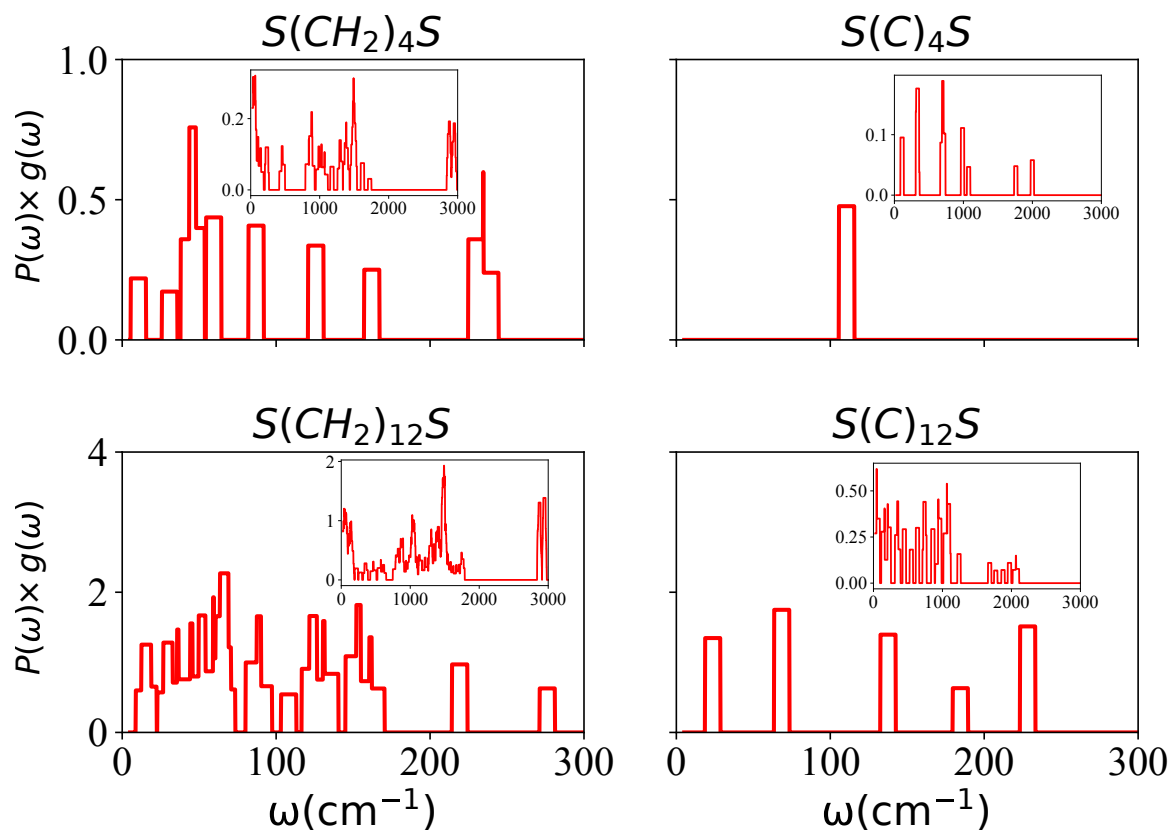


Figure 2.8: Product of participation ratio defined in Equation 2.17 and density of state of the normal modes for different hydrocarbon molecules. (Smoothed as in Eqn. 2.21 with  $\Delta\omega = 10\text{cm}^{-1}$ ) This quantity is displayed as function of frequency for 4-carbon chains (upper panels) and 12-carbon chains (lower panels) capped with thiol groups. (The inserts show the same quantities plotted for the 0 – 3000  $\text{cm}^{-1}$  range with smoothing parameter  $\Delta\omega = 50\text{cm}^{-1}$ .)

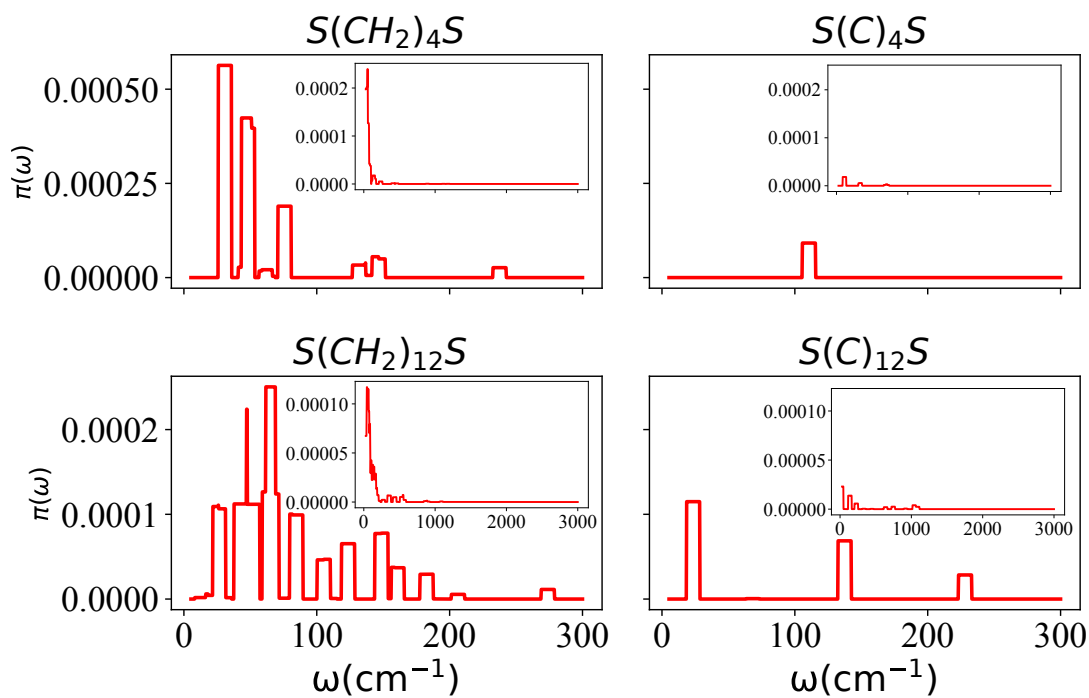


Figure 2.9: The end-to-end mode delocalization parameter (Eqn.2.20) calculated for different hydrocarbon molecules and displayed as function of frequency for 4-carbon chains (upper panels) and 12-carbon chains (lower panels) capped with thiol groups. (The inserts shows the same quantities plotted for  $0 - 3000\text{cm}^{-1}$  range with smoothing parameter  $\Delta\omega = 50\text{cm}^{-1}$ .) Unlike Figure 2.7, in which the full force-field has been used, the unified-atom force field (no explicit hydrogens) is used here for the alkanedithiol chains.

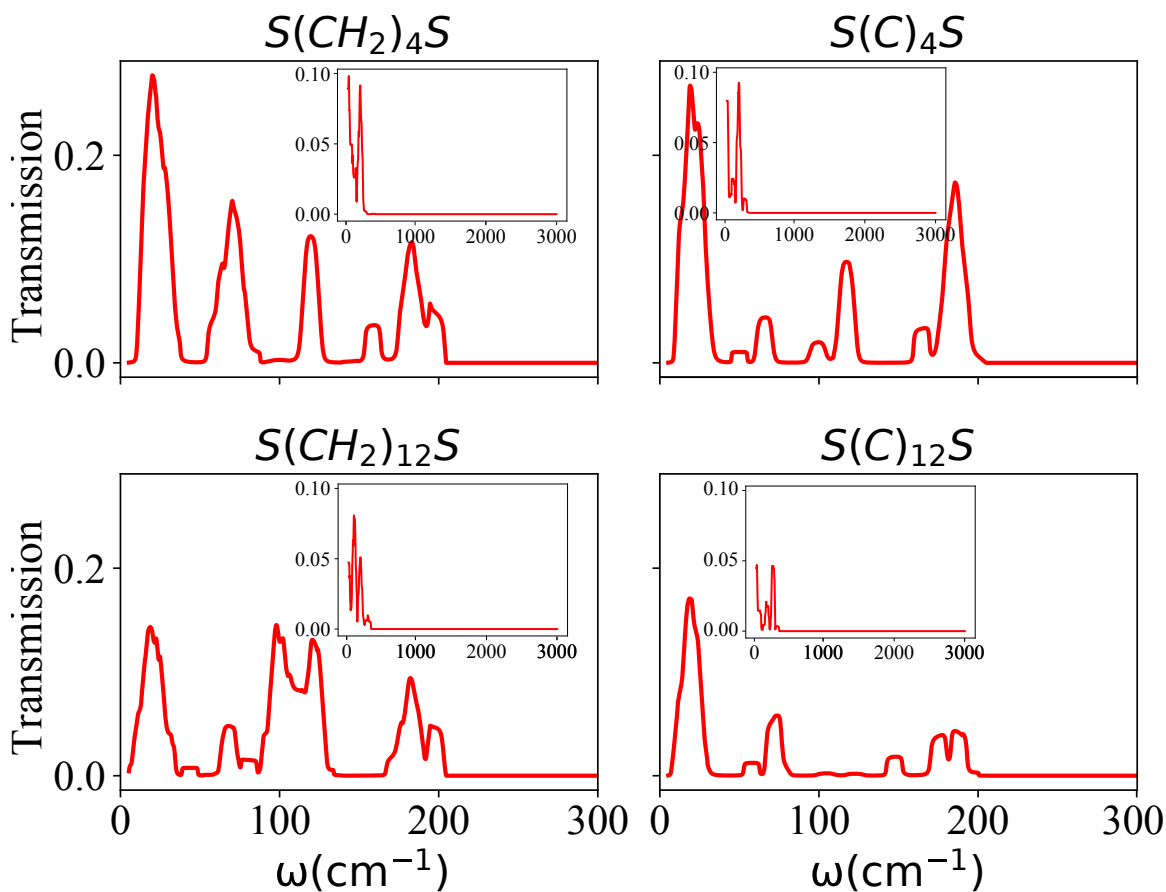


Figure 2.10: The quantum transmission function, Eqn. 2.13 displayed as function of frequency for different hydrocarbon molecules and shown as function of frequency for 4-carbon chains (upper panels) and 12-carbon chains (lower panels) capped with thiol groups. Smoothing  $\Delta\omega = 10\text{cm}^{-1}$  has been applied to this spectrum. The inserts shows the same quantities plotted for the  $0 - 3000\text{cm}^{-1}$  range with smoothing parameter  $\Delta\omega = 50\text{cm}^{-1}$ .

Finally, recall that as explained in Section 2.2, we have built into our code the capacity to make a rough estimate of the pathway map for energy flow between different molecular regions. An example of such map can be seen in Figure 6 of Ref.<sup>3</sup>. Another way to deconstruct the overall energy flow through the molecule is to estimate the contributions of different interaction to the overall energy flow. In

the present calculation, using Eqn. 2.8, we can determine the relative importance of nearest neighbor (2-body interactions), next nearest neighbor (3-body interactions) and 4-body interactions connecting carbons separated by three bonds. For saturated alkane chain of six carbon atoms we have found that these relative contributions are 1 : 0.16 : 0.014, respectively.

## 2.4 Conclusion

We have developed a numerical package based on the GROMACS code for simulating classical phononic heat conduction in molecular junctions as well as evaluating the quantum heat conduction based on the Landauer formula for the harmonic approximation to the given molecular force field. Here we used this package to evaluate the heat conduction properties of molecular junctions comprising saturated and conjugated hydrocarbon chains connecting gold leads. Multiple layers of explicit gold substrates act as filters of larger environmental white noise and bring characteristic bath effects to the heat conducting molecular systems under investigation. Our focus was not on achieving the highest possible accuracy of calculation but to demonstrate the utility of the developed package on one hand and compare quantum/harmonic and classical calculations on the same junction model as well as examine the correlation between molecular heat conduction and its mode localization behavior. Still, the close agreement between our simulations and the most recent experimental measurements<sup>16</sup> indicates that our model encompasses the molecular details most important for this transport process. It is interesting to note that for the alkanedithiols, the room temperature results from the classical MD simulation using the full molecular force field agree better with the experimental results of Ref<sup>16</sup> than the quantum calculations. This may be just an accidental property of our force-field model or may hint that at ambient conditions, the explicit treatment of quantum effects is less rel-

evant than explicit treatment of anharmonicity. It is also notable (however not very surprising) that while electronic conduction of polyynes is much higher than their saturated counterparts<sup>79</sup>, we find that their thermal conductance is lower, flagging them as potentially good candidates for thermoelectric nanomaterials.

The calculations presented in this section are done under steady state conditions. The success of the classical room temperature calculation is gratifying since the classical code can be easily used also to investigate non-steady state situations such as junctions driven by time dependent optical or mechanical driving. Such systems will be subjects of our future studies.

## **2.5 Disorder effect on molecular thermal transport**

### **2.5.1 Introduction**

Dissimilar to the diffusive heat conduction in macroscopic materials, molecular heat transport often shows ballistic property with constant propagating speed or insignificant temperature drop along the molecular chains. The changing sizes of the systems with respect to the characteristic mean free paths of the heat-carrying phonons in subsystems offers a viable general high-level explanation for the micro-to-macro transition.<sup>11</sup> However, even with molecular systems of a few nanometers length, such a ballistic-to-diffusive crossover may still occur under certain conditions. For example, it has been shown to be achievable theoretically by attaching self-consistent reservoirs (interior heat reservoirs whose temperatures are determined self-consistently on the criterion that average currents reach zero at the steady state) to the systems, and the diffusion degree can be also tuned.<sup>93</sup> Another way is to introduce disorders (e.g. masses, bonds) into the molecular systems. Recent experiments as well as theoretical studies have shown altered thermal conduction properties and temperature

distribution profiles with the presence of disordered atoms in the molecular systems. Luckyanova *et. al.* have experimentally demonstrated a transition from ballistic to diffusive thermal transport in superlattices by tuning the densities of ErAs nanodots at the interfaces.<sup>94</sup> Energy redistribution have been observed within certain chain molecules, showing altered energy transport speed at the middle of the chains, by embedding interfacial disorders (e.g. amide group) to the original structures.<sup>95</sup>

Early theoretical studies of disorder effects on nanoscale thermal transport have been focusing on mass disorder in low-dimensional harmonic chain lattices.<sup>96,97</sup> Recently, a new study has included force disorder as well to show cooperative effects of phononic thermal transport.<sup>98</sup> Nevertheless, this investigation is confined with toy-model study, with implications still unclear to the experimental implementations or actual device design. With our proven GROAMCS-based MD tool, we show the effects atomic disorder (metallic atoms in organic molecules) may have on heat conduction processes under single molecule junction settings. We also demonstrate these effects might be tuned by changing the types and portions of the disorder (group) in the molecules.

### 2.5.2 Results for this section

Before we start doing MD simulations for effects on thermal (phononic) transport on molecular systems (e.g. in the junctions) with certain force-fields, it is helpful to first look at a simplified case: A 1-D chain model with a single impurity (e.g. different masses) in the middle of the chain, in which an analytical expression based on Landauer-type formalism can be obtained at steady-state. Such an approach will provide us some minimal physical intuition of disorder effects and help us understand how more complex molecular structures and junction setups might deviate from simple models.



## Chains of harmonic oscillators

The heat conduction along the mass-disordered one-dimensional harmonic crystals has been first studied in the 70's<sup>99-101</sup>, and later extensively analyzed by Dhar and coworkers<sup>88,96,97</sup>. For a system with only nearest-neighbor harmonic interactions (assuming 1-D), the Hamiltonian can be written as:

$$H = \sum_{l=1}^N \frac{p_l^2}{2m_l} + \sum_{l=1}^{N-1} \frac{1}{2} k_l (x_{l+1} - x_l)^2 + \frac{1}{2} k' (x_1^2 + x_N^2) \quad (2.22)$$

$x$ 's are displacements of the particles from their equilibrium position,  $p_l$  and  $m_l$  are the momentum and mass of the  $l$  th particle in the system,  $k_l$  is the force constants between  $l$  th and  $l+1$  th particles (for mass-disorder-only case,  $k_l$  is set to be constant throughout), and  $k'$  is the pinning potential to the first and last particle on the harmonic chain.

This is a classical system of harmonic oscillators. The steady-state heat current solution can be obtained with the Landauer-type formula<sup>88,96</sup>, (The expression can also be generalized to quantum system<sup>6,33</sup>).

$$J = \frac{k_B (T_L - T_R)}{\pi} \int_{-\infty}^{\infty} d\omega \mathcal{T}_N(\omega), \quad (2.23)$$

where (see Eqn.(2.13))

$$\mathcal{T}(\omega) = \text{Tr} [\mathbf{G}^\dagger(\omega) \mathbf{\Gamma}_L(\omega) \mathbf{G}(\omega) \mathbf{\Gamma}_R(\omega)], \quad (2.24)$$

and

$$G^{-1}(\omega) = -\mathbf{M}\omega^2 + \mathbf{\Phi} + i\mathbf{\Gamma}_L(\omega) + i\mathbf{\Gamma}_R(\omega), \quad (2.25)$$

with  $\mathbf{M}$  being the mass matrix of all the particle masses on its diagonal,  $\mathbf{\Gamma}_{L/R}$  is coupling matrices(see Eqn.(2.15)) and  $\mathbf{\Phi}$  is the force constants matrix.

To illustrate the model, we take a chain of 11 identical atoms, and varying the mass of the middle atom (6th) and middle force constant (5th out of 10, between the 5th and 6th atoms). For Ohmic (or Lebowitz) bath model, in which  $\Sigma(\omega) = i\gamma\omega$ ,<sup>88,97</sup> the mass dependence of heat current can be shown in Figure 2.11. It is shown that the heat current decrease monotonically (slow at first and faster with increased masses) as the disorder mass (only one atom difference in the middle of the chain) on the harmonic chain (with 11 atoms comprise the backbone) increases from identical to 20 times larger.

Meanwhile, if we set all the masses to be equal, by just varying one of the force constants in the middle (between the 5th and 6th atoms) of the harmonic chain, we get force-dependent heat current in Figure 2.12. In contrast to the mass dictated disorder, the current starts increase drastically, reaches maximum when the force constants become identical, and decrease very slowly when the force disorder grows.

### **Effects of disorder atoms on alkane bridged molecular junction heat conduction**

We have carried out a series of simulations on the disorder effects to heat conduction across alkane chain molecules in the junction. Most computational details can be found in Section 2.2 of this thesis. We show the diffusive transport behavior may gradually emerge through changing the mass of the impurity atom and length of the chain, reflected on the temperature profiles (Fig. 2.13 and Fig. 2.14).

Figure 2.13 shows state-steady temperature profiles of disordered alkane chains (the total number of the backbone atoms the chains vary from 3 to 19, as show in the legend as well as along the x-axis in the figure). Adding disorder in this

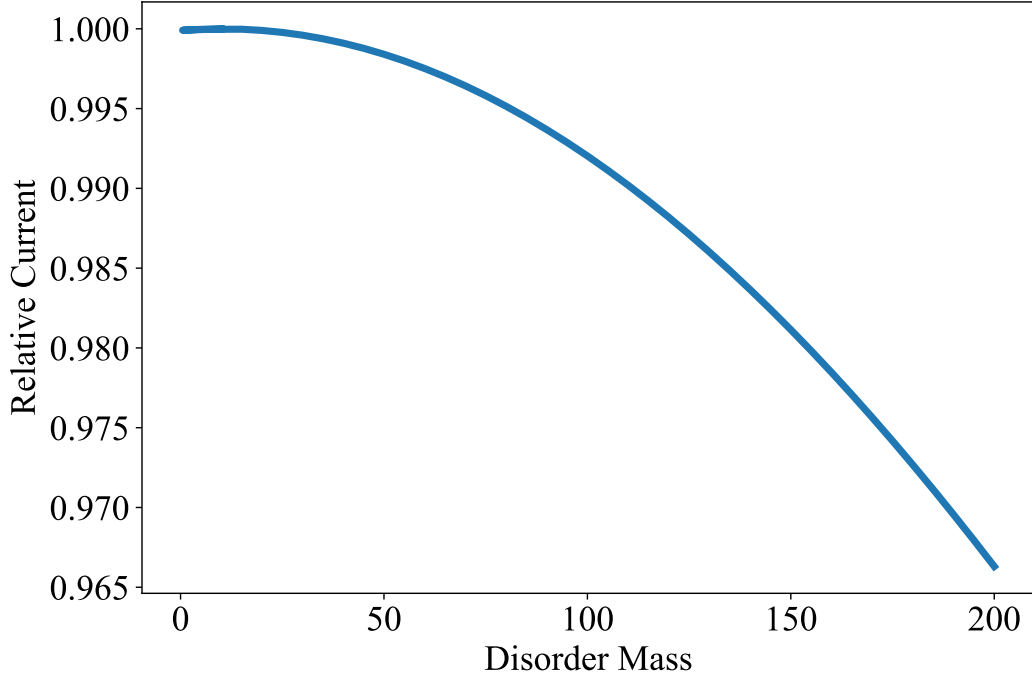


Figure 2.11: Heat current change of a harmonic 1-D chain, with respect to the change of disorder mass, calculated with Landauer-type formalism. The mass of the middle atom on the chain is set to be different (disorder) to the rest of the lattice (in this example, the 6th atom on a lattice of 11 atoms. Force constants are the same throughout). The parameters are: force constant  $k=1$ ,  $\gamma=10$ ,  $m=10$ (ordered),  $T_L=1$ , and  $T_R=1.5$ , all of which are given in reduced units with characteristic dimensions:  $\tilde{\sigma}=1\text{nm}$ ,  $\tilde{\tau}=1\text{ps}$ ,  $\tilde{m}=1m_{amu}$ ,  $\tilde{k}=10^5(\text{kJ mol}^{-1} \text{nm}^{-2})$  and  $\tilde{T}=300\text{K}$ . The curve is scaled by the ordered chain case (i.e. all the masses are equal to  $10\tilde{m}$ )

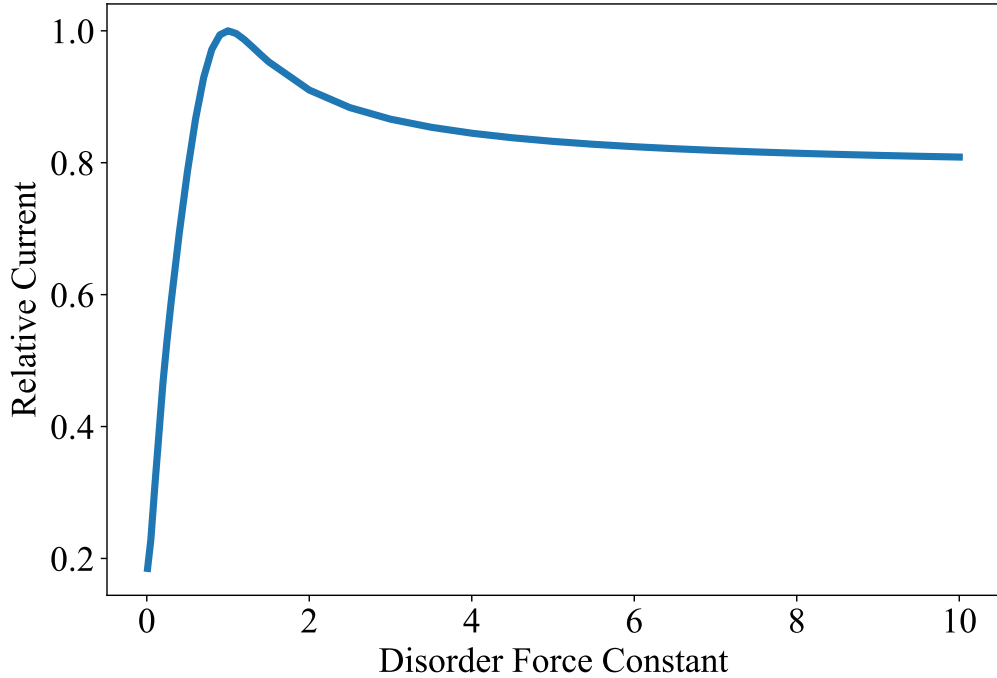


Figure 2.12: Heat current change of a harmonic 1-D chain, with respect the change of force constant, calculated with Landauer-type formalism. The force in the middle of the chain is set to be different (disorder) to the rest of the lattice (in this example, the 5th  $k$  on a lattice of 11 atoms with 10 constants). The parameters are: force constant  $k=1$ (ordered),  $\gamma=10, m=10, T_L=1$ , and  $T_R=1.5$ , all of which are given in reduced units with characteristic dimensions:  $\tilde{\sigma}=1\text{nm}$ ,  $\tilde{\tau}=1\text{ps}$ ,  $\tilde{m}=1m_{amu}$ ,  $\tilde{k} = 10^5$  ( $\text{kJ mol}^{-1} \text{ nm}^{-2}$ ) and  $\tilde{T}=300\text{K}$ . The curve is scaled by the ordered chain case (i.e. all the force constants are equal to  $1 \tilde{k}$ )

case is done by replacing the carbon in the middle of each chain with silicon. The first and last backbone carbons are attached to infinitely large thermal baths (i.e. white noise) of temperature 350K to the left and temperature 300K to the right. It is interesting to see that while the shorter chains (e.g.  $N=3$ ,  $N=5$ ) seem to change their transport to largely diffusive reflected from straight temperature gradient slopes (which is reasonable since the disorder has a bigger portion in these systems), the longer chains show local thermal resistance, expressed as a local temperature step, mostly in the middle, that is, near the impurity, keep the changes on the segments before and after the disorder mild. One could expect that when the chain grows much longer (e.g. 40 carbons or more), the transport might behave quasi-ballistically first, interrupted in the middle disordered site (e.g. by changing energy transport velocities suddenly), and then propagate ballistically again, just as has been observed in energy transport of amide bridged alkyl chains experiments <sup>95</sup>.

As we tweak the molecules further by changing the type of the atoms (from carbons) in the middle of the chains (Figure 2.14), we find that the heavier the impurity mass, the larger the temperature drops at the site of the disorder. Furthermore, such correlation is not linear. When the atomic masses of the impurities increase over 60 AMU (e.g. Pd in the figure), that is around 5 times over pure carbon atom, the drops of the temperature profiles seem to plateau. On the other hand, decreasing the atomic mass (the case for boron) leads to the similar effect as increasing it. That is the reduced impurity mass also makes the conducting chain more diffusive. One might have noticed the overall trends observed somehow aligns with the heat currents for the 1-D toy model (see Figure 2.11): as increased disorder undermines the total heat currents (with steeper drops in temperatures). However, the nuances are also important. First, if we look only at the impurity mass changes (disregarding other factors like force constants and degrees of anharmonicity for the MD results) it seems easier

to see noticeable changes in Figure 2.14 than what we have observed on the toy model (the change of temperature drops for the two atoms besides the impurity is more than doubled when carbon atom changes to silicon, while the relative current dips start mostly after tens to a few hundreds mass differences in Figure 2.11). Second, the curve of the harmonic model does not flatten along the increased masses(Fig. 2.11), while the temperature discontinuity seem to converge as the impurity becomes heavier (Fig. 2.14). The differences might be attributed to the fact that a simple substitution of atoms introduces not only mass disorder, but also structural disorder (i.e. forces and interaction differences). Ideally, it would be a combination of Figure 2.11 and Figure 2.12 together with molecular geometries in order to more accurately theorize thermal transport behaviors that could be been simulated or experimented on.

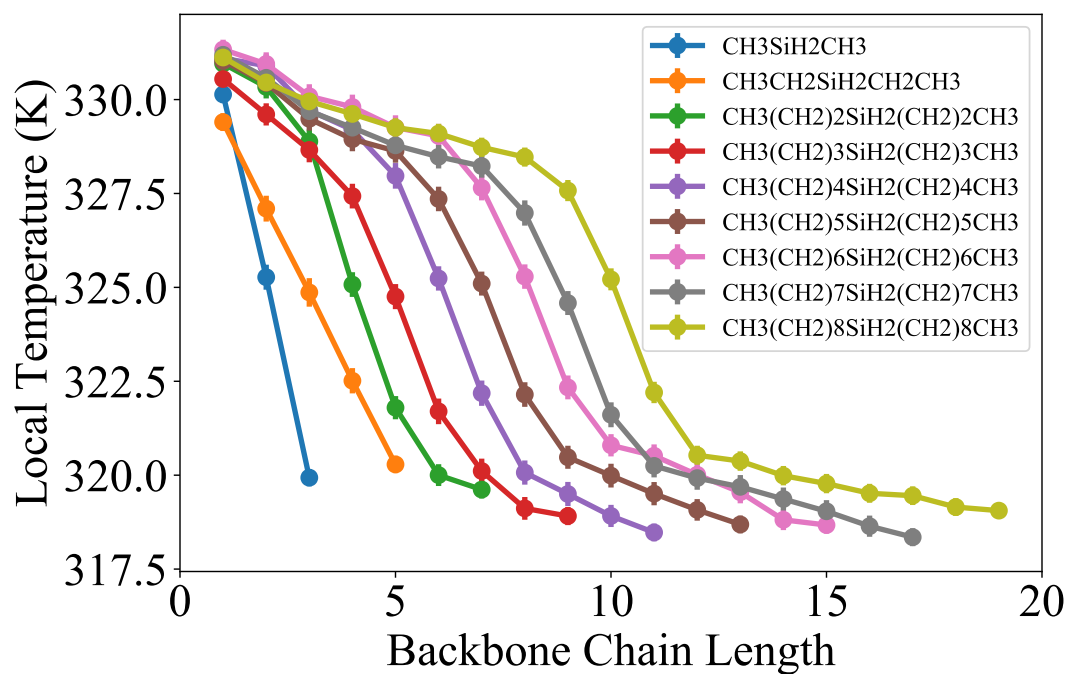


Figure 2.13: Temperature profile for disordered alkanes of various lengths. The number of backbone atoms in the molecules are 3, 5, 7, 9, 11, 13, 15, 17, 19, respectively, with Si sitting at the middle of every chain and the rest are carbons. The horizontal axis is labeled according to the index of the backbone atoms. The temperatures of the left and right baths are set at 350K and 300K respectively. The error bars are standard errors<sup>1,2</sup> of the temperature measurements.

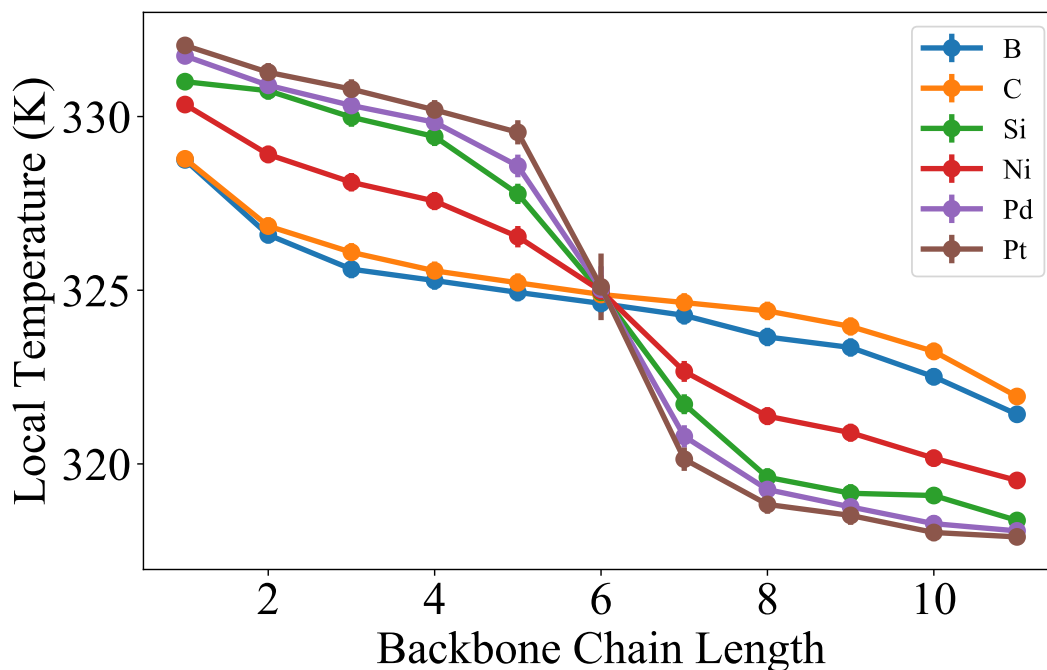


Figure 2.14: Temperature profile for disordered alkanes of 11 backbone atoms with different elements being the 6th atom of each chain, (different elements labeled in the legend) and rest are carbons. The horizontal axis is labeled according to the index of the backbone atoms. The temperatures of the left and right baths are set at 350K and 300K respectively. The error bars are standard errors<sup>1,2</sup> of the temperature measurements. (the computed values of the errors is smaller than the size of the circle points in the graph. So that is why bars cannot be seen for most points except the middle impurity sites)

Substituting one atom in the chain molecules is comparatively a straightforward way to probe the effects of impurities on heat conduction. What if a large portion (e.g. half) of molecules is substituted or structurally altered? In what follows we present a different compounded structure that show these effects in a broader sense (we may



call it asymmetric effect, with half of the chain molecule replaced by a aromatic ring molecule) than a single impurity in a structurally symmetric chain molecule.

Figure 2.15 shows three molecular structures that have the same backbone group number along the horizontal direction (single carbon along the chain or two vertical (normal direction) carbons as one group circled in red as examples shown in the figure). As we attach white bath (that is random noises based on Langevin dynamics, parameters detailed in Section 2.2 and Appendix A) of temperature 350K to the leftmost carbon atom and a similar bath of temperature 300K to the rightmost carbon atom (to the rings we take the averages by put the thermostats to either one of the two atoms that are normal to the horizontal chain direction and parallel to each other on the outer-most side), and compute the temperature distributions at steady state. We plot the results in Figure 2.16. We first notice that the ring pentacene seem more ballistic (less temperature drop) than the chain undecane molecule, thus could conduct more heat under same bias conditions. The reason besides possible artificial introduction of thermal averaging (between the normal two carbon atoms), could be increased heat transport channels and phonon modes that help the overall conduction. We can also see that the asymmetric naphthalene plus hexane hybridized structure has significant higher temperature drops both between the left end the right end and in the middle interface than the other two more symmetric structures (namely, undecane and pentacene). This implies that the asymmetric structure of the compounded molecule creates a discontinuity at the interface when the delocalized phonons travel across the molecular bridge, which effectively acts like a single impurity in the middle of the bridge.

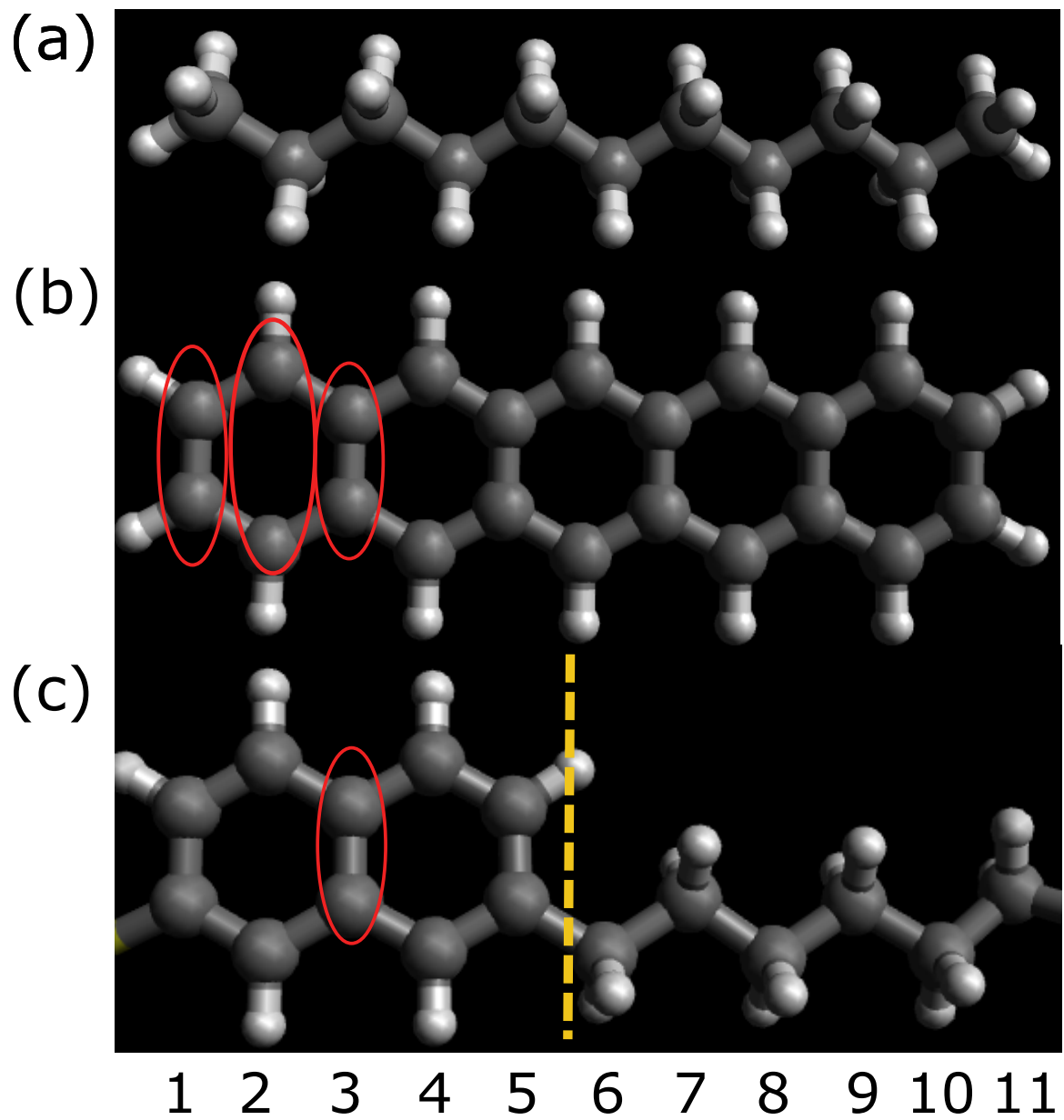


Figure 2.15: Configurations of molecular structures for the asymmetric interface effects on molecular heat conduction. (a) undecane; (b) pentacene; (c) naphthalene+hexane.

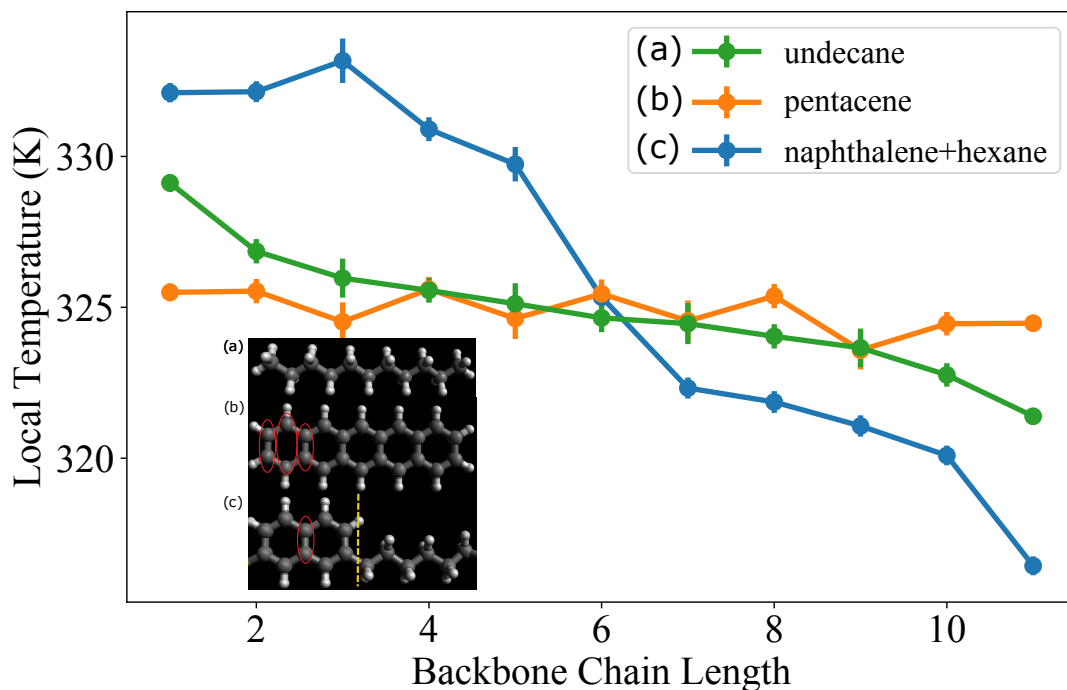


Figure 2.16: Temperature profile for three molecular configurations (as labeled in the legend) shown in Figure 2.15 and the insert. The horizontal axis is labeled according to the index of the backbone atom groups. That is, one index is for a single carbon group along the chain or two vertical (normal direction) carbons as (with averaged temperature) one group for the rings circled in red as examples shown in the Figure 2.15. The temperatures of the left and right baths are set at 350K and 300K respectively. The error bars<sup>1,2</sup> are standard errors of the temperature measurements.

### 2.5.3 Conclusion

We have shown the diffusive signature in heat transport may emerge from ballistic transport in the alkane-chain based molecular junctions, by simulating heat conduction of chain molecules in which one carbon (e.g. in the middle) is replaced by other

type of atoms (which we refer to as impurities, e.g. silicon). Similar effects could also be achieved by replacing parts of the molecules with different types of compositions (e.g. aromatic rings into alkane chains), creating asymmetric interfaces inside the molecular bridges, which leads to discontinuities in steady state temperature profiles.

There have been theoretical and toy model studies discussing disorder effects in nanoscale (in particular low-dimensional materials) thermal transport previously, but few have reported the degree of how these disorders affect heat conductions in molecular junctions that could be prepared and measured in an experimental setting. Our MD simulations fill the gap by demonstrating the distinctions in thermal transport among different disordered molecular species and structures. Though not a thorough survey of all the possible molecular and disorder types, we hope through our sample comparisons, a prescription of design principles will emerge for molecular junctions manipulations of high and low molecular thermal conductors by controlling disorders in the molecular systems.

## 2.6 Calculation of energy resolved transmission

Under harmonic limit, energy transmission may also be quantified classically for the molecular bridge systems in the study. Consider the molecular bridge segment (e.g. alkanedithiols) as multi-atom driven damped harmonic system defined by the equation of motion

$$\ddot{\mathbf{X}} = -\frac{1}{2}\mathbf{K}\mathbf{X} - \mathbf{G}\dot{\mathbf{X}} + \mathbf{A}(t) \tag{2.26}$$

where  $\mathbf{X}$  is a vector of mass weighted atomic deviations from equilibrium,  $\mathbf{K}$  is the Hessian matrix associated with the molecular force field,  $\mathbf{G}$  is a damping matrix and  $\mathbf{A}(t)$  is a vector of externally imposed driving forces on the different atoms. We are interested in the particular situation in which periodic forces  $\mathbf{A}(t)$  reduce to



Figure 2.17: One dimensional damped and driven harmonic chain

harmonic driving  $\mathbf{A} \cos(\omega t)$  of the atom that in the corresponding junction is attached to one lead, while friction, not necessary isotropic, is imposed on the atom that in the corresponding junction is connected with the other lead. A 1-dimensional cartoon is seen in Figure 2.17. In this 1-dimensional case  $\mathbf{A}$  and  $\mathbf{G}$  are

$$\mathbf{A}(t) = \mathbf{A} e^{i\omega t} = \begin{pmatrix} 0 \\ 0 \\ \vdots \\ a \end{pmatrix} e^{i\omega t}, \quad \mathbf{G} = \begin{pmatrix} \gamma & 0 & \dots & 0 \\ 0 & 0 & \dots & 0 \\ \vdots & \vdots & \ddots & \vdots \\ 0 & 0 & \dots & 0 \end{pmatrix} \quad (2.27)$$

(the real part of the solution is to be used) and in the 3-dimensional case the non-zero blocks correspond to the atom(s) that in the junction is(are) attached to the lead, taken in the present calculation to be the sulfurs. At long time all atomic displacements oscillate with the driving frequency  $X_j(t) = x_j(\omega) e^{i\omega t}$  and the amplitudes  $x_j$  may be obtained from  $\mathbf{x} = (-\omega^2 \mathbf{I} + \frac{1}{2} \mathbf{K} + i\omega \mathbf{G})^{-1} \mathbf{A}$ . The dissipated energy flux (averaged over a period) is then obtained from

$$J(\omega) = \overline{\dot{\mathbf{X}} \cdot \mathbf{G} \dot{\mathbf{X}}} = \frac{1}{2} \omega^2 \mathbf{x} \cdot \mathbf{G} \mathbf{x} \quad (2.28)$$

which is just  $(1/2)\omega^2 \gamma x_1^2$  in the 1-dimensional example. In three dimensions, when the lead-molecule coupling involves a single molecular atom we take  $\mathbf{x} \cdot \mathbf{G} \mathbf{x} = \sum_{k=1}^3 \gamma_k x_{1k}$  to reflect possible anisotropy of the friction. As defined,  $J(\omega)$  expresses an intrinsic transmission property of the molecule.

As direct examples of applying such method, we take the hydrocarbon chain molecules whose heat conductance have been simulated in Section 2.3, and calculate the energy resolved classical transmission (Figure 2.18 and 2.19) with regard to the external driving frequencies as prescribed above. In particular, alkanedithiol (also referred as saturated) and polyynedithiol (also referred as unsaturated) molecules are chosen (with total backbone atoms equal to 4 and 12 respectively). The harmonic part of the molecular force field is taken and imaginary (periodic) driving is applied to the outer-most sulfur atoms. Such fluxes (from Eqn.(2.28)) represent the heat transmission spectrum of the unbound molecular species itself, and in Figure 2.18 it is plotted against the driving frequency  $\omega$ . The result depends on the relative magnitudes of the frictions  $\gamma_k$  and in the simulations shown in Figure 2.18 we have assumed that the friction is dominated by the motion along the S-C bond.

Though only the hydrocarbon molecular bridges are taken into account in these two figures, the frequency resolved energy fluxes (Figure 2.18) and their accumulated values (Figure 2.19) provide useful insights into the overall heat conduction across the junctions without doing MD simulations. With imaginary periodic driven forces, The transmitted energy analysis under different frequency values imply more energy is transferred at low frequencies, aligning with the mode delocalization analysis (Figure 2.9) and transmission properties (Figure 2.10) shown in Section 2.3. Also, though it is not immediately clear that if 4-carbon polyynes has higher conductance than 12-carbon alkane, the overall trends of alkanes having higher conductance and shorter hydrocarbons conducting more heat currents than longer ones, are already noticeable by looking at the energy resolved transmissions of these chain molecules. In general, such analysis is effective and intuitive for most molecular structures whose thermal transports are dominated by harmonic normal modes, we will see more results in the light of these calculations in the next chapter on the topic of classical interference.

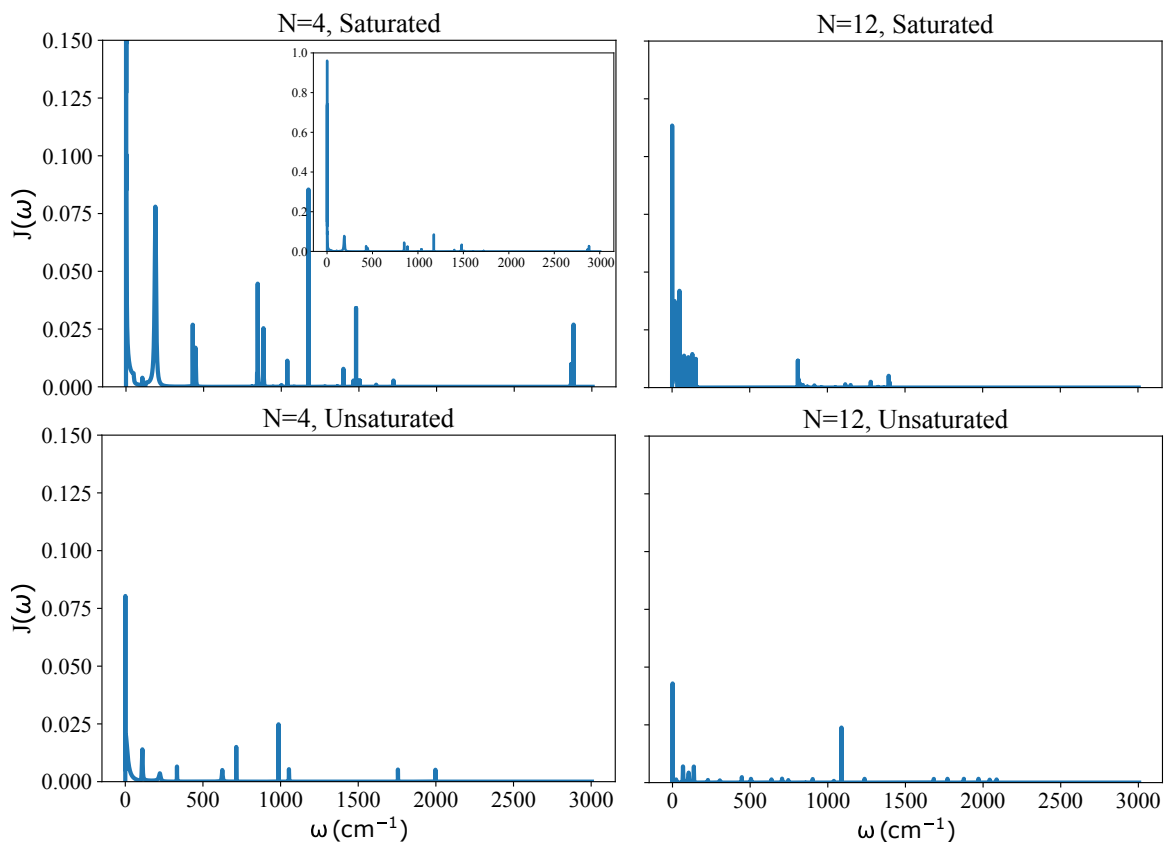


Figure 2.18: Frequency resolved energy flux (arbitrary units) generated by driving one sulfur atom the chain molecule and evaluating the heat generation per unit time on the other sulfur taking friction  $\gamma = 20 \text{ cm}^{-1}$  to affect the motion along the S-C bond, calculated according to Eqn (2.28).  $N$  is the number of backbone carbon atoms, and all molecules are capped with thiol groups. "Saturated" refers to alkanedithiols, while "Unsaturated" refers to conjugated carbon chains with alternating single and triple bond (polyyenes). The insert in the first figure is a zoom-out of a larger y-scale (0-1) of the same flux.

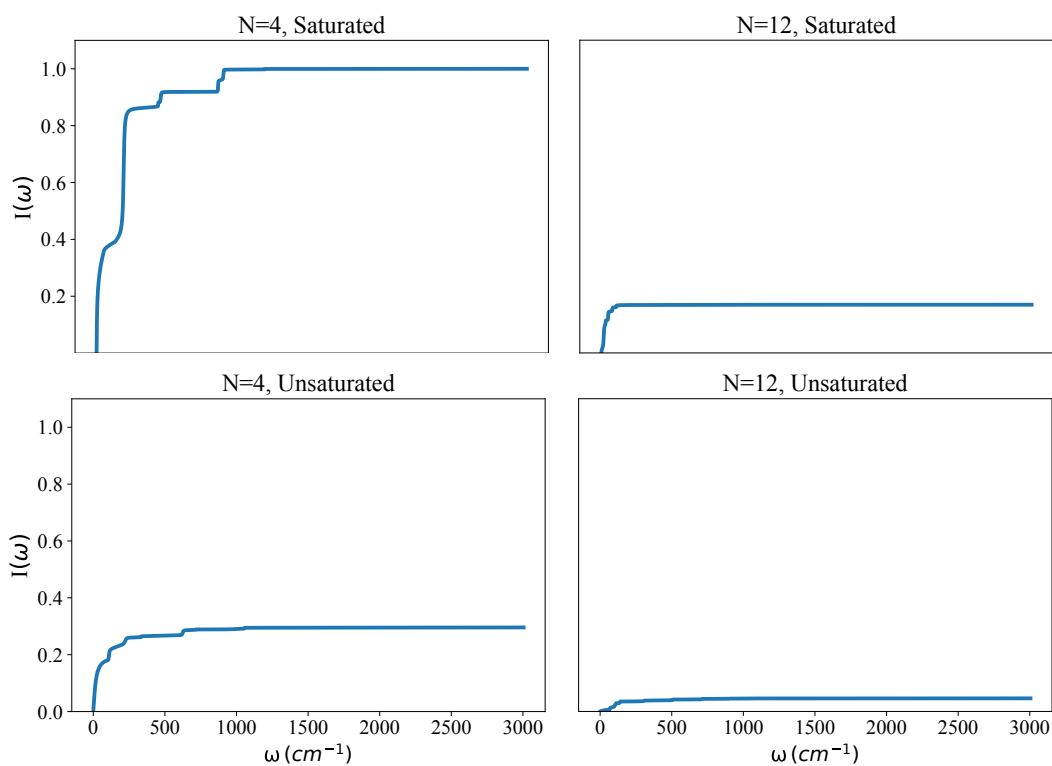


Figure 2.19: The intergrals  $I(\omega) = \int_0^\omega J(\omega)$  over the frequency resolved heat fluxes of Figure 2.18, normalized by  $I_{N=4,saturated}(3000\text{cm}^{-1})$  and displayed against  $\omega$  for the four hydrocarbon species.  $N$  is the number of backbone carbon atoms, and all molecules are capped with thiol groups. "Saturated" refers to alkanedithiols, while "Unsaturated" refers to conjugated carbon chains with alternating single and triple bond (polyynes).



## CHAPTER 3

### Local Atomic Heat Currents and Classical Interference in Single-Molecule Heat Conduction

This chapter is adapted from *The Journal of Physical Chemistry Letters* **11**, 4261–4268 (2020)

#### 3.1 Introduction

Quantum interference (QI) has been often reported to play a role, sometimes important, in molecular electronic conduction.<sup>102–110</sup> While nuclear motions (henceforth sometimes termed phonons) usually dominate molecular heat conduction<sup>6,12,37,111–115</sup>, calculations based on the quantum Landauer formula for heat conduction in the harmonic molecule limit indicate that interference may affect phononic thermal conduction as well, and these observations have been also termed quantum interference.<sup>14,116</sup> Figure 3.1 illustrates the main difference between electron and phonon transport in molecular junctions. First, the different statistics of these carriers implies different occupation distributions in the leads. Consequently, the corresponding transmission functions are sampled differently in the two cases and, in particular, electron transmission can be tailored to sample a narrower energy window thereby displaying interference effect on transport more prominently. The basic origin of interference in both cases is the spatial structure of the conducting orbital(s) in the electronic case or delocalized modes in the vibrational one that are both determined by atomic positions in the molecular bridge. For example, comparing commonly used tight binding models for electronic structure to harmonic atomic structures with nearest neighbor

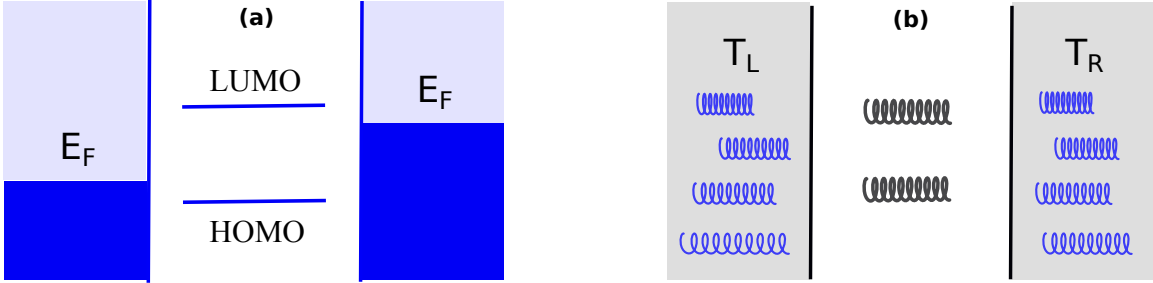


Figure 3.1: Schematic diagram of electron transport (a) and vibrational energy transfer (b) in molecular junctions

interactions shows a close mathematical similarity that implies similar implications of geometrical structure to interference. Nonetheless, since phonons are classical waves, their dynamic properties are mostly determined by classical mechanics, and it may be expected that interference phenomena will show in classical phononic thermal transport.

Here we examine the vibrational heat conduction behavior of a benzene molecule connected to gold substrates via thiol bonds using classical molecular dynamics (MD) simulations with the full molecular forcefield as well as the quantum Landauer expression with harmonic part of the same forcefield. We focus on the conduction properties of para-, meta-, and ortho-connected rings and find considerable differences that can be traced to interference between different phonon-transfer pathways. Remarkably, at room temperature, the quantum and classical calculations yield qualitatively similar results. Both show similar trends that indicate interference between conduction pathways when comparing the heat conduction properties of para, meta, and ortho benzenes.<sup>1</sup>

<sup>1</sup>Such trend cannot be depicted alone by the normal mode distributions of different molecular configurations (Figure B.1), which are similar across the spectral densities.

## 3.2 Model and methods

### 3.2.1 Molecular dynamics simulation

The junction model used in the simulations comprises the molecule and the explicit leads that together form an extended inner system (referred to below as “extended molecule”) and the thermal reservoirs (Figure 3.2). The explicit leads each have three layers of gold atoms in a cone-like structure (one, three and nine gold atoms in the first, second and third layer, respectively) that mimics scanning tunneling microscope (STM) tips. The external reservoirs are equilibrium Markovian baths, characterized by specific temperatures ( $T_L$  and  $T_R$ ) that represent the experimentally tuned macroscopic substrates. Unless otherwise stated, the friction associated with the coupling between the extended molecule and the external thermal reservoir is taken to be  $1 \text{ ps}^{-1}$ . The stochastic MD simulation is implemented using stochastic nonequilibrium Langevin dynamics by utilizing customized GRONingen MACHine for Chemical Simulations (GROMACS, currently version 4.5<sup>117</sup>) platform. The universal force field (UFF) of Rappe *et al.*<sup>81</sup> is employed for all the molecules in the study. The molecular system (together with the segments of the substrates embedded in the molecular subsystem to form an extended molecule) is first equilibrated to the average temperature of the thermal baths starting with its minimum energy configuration, and then brought to a nonequilibrium steady state (SS) with the two leads kept at different temperatures. This part of the simulation is typically a few ns long. Once SS is reached, thousands of production runs are used to get an ensemble of MD trajectories and forces needed for the steady state heat currents.

### 3.2.2 Landauer-type calculations

The quantum Landauer-type calculations are done by using the harmonic part of the extended molecule forcefield to calculate the phonon transmission probability  $\mathcal{T}(\omega)$  (An example, for room temperature structures, is shown in Section 2.6). The (phononic) heat current is obtained from Landauer expression<sup>6,33,87</sup>,

$$J = \frac{\hbar}{2\pi} \int_0^\infty \mathcal{T}(\omega) [f(\omega, T_L) - f(\omega, T_R)] \omega d\omega. \quad (3.1)$$

Here  $f$  function is the Bose-Einstein distribution function which depends the temperature of the bath,  $f(\omega, T) = (e^{\hbar\omega/k_B T} - 1)^{-1}$ . ,and  $\mathcal{T}$  is the transmission probability, which in general can be shown as the trace of matrix multiplication of the Green's functions and spectral functions<sup>88-90</sup>. Our implementation is achieved by incorporating GROMACS utilities into home-made code. From a high-level description, the Hessian (dynamical force matrix) of the molecular system is obtained, followed by its diagonalization in order to get the normal modes. The eigenstates of the modes are then used to calculate the basic quantities (e.g. self-energies, Green's function, *etc.*), which are used to evaluate  $\mathcal{T}(\omega)$ . Further details on technical aspects of these simulations are provided in Ref<sup>4</sup>.

We note that although the thermal properties of the external baths are affected by imposing Markovian dynamics (white noise) for the relaxation at the boundary between the explicitly addressed substrate segment and the outer thermal environment, this white noise is adequately filtered through the explicit substrate layers so that it acts on the molecule itself with the characteristic spectral density features of the simulated gold. Results obtained using this model to simulate heat conduction through alkanedithiol chains<sup>4</sup> show good agreement with experimental observations<sup>16</sup>. The fact that the filtered noise emphasize the low frequency regime is one reason why

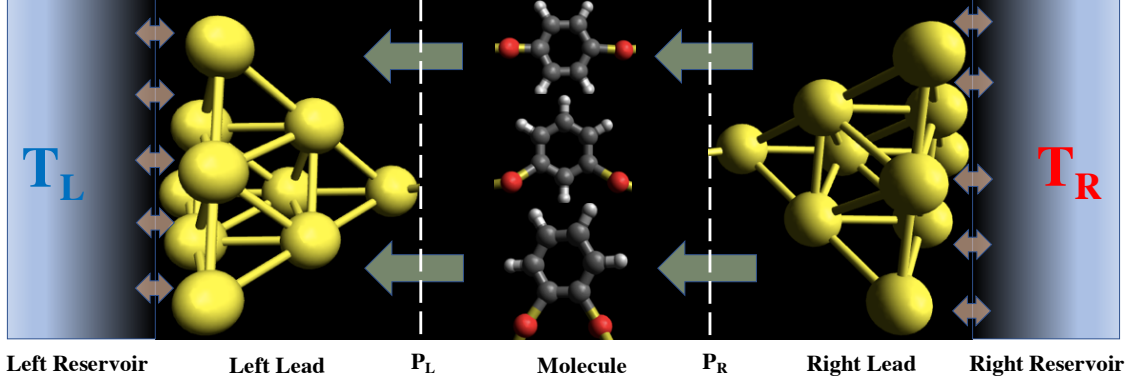


Figure 3.2: Artist representation of a typical system studied in this work. The unidirectional arrows across left plane ( $P_L$ ) and right plane ( $P_R$ ) denote the direction of heat flows. The double arrows show the connections between the exterior layer of gold lead to the thermal reservoirs, which are characterized with temperature  $T_L$  and  $T_R$  respectively.

quantum and classical results about room temperature are qualitatively similar as shown below.

Because the classical simulation yields atomic positions, velocities and forces along the simulated trajectories, it is evident that we can address not only the total steady state heat current (phononic energy flux) carried by the molecule but also the energy flux associated with individual atoms. However the procedure for doing this is not absolutely unique because to define energy currents involving individual atoms within the molecule we need first to define individual atomic energies, a task which is somewhat arbitrary for the potential energy because of its non-local nature. In Ref.<sup>4</sup> we have done so by assigning portions of the potential energy to individual atoms as follows: First identify different contributions to the potential energy associated with atom  $j$  as  $V_{jn}$  ( $n = 2, 3, \dots$ ) which are sums over all  $n$ -atom interaction terms in the molecular forcefield that involve this atom. A coarse-grained description of the energy distribution between the atoms is obtained by assigning to atom  $j$  the potential energy  $\sum_n n^{-1} V_{jn}$ . Once this choice is made, the force on the atom can be evaluated

as well, and the rate of energy change for this atom is obtained as a product of this force and the atom speed. This leads to the energy current between two atoms,  $i$  and  $j$ , in the form  $J_{ij} = \sum_n J_{n,ij}$  where<sup>4,86</sup>

$$J_{n,ij} = C_{n,j} \mathbf{f}_{n,i} \cdot \mathbf{v}_i - C_{n,i} \mathbf{f}_{n,j} \cdot \mathbf{v}_j, \quad (3.2)$$

in which  $\mathbf{f}_{n,j}$  is the force derived from interaction  $V_n$  with respect to the coordinate of atom  $j$ .<sup>2</sup>

### 3.3 Results and discussion

The simulated total heat conductance of the benzenedithiols in the three junctions is displayed in Figure 3.3. The steady state heat current is calculated by summing up all the interatomic currents going through a plane perpendicular to the molecular chain, e.g. the current  $J_L$  and  $J_R$  through, respectively, the planes  $P_L$  and  $P_R$  in Figure 3.2, and averaging over time (after steady state was achieved) and trajectories. The resulting averaged  $J_L$  and  $J_R$  are found to be the same within 0.5%. The heat conductance is the ratio of this heat current and the temperature difference  $\Delta T$ .

The non-monotonic behavior seen in Figure 3.3 as the junction structures change from para to meta and ortho configurations obviously does not result from changing interactions, and the possibility that interference between energy fluxes propagating along different paths is the source of this behavior, analogous to similar observation of electronic conduction through these configurations<sup>105,110,118,119</sup>, suggests itself. Indeed, when one of the paths is blocked as shown in Figure 3.3 for the meta configuration, conduction increases. Simulations done under different conditions are consistent with this assessment. (We have also shown a phonon transport general expression

---

<sup>2</sup>This choice, used to produce Figure 3.6 below has no bearing on the heat conduction calculations shown in Figure 3.3-3.5.

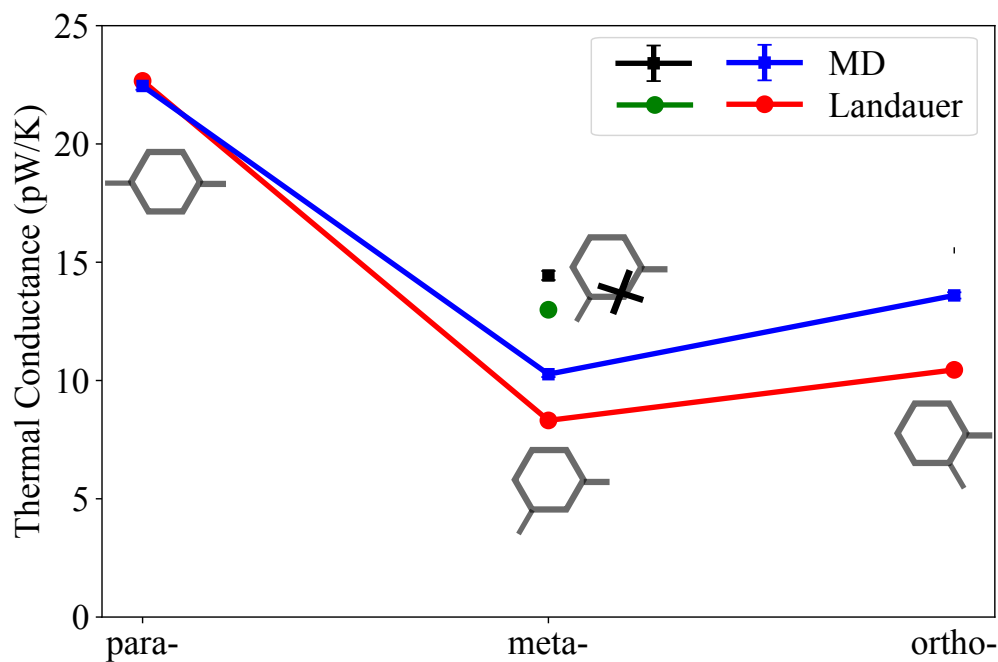


Figure 3.3: Thermal conductance of dithiolated-benzene molecules in gold-molecule-gold junctions with different connection (para, meta, and ortho) configurations. Shown are results from classical MD simulations and from the quantum Landauer's formula. The error bars represent standard errors (= standard deviation / square root of the sample size, which is a statistical uncertainty indicator of the estimated mean value of the conducted measurements.<sup>2</sup>). The green and black dots represent the conduction calculated using the Landauer formula and classical MD simulations, respectively, for the meta configuration in which heat transport through the site marked X is blocked by taking the mass to be artificially large (100 carbon atom mass).

for a nearest-neighbour harmonic model to indicate potential interference effects in over-simplified analytical cases. Detailed in Appendix B). Figure 3.4 compares heat conduction for three different sets of temperature biases, using both MD simulations and Landauer’s calculations. Panel (a) shows the same results as Figure 3.3, while (b) and (c) show results for high (600K and 650K) and low (10K and 60K) temperatures respectively. Figure 3.5 examines the effect of disorder, comparing the para and meta signals from the original molecule, and from a similar molecule in which a single hydrogen atom is replaced by a fluorine atom. The following observations can be made:

(a) While interference is seen also in the higher temperature simulations (Figure 3.4(b)), the difference between the conductions of the para-, meta- and ortho-configurations is smaller at this higher temperature.

(b) The classical simulations and the Landauer formula results are closer to each other at room temperature (Figure 3.4(a)) than at 600K (Figure 3.4(b)). The reason may be that the Landauer results are obtained for a molecular model described only by the harmonic part of the full potential. Errors in this approximation become more pronounced at higher temperatures where the system explore more of the anharmonic part of its forcefield.

(c) Although the physical distance between the contact is smaller in the ortho- and meta- configurations, the total heat current appears to be highest in the para-connected structure, where the thermal contacts are physically furthest from each other. Such a counterintuitive heatmap can again be taken as an indication of interference effect.

(d) At low temperature (Figure 3.4(c)) we see that the quantum result deviates strongly from the classical calculation. Remarkably the interference pattern all but disappears. At such low temperature only very low frequency modes contribute to the



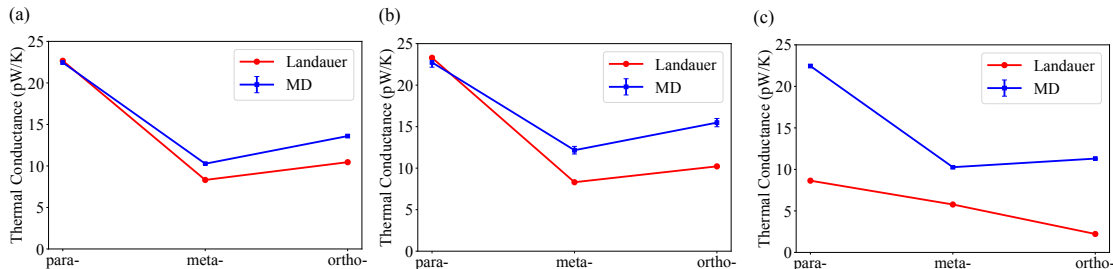


Figure 3.4: Thermal conductance for para-, meta- and ortho- benzenedithiol molecules, calculated from classical MD simulations and from the Landauer expression under different temperatures: a)  $T_{hot}=350\text{K}$  and  $T_{cold}=300\text{K}$ ; b)  $T_{hot}=650$  and  $T_{cold}=600\text{K}$ ; c)  $T_{hot}=60$  and  $T_{cold}=10\text{K}$ . The error bars for MD represent standard errors (as in Figure 3.3).

transport, more so in the quantum calculation. Such modes usually involve motions of many atoms so that “transport paths” becomes less distinct, quenching interference between paths.

(e) Introducing an impurity atom into the system has a strong effect on path interference, as is seen in Figure 3.5. In particular, the destructive interference that characterizes the meta structure is strongly reduced by such impurity even if it involves a substitution of an hydrogen atom that by itself does not make a large effect on the phonon transmission (however substitution by fluorine does).

A cautionary note is in place. While the configurations studied appear to be molecular analogs of a double slit system where phonon amplitudes propagating along different paths interfere, the actual situation is more involved as can be seen by looking at real-space steady state atomic heat flows in these junctions. Figure 3.6 shows local heat fluxes obtained from Eqn. (3.2), indicating their direction and magnitudes by arrows of various thickness. (Local temperatures are shown in Figure B.2) These currents take place between each atom pair, although they are naturally higher between nearest neighbors. It should be emphasized that, while partial cancellation between currents going in (partly) in opposite directions give rise some of the ob-

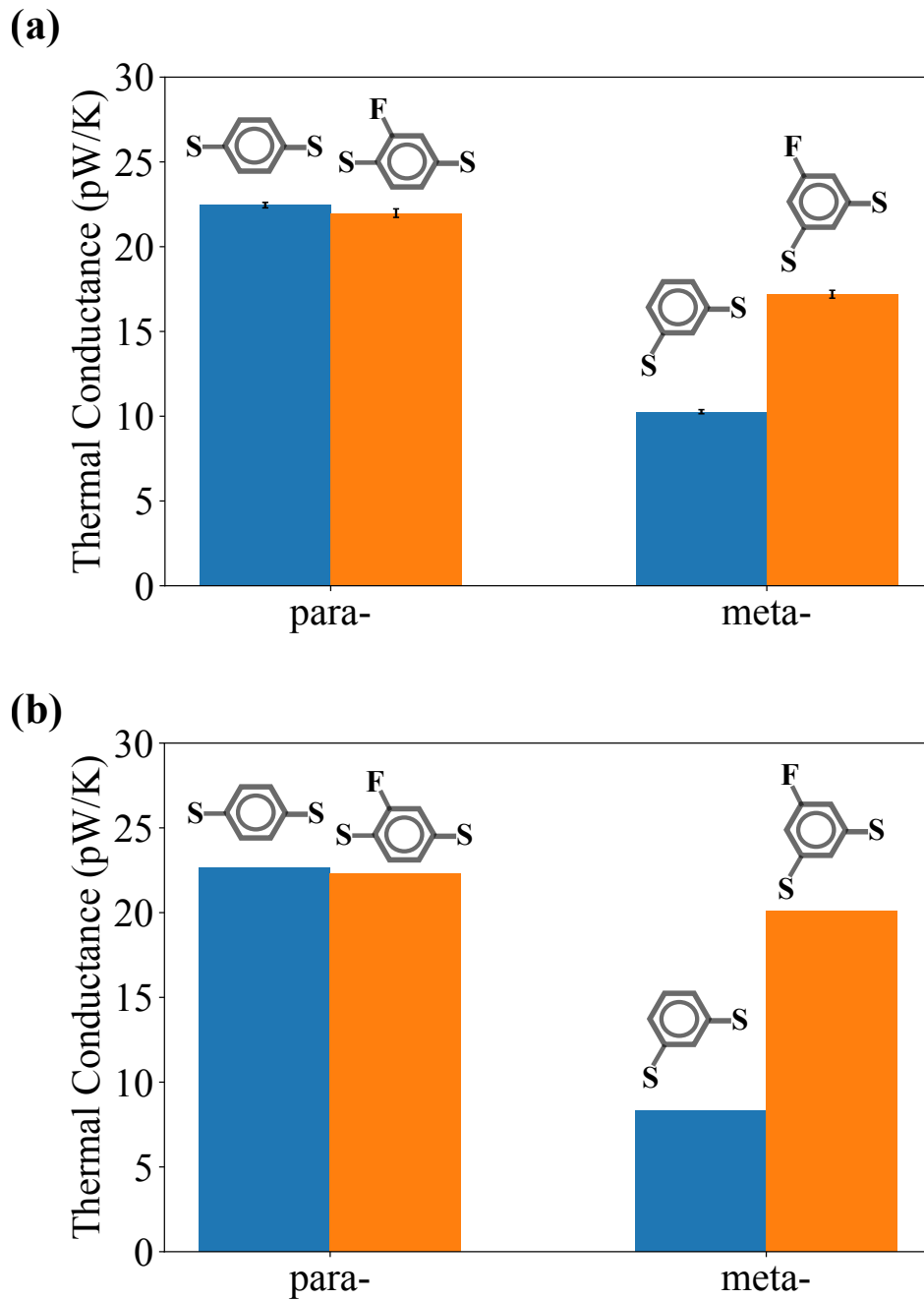


Figure 3.5: Thermal conductance for para- and meta- benzenedithiol molecules, simulated for the configurations with and without replacing one hydrogen with one fluorine at the position indicated in the molecular diagram, for the temperature bias of 300K to 350K. Panel (a) and (b) show results from MD and Landauer calculations, respectively. The error bars in Panel (a) represent standard errors (see caption of Figure 3.3).

served trends in Figure 3.3 and 3.4, interference is also manifested in the velocities of and total forces experienced by individual atoms, an effect not seen in this figure. The total heat currents express a complex interplay between these forces and velocities that eventually results in these current maps.

Furthermore, it should be kept in mind that interference is, to a large extent, a matter of representation. In a harmonic junction heat is carried independently by the system normal modes, and in the normal mode representation interference between different propagation paths translate into transmission properties of individual nodes, e.g. a node assumed by a mode at the molecule-lead bond which will render this mode unable to contribute significantly to the heat conduction process. Figure 3.7 demonstrates this point by showing the frequency resolved classical transmission (propagating wavepacket picture and analysis on a nearest-neighbour harmonic ring provides another perspective. Figure B.3 and Figure B.4 in Appendix B). We have presented details of the method in Section 2.6, here we briefly explain how it is done: We consider just the benzenedithiol species, use the harmonic part of the molecular forcefield and focus on the two sulfur atoms. One sulfur atom (say, atom 12 in Figure 3.6a) is driven by a periodic force that makes its coordinate (deviation from equilibrium) oscillates with frequency  $\omega$ . A friction  $\gamma$  is applied to the motion of the other sulfur atom (atom 11 in Figure 3.6a) thus forming a driven-damped harmonic system (see Section 2.6). At steady state there is a constant heat flux  $J(\omega) = \sum_j \gamma_j \langle \dot{x}_j \rangle^2$ , where the sum is over directions in the local coordinate system that defines the deviation of atom 11 from its equilibrium position. This flux represent the heat transmission spectrum of the unbound molecular species itself, and is plotted against the driving frequency  $\omega$  in Figure 3.7. The result depends on the relative magnitudes of the frictions  $\gamma_j$  and in the simulations shown in Figure 3.7 we have assumed that the friction is dominated by the motion along the S-C bond, which

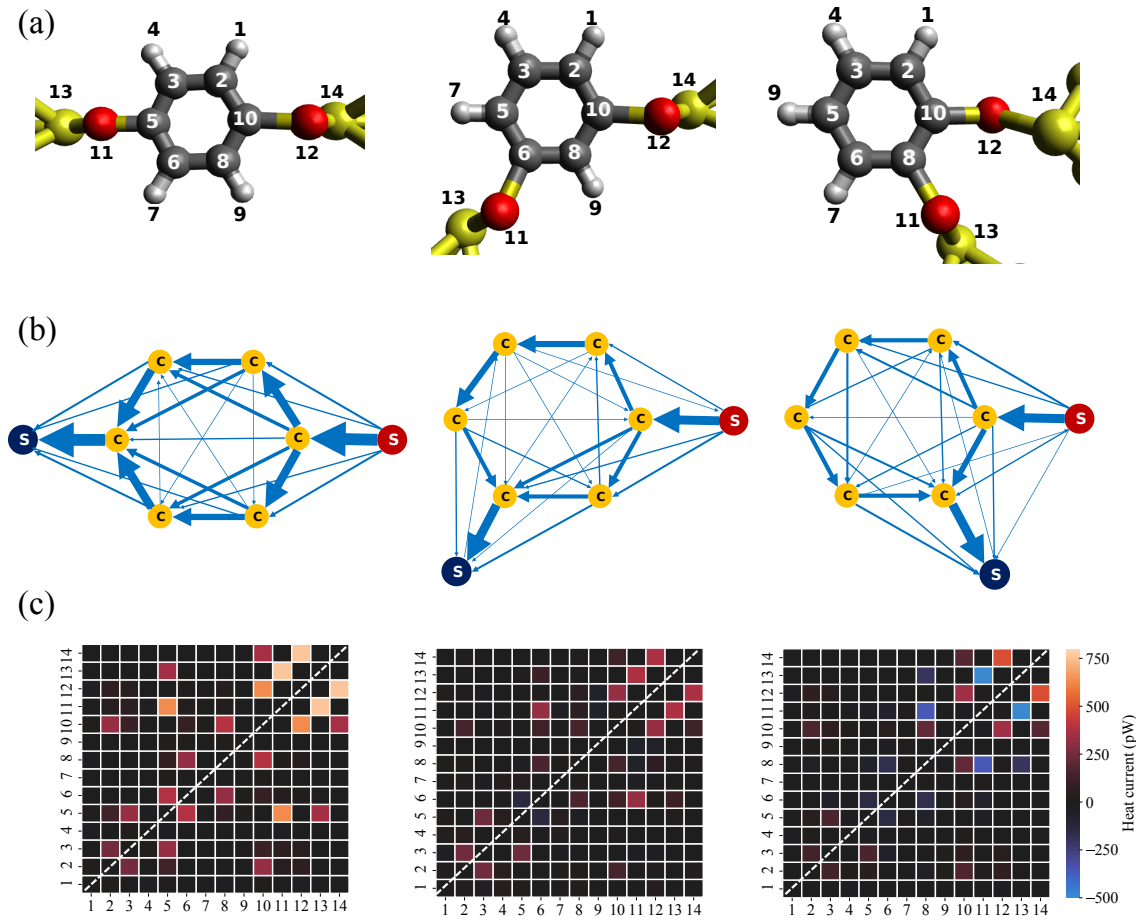


Figure 3.6: Heat currents maps in junctions comprising benzene molecules connecting in (from left to right) para, meta, and ortho configurations between gold substrates, computed by MD simulations at steady state under temperature bias of 300K and 350K on the two sides of the junction. (a). Molecular structures indicating atom numbering that is used in panel (c). Small light gray balls, bigger dark gray balls, red balls and yellow balls represent hydrogen, carbon, sulfur and gold atoms, respectively. (b) A map of local heat currents calculated at steady state for the three junction configurations. Arrows and thickness correspond to directions and magnitudes of the local currents. (c) two-dimensional map of local currents between atoms arranged according to the numbering shown in panel (a). Current direction is here indicated by sign: positive corresponds to leftward or leftward-tilted flux, or for vertical flow (for example between atom 3 and 6) – to upward flux. Note that the heat current maps shown in (panel c) are symmetric with respect to the white dashed diagonal line.

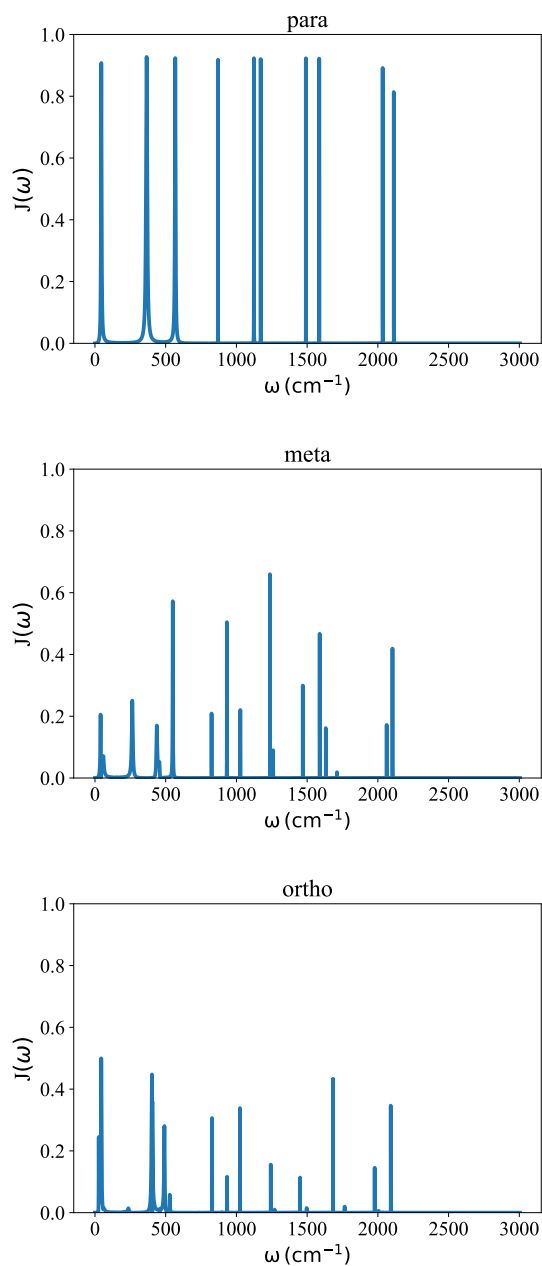


Figure 3.7: Frequency resolved energy flux (arbitrary units) generated by driving one sulfur atom of a benzenedithiol molecule and evaluating the heat generation per unit time on the other sulfur taking friction  $\gamma = 20 \text{ cm}^{-1}$  to affect the motion along the S-C bond, calculated according to Eqn. (2.28).

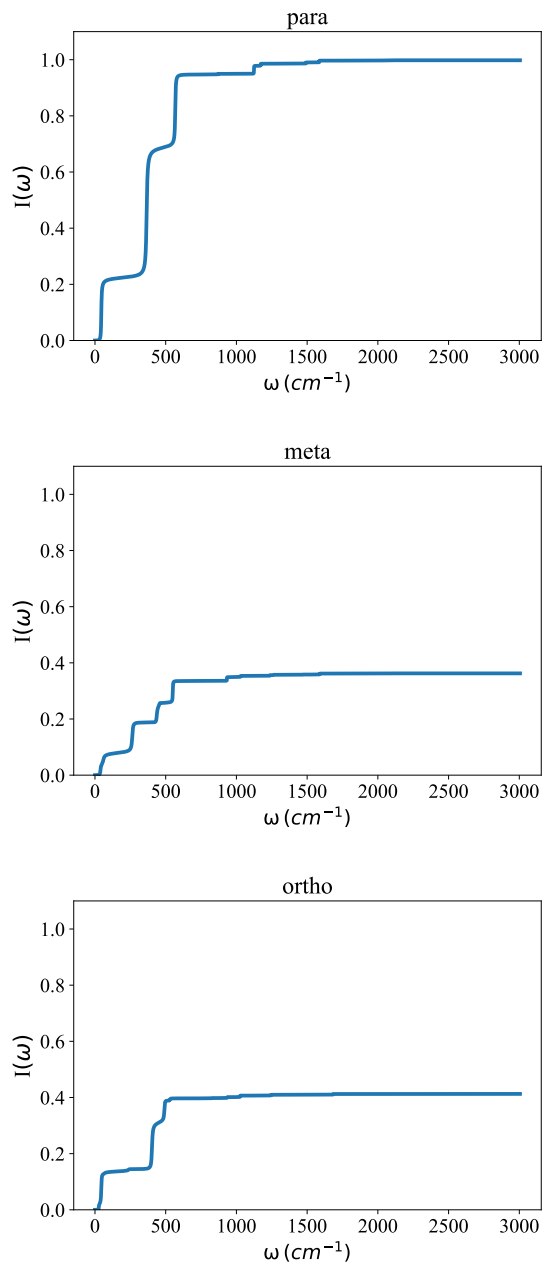


Figure 3.8: The intergrals  $I(\omega) = \int_0^\omega d\omega J(\omega)$  over the frequency resolved heat fluxes of Figure 3.7, normalized by  $I_{para}(3000 \text{ cm}^{-1})$  and displayed against  $\omega$  for the three benzendithiol species.

in the full simulations shown in Figure 3.3 and 3.4 correspond to a direction nearly perpendicular to the gold substrate. Integrals of these spectra  $I(\omega) = \int_0^\omega d\omega J(\omega)$  are shown as functions of  $\omega$  in Figure 3.8, showing a trend similar to that observed in Figure 3.3 and 3.4.

These results, which lacks information about molecule-leads binding and lead spectral function, as well as mode populations, do not directly apply to the actual heat transfer process, but they provide insight into the meaning of interference. Obviously, when the calculated transport is resolved to emphasize the contribution of different normal modes to the overall transmission, the “interference” concept is not necessarily useful. It becomes useful when we develop understanding of transport along individual spatial paths, then observe that opening a path may reduce transport rather than increase it, as was seen in Figure 3.3, or more generally, that transport in a system comprising several paths is not a simple sum over individual paths. The fact that this interference has a classical origin is not surprising given the nature of phonons as traveling waves.

### 3.4 Conclusion

In summary, we have computationally analyzed the heat conduction properties of benzenedithiol based single-molecule junctions with different bridging configurations using both classical MD simulations and quantum Landauer’s calculations. Our results indicate that the harmonic representation (used in the quantum calculations) as well as quantum effects (neglected in the classical calculation) are of secondary importance for such junctions at room temperature. Interesting deviations between the two calculations are found at low temperatures (where classical mechanics fails) and higher temperatures (where the harmonic approximation, used in the quantum calculation, fails). Comparing heat conduction trends between para-, meta- and ortho-connected

molecules shows strong indications of the role played by interference between different energy flow paths. This interference persists in the classical calculation, indicating its classical origin. We have examined the manifestation of this phenomenon when examined with frequency resolution and have pointed out that in the normal mode basis path interference translates into transmission properties of individual normal modes. It will be interesting to explore these types of behaviors further, to discern quantum from classical effects and to examine, for more anharmonic systems the effect of anharmonicity. Beyond such studies, it is of interest to examine the possibility of using interference as a tool for controlling heat conduction properties of different molecular structures.



## CHAPTER 4

### Quantum bath augmented classical simulation for heat conduction

#### 4.1 Methodology

##### 4.1.1 Formalism for quantum bath effects in Langevin dynamics

Let us start with Langevin's equation, for a simple particle at position  $x$  under the potential  $V(x)$ .

$$m\ddot{x}(t) = -\frac{\partial V(x)}{\partial x} - m\gamma\dot{x} + R(t). \quad (4.1)$$

$\gamma$  is the friction term, and  $R(t)$  is the random fluctuation forces, which obeys fluctuation-dissipation theorem,

$$\langle R(t)R(t') \rangle = 2m\gamma k_B \mathcal{T} \delta(t - t'), \quad (4.2)$$

where  $k_B$  is the Boltzmann constant and  $\mathcal{T}$  refers to the corresponding bath temperature.

Now we will have some detailed analysis about the random fluctuation term. Suppose we observed the system in time interval  $0 \leq t \leq T$  and expand  $R(t)$  in Fourier series.

$$R(t) = \sum_{n=-\infty}^{n=\infty} R_n e^{i\omega_n t} \quad (4.3)$$

$$\omega_n = \frac{2\pi n}{T}, \quad n = 0, \pm 1, \pm 2 \dots \quad (4.4)$$

$$R_n = \frac{1}{T} \int_0^T dt R(t) e^{-i\omega_n t} \quad (4.5)$$

The power spectrum can be written as<sup>40</sup>:

$$I_R(\omega) = \lim_{T \rightarrow \infty} \left( \frac{\sum_{n \in W_{\Delta\omega}} \langle |R_n|^2 \rangle}{\Delta\omega} \right); \quad (4.6)$$

where

$$W_{\Delta\omega} = \{n | \omega - \Delta\omega/2 \leq 2\pi n/T \leq \omega + \Delta\omega/2\}, \quad (4.7)$$

which can further change to

$$I_R(\omega) = \lim_{T \rightarrow \infty} \sum_{n \in W_{\Delta\omega}} \langle |R_n|^2 \rangle \delta(\omega - \omega_n); \quad \omega = \frac{2\pi n}{T}. \quad (4.8)$$

$I_R(\omega)\Delta\omega$  is the intensity of the random noise in the frequency range  $\omega \cdots \omega + \Delta\omega$ , which is obtained by summing up the magnitudes of different components  $R_n^2$ .

The Wiener-Khintchine theorem states:

$$I_R(\omega) = \frac{1}{2\pi} \int_{-\infty}^{\infty} dt e^{-i\omega t} \langle R(t)R(0) \rangle. \quad (4.9)$$

Together with Eqn.(4.2), we get

$$I_R = \frac{m\gamma k_B \mathcal{T}}{\pi} \quad (4.10)$$

Here we want to find an approximate coarse-grained frequency resolution of the heat flux. To this end we divide the frequency axis into many segments: if the relevant frequency domain is:  $0 \cdots \omega_{max}$ , then we can define  $\Delta\omega = \omega_{max}/N$  ( $N$  being the total number of segments), and the  $n$ th segment is between  $\omega_{n-1} = (n-1)\Delta\omega$  and  $\omega_n = n\Delta\omega$ . For each such segment the random noise can be taken as,

$$R_n = \sqrt{\Delta\omega \frac{m\gamma k_B \mathcal{T}}{\pi}} \left( e^{i\omega^{(n)}t} + e^{-i\omega^{(n)}t} \right) = 2\sqrt{\Delta\omega \frac{m\gamma k_B \mathcal{T}}{\pi}} \cos(\omega^{(n)}t), \quad (4.11)$$

where  $\omega^{(n)}$  is best chosen in the middle of the segment, that is  $\omega^{(n)} = (n - 1/2)\Delta\omega$ .

The approximation lies in the assumption that the currents obtained from these drivings are additive, so that if we act together with two segments  $n$  and  $n+1$  the heat current will be the sum of the individual contributions. This is certainly so in harmonic systems but is only an approximation for anharmonic ones. The reason why the approximation might be feasible is that contributions from different segments will come with random phases so that mixed signal might average to zero when average over phases is done. Note here we do not need to calculate the frequency resolved current. All we need is to replace the random noise with a similar one but with a frequency dependent effective temperature.

$$R(t) = \sum_n R_n(t) \quad (4.12)$$

$$R_n = 2\sqrt{\frac{\Delta\omega}{M_n} \frac{m\gamma k_B \mathcal{T}_{eff}(\omega_j^{(n)})}{\pi}} \sum_j \cos(\omega_j^{(n)}t + \phi_j), \quad (4.13)$$

where

$$\mathcal{T}_{eff}(\omega) = \frac{\hbar\omega/k_B}{e^{\hbar\omega/k_B T} - 1} \quad (4.14)$$

Taking more frequencies is just like taking smaller segments. Therefore, we final expression can be written as

$$R_n = 2\sqrt{\Delta\omega \frac{m\gamma k_B \mathcal{T}_{eff}(\omega^{(n)})}{\pi}} \cos(\omega^{(n)}t + \phi_n), \quad R(t) = \sum_n R_n(t) \quad (4.15)$$

Different realizations of the random noise come from different choices of  $\phi_n$ . Note that now that we reformulated the the random noise we can do standard heat conduction without calculating frequency resolved transmission coefficients.

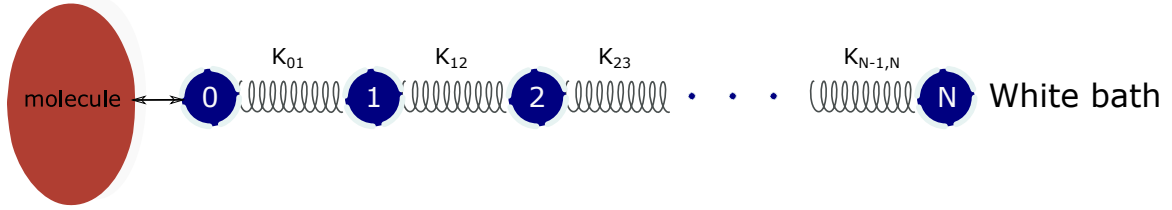


Figure 4.1: Schematic drawing of the Debye bath composed of  $N$  atoms, attaching a bridge molecule on the left and white bath on the right.

#### 4.1.2 Specifications of systems with Debye bath signature

To test the performance of this approach, we use an approximate Debye bath, because its spectrum behaves  $\omega^2$  for small  $\omega$ 's, and has a cutoff frequency ( $\omega_D$ ) when  $\omega \rightarrow \infty$ . One way to characterize such a colored bath spectrum is through mathematical filtering, as we have discussed in Appendix A.6. Another way is via modifying bath atom properties, which works well for toy model studies<sup>120</sup> and is much more straightforward computationally. For the purpose of this study, we will choose the latter approach.

Suppose the colored bath is consisted of  $N$  atoms (See Fig. 4.1). We want the atom number 0 to represent a Debye bath effect. We start by regarding the system without the molecule. The potential for bilinear interactions can be written as (in 1-dimensional notations):

$$V(x_0, x_1, \dots, x_N) = \frac{1}{2} \sum_{j=1}^N \sum_{l=1}^N K_{jl} x_j x_l \quad (4.16)$$

$$\frac{d^2 x_n}{dt^2} = -\frac{1}{M_n} [K_{n,n+1} x_{n+1} + K_{n,n-1} x_{n-1} + K_{nn} x_n]; \quad n \neq 0, N \quad (4.17)$$

The last atom (N) is connected to white noise,

$$\frac{d^2x_N}{dt^2} = \frac{1}{M_N}[K_{N,N-1}x_{N-1} + K_{NN}x_N] - \gamma \frac{dx_N}{dt} + \frac{1}{M_N}R(t), \quad (4.18)$$

$$\langle R(t)R(0) \rangle = 2M_N\gamma k_B T \delta(t). \quad (4.19)$$

Go to mass-weighted coordinates,

$$\frac{d^2y_n}{dt^2} = -(k_{n,n+1}y_{n+1} + k_{n,n-1}y_{n-1} + k_{nn}y_n); \quad n \neq 0, N \quad (4.20)$$

$$\frac{d^2y_0}{dt^2} = -(k_{0,1}y_1 + k_{00}y_0) \quad (4.21)$$

$$\frac{d^2y_N}{dt^2} = -(k_{N,N-1}y_{N-1} + k_{NN}y_N) - \gamma \frac{dy_N}{dt} + \rho(t), \quad (4.22)$$

where we have defined,

$$y_n = \sqrt{M_n}x_n, \quad k_{ij} = \frac{K_{ij}}{\sqrt{M_i M_j}}, \quad k_{nn} = \frac{K_{nn}}{M_n}, \quad \rho(t) = \frac{R(t)}{\sqrt{M_N}}, \quad (4.23)$$

$$\langle \rho(t)\rho(0) \rangle = 2\gamma k_B T \delta(t). \quad (4.24)$$

Now as we transfer to Fourier space,

$$f(t) = \tilde{f}(\omega)e^{-i\omega t} + \tilde{f}(-\omega)e^{i\omega t} \quad (4.25)$$

We have,

$$\omega^2 \tilde{y}_0 = k_{01} \tilde{y}_1 + k_{00} \tilde{y}_0 \quad (4.26)$$

$$\omega^2 \tilde{y}_n = k_{n,n+1} \tilde{y}_{n+1} + k_{n,n-1} \tilde{y}_{n-1} + k_{nn} \tilde{y}_n \quad (4.27)$$

$$\omega^2 \tilde{y}_N = k_{N,N-1} \tilde{y}_{N-1} + k_{NN} \tilde{y}_N - i\omega \gamma \tilde{y}_N - \tilde{\rho}(\omega). \quad (4.28)$$

We may further put them into matrix form.

$$\mathbf{M}\mathbf{y} = \mathbf{r}, \quad (4.29)$$

where

$$\mathbf{r} = \begin{bmatrix} 0 \\ 0 \\ \vdots \\ \tilde{\rho} \end{bmatrix} \quad (4.30)$$

$$\mathbf{M} = \begin{bmatrix} k_{00} - \omega^2 & k_{01} & \dots & 0 \\ k_{10} & k_{11} - \omega^2 & k_{12} & 0 \\ \vdots & \vdots & \ddots & \vdots \\ 0 & \dots & k_{N,N-1} & k_{NN} - \omega^2 - i\omega\gamma \end{bmatrix} \quad (4.31)$$

The matrix can be inverted analytically,

$$\tilde{y}_0(\omega) = [\mathbf{M}^{-1}]_{0N} \tilde{\rho}(\omega) \quad (4.32)$$

For the velocity, we have

$$|\tilde{y}_0(\omega)|^2 = |[\mathbf{M}^{-1}]_{0N}|^2 \omega^2 |\tilde{\rho}(\omega)|^2 \quad (4.33)$$

$\langle |\rho(\tilde{\omega})|^2 \rangle$  is the Fourier transform of the random noise  $\rho$  and is equal to<sup>40</sup>

$$\langle |\rho(\tilde{\omega})|^2 \rangle = \frac{\gamma k_B T}{\pi}, \quad (4.34)$$

note the mass is unity in the mass-weighted representation. We then have

$$|\tilde{y}_0(\omega)|^2 = |[\mathbf{M}^{-1}]_{0N}|^2 \omega^2 \frac{\gamma k_B T}{\pi} \quad (4.35)$$

The LHS is the Fourier transform of the velocity correlation function of atom 0 – the atom seen by the molecule it connects to.

When we connect the bath spectrum density to the v-v correlation<sup>40</sup>

$$g(\omega) = \frac{3mN}{\pi k_B T} \int_{-\infty}^{\infty} dt \langle \dot{x}(0)\dot{x}(t) \rangle e^{-i\omega t}. \quad (4.36)$$

We have the expression that takes into account the force constants matrix.

$$g(\omega) = |[\mathbf{M}^{-1}]_{0N}|^2 \omega^2 \frac{3\gamma}{\pi^2} \quad (4.37)$$

With parameters of force constants (i.e.  $k_{ij}$ ) and the coupling ( $\gamma$ ), we can fit the density of modes into Debye-shape (with a normalization factor C),

$$g(\omega) = C \frac{\omega^2}{1 + (\omega/\omega_D)^{2(N+1)}}, \quad (4.38)$$

which shows in the same form of the math filter method<sup>76</sup>.

As an example of the above formalism, we will use two layers (one atom for each layer) of representative bath atoms that give rise to the eighth power of  $\omega$  when fitted into Eqn. 4.38 (derived below, with three specific tunable parameters), which could be a roughly good estimator for the purpose of simple model investigations.

For two-atoms bath (See Fig. 4.2 the left atom, number 0, is supposed to connect with the molecule):

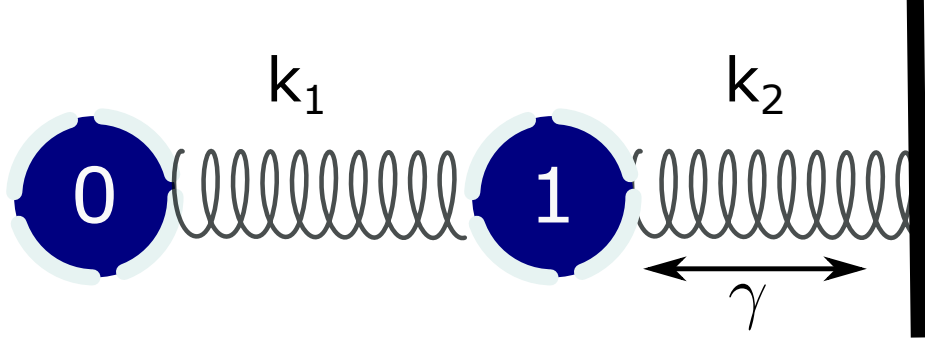


Figure 4.2: Schematic drawing of the Debye bath composed of 2 atoms (simplified version of Fig 4.1)

$$\mathbf{M} = \begin{bmatrix} k_{00} - \omega^2 & -k_1 \\ -k_1 & k_{11} - i\gamma\omega - \omega^2 \end{bmatrix} \quad k_{00} = k_1, \quad k_{11} = k_1 + k_2 \quad (4.39)$$

$$\det(\mathbf{M}) = \omega^4 + i\gamma\omega^3 - (2k_1 + k_2)\omega^2 - i\gamma k_1\omega + k_1 k_2 \quad (4.40)$$

$$\mathbf{M}^{-1} = \frac{1}{\det(\mathbf{M})} \begin{bmatrix} k_1 + k_2 - i\gamma\omega - \omega^2 & k_1 \\ k_1 & k_1 - \omega^2 \end{bmatrix} \quad (4.41)$$

$$|\mathbf{M}^{-1}|_{12} = \frac{k_1}{\det(\mathbf{M})} \quad (4.42)$$

The denominator of  $(|\mathbf{M}^{-1}|_{12})^2$  is

$$\omega^8 + c_6\omega^6 + c_4\omega^4 + c_2\omega^2 + c_0 \quad (4.43)$$



where

$$c_6 = \gamma^2 - 2(2k_1 + k_2) \quad (4.44)$$

$$c_4 = (2k_1 + k_2)^2 + 2k_1k_2 - 2\gamma^2k_1 \quad (4.45)$$

$$c_2 = \gamma^2k_1^2 - 2k_1k_2(2k_1 + k_2) \quad (4.46)$$

$$c_0 = k_1^2k_2^2 \quad (4.47)$$

Under the condition,  $c_6 = c_4 = c_2 = 0$  and  $k_1 \neq 0$  and  $k_2 \neq 0$ , we fit the parameters

$$k_1 = 0.151388, \quad k_2 = 0.131483, \quad \gamma = 0.868517 \quad (4.48)$$

We can then go back to the expression of the density of modes,

$$g(\omega) = (|\mathbf{M}^{-1}|_{12})^2 \omega^2 \frac{3\gamma}{\pi^2} \quad (4.49)$$

and plot  $g(\omega)$ . If we assume

$$g(\omega) = C \frac{\omega^2}{1 + (\frac{\omega}{\omega_D})^8}, \quad (4.50)$$

then we have

$$\omega_D = (c_0)^{1/8} \approx 0.375126 \quad (4.51)$$

We show in Appendix C.1, the Fourier transform (Fig. C.2) of the auto-correlation (Fig. C.1) of the of atom 0 with these fitted parameters, does act as Debye bath, with a sharp cut-off at around one Debye frequency.

## 4.2 Numerical tests

### 4.2.1 Equilibrium energies obtained after long-time relaxation

The first and simplest case we will check is how a single particle within the vicinity of a thermal bath relaxes to equilibrium. We know from statistical mechanics that the energy of the system will be characterized by the temperature of the bath for the long run when it equilibrates with the bath.

For a harmonic oscillator, the system energy  $\langle E \rangle \sim k_B T$ , if the bath is in classical Boltzmann distribution, while  $\langle E \rangle \sim \hbar\omega / (e^{\hbar\omega/k_B T} - 1)$  ( $\omega$  being the frequency of the oscillator), if the phonons in the bath is occupied according to quantum boson distribution<sup>40</sup>. For an anharmonic oscillator, we take Morse potential here. The Morse potential of a particle is

$$V_{mor} = D[e^{-\alpha(x-x_0)} - 1]^2, \quad (4.52)$$

where  $D$  is the depth of the potential (Dissociation energy), and  $x_0$  is the equilibrium position.  $\alpha$  is a parameter usually defined by  $\alpha = \sqrt{m\omega^2/2D}$ , where  $\omega$  is the harmonic oscillating frequency at the minimum position.

For classical calculations, phase space partition function under equilibrium for the particle can be written as

$$Z = \frac{1}{h} \int dv dx e^{-\beta(\frac{1}{2}mv^2 + V_{mor})} \quad (4.53)$$

where  $\beta = 1/k_B T$ .

The average energy is

$$\langle E \rangle = \frac{\frac{1}{h} \int dv dx (\frac{1}{2}mv^2 + V_{mor}) e^{-\beta(\frac{1}{2}mv^2 + V_{mor})}}{Z} \quad (4.54)$$

$$= \frac{1}{2}\beta^{-1} + \frac{\int dx V_{mor} e^{-\beta V_{mor}}}{\int dx e^{-\beta V_{mor}}} \quad (4.55)$$

$$\equiv \langle K \rangle + \langle V_{mor} \rangle \quad (4.56)$$

For the quantum calculation, the energy levels of the so called Morse oscillator<sup>121</sup> can be expressed as,

$$E_n = [n + \frac{1}{2} - \frac{1}{2\lambda}(n + \frac{1}{2})^2] \hbar\omega_0 \quad (4.57)$$

$$\omega_0 = \left( \frac{2D\alpha^2}{m} \right)^{1/2}, \quad n = 0, 1, 2, \dots, (\lambda - \frac{1}{2}), \quad \lambda = \frac{\sqrt{2mD}}{\alpha\hbar} \quad (4.58)$$

The reason why there is a upper limit of the energy level of the Morse oscillator, that is  $n_{max} = \lambda - 1/2$ , is that the Morse potential (Eqn.(4.52)) is not infinitely bounded. It has a dissociation energy ( $D$ ), beyond which the potential energy no longer has bound states (in another word, the molecule does not exist any more). One can rigorously work out the exact expression for such upper bound by solving the wavefunctions for the Schrodinger's equation<sup>121</sup>, but it may also help if we intuitively deduce it from the energy level expression itself.

$$E_{n+1} - E_n = 1 - \frac{1}{\lambda}(n + 1) - \frac{1}{2\lambda} > 0. \quad (4.59)$$

This relation has to hold obviously, since higher energy level should not "below" lower energy level, which gives us  $n < \lambda - 3/2$ . Since energy levels are integers, the upper limit  $n_{max} = \lambda - 1/2$ .

The quantum calculation of average energy can be written,

$$\langle E \rangle = \frac{\sum_n E_n e^{-\beta E_n}}{\sum_n e^{-\beta E_n}}. \quad (4.60)$$

Now we have the analytical expressions for both classical and quantum equilibrium energies of harmonic and anharmonic (Morse) oscillators, we will check how the classical constant-T MD approach and the “effective temperature” (ET) (Eq.4.14) dynamics approach (Eq.4.15) we have developed compare to the actual values.

Fig.4.3 shows the temperature dependent total system energies at equilibrium for different calculations and model simulations (namely, classical versus quantum). For the harmonic oscillator (also see Fig C.3 for the simulated results) at a large bath temperature (e.g. temperature three times larger than the oscillator frequency), the temperature dependency of the energies all become linear (1 to 1 ratio),  $\langle E \rangle \sim k_B T \sim \hbar\omega / (e^{\hbar\omega/k_B T} - 1)$ , when  $T \rightarrow \infty$ . On the other hand, on the low temperature end, the classical energies (either simulations or analytical results) diverge from their quantum counterparts quickly. Specifically, while the particle energy still scales linearly to the classical bath, the quantum effect make the energy decrease exponential (with zero-energy taken into account), most obvious for  $T < 1$ .

Under anharmonic potential(that is Morse oscillator, more details see Appendix C.2) we can see similar trends: The quantum results (analytical or simulated with the effective temperature dynamics) differ more to the classical results (analytical or simulated constant-T Langevin dynamics) at the lower temperatures, while the two gradually converge at high-T limit. One difference between harmonic and anharmonic potentials to be noticed is that the anharmonic energies at equilibrium do not proportionally depend on the bath temperatures as the harmonic potential does (Fig.C.3).

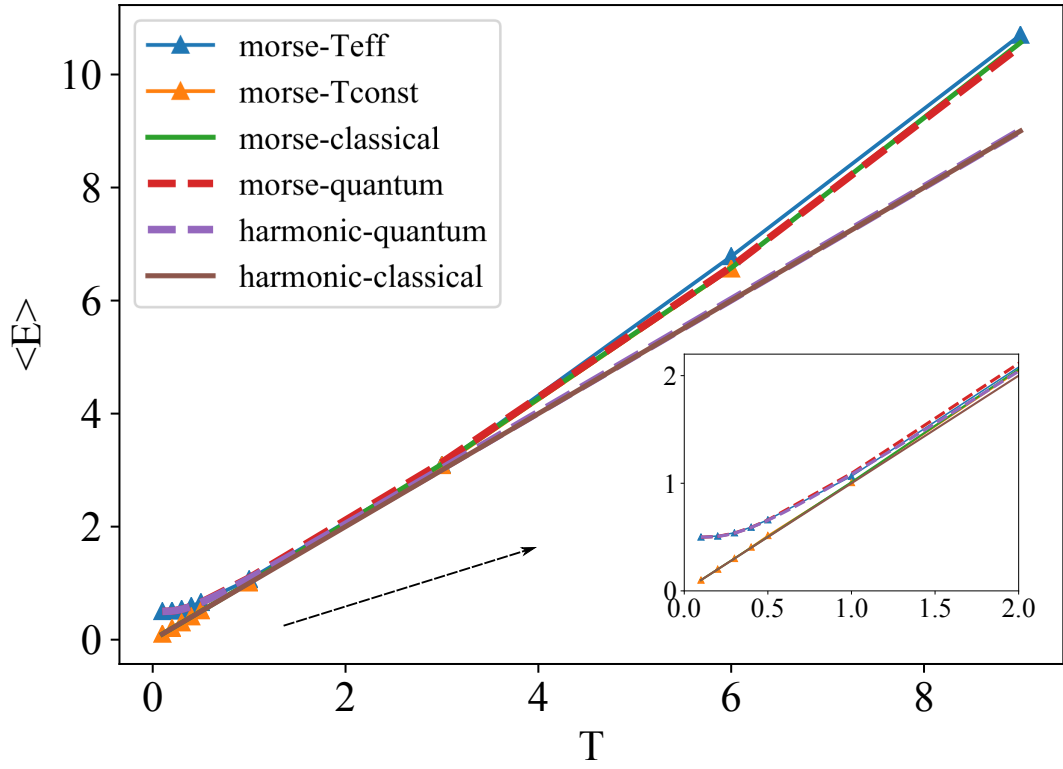


Figure 4.3: Equilibrium energies of a single particle in a Morse potential connected to thermal bath of different characteristic temperatures ( $T$  indicated on the x-axis). All dimensionless quantities are scale with respect to the oscillating frequency ( $\omega$ ) of the corresponding harmonic potential with the relation  $2D\alpha^2 = m\omega^2$  (see Appendix C.2). Specifically, the unit for  $T$  is  $\hbar\omega/k_B$ , the unit of inverse length  $\alpha$  is  $\sqrt{m\omega/\hbar}$  and the energy unit is  $\hbar\omega$ . The insert is a zoom-in of the full figure to the  $T$  range of 0 to 2.

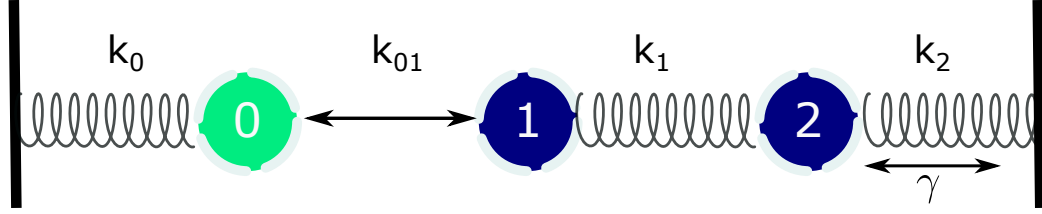


Figure 4.4: Schematic drawing of the diatomic molecule attached to a Debye bath simulated with two harmonically bonded atoms. The molecule is represented as number 0, connected to the bath atoms, which are parameterized according to Eqn. 4.48.

Overall, the MD simulation of modified Langevin dynamics, which considers quantum effect of the reservoirs, has accounted for both high and low temperature limits at equilibrium, by encoding an effective temperature that incorporates quantum boson distribution into the molecular dynamics.

#### 4.2.2 Vibrational relaxation of a diatomic molecule

Another way to check the quantum bath (ET approach) properties as well as anharmonicity effects is by looking at the energy relaxation of a diatomic molecule near the bath surface. Here we show the results for such a model system with different interactions and parameters (see Fig. 4.4), and their rates of energy relaxation with respect to bath temperature changes.

Two types of interactions are taken between the molecule and the bath (i.e. between atom 0 and 1). a). Harmonic ( $k_{01} = 0.002$  as default); b). Anharmonic (Morse potential detailed in Appendix C.2,  $\alpha = 0.1$  and  $D = 0.1$  with dimensionless units Appendix C.3). Fig. 4.5 shows energy relaxation for the harmonic diatomic oscillator within the range of Debye spectrum. Initial states of the oscillator are sampled from the same total energy with random displacements and velocities. The relaxation energy is calculated as statistical ensemble averages of the time-dependent total energy changes minus the energy when the system is equilibrated to the baths. While in

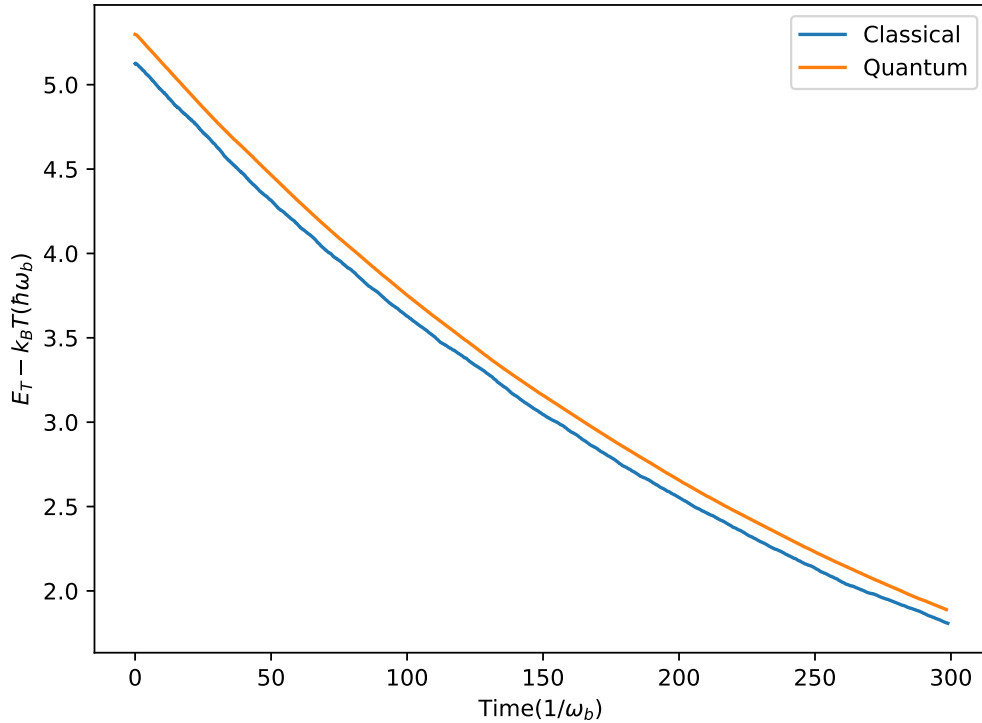


Figure 4.5: Examples of energy relaxation rates of the diatomic molecule shown in Fig. 4.4, with classical and quantum (effective temperature method) baths. With internal vibration frequency about 1/4 of Debye and temperature 0.2 ( $\hbar\omega_D/k_B$ ). The x-axis is the evolution time. The slopes of the logarithmic fits of the energy changes (y-axis values) are 0.000209 for the classical and 0.000207 for the quantum, which correspond to their relaxation rates respectively.

the classical case the temperature is constant, the effective temperature for the ET approach arises from phonons in the quantum bath that follow boson distribution. That is why the quantum curve appears slightly higher than the classical line, because the equilibrium energy of the augmented quantum bath is smaller caused by overall lower effective temperature. As the energy decays exponentially, we can do logarithmic fit to get the relaxation rates from the slopes of the fitted lines. It is shown that the classical and quantum cases align with each other well ( $\sim 0.0002$  in Fig. 4.5). Later we will see it is not always the case for anharmonic oscillators.

When the of harmonic oscillator is bilinearly connected to the bath and its fre-

quency is well below the cutoff of Debye spectrum, it is expected that the rate is temperature-independent (See Section 13.4 in Ref<sup>40</sup>). To see the effect of Debye colored bath, we take comparatively larger vibrational frequencies for the diatomic molecule: 1.5 times and 3 times of Debye cut-off (Fig. 4.6). While when the internal frequency reaches 3 times larger than Debye frequency, all the relaxations cease, because of lack of available modes from the color bath, 1.5 times higher frequency shows some interesting effect. The harmonic versions are still flat, but the anharmonic potential (the oscillator is connected to the bath via a Morse potential, detailed in the Appendix C.2. The parameters are chosen so that the harmonic potential is an approximation when the displacement of the oscillator is small from its equilibrium position) gives higher rates, indicating the ability of the anharmonicity to create effective modes (Fourier components of the dynamics) outside the range of Debye spectrum. Moreover, the quantum simulation always deviates from the classical anharmonic results, which is not seen in the harmonic case.

The up trend for the higher temperature (e.g. at 0.8) is not generic. We show in the following that when the interactions (molecule-bath coupling strength, i.e.  $k_{01}$  in Fig. 4.4) become smaller, this trend disappears (Fig. 4.7). Therefore, to be in the linear-response regime, the coupling between the molecule and the bath has to be smaller enough so that the broadening will not affect the results.

### 4.2.3 Heat conduction through a diatomic molecule

This section shows results of comparison for molecular heat conduction among the quantum augmented MD approach, constant temperature MD simulations and Landauer's formalism<sup>4,6</sup>. Specifically, we choose a diatomic molecule which is connected to two baths <sup>1</sup> of different temperatures, allowing for steady-state heat current cal-

---

<sup>1</sup>For simplicity, white baths are chosen here, meaning the two atoms in the molecule are directed subjected to white random noise in Langevin's dynamics, instead of the Debye bath as in the previous



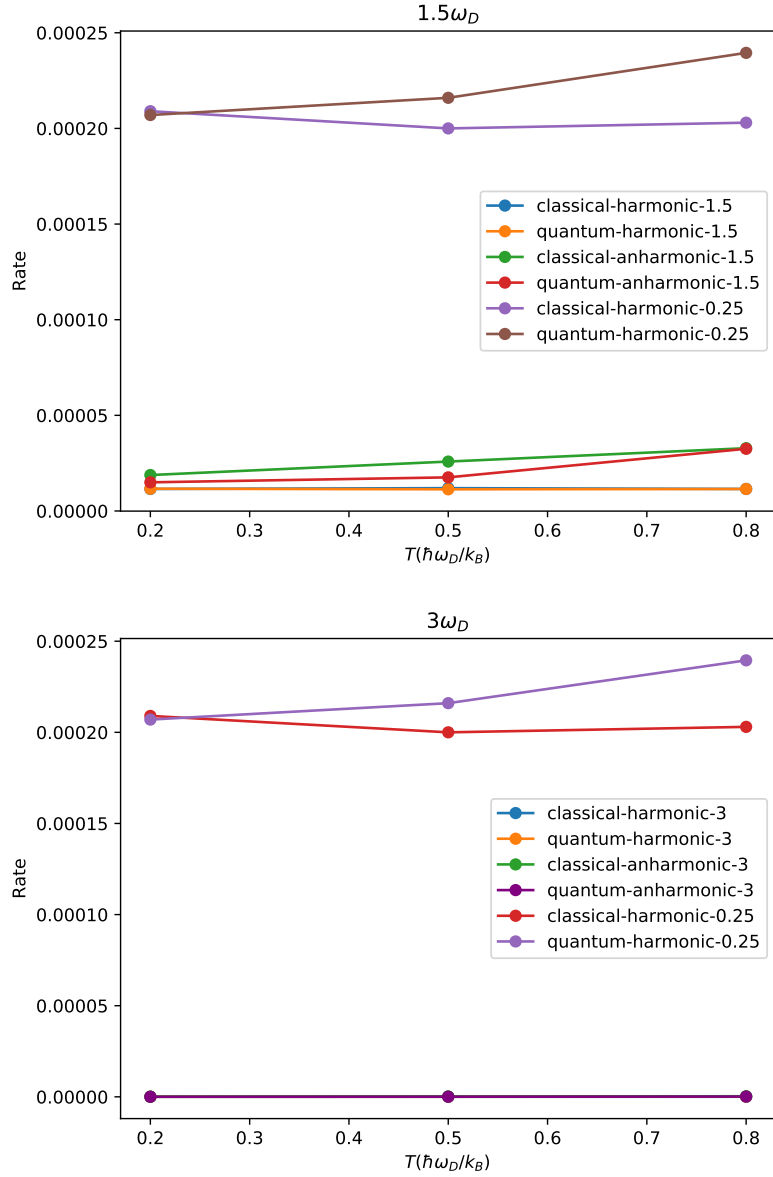


Figure 4.6: Relaxation rates for the diatomic molecule with respect to different temperatures, under Debye bath composed of two layers of atoms shown in Fig. 4.4. Two sets of internal vibration frequencies of  $1.5\omega_D$  and  $3\omega_D$  are compared to the frequency of  $0.25\omega$ . The force constant ( $k_{01}$ ) is 0.002 in all cases. The comparative data are all labeled in the legend, the numbers (e.g. 1.5, 0.25) denote the internal vibrational frequencies in which the oscillators are simulated (in the anharmonic cases, the potential energies depth and characteristic lengths are chosen to be equal to the harmonic force constants, i.e.  $k_{01} = 2\alpha^2 D$ , details in Appendix C.2). The quantum results refer to the “effective temperature (ET) approach”, while classical results is for traditional constant temperature method.

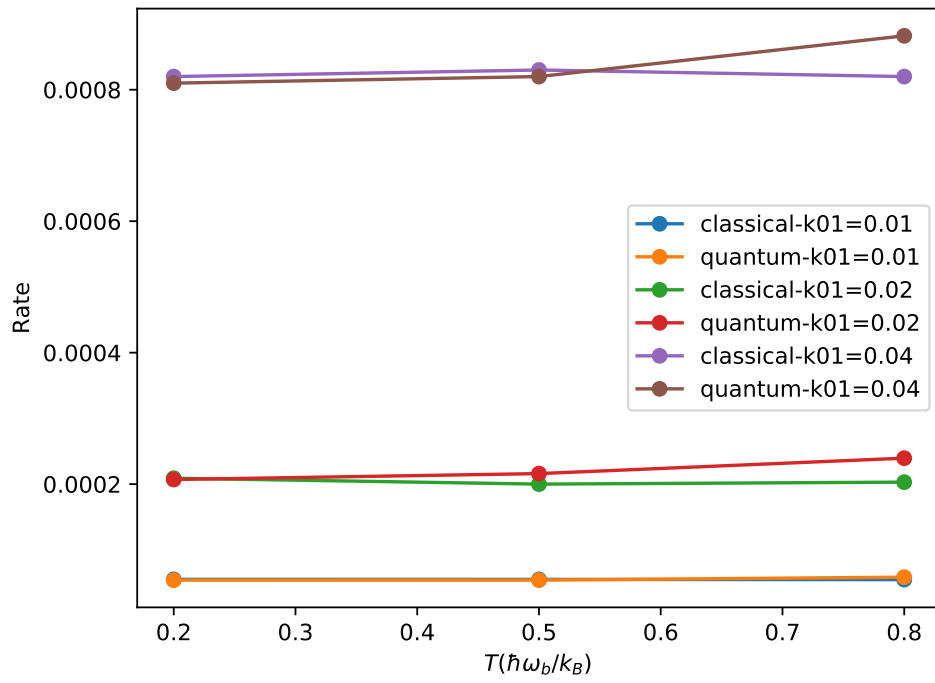


Figure 4.7: Comparisons of relaxation rates for the diatomic molecule with different interacting/coupling strengths ( $k_{01}$  in the model, other parameters are the same as in Fig. 4.6). The x-axis is temperature.

culations.

The parameters are chosen within the range of general MD force-fields: the masses of the two atoms are 15 A.M.U. (the mass of one carbon plus three hydrogen atoms); the harmonic bond between the atoms is  $292900 \text{ kJmol}^{-1}\text{nm}^{-2}$  ( $\sim$ C-C bond); the system-bath coupling ( $\gamma$ ) is  $1 \text{ ps}^{-1}$ . As for the quantum (ET approach) simulation, the maximum sampling frequency ( $\omega_{max}$ ) is taken to be  $100 \text{ ps}^{-1}$  (with slicing number of  $5 \times 10^4$ ). During the MD simulations, the temperature bias is fixed to 50K, and the temperature of the left side bath changes from low to high and always smaller than the right bath.

Fig.4.8 summarizes the results. A few observations can be made: (a) The heat current from constant temperature MD approach is almost T-independent across the low, middle to high bath temperatures, as long as the bias itself is kept constant. (b) The Landauer's calculation reduces to about half of the value at lower temperature limit compared to the constant temperature case (the reason it does not go to zero is that 50K thermal bias always provides transporting phonons in the right bath even when the left bath has close-to-zero temperature), and catches up gradually as temperature rises. The trend of the ET MD simulations aligns well with the Landauer's results. (c) All three approaches converge to the same values, as temperature of the left bath becomes high, which is expected that quantum effect reduces to its minimum at the classical (high-T) limit.

Since there is only one harmonic interaction in the diatomic system, the Landauer's calculations depict the true behavior of the system for the full temperature range, while the constant-T Langevin's MD results act as its approximation for high-T limit. By showing the agreement of the quantum augmented MD method to the

---

section of relaxation study. There will not be considerations as to which particular internal frequency to choose to be in the bath spectrum range.

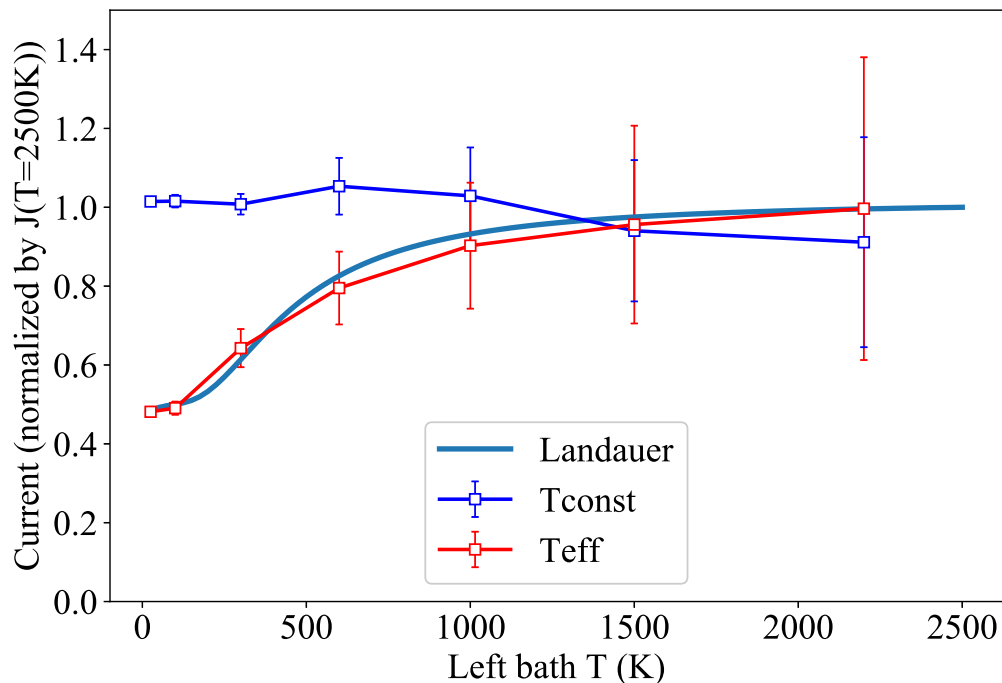


Figure 4.8: Heat currents for the 1-D diatomic system under three different approaches. The Landauer-type calculations are based on the normal modes in the system, while the other two with error bars (standard deviations) are results from MD simulations. Tconst means classical constant temperature baths while Teff refers to the quantum augmented baths formulated in the method section. X-axis is the temperatures for the left bath, while the right bath is always 50K higher in all the settings. Y-axis are normalized (by Landauer's current at 2500K) heat currents (MD results are sampled from steady-state inter-atomic heat currents<sup>3,4</sup>) The units for the system are: 15 a.m.u. for the atomic masses;  $292900 \text{ kJmol}^{-1}\text{nm}^{-2}$  for the harmonic bond;  $1 \text{ ps}^{-1}$  for the molecule-bath coupling (as in Langevin's dynamics); and  $100 \text{ ps}^{-1}$  for the maximum quantum bath frequency (with 50000 small intervals).

Landauer's calculation, we confirm indeed this method is capable of capturing full dynamics of the molecular heat conduction, through carefully engineering the bath properties to introduce the boson distribution of quantum mechanical phonons.

## CHAPTER 5

### **Electron-transfer-induced and phononic heat transport in molecular environments and energy partitioning in relaxation and activation**

This chapter is adapted from *The Journal of Chemical Physics* **147**, 124101 (2017) & *The Journal of Chemical Physics* **149**, 104103 (2018)

#### **5.1 Introduction**

The interplay between electric current and heat transfer drives energy conversion in diverse thermoelectric applications and results in a multitude of chemical functionalities which can be harnessed to perform operations in molecular devices, junctions, and machines.<sup>122–131</sup> Understanding the physical underpinnings of these processes and how they can be utilized for optimal functionality is a critical focus in nonequilibrium dynamics. In the regime where electron dynamics are strongly coupled with the motions of a surrounding thermal environment, charge transport between donor and acceptor molecules is dominated by hopping-type events, and electron transfer (ET) reactions can be described using the theory developed largely by Marcus,<sup>40,132–137</sup> Levich,<sup>138</sup> and Hush.<sup>139–141</sup> So-called Marcus theory is a semiclassical theory that connects electron tunneling with transition state theory (TST),<sup>40,142–147</sup> and gives qualitative and sometimes quantitative predictions of reaction rates in the limit of strong electron-phonon coupling where a system's dynamical evolution can be described by electron occupation probabilities on the donor and acceptor sites. Multidimensional variants of Marcus theory have also been applied to cases where electron transport is coupled with other reactive coordinates, such as in proton-coupled electron transfer, and also

to reactions that involve the transfer of multiple electrons.<sup>148–157</sup>

Energy (heat) transport in metals is dominated by electronic motion. By contrast, energy transport in molecular systems can occur through several channels depending on the form of energy transferred. Thermal energy (heat) transport is dominated by the phononic mechanism, i.e., the interaction and subsequent energy transfer between vibrational modes which are in contact with thermal environments of different temperatures.<sup>99,158–168</sup> In addition to studies that have elucidated the connection between composition, morphology and microscopic structure of different environments and their heat conduction properties,<sup>8,10,12,45,88,169–175</sup> many recent studies have resulted in the development of molecular devices<sup>12</sup> such as thermal transistors<sup>176–178</sup> and thermal rectifiers<sup>162,179,180</sup> which use heat to perform useful functions and logical operations.

In contrast to metals, in the development of theories for charge and energy transport in molecular systems, a principal postulate is the absence of direct interdependence: charge transport takes place through electron transfer while heat transport occurs through phononic interactions. However, it has been recently shown that the transfer of electrons between a donor and acceptor whose environments are at different local temperatures generates a heat current solely from the electron transport.<sup>19–21</sup> In previous work, this ET-induced heat transport (ETIHT) has been examined between redox molecular motifs, at molecule-metal interfaces, and in molecular junctions using two significant approximations: (a) vibrational contributions to the total heat conduction were ignored to concentrate solely on the heat transport due to electron transfer and (b) the nuclear modes involved in the ET process were assumed to couple to, and to be in thermal equilibrium with, their local environments – e.g. the donor or acceptor neighborhoods. Here, we augment this formalism to include vibrational heat transfer by allowing mode coupling to both sites. At steady state, each mode carries

heat currents between the environments of different local temperatures to which it is coupled. At the same time, such modes promote electron transfer as described by the generalized Marcus theory of Refs. 19 and 20. This augmented theory allows comparison between the magnitude of the ET-induced and phononic heat conduction.

The remainder of the chapter is organized as follows: In Section 5.2 and the subsections therein, we discuss details of the applied model and develop a unified theory for electron transfer, ETIHT, and phononic heat transfer by merging stochastic Langevin dynamics with multithermal Marcus theory. Section 5.3 contains the results obtained through application of the developed theory to different systems, with a specific focus placed on the interplay and magnitude comparison between phononic and electron-transfer-induced heat transport. Concluding remarks are given in Sec. 5.4, and the outlook for future work is also discussed.

## 5.2 Theory of Multithermal Electron Transfer and Heat Conduction

### 5.2.1 System details

To examine heat conduction, electron transfer and their couplings as expressed by the ETIHT phenomenon, we apply a model that incorporates nonequilibrium Langevin-type stochastic dynamics into semiclassical Marcus-Levich ET theory.<sup>40,132,133,181</sup> The model is based on the Marcus-Levich picture of energy transfer in which a two-state (electron on donor and electron on acceptor) electronic system is coupled to  $N$  vibrational modes whose dynamics control the electron transfer. In departure from the Marcus-Levich picture, each mode is assumed to be in contact with two heat bath sites, denoted  $a$  and  $b$ , (we will henceforth take these to be the donor and acceptor sites) with respective local temperatures  $T_a$  and  $T_b$ .



The motion of mode  $i$  is modeled by the Langevin equation,

$$\ddot{x}_i = -\gamma_a^{(i)}\dot{x}_i - \gamma_b^{(i)}\dot{x}_i - \frac{\partial \tilde{E}_s(\mathbf{X})}{\partial x_i} + \xi_a^{(i)}(t) + \xi_b^{(i)}(t), \quad (5.1)$$

where  $\mathbf{X} = \{x_1, \dots, x_N\}$ ,  $\tilde{E}_s(\mathbf{X})$  is a mass-weighted energy surface whose geometry depends on the electronic state  $s$  of the system,  $\gamma_a^{(i)}$  and  $\gamma_b^{(i)}$  are coupling strengths to baths  $a$  and  $b$ , and  $\xi_a^{(i)}(t)$  and  $\xi_b^{(i)}(t)$  are stochastic noise terms of the respective bath. The stochastic terms obey the relations

$$\langle \xi_K^{(i)}(t) \xi_K^{(i)}(t') \rangle = 2\gamma_K^{(i)} k_B T_K m_i^{-1} \delta(t - t'), \quad (5.2)$$

$$\langle \xi_a^{(i)}(t) \xi_b^{(i)}(t') \rangle = 0, \quad (5.3)$$

$$\langle \xi_K^{(i)}(t) \rangle = 0, \quad (5.4)$$

where  $K \in \{a, b\}$  and  $\langle \dots \rangle$  denotes an average over the realizations of the noise. These correlations imply that the noise from each thermal source is white and is not correlated with the noise in the other bath or the noise in any other mode. The full dynamics of the system is described by  $N$  equations analogous to (5.1) – one for each mode – which are represented in a diagonal basis. However, electron transfer is a collective nuclear process involving all modes that are sensitive to the electronic occupations of the donor and acceptor sites. Consequently the modes interact through the geometrical modification of the underlying energy surface associated with the electronic states. Here, electronic transport and ETIHT are modeled using a multi-thermal variant of Marcus ET theory.<sup>19,20</sup>

The system has two electronic states:  $A$  and  $B$ , which correspond to electron localization on site  $a$  and site  $b$ , respectively. When the system is in electronic state

$A$ , the energy is,

$$E_A(x_1, \dots, x_N) = E_0^{(A)} + \sum_i^N \frac{1}{2} k_i \left( x_i - \lambda_i^{(A)} \right)^2, \quad (5.5)$$

and in electronic state  $B$ ,

$$E_B(x_1, \dots, x_N) = E_0^{(B)} + \sum_i^N \frac{1}{2} k_i \left( x_i - \lambda_i^{(B)} \right)^2, \quad (5.6)$$

where  $k_i$  is the force constant of the  $i$ th mode and  $E_0^{(s)} : s \in \{A, B\}$  is the electronic energy origin of the respective state. The factors  $\lambda_i^{(s)} : s \in \{A, B\}$  parameterize configurational changes in the environment of the respective mode due to electron localization on the corresponding site. The contribution to the total energy from the  $i$ th mode when the system is in the  $s$ th state is

$$E_s^{(i)}(x_i) = \frac{1}{2} k_i \left( x_i - \lambda_i^{(s)} \right)^2 : s \in \{A, B\}, \quad (5.7)$$

and each mode is characterized by a reorganization energy (same for  $A \rightarrow B$  and  $B \rightarrow A$  transitions) given by

$$E_{Ri} = \frac{1}{2} k_i \left( \lambda_i^{(A)} - \lambda_i^{(B)} \right)^2. \quad (5.8)$$

The total reorganization energy for the system is

$$E_R = \sum_{i=1}^N E_{Ri}. \quad (5.9)$$

Each mode is in contact with two heat baths ( $a$  and  $b$ ) with temperatures  $T_a \neq T_b$ ,

therefore, due to the thermal gradient, the system is intrinsically nonequilibrium even when electronic equilibrium (i.e., zero net electron transfer between the sites) has been reached. Solving the corresponding Fokker-Planck equation associated with Eq. (5.1)<sup>158,159,165,166</sup> yields that, at steady-state, each mode is characterized by an effective temperature,

$$T_i = \frac{\gamma_a^{(i)}T_a + \gamma_b^{(i)}T_b}{\gamma_a^{(i)} + \gamma_b^{(i)}}. \quad (5.10)$$

and the probability distribution in each mode will take a Gibbs form,

$$P_i \propto \exp [-\beta_i E_s^{(i)}(x_i)] : s \in \{A, B\}, \quad (5.11)$$

where  $\beta_i = 1/k_B T_i$ , with  $k_B$  being Boltzmann's constant, and  $E_s^{(i)}(x_i)$  is the energy of  $i$ th mode (see Eq. (5.7)) in the  $s$ th state. Correspondingly, the total probability distribution for the system of  $N$  modes is:

$$\begin{aligned} P &\propto \prod_{i=1}^N \exp [-\beta_i E_s^{(i)}(x_i)], \\ &\propto \prod_{i=1}^N \exp \left[ -\frac{\gamma_a^{(i)} + \gamma_b^{(i)}}{k_B(\gamma_a^{(i)}T_a + \gamma_b^{(i)}T_b)} E_s^{(i)}(x_i) \right], \end{aligned} \quad (5.12)$$

with  $s \in \{A, B\}$ , which illustrates that the Boltzmann weight of each mode is characterized by the respective effective temperature of that particular mode.

### 5.2.2 Multithermal electron transfer theory

In Refs. 19 and 20 a theory was developed to treat multithermal ET reactions and this formalism can be adapted to treat the present model. The general form of the ET rate in the nonadiabatic limit is<sup>40</sup>

$$k_{A \rightarrow B} = \langle \mathcal{T}_{A \rightarrow B} v_{\perp} \rangle P_{A \rightarrow B}, \quad (5.13)$$

where  $\mathcal{T}_{A \rightarrow B}$  is the tunneling probability from state  $A$  to  $B$ ,  $v_{\perp}$  is the velocity in the direction normal to a transition surface (TS) separating reactant and product regions,  $P_{A \rightarrow B}$  is the probability density about the TS when the system is in state  $A$ , and  $\langle \dots \rangle$  denotes a multithermal average. The TS is defined by mode configurations that satisfy  $g_c(x_1, \dots, x_N) = E_B(x_1, \dots, x_N) - E_A(x_1, \dots, x_N) = 0$ , which arises from the requirement that energy be conserved during an ET event.

The probability about the TS for the  $A \rightarrow B$  transition is,<sup>19–21</sup>

$$\begin{aligned}
P_{A \rightarrow B} &= \int_{\mathbb{R}^N} \prod_{i=1}^N dx_i \exp \left[ \sum_{i=1}^N -\beta_i \frac{k_i}{2} \left( x_i - \lambda_i^{(A)} \right)^2 \right] \\
&\quad \times |\nabla g_c| \delta(g_c(x_1, \dots, x_N)) \\
&\quad / \int_{\mathbb{R}^N} \prod_{i=1}^N dx_i \exp \left[ \sum_{i=1}^N -\beta_i \frac{k_i}{2} \left( x_i - \lambda_i^{(A)} \right)^2 \right],
\end{aligned} \tag{5.14}$$

and for the  $B \rightarrow A$  transition,

$$\begin{aligned}
P_{B \rightarrow A} &= \int_{\mathbb{R}^N} \prod_{i=1}^N dx_i \exp \left[ \sum_{i=1}^N -\beta_i \frac{k_i}{2} \left( x_i - \lambda_i^{(B)} \right)^2 \right] \\
&\quad \times |\nabla g_c| \delta(g_c(x_1, \dots, x_N)) \\
&\quad / \int_{\mathbb{R}^N} \prod_{i=1}^N dx_i \exp \left[ \sum_{i=1}^N -\beta_i \frac{k_i}{2} \left( x_i - \lambda_i^{(B)} \right)^2 \right],
\end{aligned} \tag{5.15}$$

where the factor

$$|\nabla g_c| = \left( \sum_{i=1}^N 2k_i E_{Ri} \right)^{1/2}, \tag{5.16}$$

ensures that the  $\delta$ -function constraint is unique.<sup>19,20,182</sup> Evaluating the integrals yields

$$P_{A \rightarrow B} = \left( \frac{\sum_{i=1}^N k_i E_{Ri}}{2\pi k_B \sum_{i=1}^N T_i E_{Ri}} \right)^{1/2} \exp \left[ \frac{-(\Delta E_{BA} + E_R)^2}{4k_B \sum_{i=1}^N T_i E_{Ri}} \right], \tag{5.17}$$

and

$$P_{B \rightarrow A} = \left( \frac{\sum_{i=1}^N k_i E_{Ri}}{2\pi k_B \sum_{i=1}^N T_i E_{Ri}} \right)^{1/2} \exp \left[ \frac{-(\Delta E_{BA} - E_R)^2}{4k_B \sum_{i=1}^N T_i E_{Ri}} \right], \quad (5.18)$$

where  $\Delta E_{BA} = -\Delta E_{AB} = E_0^{(B)} - E_0^{(A)}$  is the free energy difference between energy origins of the respective states for the  $A \rightarrow B$  transition. The probability densities (and hence the ET reaction rates themselves) take the general forms derived in Refs. 19 and 20, but through their dependence on the modes effective temperatures, also contain friction terms that arise from the Langevin description of the dynamics. Thus, the developed expressions for the multithermal ET transfer rate directly include terms that parameterize strengths of coupling to each bath.

The tunneling probability can be evaluated using the Landau-Zener approximation giving

$$\mathcal{T}_{A \rightarrow B} = \mathcal{T}_{LZ} = 1 - \exp \left[ -\frac{2\pi |V_{A,B}|^2}{\hbar |\Delta F| v_{\perp}} \right], \quad (5.19)$$

where  $\hbar$  is Planck constant,  $|\Delta F| = |\nabla g_c|$  represents the force difference normal to the TS on the potential energy surface configuration, and  $V_{A,B}$  is the energy coupling between diabatic surfaces. In the adiabatic limit,  $\mathcal{T}_{LZ} \rightarrow 1$ , and in the nonadiabatic limit a first-order approximation to (5.19) yields

$$\mathcal{T}_{LZ} = \frac{2\pi |V_{A,B}|^2}{\hbar |\Delta F| v_{\perp}}. \quad (5.20)$$

In the nonadiabatic case, the expectation value  $\langle \mathcal{T}_{A \rightarrow B} v_{\perp} \rangle$  is independent of the nor-

mal velocity and the expression for the ET rate from state  $A$  to state  $B$  is:

$$k_{A \rightarrow B}^{(\text{na})} = \frac{|V_{A,B}|^2}{\hbar |\Delta F|} \left( \frac{2\pi \sum_{i=1}^N k_i E_{Ri}}{k_B \sum_{i=1}^N T_i E_{Ri}} \right)^{1/2} \exp \left[ \frac{-(\Delta E_{BA} + E_R)^2}{4k_B \sum_{i=1}^N T_i E_{Ri}} \right], \quad (5.21)$$

and from state  $B$  to state  $A$ ,

$$k_{B \rightarrow A}^{(\text{na})} = \frac{|V_{A,B}|^2}{\hbar |\Delta F|} \left( \frac{2\pi \sum_{i=1}^N k_i E_{Ri}}{k_B \sum_{i=1}^N T_i E_{Ri}} \right)^{1/2} \exp \left[ \frac{-(\Delta E_{BA} - E_R)^2}{4k_B \sum_{i=1}^N T_i E_{Ri}} \right]. \quad (5.22)$$

The nonadiabatic rate constant is most relevant when the distance between donor and acceptor is large, and thus the energy coupling  $V_{A,B}$  between diabats is small. We expect that this is the typical regime in which multithermal ET may be experimentally realizable because to hold the donor and acceptor environments at appreciable different temperatures requires such length scales. In the adiabatic limit the rate is proportional to the average velocity in the normal direction to the TS:

$$k_{A \rightarrow B}^{(\text{ad})} = \frac{\langle v_{\perp} \rangle}{2} P_{A \rightarrow B} \quad \text{and} \quad k_{B \rightarrow A}^{(\text{ad})} = \frac{\langle v_{\perp} \rangle}{2} P_{B \rightarrow A}, \quad (5.23)$$

where the normal velocity is,<sup>20</sup>

$$\langle v_{\perp} \rangle = \left( 4k_B \sum_{i=1}^N k_i T_i E_{Ri} / \pi |\nabla g_c|^2 m_i \right)^{1/2}, \quad (5.24)$$

and a pre-factor 1/2 is included in (5.23) because, under standard TST assumptions,

on an adiabatic surface only positive velocities contribute to the reactive flux and thus the reaction rate. In the case where  $T_a = T_b$  the multithermal rates  $k^{(\text{na})}$  and  $k^{(\text{ad})}$  reduce to the standard Marcus expressions.<sup>39,40</sup>

### 5.2.3 Derivation of energy partitioning using master equations

A system is coupled linearly to  $N$  thermal baths at different temperatures:  $T_1, T_2, \dots, T_N$ . The relaxation rates into each bath when the system is coupled to each bath separately are  $\gamma_1, \gamma_2, \dots, \gamma_N$ . We ask when the system has fluctuated to energy  $E$  above the ground state, how much (on the average) of this energy came from each thermal bath. Similarly, when it relaxes from  $E$  to steady state, how much energy is released to each bath. Denote the probability to reach energy  $E$  by  $P(E)$ . Suppose that just before reaching  $E$ , the system was in a state with energy  $E - \Delta E$ . When coupled to a single bath  $k$ , the rate to go up in energy is  $\gamma_k n_k(\Delta E)$  and the rate to go down is  $\gamma_k [n_k(\Delta E) + 1]$ , where

$$n_k(\Delta E) = \frac{1}{e^{\Delta E/k_B T_k} - 1} \quad (5.25)$$

The kinetic equation describing the time evolution of the of the occupation probability at energy level  $E$  is

$$\dot{P}(E) = \sum_k^N \gamma_k n_k(\Delta E) P(E - \Delta E) + \sum_k^N \gamma_k [(n_k(\Delta E) + 1) P(E) \quad (5.26)$$

and in the steady-state limit where  $\dot{P}(E) = 0$ ,

$$- \sum_k^N \gamma_k n_k(\Delta E) P(E - \Delta E) = \sum_k^N \gamma_k [n_k(\Delta E) + 1] P(E). \quad (5.27)$$

If we consider a two-level requirement, then

$$P(E) + P(E - \Delta E) = 1 \quad (5.28)$$

and we get

$$\frac{1 - P(E)}{P(E)} = \frac{\sum_k^N \gamma_k n_k e^{\Delta E/k_B T_k}}{\sum_k^N \gamma_k n_k} \quad (5.29)$$

which implies that

$$P(E) = \frac{\sum_k^N \gamma_k n_k}{\sum_k^N \gamma_k n_k (e^{\Delta E/k_B T_k} + 1)} \quad (5.30)$$

From these equations, we deduce that energy contributed by bath  $k$  when the system energy increase ( $\uparrow$ ) or decrease ( $\downarrow$ ) are, respectively,

$$\begin{aligned} \Delta E_{k\uparrow} &= \frac{\gamma_k n_k}{\sum_k^N \gamma_k n_k} \Delta E \\ \Delta E_{k\downarrow} &= - \frac{\gamma_k (n_k + 1)}{\sum_k^N \gamma_k (n_k + 1)} \Delta E \end{aligned} \quad (5.31)$$

In the classical limit, these expressions reduce to

$$\begin{aligned} \Delta E_{k\uparrow} &= \frac{\gamma_k T_k}{\gamma T} \Delta E \\ \Delta E_{k\downarrow} &= - \frac{\gamma_k T_k}{\gamma T} \Delta E. \end{aligned} \quad (5.32)$$



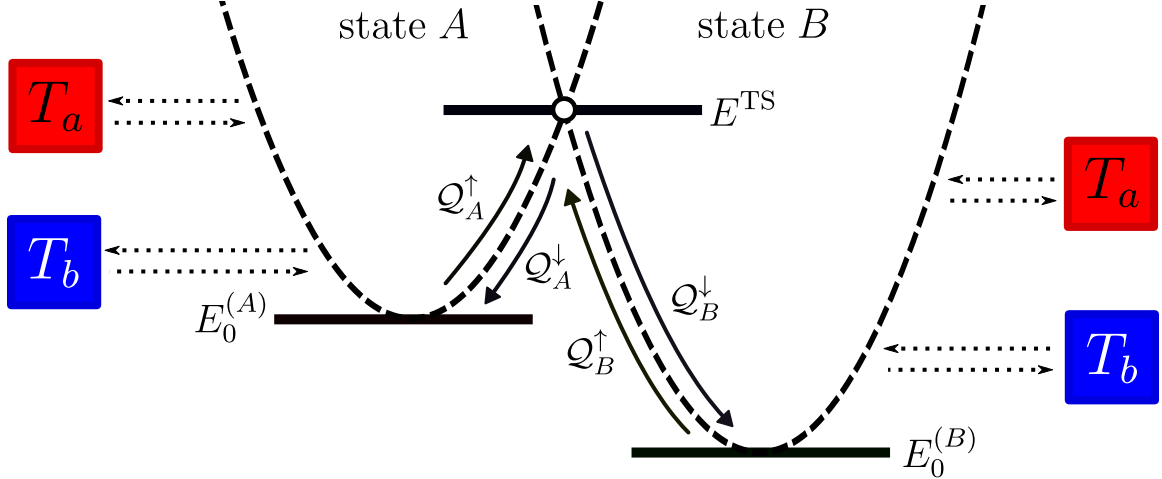


Figure 5.1: Schematic of the energetics of heat exchange and energy partitioning between baths during the ascent to the transition state (shown as a circular marker) and the descent to the energy origin of the respective state. The dashed curves represent the energy surfaces  $E_A$  and  $E_B$ .

#### 5.2.4 Electron-transfer-induced heat transport (ETIHT)

Electron transfer across a thermal gradient can induce a net heat current between molecules,<sup>19–21</sup> and although we have a significant understanding of the physical manifestations underlying thermoelectric effects and phononic heat transport<sup>127,168,183</sup> in materials and molecular junctions,<sup>123,129–131,184</sup> the interplay between electronic and thermal currents is less understood when considering ETIHT effects in the strongly coupled electron-phonon limit of transport. We have previously developed a theory for the heat current induced by electron transfer in thermal heterogeneous environments for a two-mode system in which each mode is in equilibrium with a single thermal reservoir, and the two reservoirs have different temperatures.<sup>19</sup> Here, we generalize that theory to the case of multiple modes whose evolution is governed by stochastic Langevin dynamics and each mode is coupled to multiple thermal baths.

Consider a vibrational mode  $i$  and denote a point on the TS along the corresponding coordinate by  $x_i^{\text{TS}}$ . To reach this point for the  $A \rightarrow B$  transition the mode needs

to obtains energy  $\mathcal{Q}_{Ai}^\uparrow$  from the baths during the ascent to  $x_i^{\text{TS}}$ . It will then release energy  $\mathcal{Q}_{Bi}^\downarrow$  into the baths during the descent on the  $B$  surface after the electronic transition occurs.

Similarly, for the  $B \rightarrow A$  transition the mode obtains energy  $\mathcal{Q}_{Bi}^\uparrow$  from the baths during the ascent to the TS and then releases energy  $\mathcal{Q}_{Ai}^\downarrow$  during the descent after the  $B \rightarrow A$  electronic transition. The contribution of this modes to the energy change of the baths due to the process considered is thus given by:

$$\begin{aligned}\mathcal{Q}_i^{A \rightarrow B} &\equiv -\mathcal{Q}_{Ai}^\uparrow + \mathcal{Q}_{Bi}^\downarrow \\ &= -\frac{1}{2}k_i \left(x_i^{\text{TS}} - \lambda_i^{(A)}\right)^2 + \frac{1}{2}k_i \left(x_i^{\text{TS}} - \lambda_i^{(B)}\right)^2,\end{aligned}\quad (5.33)$$

$$\begin{aligned}\mathcal{Q}_i^{B \rightarrow A} &\equiv -\mathcal{Q}_{Bi}^\uparrow + \mathcal{Q}_{Ai}^\downarrow \\ &= -\frac{1}{2}k_i \left(x_i^{\text{TS}} - \lambda_i^{(B)}\right)^2 + \frac{1}{2}k_i \left(x_i^{\text{TS}} - \lambda_i^{(A)}\right)^2.\end{aligned}\quad (5.34)$$

where we have used the convention that energy released by the bath has a negative sign and energy obtained by the bath has a positive sign. A schematic of these energetics is shown in Fig. 5.1.

Electron transfer can occur at any configuration  $\mathbf{X}$  on the TS, therefore Eqs. (5.33) and (5.34) must be averaged of these configurations . It is an important characteristic of the multi-thermal situation considered the the probability densities to be on the TS when coming from the  $A$  or  $B$  sides are not equal. They are given

by<sup>19</sup>

$$P_{A \rightarrow B}^\dagger(\mathbf{X}) = \delta(g_c) \exp \left[ \sum_{i=1}^N -\beta_i \frac{k_i}{2} (x_i - \lambda_i^{(A)})^2 \right] \\ \left/ \int_{\mathbb{R}^N} \prod_i dx_i \delta(g_c) \exp \left[ \sum_{i=1}^N -\beta_i \frac{k_i}{2} (x_i - \lambda_i^{(A)})^2 \right] \right., \quad (5.35)$$

$$P_{B \rightarrow A}^\dagger(\mathbf{X}) = \delta(g_c) \exp \left[ \sum_{i=1}^N -\beta_i \frac{k_i}{2} (x_i - \lambda_i^{(B)})^2 \right] \\ \left/ \int_{\mathbb{R}^N} \prod_i dx_i \delta(g_c) \exp \left[ \sum_{i=1}^N -\beta_i \frac{k_i}{2} (x_i - \lambda_i^{(B)})^2 \right] \right.. \quad (5.36)$$

Averaging over all configurations on the TS using the corresponding probability densities, we find that the expectation value of the total heat transferred by mode  $i$  during the respective transitions are

$$\langle \mathcal{Q}_i^{A \rightarrow B} \rangle = \int_{\mathbb{R}^N} \mathcal{Q}_i^{A \rightarrow B} P_{A \rightarrow B}^\dagger(x_1, \dots, x_N) dx_1 \cdots dx_N \\ E_{Ri} \left[ \Delta E_{AB} T_i + \sum_{k \neq i}^N E_{Rk} (T_k - T_i) \right] \\ = \frac{\quad}{\sum_k^N T_k E_{Rk}}, \quad (5.37)$$

and

$$\langle \mathcal{Q}_i^{B \rightarrow A} \rangle = \int_{\mathbb{R}^N} \mathcal{Q}_i^{B \rightarrow A} P_{B \rightarrow A}^\dagger(x_1, \dots, x_N) dx_1 \cdots dx_N \\ E_{Ri} \left[ \Delta E_{AB} T_i - \sum_{k \neq i}^N E_{Rk} (T_k - T_i) \right] \\ = - \frac{\quad}{\sum_k^N T_k E_{Rk}}. \quad (5.38)$$

Equations (5.37) and (5.38) are expressions for the net heat exchange associated with mode  $i$  in the corresponding ET processes. In Ref. 19 knowledge of these quantities was sufficient for calculating the heat transfer between baths because each mode

was coupled specifically to a single bath. Here however the mode can be coupled to both baths, and to translate the net heat exchange by such modes requires knowledge of the energy partitioning between baths. Specifically, we require an answer to the following question: If the net heat exchange with the baths (-accumulated during ascent plus released during descent) is  $\mathcal{Q}$ , how is  $\mathcal{Q}$  partitioned between the two baths?

From the kinetic master equations (detailed above) of a two-level system with energy level spacing  $\Delta E$  that is coupled to two baths we find that the fraction of energy  $\Delta E_K$  that is obtained/released by the  $K$ th bath during a state transition is,<sup>185,186</sup>

$$\Delta E_K = \frac{\gamma_K \langle n_K \rangle}{\gamma_a \langle n_a \rangle + \gamma_b \langle n_b \rangle} \Delta E : K \in \{a, b\} \quad (5.39)$$

where

$$\langle n_K(\Delta E) \rangle = \frac{1}{e^{\beta_K \Delta E} - 1} \quad (5.40)$$

is the quantum population in equilibrium with the respective thermal bath. In the classical limit  $\langle n_K \rangle \sim T_K$ , and, thus, in the limit where the Langevin dynamics of Eq. (5.1) adequately describe the system's evolution:

$$\Delta E_K = \frac{\gamma_K T_K}{\gamma_a T_a + \gamma_b T_b} \Delta E : K \in \{a, b\}, \quad (5.41)$$

which states that bath  $K$  provides/absorbs  $\gamma_K T_K / (\gamma_a T_a + \gamma_b T_b)$  of the total energy change during each transition.

Using this partitioning during both activation and relaxation events, we arrive at general expressions for the heat current generated into each bath at steady state

solely from the transfer of electrons across a thermal gradient:

$$\begin{aligned}
J_{\mathcal{Q}}^{(a)} &= J_{\text{el}} \sum_i^N \frac{\gamma_a^{(i)} T_a}{\gamma_a^{(i)} T_a + \gamma_b^{(i)} T_b} \left( \langle \mathcal{Q}_i^{A \rightarrow B} \rangle + \langle \mathcal{Q}_i^{B \rightarrow A} \rangle \right), \\
&= 2J_{\text{el}} \sum_i^N \frac{\gamma_a^{(i)} T_a}{\gamma_a^{(i)} T_a + \gamma_b^{(i)} T_b} \left[ \frac{E_{\text{R}i} \sum_{k \neq i}^N E_{\text{R}k} (T_k - T_i)}{\sum_k^N T_k E_{\text{R}k}} \right], \tag{5.42}
\end{aligned}$$

$$\begin{aligned}
J_{\mathcal{Q}}^{(b)} &= J_{\text{el}} \sum_i^N \frac{\gamma_b^{(i)} T_b}{\gamma_a^{(i)} T_a + \gamma_b^{(i)} T_b} \left( \langle \mathcal{Q}_i^{A \rightarrow B} \rangle + \langle \mathcal{Q}_i^{B \rightarrow A} \rangle \right) \\
&= 2J_{\text{el}} \sum_i^N \frac{\gamma_b^{(i)} T_b}{\gamma_a^{(i)} T_a + \gamma_b^{(i)} T_b} \left[ \frac{E_{\text{R}i} \sum_{k \neq i}^N E_{\text{R}k} (T_k - T_i)}{\sum_k^N T_k E_{\text{R}k}} \right], \tag{5.43}
\end{aligned}$$

where  $J_{\text{el}}$  is the unidirectional electronic current at steady state. In this state, the electronic system has reached quasi-equilibrium where the electronic state populations  $p_K^{(\text{ss})} : K \in \{A, B\}$  do not change, so that

$$J_{A \rightarrow B}^{(\text{ss})} = J_{B \rightarrow A}^{(\text{ss})} \equiv J_{\text{el}} = p_A^{(\text{ss})} k_{A \rightarrow B}. \tag{5.44}$$

where  $p_A^{(\text{ss})}$  is the steady state probability that the system is in electronic state  $A$ . It is easily confirmed that these currents satisfy the energy conservation condition  $J_{\mathcal{Q}}^{(a)} = -J_{\mathcal{Q}}^{(b)}$ .

Some insight on these results can be obtained by considering special cases. Consider first a system with a single vibrational mode that is coupled to sites  $a$  and  $b$ . The total heat energies transferred between the baths during the and  $A \rightarrow B$  and

$B \rightarrow A$  transitions are

$$\langle Q_i^{A \rightarrow B} \rangle = \Delta E_{AB} \quad (5.45)$$

$$\langle Q_i^{B \rightarrow A} \rangle = -\Delta E_{AB} \quad (5.46)$$

where  $E_{AB}$  is the free energy difference between the two electronic states. These energies cancel each other when summed to yield the total heat associated with a “round trip” between the states, therefore there is no ET-induced heat current for a single mode coupled to two thermal sources. One way to understand the reason for this is to note that the single mode is associated with a single effective temperature so the electron transfer process is not subjected to a temperature difference between the thermal baths. Obviously, such a single mode, being coupled to two baths of different temperatures, will contribute to the standard (phononic) heat transport (see Sec. 5.2.5).

Next consider a two modes system. Eqs. (5.42) and (5.43) now yield

$$J_Q = J_Q^{(a)} = -J_Q^{(b)} = 2J'_{\text{el}} \frac{E_{R1} E_{R2} (T_2 - T_1)}{T_1 E_{R1} + T_2 E_{R2}}, \quad (5.47)$$

where

$$J'_{\text{el}} = J_{\text{el}} \frac{T_a T_b \left( \gamma_a^{(1)} \gamma_b^{(2)} - \gamma_a^{(2)} \gamma_b^{(1)} \right)}{\left( \gamma_a^{(1)} T_a + \gamma_b^{(1)} T_b \right) \left( \gamma_a^{(2)} T_a + \gamma_b^{(2)} T_b \right)}. \quad (5.48)$$

which has the same form as derived in Ref. 19, except that now the temperatures  $T_1$  and  $T_2$  and the flux  $J'_{\text{el}}$  are effective quantities that depend on the different system-bath coupling strengths.

It is interesting to realize that at least two vibrational modes, characterized by different effective temperatures and sensitive to the electronic site occupations, are needed for ETIHT. Also notable is the nonlinear dependence of this effect on the

temperature difference between baths and the system-bath couplings. Aside from the system-bath coupling terms which appear explicitly in Eqs. (5.42) and (5.43), the steady state unidirectional electron current  $J_{el}$  is also determined by the ET rates, which themselves are affected by these couplings. We study these dependences in Section 5.3.

### 5.2.5 Vibrational heat transfer

For a single harmonic mode  $i$  coupled to two thermal baths  $a$  and  $b$  according to the Langevin equations (5.1)-(5.4), the vibrational heat current is<sup>158</sup>

$$J_{Q_i}^{(a)} = -J_{Q_i}^{(b)} = k_B \frac{\gamma_a^{(i)} \gamma_b^{(i)}}{\gamma_a^{(i)} + \gamma_b^{(i)}} (T_b - T_a). \quad (5.49)$$

which is a classical high temperature ( $k_B T \gg \hbar \omega_i$ ) limit of a more general quantum results<sup>162</sup>

$$J_{Q_i}^{(a)} = -J_{Q_i}^{(b)} = \hbar \omega \frac{\gamma_a^{(i)} \gamma_b^{(i)}}{\gamma_a^{(i)} + \gamma_b^{(i)}} (n_b - n_a), \quad (5.50)$$

valid for  $k_B T \gg \hbar \gamma_i$  with

$$n_K \equiv \langle n_K \rangle = \frac{e^{-\beta_K \hbar \omega}}{(1 - e^{-\beta_K \hbar \omega})}, \quad (5.51)$$

where  $K \in \{a, b\}$  and  $\langle \dots \rangle$  is a thermal average. Limiting ourselves to the classical limit, the total vibrational heat current is given by the sum over modes:

$$J_Q^{(a)} = -J_Q^{(b)} = k_B (T_b - T_a) \sum_{i=1}^N \frac{\gamma_a^{(i)} \gamma_b^{(i)}}{\gamma_a^{(i)} + \gamma_b^{(i)}}. \quad (5.52)$$

The contribution of each modes depend on the temperature difference between baths, weighed by the mode-bath coupling strength.

Next, we use these results to estimate the relative importance of the vibrational and ET-induced heat conductivities in molecular systems.

### 5.3 Results and Discussion

To gain insights into the interplay between ETIHT and purely vibrational contributions to heat transport we consider a model of two vibrational modes with the following attributes: mode 1 is assumed to be preferably localized near site  $a$ , so its coupling to the thermal environment near this site is stronger than its coupling to the environment of site  $b$ . Conversely, mode 2 is more localized about site  $b$ , and therefore more strongly coupled to that site. This also implies that mode 1 may be more sensitive to the electronic occupation of site  $a$  while mode 2 is more affected by the electronic occupation on site  $b$ , but this difference does not affect as such the way these modes are expressed in the electron transfer rate between these sites because their effect enters through the symmetric coupling  $(\lambda^{(A)} - \lambda^{(B)})^2$ .

In the model considered, where the coupling between the electronic and vibrational subsystems maintains the character of the vibrational modes in the two electronic states, the two heat transfer channels: vibrational and ETIHT, operate essentially additively. The electron transfer process depends of course on the effective vibrational temperatures, however the vibrational heat transport is not affected by the electron transfer and is independent of molecular parameters, such as the reorganization energies and the free energy difference between the electronic states, that affect the electron transfer. The relative importance of these channels as determined by their contributions to the heat transfer is therefore derived from their essentially independent efficiencies.

Figure 5.2 illustrates how the heat current from the ETIHT and phononic conduction channels vary with changing reaction free energy  $\Delta E_{BA}$  and the coupling of the



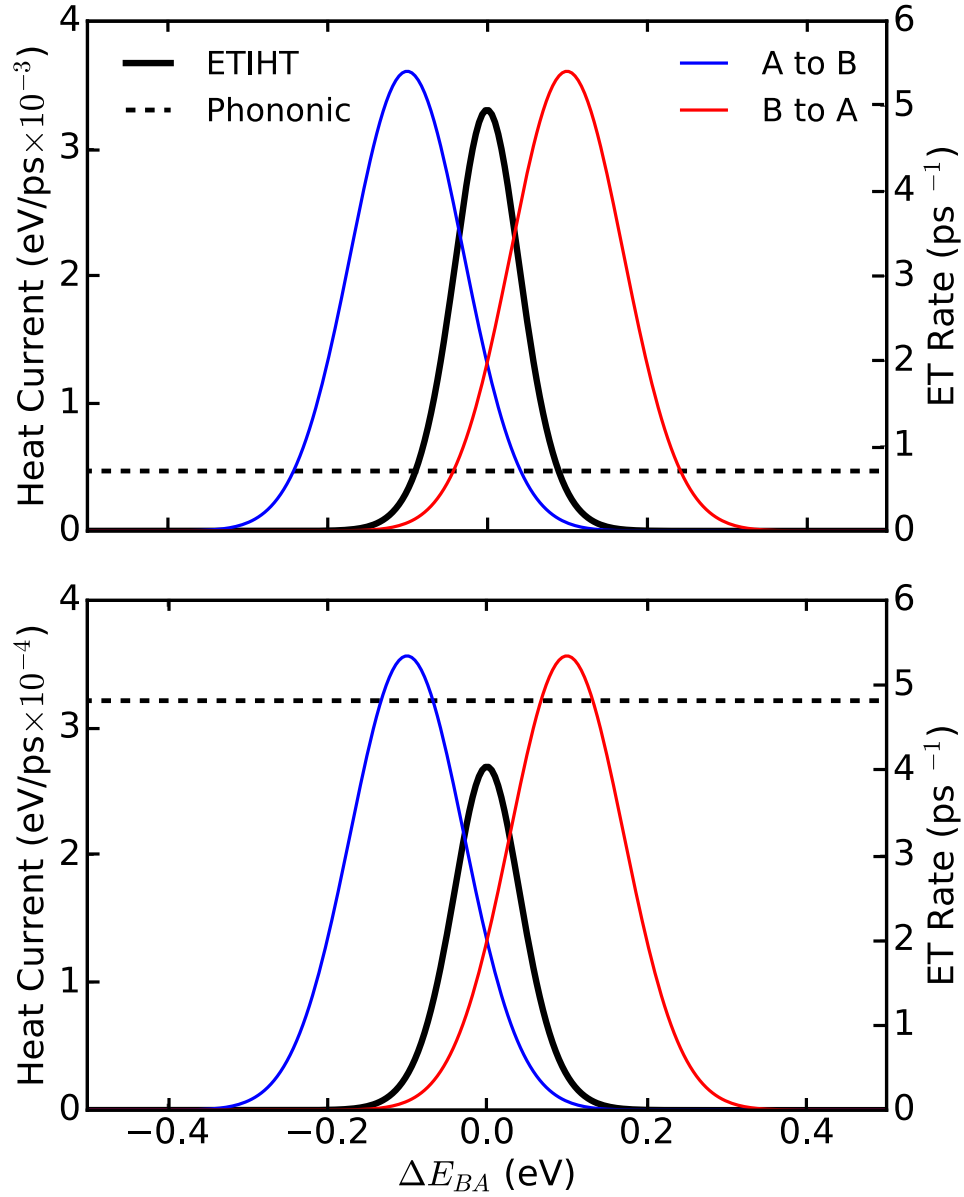


Figure 5.2: Electron-transfer-induced (solid; black) and phononic (dashed; black) heat currents  $\mathcal{J}_Q$  (current direction from left to right) and electron transfer rates  $k_{A \rightarrow B}$  (solid; blue) and  $k_{B \rightarrow A}$  (solid; red) as functions of the free energy difference  $\Delta E_{BA}$ . Units and scale of the heat currents and electron transfer rates are shown on the left and right axes, respectively. The system-bath couplings are  $\gamma_a^{(1)} = 1.0 \text{ ps}^{-1}$ ,  $\gamma_b^{(1)} = 0.1 \text{ ps}^{-1}$ ,  $\gamma_a^{(2)} = 0.1 \text{ ps}^{-1}$  in both panels, and in (a)  $\gamma_b^{(2)} = 1.0 \text{ ps}^{-1}$  and (b)  $\gamma_b^{(2)} = 0.05 \text{ ps}^{-1}$ . Other parameters are:  $V_{A,B} = 0.01 \text{ eV}$ ,  $E_{R1} = 0.06 \text{ eV}$ ,  $E_{R2} = 0.04 \text{ eV}$ ,  $T_a = 300 \text{ K}$ , and  $T_b = 270 \text{ K}$ .

vibrational modes to the thermal environments of the donor and acceptor. Figure 5.3 shows the dependence of these heat transport channels on the temperature difference between the donor and acceptor sites. The following observations can be made:

(a) In the parameters ranges examined here, the vibrational heat conduction is  $\sim 5 \times 10^{-4}$  eV/ps, which is within the range of the heat current magnitude measured by state-of-the-art experimental technique in molecular junctions.<sup>46,51</sup> This also indicates that an electron-transfer-induced heat current could be detected experimentally. A specific case where ETIHT could be the dominant conduction mechanism is in molecular junctions in which the phononic heat current is effectively suppressed due to the electronic characteristics of the molecular structure.<sup>115</sup>

(b) As explained above, and seen in Fig 5.2, the phononic heat current does not depend on  $\Delta E_{BA}$ . In contrast, the dependence of the ETIHT on this parameter is dramatic—it peaks at  $\Delta E_{BA} = 0$  and dies down quickly as  $|\Delta E_{BA}|$  is increased. This behavior reflects the fact that ETIHT depends on the rates of electron transfer in both directions and is therefore maximum when both rates,  $D \rightarrow A$  and  $A \rightarrow D$ , are appreciable rather than when one rate dominates the other.

(c) The couplings between the oscillator modes and the thermal environments of the electronic centers influences the heat transport between these centers as seen in Fig. 5.2. Its effect on the phononic part of the heat current is obvious, and an important effect on the electron transfer rate results from the fact that the latter depends on the effective modes temperatures that depend on these couplings. Another important effect of these couplings on the relative magnitudes of the ETIHT and the purely vibrational contributions stems from their symmetry properties. In panel (b) of Fig. 5.2, the coupling of the mode 2 to the bath  $b$  is decreased by a factor of two with respect to panel (a) and the ETIHT current goes down by nearly an order of magnitude. The origin of this behavior lies in the symmetry properties of the coupling

parameters. Fig. 5.2(a) refers to the case where one mode is strongly coupled to site  $a$  while the other mode is strongly coupled to site  $b$ , as compared to the Fig. 5.2(b) where both modes are coupled more strongly to site  $a$ . It is the former scenario that gives the strongest ETIHT effect. In the limit in which one mode is coupled only to site  $a$  while the other sees only site  $b$ , i.e.,  $\gamma_b^{(1)} = \gamma_a^{(2)} = 0$ , there is no direct vibrational coupling between the thermal environments of sites  $a$  and  $b$  and the total contribution to the heat transport comes solely from the ETIHT channel. In another special limit where the ratios of the couplings satisfy the equalities

$$\frac{\gamma_a^{(1)}}{\gamma_a^{(2)}} = \frac{\gamma_b^{(1)}}{\gamma_b^{(2)}} \quad \text{or} \quad \frac{\gamma_a^{(1)}}{\gamma_b^{(1)}} = \frac{\gamma_a^{(2)}}{\gamma_b^{(2)}}, \quad (5.53)$$

the ETIHT contribution to the heat current is zero while the phononic counterpart is nonzero and proportional to the temperature difference between sites.

(d) Variation of  $\Delta T = T_a - T_b$  seen in Fig. 5.3 for various constant  $\Delta E_{BA}$  values is expressed differently in the different heat transport channels. While the phononic heat current increases linearly with  $\Delta T$ , increasing the temperature difference between baths does not linearly add to the magnitude of the ETIHT current. Figure 5.3 illustrates these behaviors for different sets of system-bath couplings.

A corollary of this observation is that while the phononic heat current depends linearly on  $\Delta T$ , the non-linear response of the ETIHT current may lead to situations (usually at small  $\Delta T$ ) which it exceeds its phononic counterpart. For instance, in the  $\Delta E_{BA} = 0.1$  eV case in Fig. 5.3(a), the ETIHT current is less than the phononic current for small temperature biases, while for  $\Delta T > 150$  K the ETIHT current is greater than that generated in the phononic channel. These results imply that by tuning the coupling strength between donor and acceptor molecules and their local environments, the comparative magnitude of ETIHT current can be increased over

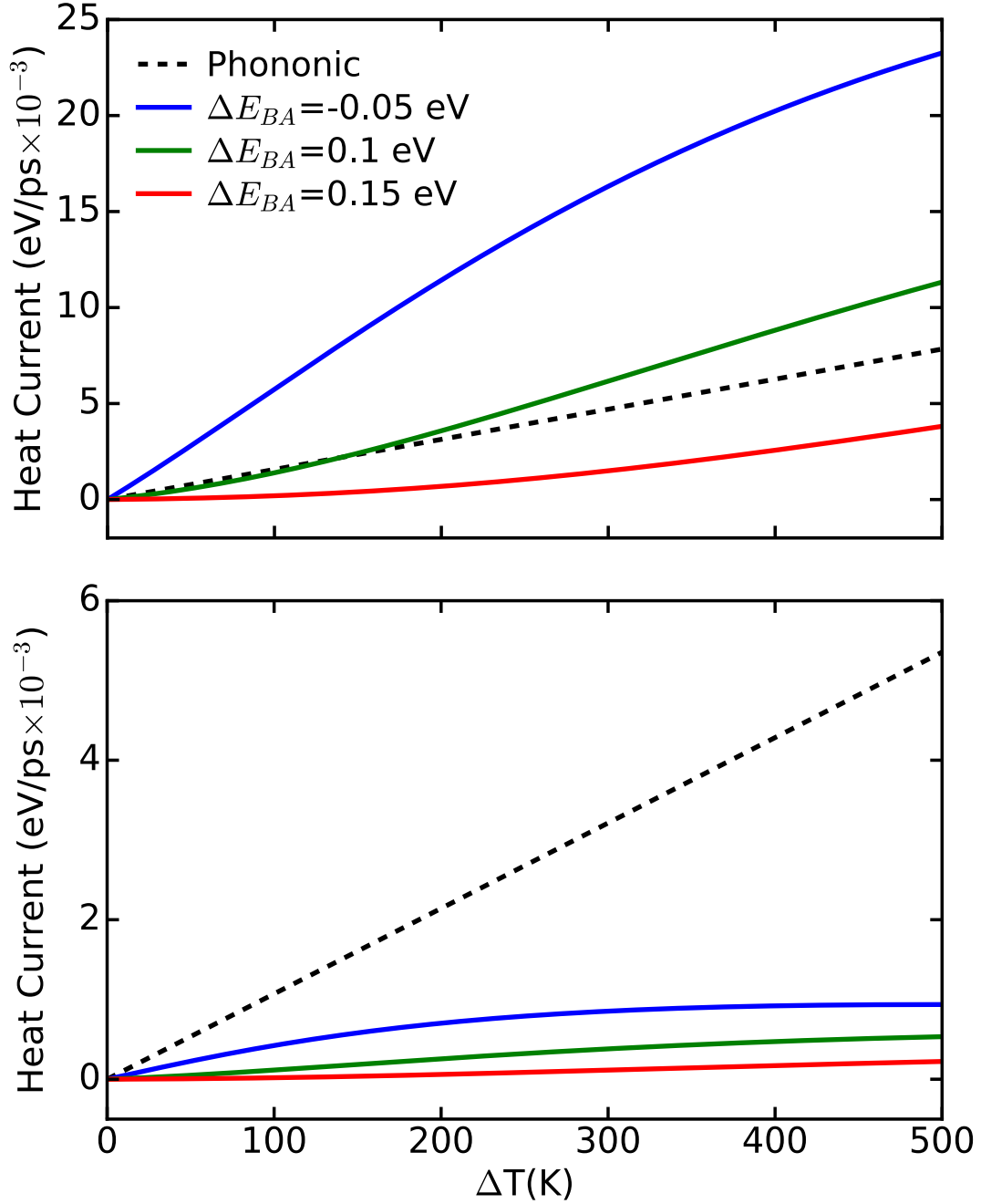


Figure 5.3: Electron-transfer-induced and phononic heat currents  $\mathcal{J}_Q$  (current direction from left to right) as a function of temperature difference  $\Delta T = T_a - T_b$  for various values of the reaction free energy  $\Delta E_{BA}$  shown in the legend of (a). The system-bath couplings are:  $\gamma_a^{(1)} = 1.0 \text{ ps}^{-1}$ ,  $\gamma_b^{(1)} = 0.1 \text{ ps}^{-1}$ ,  $\gamma_a^{(2)} = 0.1 \text{ ps}^{-1}$  in both panels, and in (a)  $\gamma_b^{(2)} = 1.0 \text{ ps}^{-1}$  and (b)  $\gamma_b^{(2)} = 0.05 \text{ ps}^{-1}$ . Other parameters are:  $V_{A,B} = 0.01 \text{ eV}$ ,  $E_{R1} = 0.06 \text{ eV}$ ,  $E_{R2} = 0.04 \text{ eV}$ , and  $T_b = 270 \text{ K}$ , which is fixed.

that of phononic heat current in some multithermal ET reactions.

## 5.4 Conclusions

In this chapter we have developed a theory to describe electron transfer and phononic heat conduction, and their coupling that gives rise to electron transfer induced heat transport (ETIHT), using a multithermal Marcus formalism merged with stochastic Langevin dynamics. Application of this theory allows a comparison between the magnitude of heat conduction from phononic and electron-transfer-induced channels over a diverse set of reaction geometries and thermal environments. An efficient ETIHT channel requires fast bidirectional electron exchange between the molecular sites, which usually translates into the requirement that the free energy change associated with the electron transfer reaction is small, such as in the case of exchange between identical sites. In such cases, situations could be found where this channel dominates the heat transport process, however one should be cautious about his conclusion because we have made our comparison for modes that are strongly coupled to both thermal environments and at the same time are also coupled to the electron transfer process. Other heat carrying modes may be uncoupled to the electronic process. Obviously there are also modes that couple to the electronic process but do not carry heat (in the harmonic limit) because they are localized near their respective environments. We note in passing that the harmonic part of the nuclear potential energy surface indeed dominates heat transport across distance scales that are relevant for the present study.<sup>161</sup>

A system in which ETIHT could be the dominant thermal conduction mechanism is  $\pi$ -stacked molecular junctions where the phononic transport channel is suppressed by tuning specific bonding characteristics of the molecular structure.<sup>115</sup> In the limit that electron charge density is strongly coupled with a thermal environment, the

results presented here will guide experimental investigation of ETIHT.

Apart from the harmonic approximation, our treatment relies on two assumptions. First is the assumed independence of the ETIHT and the phononic contributions to heat transfer. This assumption is valid in the limit in which the vibrational transport mechanism does not affect the energetic distributions relevant to electron transport. This holds at steady state for the standard model of electron transfer (parallel shifted potential energy surfaces) except that the temperature associated with the relevant nuclear motions has to be set as the effective temperature derived for each modes from its coupling to the non-equilibrium environment. Second is an assumption concerning the partitioning of energy extracted from and released into the non-equilibrium thermal baths during the activated electron transfer process. This assumption, expressed by Eq.(5.41) is derived from a master equation approach. We are currently developing a theory of the energy partitioning from a trajectory-based picture of the dynamics, and our preliminary results agree with the energy partitioning principle derived from the kinetic master equations.<sup>185,186</sup>

Finally we note that the semiclassical formalism that has been implemented here is applicable for low frequency intermolecular vibrations in the strong electron-phonon coupling limit in which electron hopping is the dominate transport mechanism. At low temperatures and for high molecular vibrations nuclear tunneling plays a role in the system's dynamical evolution, and a description of ETIHT will require a quantum description of the nuclear dynamics. Carrying the theory to such situation is a focus of our current work.

## CHAPTER 6

### Conclusion and outlook

We have so far conducted a series of studies on the topic of heat transport processes in molecular systems and elaborated them as the main body of this dissertation. Here we want to summarize what we have achieved and also provide perspectives for future research directions.

Chapter 2 introduces a numerical strategy and its implementation of investigating heat conduction processes in molecular junctions of different topologies. There we demonstrate heat fluxes can be simulated through explicitly extended substrate layers of the molecular junctions and show the quantities (*e.g.* thermal conductance) calculated at steady-state are in agreement with the most recent experimental data<sup>16</sup> on alkane chain molecules. Both classical MD simulations and quantum Landauer-type calculations are embedded in the process, making the method feasible for anharmonic systems and larger environmental temperature range. To further extend the project, one of the future directions can be considering the inter-molecular interactions, (*e.g.* similar structures shown in Figure A.4, but without taking into account chain-chain interactions) which makes the method capable of simulating large cluster of systems or bulks. The heat conduction in these systems will be much more complicated than single-molecule junctions. The increased ability of numerical tools will help disentangle interplays of different contributions to the overall heat conduction process.

In chapter 3 we have described an intriguing thermal transport phenomenon in ring-based aromatic molecular systems, that is interference effect in heat conduction. This effect is demonstrated, explored and explained using the tools we have developed in the previous chapter. Surprisingly, the normally termed “quantum interference”

is seen not only with Landauer’s quantum description, but also clearly shown within classical mechanics regime for the phononic heat transport. In addition, local atomic heat flows are visualized with the help of the energy partition scheme introduced earlier. Interesting patterns of both increasing and decreasing currents are illustrated throughout the benzenedithiol configurations (para-, meta-, and ortho-) upon applying of temperature biases. Many promising projects might follow along this direction of research. More complex structures (*e.g.* more rings as shown in Figure B.5) could be one probable direction, as to investigate how potential constructive/destructive phononic interference might interact with each other in more complex molecules. Furthermore, to find out if there is a possibility of design principles (with compounds of chemicals) that facilitates tunable nanoscale thermal device by making use of such basic interference effect.

In chapter 4, we have shown the quantum bath effects can be integrated into MD simulations effectively in the thermal transport simulations in the molecules, without sacrificing all the benefits (*e.g.* anharmonic effects) inherited from classical simulations. We have also elaborated on the detailed formalism of incorporating such effects through an effective temperature reconstruction. and shown the method being implemented in toy models.

Previously, the GROMACS-based computational toolkit that utilizes stochastic baths and substrate filterings has been developed to simulate heat conduction across molecular junctions of any topologies and has been shown to be relatively accurate and powerful for room temperature settings.<sup>4</sup> However, we see the accuracy drifts away from its quantum benchmarks when the temperatures are pushed to a much lower end(*e.g.* 25K). One of the main reasons for such a failure is the inability of classical mechanics in capturing the dominant quantum effect at low temperatures which arises from quantum Bose-Einstein distribution. With the new method of quantum



augmented bath dynamics, we could overcome the inherent shortcomings of the previous classical MD simulations, particularly at the limits of low-T and high-frequencies. The future work will be completing the integration of this augmented quantum bath approach into the existing nonequilibrium stochastic MD in the GROMACS source code, and provide a full dynamics of quantum mechanical heat transport at the capacities of classical MD simulations in the molecular systems.

In chapter 5, we have switched our gears, discussing our research on another important thermal transport topic in the molecular systems (e.g. electron donor-acceptor systems), the electron-transfer-induced-heat-transport (ETIHT). The ETIHT does not involve the interplay between vibrational modes in the molecular systems. In this sense, the newly discovered heat transport channel is more of electronic (with respect to phononic) in nature. By connecting the left and right sides thermal baths with vibrational modes, we effectively bring in the phononic contribution at the same setting of the ETIHT. Our work unveils the electronic contribution is comparable to that of the standard phononic transport for donor-acceptor pairs with efficient bidirectional electron transfer rates, while in most other situations, phononic transport is the dominant heat transfer mechanism. Our research mainly focus on classical Marcus ET theory. A more generalized theory of ETIHT in which the nuclei are quantum mechanical is desirable, for the applicability and generalisability of the theory to different molecular systems and environments. This work has been done by Dr. Cui in our group recently, and the quantum effects are shown to be appreciable at certain temperature range<sup>187</sup>.

## APPENDIX A

### Appendix of chapter 2

#### A.1 Setting the substrate

The substrate is constructed in a pyramid-like shape consists of increased numbers of gold atoms from the inner layer bridging the molecules to the outer layers connecting the white baths (e.g. 1, 3, 6, *etc.*). Adding coupling of the outer layer to a white bath and undergoing Langevin dynamics, the equation of motion becomes,

$$\ddot{x}_i = -\frac{\partial E(x_i)}{\partial x_i} - \gamma_K \dot{x}_i + R_K^{(i)}(t), \quad (\text{A.1})$$

where  $E(x_i)$  is a mass-weighted energy as a function of the coordinate of the  $i$ th particle  $x_i$ ,  $\gamma_K$  is the friction coupling to the bath  $K$  (in our case  $K \in \{L, R\}$  for the left and right bath), and  $R_K^{(i)}(t)$  is the stochastic noise terms of the respective bath, assumed independent for different connected atoms. The stochastic terms obey the usual fluctuation-dissipation relations

$$\langle R_K^{(i)}(t) R_K^{(j)}(t') \rangle = 2\gamma_K k_B T_K m_i^{-1} \delta(t - t') \delta_{ij}, \quad (\text{A.2})$$

$$\langle R_L^{(i)}(t) R_R^{(i)}(t') \rangle = 0, \quad (\text{A.3})$$

$$\langle R_K^{(i)}(t) \rangle = 0, \quad (\text{A.4})$$

where  $i$  and  $j$  are the atoms in the outermost layers in the substrates coupled independently to their respective baths.

To enforce the junction geometry, the explicit bulk is position-restrained by a

harmonic force acting on the layer of atoms furthest from the molecule. The spring constants of such restraints are in general set to be less than a few thousand  $kJ \cdot mol^{-1} \cdot nm^{-2}$  ( $\ll 1\%$  of the bond stretching forces of the simulated molecules)

Figure A.1 displays, for a hexanedithiol molecule bridging between gold surfaces, a numerical experiment is carried out with respect to the number of explicit atomic layers used to represent the left and right gold substrates. The calculated thermal conductance appears to plateau when three layers of explicit gold are used to represent these substrates and simulations reported below were using such substrate models. In agreement with this observation, a study by Zhang *et. al.* on self-assembled monolayers showed that the effect of the baths on the molecular system is mainly due to the first few layers of gold substrate<sup>188</sup>. Figure A.2 compare the Fourier transforms of the velocity correlation function (essentially the density of states) of the gold atom at the edge of the gold cluster, that in the junction is adjacent to the molecular thiol group. While plateau is not yet quantitative, spectral densities associated with the 3 and 4-layers clusters are similar both to each other and to the experimental vibrational DOS for gold nanoparticles<sup>189</sup>. Note that the spectral densities in Figure A.2 are calculated for the position-restrained clusters, which is therefore expressed in the calculated spectral densities of the smaller clusters at about  $40 \text{ cm}^{-1}$  but appears to shift to lower frequencies for the bigger clusters. In the calculations presented in the main text, the gold substrates were represented by pyramids of 3 gold layers. This cost saving choice would not yield quantitatively accurate results for the actual hydrocarbon-gold junctions, but it suffices for our main goals of demonstrating the essentially classical nature of the heat transport dynamics at room temperature, showing the importance of quantum effects at low temperatures and studying the connection between mode localization properties and molecular heat conduction. Somewhat surprisingly it has turned out that this modeling level also perform well by quantitative measure.

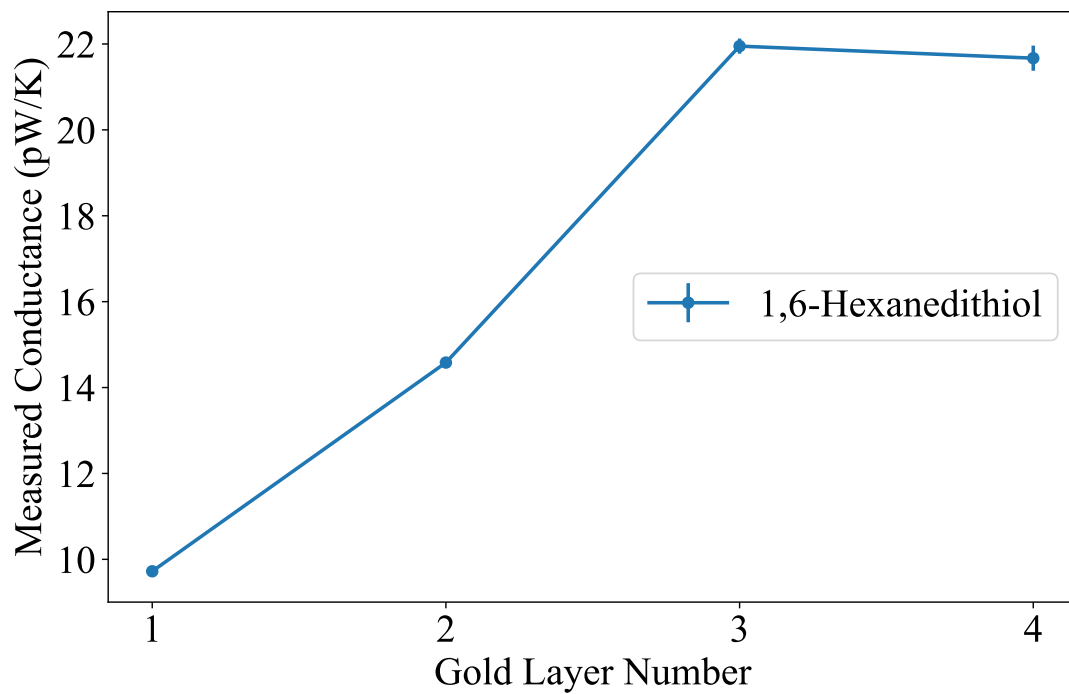


Figure A.1: Heat conductance for the molecule  $\text{HS}(\text{CH}_2)_6\text{SH}$  connecting surfaces represented by a given numbers  $n$  of gold layers interacting at their far ends with white thermal baths characterized by temperatures  $T_L = 300\text{K}$  and  $T_R = 350\text{K}$ . The bars shown in the Figure are the standard errors  $(\text{SE})^2$  of the calculated conductance.

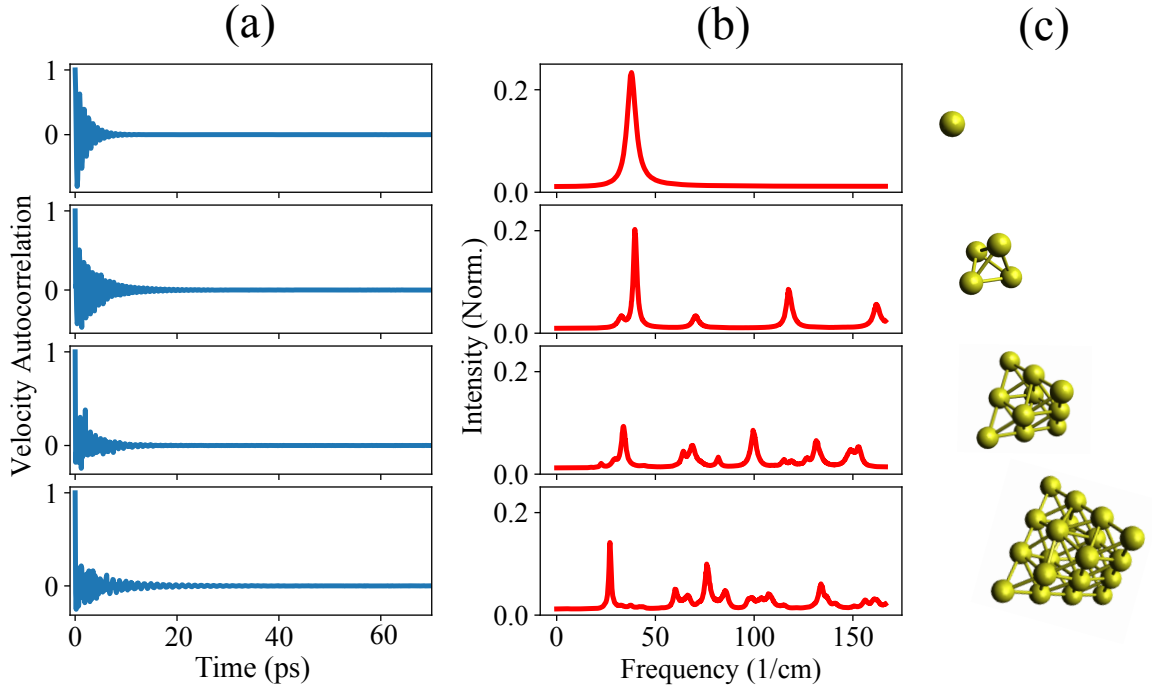


Figure A.2: Velocity-velocity autocorrelation functions of the only atom in the first layer of each of four different gold clusters. The outermost layers are attached to Markovian thermal reservoirs at temperature of 300K and the clusters are allowed sufficient time (e.g. a few nanoseconds) to relax to the temperature of the bath. Column (a): Velocity time-autocorrelations,  $C_{vv}(t)$ , which are normalized to the value at  $t = t_1 - t_2 = 0$ ; Column (b): The Fourier transforms of the corresponding correlations, normalized across the whole spectra; Column (c): Artistic representation of the corresponding gold clusters.

## A.2 Additional details on molecular configuration preparation and MD simulation procedures

There are mainly three phases in using our customized GROMACS<sup>82,117</sup> package to conduct simulations on heat conduction in molecular junctions, including both classical MD and quantum Landauer transport (as illustrated in figure A.3):

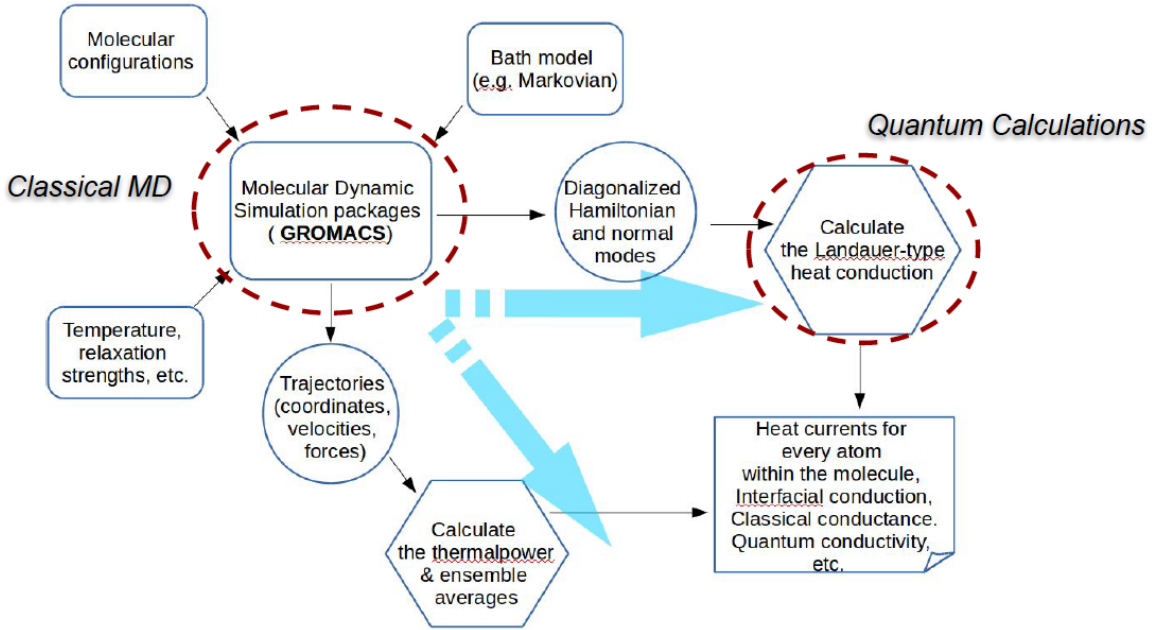


Figure A.3: Molecular heat conduction MD simulation procedure and implementation diagram, with Landauer-type quantum calculations included.

(I) Configuration preparation. The open-source graphic cross-platform molecule editor, *Avogadro*<sup>85</sup>, is used to design the initial molecular topologies as one wishes (e.g. alkanedithiols with three layers of gold substrates). Then these configurations are energy minimized with *Avogadro*'s native utility, and saved as *pdb* formats, which are eventually transformed into GROMACS's recognizable input files (*gro* and *top*) using *Open Babel*<sup>84</sup> with Universal Force Field (UFF)<sup>81</sup> implemented as molecular force field parameters.

(II) Production runs. Within GROMACS the molecular configurations are further energy minimized to ensure stable structure for subsequent dynamical runs and normal mode analysis. For MD production runs, the systems are first equilibrated to the average temperatures of the baths (usually takes a few hundred picoseconds), and then with a single long trajectory (a few nanoseconds) relaxed to nonequilibrium

steady state. From the tail of this trajectory, thousands of parallel at-steady-state trajectories are launched to get large enough statistical ensembles. At the end of this phase, as outputs, normal modes, steady-state trajectories, and inter-atomic forces are collected.

(III) Post-data processing. The heat currents are calculated according to the equation in the Main text using velocities and inter-atomic forces sampled during the steady state simulation. The Landauer-type currents are calculated through a different channel (see the illustration in Figure A.3), by using the formalism described here.

### A.3 Derivations of heat currents and end-to-end delocalization

#### A.3.1 Atomic local heat fluxes

In classical mechanics, the total energy of a molecular system consists of  $N$  atoms can be expressed as,

$$\begin{aligned}
 E_{tot} &= E_{kin} + E_{pon} & (A.5) \\
 E_{kin} &= \sum_{i=1}^N \frac{\mathbf{p}_i^2}{2m_i} \\
 E_{pon} &= V(\{\mathbf{r}_1 \dots \mathbf{r}_N\}),
 \end{aligned}$$

where  $E_{kin}$  is the total kinetic energy which is a sum of all individual atoms, and  $E_{pon}$  is the potential energy which involves many body interaction of all possible atoms. The latter in most MD force fields will be explicitly approximated to,

$$E_{pon} = V_{stretch} + V_{angle} + V_{dihedral} + V_{nonbonded}, \quad (A.6)$$

which essentially contains two-body, three-body, four-body and all the typical long-range interactions (e.g. electrostatic) within molecular systems. We introduce a partition scheme in order to describe energy changes of each atom in the molecule, that is, the total potential energy is additive from individual atom's potential which can be further expressed as a certain portion of the shared interaction terms. To write it out mathematically,

$$E_{tot} = \sum_i^N \frac{1}{2} m_i \mathbf{v}_i^2 + \sum_{\tau} V^{(\tau)} = \sum_i^N \frac{1}{2} m_i \mathbf{v}_i^2 + \sum_{\tau} \sum_j^{n(\tau)} U_{\tau,j}, \quad (\text{A.7})$$

$$U_{\tau,j}(\{\mathbf{r}_1 \dots \mathbf{r}_{n(\tau)}\}) = C_{\tau,j} V^{(\tau)}(\{\mathbf{r}_1 \dots \mathbf{r}_{n(\tau)}\}),$$

$$\sum_i^{n(\tau)} C_{\tau,j} = 1, \quad (\text{A.8})$$

where  $\tau$  is indicating different interaction terms (e.g. bond-stretching) and  $n(\tau)$  is participating atom number for that particular term.  $U_{\tau,j}$  is potential energy of  $V^{(\tau)}$  partitioned into atom  $j$ , with the partition coefficient  $C_{\tau,j}$ . We then can proceed to derive the equation of the heat flux for each atom in the molecular system.

$$\begin{aligned} J_i &\equiv \frac{dE_i}{dt} = \frac{d}{dt} \left( \frac{1}{2} m_i \mathbf{v}_i^2 + \sum_{\tau} U_{\tau,i} \right) \\ &= m_i \dot{\mathbf{v}}_i \cdot \mathbf{v}_i + \sum_{\tau} \sum_{j=1}^{n(\tau)} \frac{d\mathbf{r}_j}{dt} \frac{d(U_{\tau,i})}{d\mathbf{r}_j} \\ &= \mathbf{f}_i \cdot \mathbf{v}_i - \sum_{\tau} \sum_{j=1}^{n(\tau)} C_{\tau,i} \mathbf{f}_{\tau,j} \cdot \mathbf{v}_j \\ &= \sum_{\tau} \sum_{j=1}^{n(\tau)} (\delta_{ij} - C_{\tau,i}) \mathbf{f}_{\tau,j} \cdot \mathbf{v}_j = \sum_{\tau} \sum_{j \neq i} J_{\tau,ij}, \end{aligned} \quad (\text{A.9})$$



where we have defined  $\mathbf{f}_i$  to be the force acting on atom  $i$ , and  $\mathbf{f}_{\tau,j}$  the force derived from interaction  $V^{(\tau)}$  on atom  $j$

$$\mathbf{f}_i = -\frac{\partial V}{\partial \mathbf{r}_i} = -\sum_{\tau} \frac{\partial V^{(\tau)}}{\partial \mathbf{r}_i} = \sum_{\tau} \mathbf{f}_{\tau,i}, \quad (\text{A.10})$$

(It might also help to realize that the first term in eqn.(A.9)  $\mathbf{f}_i \cdot \mathbf{v}_i = \mathbf{v}_i \cdot \sum_j C_{\tau,j} \sum_{\tau} \mathbf{f}_{\tau,i}$ ) and heat flux arose from interaction  $V^{(\tau)}$ , going from atom  $j$  to atom  $i$  is defined as,

$$J_{\tau,ij} = C_{\tau,j} \mathbf{f}_{\tau,i} \cdot \mathbf{v}_i - C_{\tau,i} \mathbf{f}_{\tau,j} \cdot \mathbf{v}_j. \quad (\text{A.11})$$

This is the core expression we use to calculate the inter-atomic heat currents which will approach to constants when the system arrives steady-state.

### A.3.2 Derivation of end-to-end delocalization parameters of energy transfer

Here, we also propose another useful delocalization "measuring factor" involving only the anchoring atoms/groups in the molecular chains. Consider a harmonic molecular system linearly connected to a left and right atoms that representing the first atoms in the thermal baths. The equation of motion (EOM) for a single normal mode in the molecular system can be expressed as

$$\begin{aligned} \ddot{\xi}_k + \omega_k^2 \xi_k &= a_L C_{kL} x_{SL} + a_R C_{kR} x_{SR}, \\ C_{kL} &= \langle k | x_L \rangle, \quad C_{kR} = \langle k | x_R \rangle, \end{aligned} \quad (\text{A.12})$$

where  $\xi_k$  is the  $j$ th mode in the harmonic normal mode system,  $\omega_k$  is the corresponding eigenfrequency,  $x_L$  and  $x_R$  are atomic coordinates of the left-most and right-most atoms in the molecular system, the coefficient  $C_{kL}$  and  $C_{kR}$  are the projections of

them to the normal mode  $j$ ,  $a_L$  and  $a_R$  are constants (showing strength of the coupling of the system to the baths). and  $x_{SL}$  and  $x_{SR}$  are the first atoms in the left and right baths (substrates) that see the system.

Then the solution of the EOM has the form

$$\xi_k(t) = \xi_k^0(t) + a_L \int_{-\infty}^t dt' G_k(t-t') C_{kL} x_{SL} + a_R \int_{-\infty}^t dt' G_k(t-t') C_{kR} x_{SR}, \quad (\text{A.13})$$

where  $\xi_k^0(t)$  is the general solution of the homogeneous equation and  $G_k$  can be expressed as

$$G_k(t-t') = \begin{cases} 0 & \text{for } t < t' \\ \frac{1}{\omega_k} \sin[\omega_k(t-t')] & \text{for } t > t' \end{cases} \quad (\text{A.14})$$

We also have the EOM for left (right) bath atom

$$\begin{aligned} \ddot{x}_{SL} &= A_{L,bath} + a_L x_L = A_{L,bath} + a_L \sum_k C_{Lk} \xi_k \\ &= A_{L,bath} + a_L \sum_k \left[ \xi_k^0(t) + a_L C_{Lk} C_{kL} \int_{-\infty}^t dt' G_k(t-t') x_{SL}(t') + \right. \\ &\quad \left. a_R C_{Lk} C_{kR} \int_{-\infty}^t dt' G_k(t-t') x_{SR}(t') \right], \end{aligned} \quad (\text{A.15})$$

where  $A_{L,bath}$  denotes the acceleration caused by all the forces (e.g. fluctuations and damping) from the left side of the bath. The same goes for the right side bath  $x_{SR}$ . The second term on the right-hand-side can be understood as the interaction when the left bath "pushes" and the system and the system "pushes" back. The third term in the EOM is more relevant for our purposes. It shows how the left bath "sees" the

right bath. We will discuss this term in the following separately,

$$[\ddot{x}_{SL}]_{L\leftarrow R}(t) = a_L a_R \int_{-\infty}^t dt' K(t-t') x_{SR}(t') = a_L a_R \int_0^{\infty} dt' K(t') x_{SR}(t-t'), \quad (\text{A.16})$$

where

$$K(t) = \sum_k C_{Lk} C_{kR} \frac{1}{\omega_k} \sin[\omega_k t]. \quad (\text{A.17})$$

Now we start coarse-graining<sup>40</sup> of the above discrete states by writing  $K(t)$  as an integral of a density of state (DOS)  $g(\omega)$ :

$$K(t) = \int d\omega g(\omega) \frac{C_L(\omega) C_R(\omega)}{\omega} \sin(\omega t). \quad (\text{A.18})$$

For the evaluation purposes, symmetric spectrum is assumed,

$$K(t) = \frac{1}{2} \int_{-\infty}^{\infty} d\omega g(\omega) \frac{C_L(\omega) C_R(\omega)}{\omega} \text{Im}[e^{i\omega t}]. \quad (\text{A.19})$$

$$K(t) = \frac{1}{2} \text{Im} \int_{-\infty}^{\infty} d\omega \pi(\omega) e^{i\omega t}, \quad (\text{A.20})$$

where

$$\pi(\omega) = g(\omega) \frac{C_L(\omega) C_R(\omega)}{\omega} = \sum_k \frac{C_{Lk} C_{kR}}{\omega_k} \delta(\omega - \omega_k) \equiv \sum_k \pi_k \delta(\omega - \omega_k). \quad (\text{A.21})$$

$\pi(\omega)$  reflects the strength of how far the left bath extends to see the right bath in the frequency space, and is thus a reasonable quantity of measuring the delocalization of the anchoring groups in the molecular system connected to the baths with

temperature gradients.

Now we coarse grain  $\pi(\omega)$  over a small distance of  $\Delta\omega$  across the spectrum, and approximate it as

$$\pi(\omega, \Delta\omega) = N_{\Delta\omega} \sum_{\omega_k = \omega - \frac{\Delta\omega}{2}}^{\omega + \frac{\Delta\omega}{2}} \pi_k, \quad (\text{A.22})$$

where  $N_{\Delta\omega}$  is a normalization factor pertaining to the value of  $\Delta\omega$  chosen. The procedure described here can also be used to smoothen functions with steep spikes,

Assuming we want to coarse grain a function, in order to smoothen it approximately.

$$\bar{X}(\omega, \Delta\omega) = N_{\Delta\omega} \int_{-\frac{\Delta\omega}{2}}^{\frac{\Delta\omega}{2}} dx X(\omega + x). \quad (\text{A.23})$$

The integral value should be identical whatever coarse-grain length one takes,

$$\begin{aligned} \int_a^b d\omega X(\omega) &= \int_a^b d\omega \bar{X}(\omega) \\ &= \int_a^b d\omega N_{\Delta\omega} \int_{-\frac{\Delta\omega}{2}}^{\frac{\Delta\omega}{2}} dx X(\omega + x) \\ &= N_{\Delta\omega} \int_{-\frac{\Delta\omega}{2}}^{\frac{\Delta\omega}{2}} dx \int_a^b d\omega X(\omega + x) \end{aligned} \quad (\text{A.24})$$

Take the infinite upper and lower bounds.

$$\int_{-\infty}^{\infty} d\omega X(\omega) = N_{\Delta\omega} \int_{-\frac{\Delta\omega}{2}}^{\frac{\Delta\omega}{2}} dx \int_{-\infty}^{\infty} d\omega X(\omega + x). \quad (\text{A.25})$$

The function does not depend on finite shifts, and thus we have

$$N_{\Delta\omega} \int_{-\frac{\Delta\omega}{2}}^{\frac{\Delta\omega}{2}} dx = 1, \quad (\text{A.26})$$

and therefore we obtain the normalization factor

$$N_{\Delta\omega} = \frac{1}{\Delta\omega}. \quad (\text{A.27})$$

#### A.4 Supplemental MD simulation results

Figure A.4 illustrates conducting capacity with respect the change of chain (or bridge) numbers in the molecular systems under the junction setting. Without specifically considering intermolecular interactions, it appears the conductance increases almost linearly with the increase of chain numbers. In the context of self-assembled monolayers, the area density for alkanedithiols to the Gold substrates is around  $4.5 \times 10^{14}/\text{cm}^2$ , that is approximately 4.5 molecules per  $\text{nm}^{123,190,191}$ . If we take this value and assume the intermolecular spacing is large enough such that interactions between chains are negligible, then our result gives thermal conductivity estimation of around 65-75  $\text{MW}/(\text{m}^2\text{K})$ , which is exactly what Majumdar *et. al.*<sup>78</sup> measured in the recent experiment.

#### A.5 Supplemental Landauer-type results for hydrocarbon heat conduction

By adding layers to different alkane molecules(Figure A.6), we find

1. The presence of thiol groups enhances alkane conductance.
2. The trend of conductance increase and eventual decrease (as a function of chain

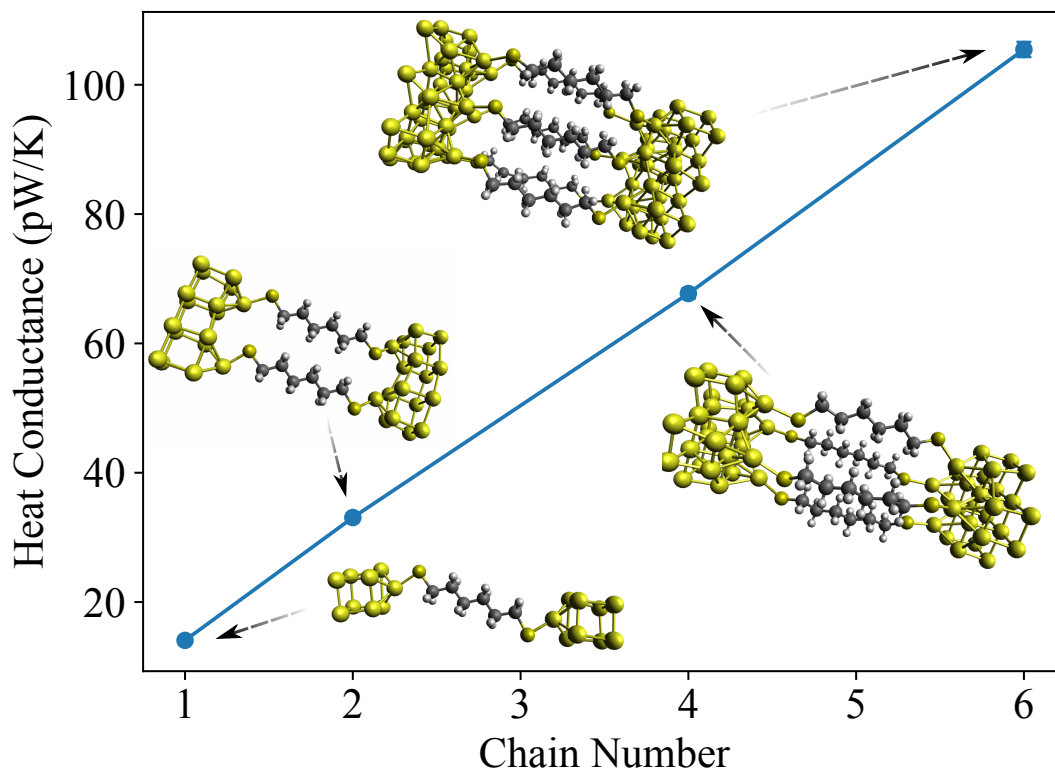


Figure A.4: Total heat conductance for molecular systems with different chain numbers. The molecule unit is hexanedithiol, with number of 1, 2, 4, and 6 chains aligned in parallel and embedded in three layers of Gold substrates in the junction. The temperature bias is set to be 50K. The conductance is calculated by dividing the total heat currents to the temperature difference, and the total currents are calculated as sums of currents in individual chains (intermolecular interaction is not considered here) that go from one side of each chain to the other side. The error bars represent Standard Error<sup>1,2</sup>.

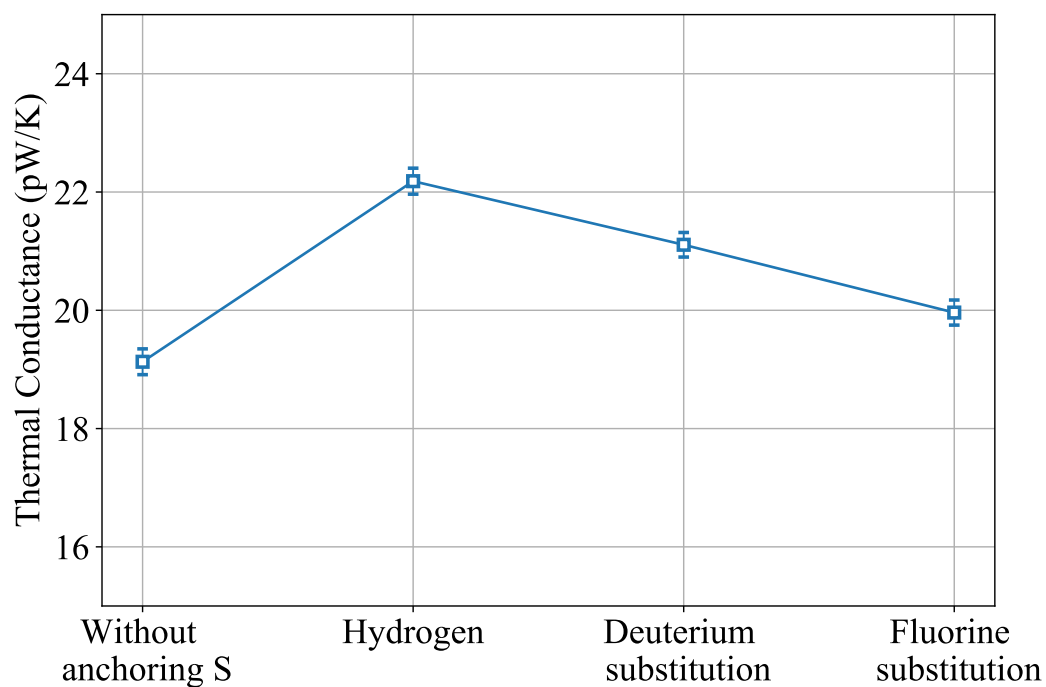


Figure A.5: Heat conductance of saturated carbon-backed chain molecules with different substitutions to hydrogens. Each species are connected with thiol groups at the two sides of the molecules and further connected to three layers of gold substrates. The temperatures are 300K and 350K on the right and left sides of the junction respectively. The error bars represent Standard Error<sup>1,2</sup>.

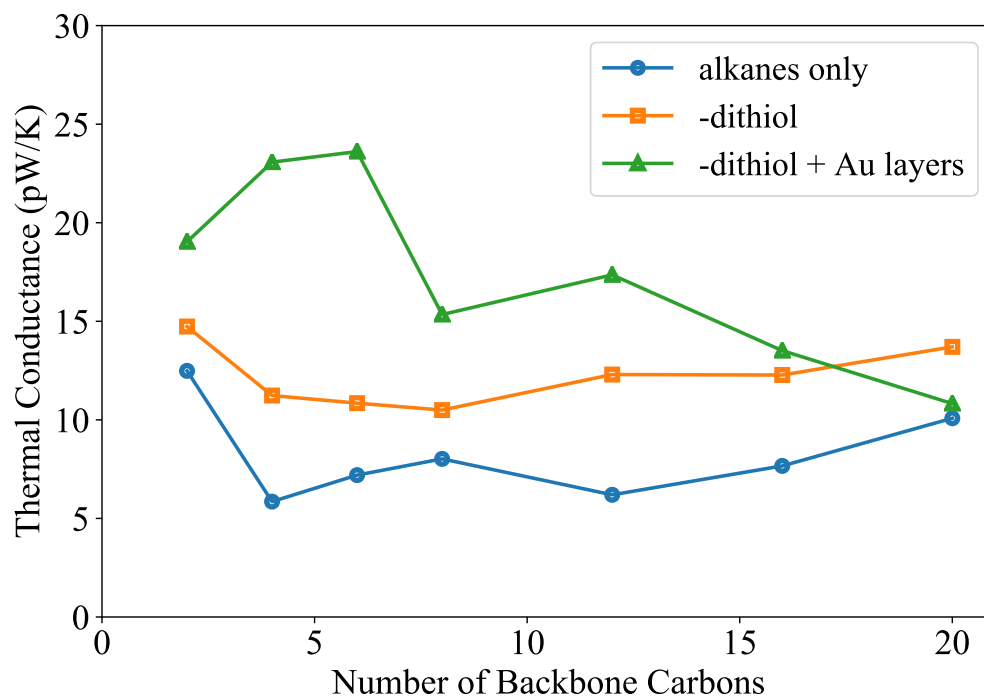


Figure A.6: Length-dependent thermal conductance, calculated through the Landauer formula. The exterior-most layers of explicit bulk are coupled to white noise baths. The conductance denotes ratio between heat current and temperature bias, with left and right baths at 300K and 350K respectively. The triangle line has three gold layers, in accordance with the MD simulations.



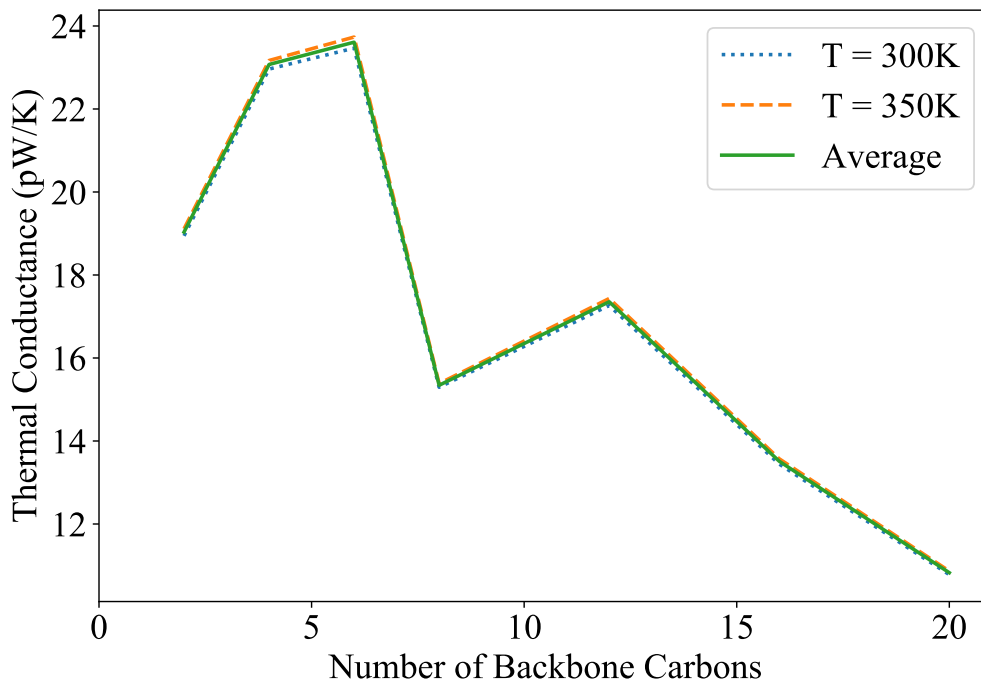


Figure A.7: Comparison between derivative conductance and finite-bias conductance. For the finite-bias case, both temperatures of 300K and 350K are taken (i.e. bias of 50K). This is compared with two derivative conductance calculations: Around a temperature of 300K and of 350K.

length), as reported in *ab-initio* calculations of similar systems<sup>34</sup>, appears only when including the layers of gold leads, explicitly.

For the choices of different conductance expressions (using the derivative form or the finite-bias form), it turns out that the influence is negligible across a range of alkane chain lengths (Figure A.7). The conductance at 350K is slightly higher and 300K slightly lower, but the difference between either of them and the finite-bias result is significantly smaller than the values of the relevant conductances themselves.

Figure A.8 shows the temperature dependence of the heat conductance of butanedithiol. Conductance increases at a higher rate until 100K, and then starts to plateau as temperature increases further. This trend agrees with results reported for

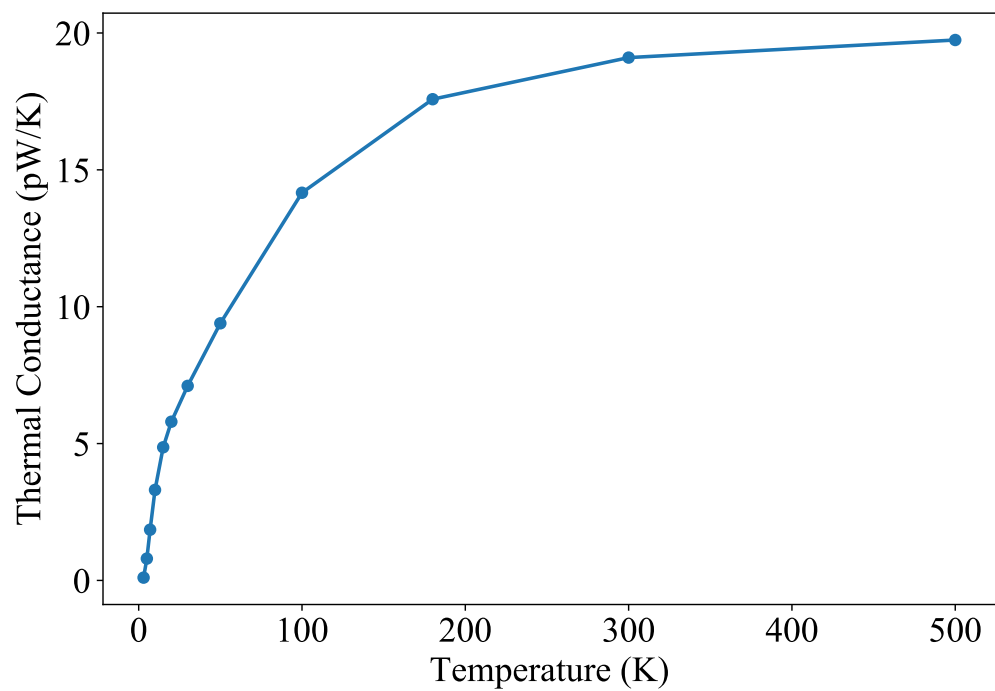


Figure A.8: Temperature dependence of the derivative Landauer thermal conductance, for butanedithiol ( $\text{HS}(\text{CH}_2)_{10}\text{SH}$ ) adsorbed on a substrate modelled by 3 layers of explicit gold atoms.

an same alkane<sup>34</sup>.

## A.6 Debye Spectrum density generator and diatomic heat conduction

### A.6.1 Introduction

Debye model is an important theoretical tool for solid state physics. But it is not obvious how to utilizing this model to stochastic trajectory-based simulational approaches, to study critical physical chemistry problems, such as relaxation and transports dynamics in the vicinity of solids and interfacial chemical reactions. In the late 70s, Nitzan and co-workers has developed a computationally feasible procedure [Ref.<sup>76</sup>] such that the overall Debye effect of the bath can be simulated a series of random forces and a damping kernel characterized by a specific form of spectral density, as people may have realized in Langevin dynamics, but with much more complex structure.

Here, we realize Nitzan Debye bath formalism with *Python* interpreted class called `Debye Generator`<sup>192</sup>. The spectrum density function, which is used to generate Debye spectrum effect is expressed as<sup>76</sup>,

$$g(\omega) = N \frac{(\omega/\omega_D)^2}{1 + (\omega/\omega_D)^{2n}}, \quad (\text{A.28})$$

where  $\omega_D$  is the Debye frequency cutoff,  $N$  is a normalization constant.  $n$  is an integer that dictates the shape of the density function. The bigger  $n$  index is, the closer the density  $g(\omega)$  approaches to the Debye spectrum. Examples of different indices give a feeling of how  $n$  should be chosen to get a decent approximation of the Debye bath. (see Figure A.9) We may see  $n$  does not have to go for hundreds or thousands, even when  $n \geq 8$  the cutoff of the spectrum is already noticeable.

Following the model (that is, the impurity atoms and the bath lattice), the for-

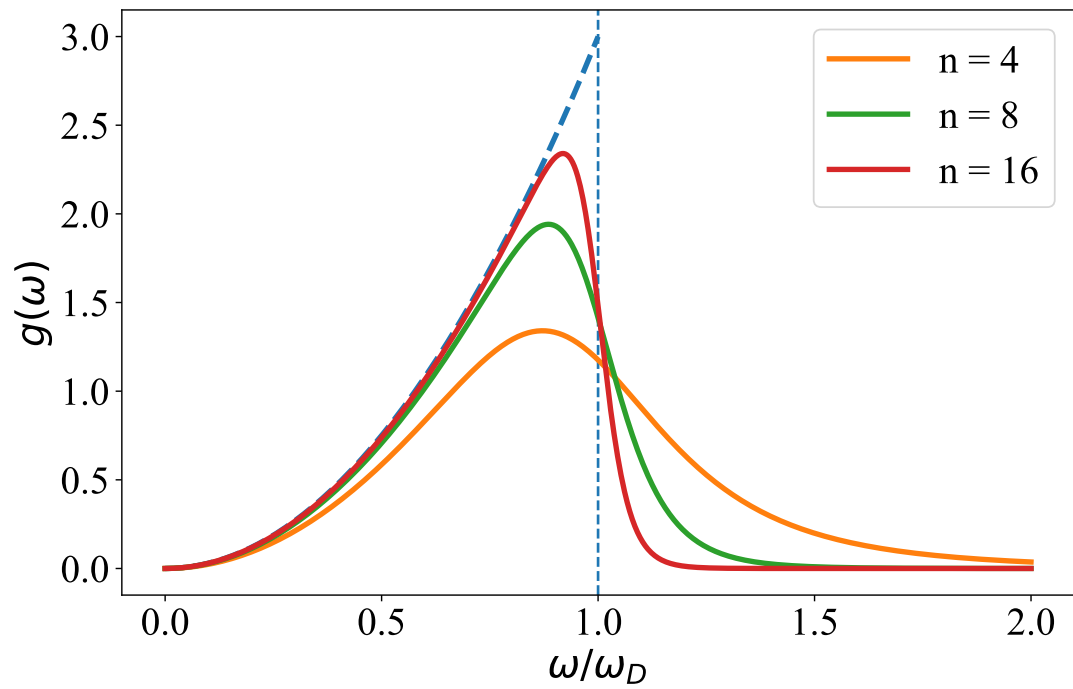


Figure A.9: Spectral densities calculated from Eqn. A.28 for different values of  $n$ . The dashed line is Debye Spectrum.

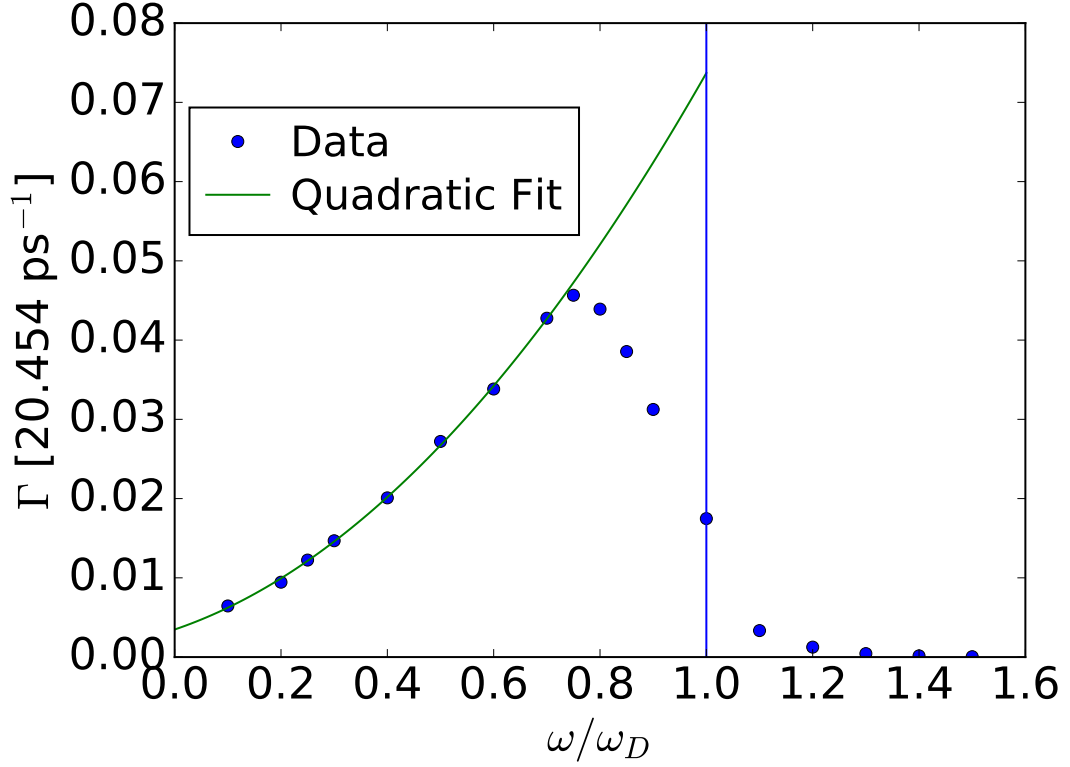


Figure A.10: Average decay rate plotted as a function of  $\omega$ . The Debye bath is simulated with the accuracy of  $n=8$  in the spectrum function. (Eqn.A.28) The circles are simulated results and the solid line is quadratic fitting of the simulated data.

malism and the recipe described in the main text and appendice of Ref<sup>[76]</sup>, we are able to construct the dissipative friction forces, and random fluctuating forces through the displacements ( $y_i(t)$ ) of the connecting atom, and reproduce the characteristics of the Debye bath in the frequency space to a high order of accuracy.

### A.6.2 Implicit bath density properties

The decay rate of a system (represented by an impurity particle here) near a Debye bath can be evaluated using the derived equations (III.11) through (III.15) in Ref<sup>[76]</sup>.

Figure A.10 shows the average decay rate of an impurity particle in the vicinity

of a Debye bath (simulated with the spectrum density function as of Eqn.A.28) The particle is harmonically restrained with a characteristic angular frequency  $\omega$ . The time evolution of the total particle energy (kinetic plus potential) is casted into an exponential form,

$$E(\omega, t) \propto e^{-\Gamma(\omega)t}. \quad (\text{A.29})$$

By varying the frequency, different energy changing rates can be measured, and the values of  $\Gamma$  extracted Figure A.10 is an example of such decay rate. With the accuracy order of  $n=8$ , the energy transferring from the system to the bath already has a basic Debye shape (that is quadratic).

It can be shown the random replacements generated from the provided procedure (in Section III.B of Ref<sup>[76]</sup>) satisfy the spectral function (Eqn.A.28), as a Fourier transform of the correlation function of the time series (see Figure A.11).

We also inspect the Debye bath generator with a equilibration test, that is put a system thermally connect to the bath, and let it relax to equilibrium (Figure A.12).

The result shows the system goes to equilibrium as expected, and the relaxation time is around 3 psecosecond for this particular system under study. (with impurity mass as oxygen, and bath representing mass as sulfur. Debye frequency as 2 rad/ps, and forces connecting bath and system formed as Eqn.(II.26) in Ref<sup>[76]</sup>)

### **A.6.3 Center of mass potential equilibrium expansion for exponential repulsive forces**

The setting here is one dimensional, we have a exponential repulsive force on the left and on the right with a system in between. Assuming a single particle system, the potentials for the system with the left bath and the system with the right bath can

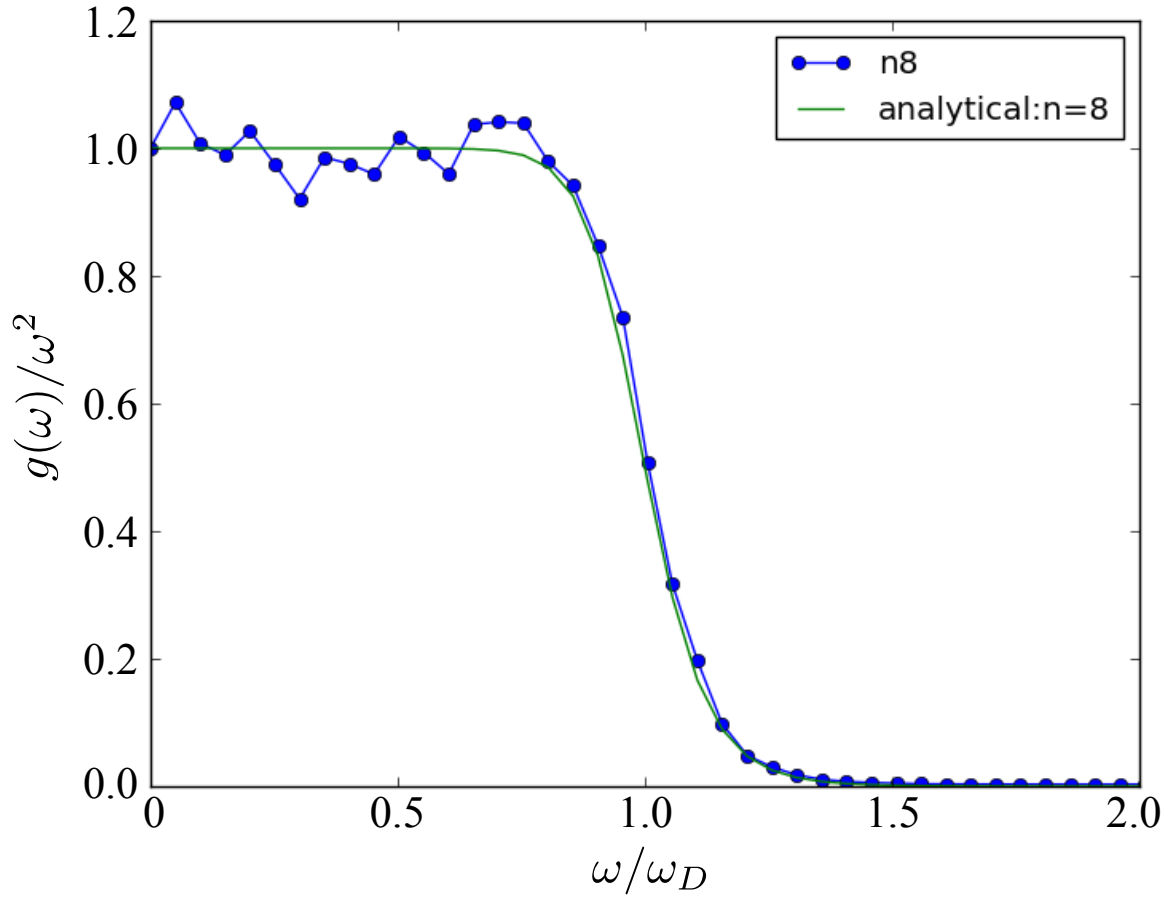


Figure A.11: Fourier transform of the random position autocorrelation function of  $\langle R(t)R(0) \rangle$  for  $n=8$ . the circles are numerical implemented data points, and the solid line is plotted according to Eqn. A.28.

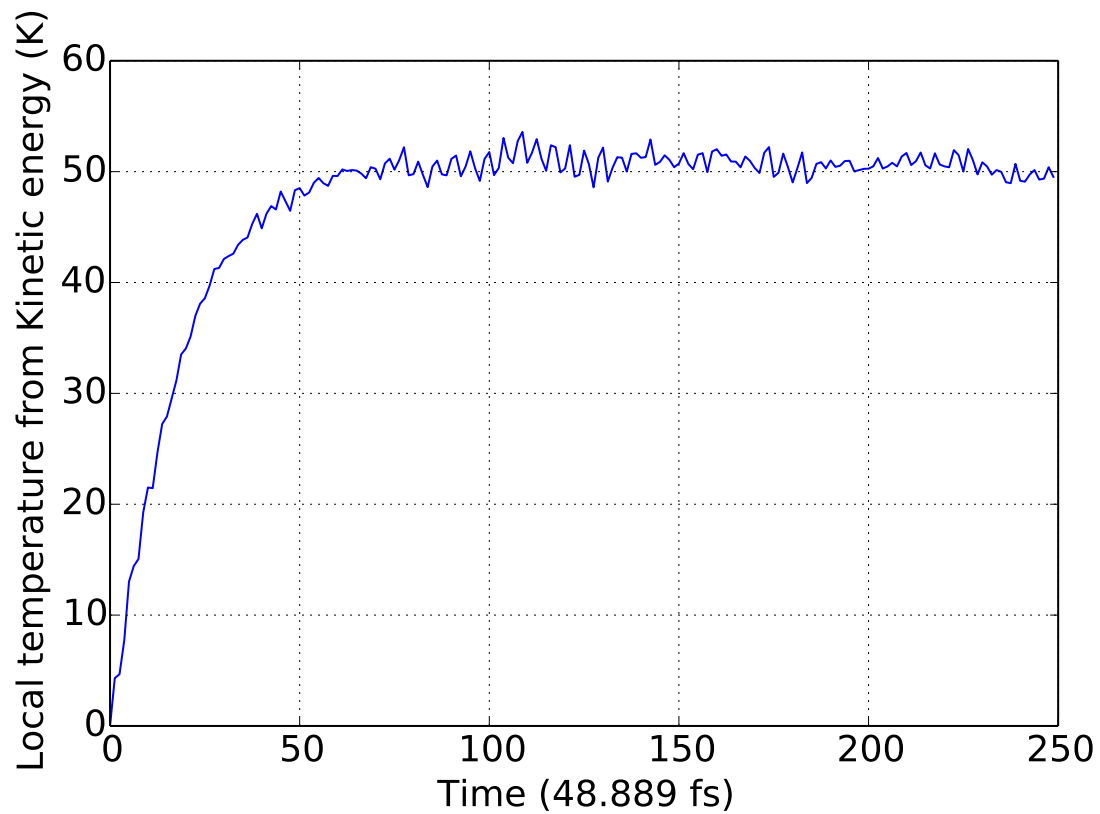


Figure A.12: Local temperature of a single impurity calculated from kinetic energy ensemble, when it is put near a Debye bath with temperature of 50K.



be expressed in general as

$$U_L = A_L e^{-\alpha_L(x-y_l-D/2)} \quad (\text{A.30})$$

$$U_R = A_R e^{-\alpha_R(y_r-x-D/2)} \quad (\text{A.31})$$

where  $x$ 's are positions and  $D$  is the bond length (which is fixed to make it as rigid box for one particle).

For simplicity, let us take the left and right couplings to be symmetric, that is the coefficients are the same, then we can write the total energy as,

$$U = A(e^{-\alpha(x-y_l-D/2)} + e^{-\alpha(y_r-x-D/2)}) \quad (\text{A.32})$$

The equilibrium position is  $x_0 = \frac{y_l+y_r}{2}$ , expand the potential at this equilibrium position to the second order, we have,

$$U(x - x_0) = 2Ae^{-\alpha\frac{y_r-y_l-D}{2}} + A\alpha^2 e^{-\alpha\frac{y_r-y_l-D}{2}}(x - x_0)^2 + \dots \quad (\text{A.33})$$

The plot in Figure A.13 gives us an idea of how this approximation looks like. The blue line is the original potential shown in the eqn(A.32), while the red is the harmonic expansion of the original potential. One can see within short range of equilibrium position, the harmonic potential can be a rather good approximation, though one also need to note when the boundaries (that is  $y_l$  and  $y_r$ ) move altogether in the simulation the shape of the potential will neither be exact nor static.

As can be seen from Eqn.A.33, the approximate force constant and angular fre-

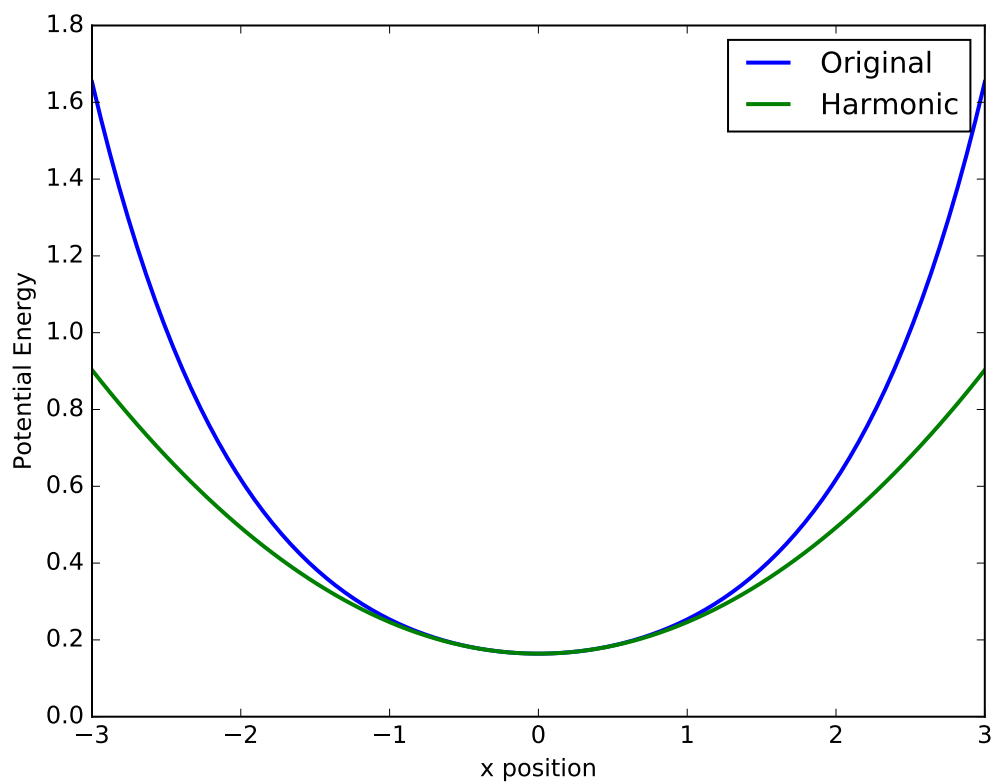


Figure A.13: Potentials with respect to the particle position. Equilibrium position is set to be at origin. position is in the unit of width of the rigid body  $D$  (The boundaries are  $y_l = -3$  and  $y_r = 3$ ). Other parameters are:  $A = 1$ ,  $\alpha = 1$ .

quency are,

$$k_c = 2A\alpha^2 e^{-\alpha \frac{y_r - y_l - D}{2}} \quad (\text{A.34})$$

$$\omega_c = \sqrt{k_c/m} \quad (\text{A.35})$$

respectively, where  $m$  is the mass of the center, and other parameters are described as above. Now we may see here, if we want to get different  $\omega_c$ 's, there are different parameters we can tune. In the following results, the parameter chosen to change is the characteristic length (that is,  $y_r - y_l - D$  in the above expressions), while all the other parameters are kept constants.

#### A.6.4 Bridge the formalism and parameters

##### Constant coupling from Debye to white noise

In reference<sup>76</sup>, a complete recipe of numerical procedure to generate Debye spectrum has been given, in which the interaction between system and bath is taken as a general form of  $U(x, y_l)$  ( $x$  is the position of the system or impurity in the language of the paper, and  $y_l$  is dynamic displacement of the bath particle that interacts with the system.). But the generalized Langevin equation (which is often derived under linear coupling regime, see Chapter 8 in Book<sup>40</sup>) is wrtten as,

$$\ddot{x} = -\frac{1}{m} \frac{\partial V(x)}{\partial x} - \int_0^t d\tau Z(t - \tau) \dot{x}(\tau) + \frac{1}{m} R(t) \quad (\text{A.36})$$

$$Z(t) = \frac{1}{m} \sum_j \frac{c_j^2}{m_j \omega_j^2} \cos(\omega_j t) \quad (\text{A.37})$$

$$R(t) = - \sum_j c_j \left( q_{j0} \cos(\omega_j t) + \frac{\dot{q}_{j0}}{\omega_j} \sin(\omega_j t) \right) \quad (\text{A.38})$$

where  $V$  is the deterministic potential the system felt,  $Z$  is the memory kernel of system-bath coupling, and  $R$  is the random force which is determined by the randomness of the initial conditions of the bath particles (represented by the initial positions  $q_{j0}$  and initial velocities  $\dot{q}_{j0}$ ). As we assume the thermal bath remains in equilibrium all the time, the initial values should be sampled from equilibrium Boltzmann distribution, which satisfy

$$\langle q_{j0} \rangle = \langle \dot{q}_{j0} \rangle = 0, \quad \langle q_{j0} \dot{q}_{j0} \rangle = 0 \quad (\text{A.39})$$

$$\frac{1}{2} m_j \langle \dot{q}_{j0} \dot{q}_{j'0} \rangle = \frac{1}{2} m_j \omega_j^2 \langle q_{j0} q_{j'0} \rangle = \frac{1}{2} k_B T \delta_{jj'}. \quad (\text{A.40})$$

From here we can easily verify the Fluctuation-Dissipation theorem is satisfied as,

$$\langle R(0)R(t) \rangle = m k_B T Z(t) \quad (\text{A.41})$$

When the relaxation timescale of the thermal environment is short relative to all the characteristic system times (e.g. electronic processes, vibrational motions), the description turns to Markovian limit in which the memory kernel in the Langevin equation changes to

$$Z(t) = 2\gamma\delta(t) \quad (\text{A.42})$$

where  $\gamma$  is a constant.

Now let us return to Ref.<sup>76</sup>, the equation of motion for the system (or impurity) is written as

$$\ddot{x} = -\frac{1}{m} \frac{\partial U[x - (r_l^{eq} + y_l)]}{\partial x} \quad (\text{A.43})$$

**Repulsive potential** One way to choose the bath-system interaction is to take the potential interaction to be exponentially repulsive,

$$U[x - (r_i^{eq} + y_l)] = Ae^{-\alpha((r_i^{eq} + y_l) - x)} \quad (\text{A.44})$$

where  $A$  and  $\alpha$  are constant parameters. Now let's expand the potential to the first order at  $y_l = 0$  point,

$$\ddot{x} = -\frac{1}{m} \frac{\partial}{\partial x} \left( U_0(x, y_l = 0) + \frac{\partial U}{\partial y_l} \Big|_{y_l=0} y_l \right) + \dots \quad (\text{A.45})$$

$$U_0(x, y_l = 0) = Ae^{-\alpha(r_i^{eq} - x)} \quad (\text{A.46})$$

$$\frac{\partial U}{\partial y_l} \Big|_{y_l=0} = -\alpha Ae^{-\alpha(r_i^{eq} - x)} \quad (\text{A.47})$$

We do one more step approximation, that is put the  $x$  position at its equilibrium for the second term in the right hand side of eqn(A.45) Thus, the equation of motion becomes

$$\ddot{x} = -\frac{1}{m} \frac{\partial}{\partial x} U_0(x, y_l = 0) + \frac{C}{m} y_l \quad (\text{A.48})$$

$$C = \alpha^2 Ae^{-\alpha(r_i^{eq} - x^{eq})} \quad (\text{A.49})$$

**Harmonic potential** One may also take the interaction to simply be harmonic,

$$U[x - (r_i^{eq} + y_l)] = \frac{1}{2} m \omega_l^2 (x - (r_i^{eq} + y_l))^2 \quad (\text{A.50})$$

where  $\omega_l$  is angular frequency connecting the system and the bath.

$$U_0(x, y_l = 0) = \frac{1}{2}m\omega_l^2(x - r_l^{eq})^2 \quad (\text{A.51})$$

$$\left. \frac{\partial U}{\partial y_l} \right|_{y_l=0} = -m\omega_l^2(x - r_l^{eq}) \quad (\text{A.52})$$

Then the equation of motion becomes,

$$m\ddot{x} = -m\omega_l^2(x - r_l^{eq}) + m\omega_l^2 y_l, \quad (\text{A.53})$$

in which the coefficient

$$C = m\omega_l^2 \quad (\text{A.54})$$

**Link Debye spectrum** When we look at Ref<sup>76</sup> again, the stochastic equation for the dynamic displacement is shown to be

$$y_l = R_l(t) - \frac{1}{M} \int_0^t d\tau \left\{ \frac{\partial U[x - (r_l^{eq} + y_l)]}{\partial y_l} \right\} F(t - \tau) \quad (\text{A.55})$$

$$R_l(t) = \sum_k S_{kl}^* \left[ z_k(0) \cos(\omega_k t) + \frac{1}{\omega_k} \dot{z}_k(0) \sin(\omega_k t) \right] \quad (\text{A.56})$$

$$F(t) = \sum_k |S_{kl}|^2 \frac{\sin(\omega_k t)}{\omega_k} = \int d\omega g(\omega) \frac{\sin(\omega t)}{\omega} \quad (\text{A.57})$$

where  $M$  is the mass of the representing bath particle, the second integral term at the right hand side of the equation encapsulates the coupling between the system and the bath, and  $R_l$  is Gaussian random process featured with colored spectrum density,

$z_k$  and  $\dot{z}_k$  have the same meanings to  $q_j$  and  $\dot{q}_j$  in Eqn(A.38), that is, the initial conditions of the normal modes in the bath lattice. The second equality for  $F(t)$  is defining a weighed density of modes  $g(\omega)$  normalized to one, which can be illustrated as following. For a possible 1-D example, the transformation matrix element  $S_{kl}$  may have the form as

$$S_{kl} = \frac{1}{\sqrt{N}} e^{ilk a} \quad (\text{A.58})$$

where  $a$  is the unit cell length,  $N$  being the number of atoms. Therefore while in general, the Debye density of modes  $g(\omega)$  can be normalized to  $N$  for 1-D lattice, these two factors will cancel out in our definition, and we make  $g(\omega)$  normalize to unity for simplicity.

Substitute Eqn (A.55) into equation of motion for  $x$  (Eqn (A.48)), we get the expression

$$\ddot{x} = -\frac{1}{m} \frac{\partial}{\partial x} U_0(x, y_l = 0) - \frac{C}{mM} \int_0^t d\tau \left\{ \frac{\partial U[x - (r_l^{eq} + y_l)]}{\partial y_l} \right\} F(t - \tau) + \frac{C}{m} R_l(t), \quad (\text{A.59})$$

which resembles the equation of motion (EOM) for generalized Langevin dynamics (shown in Eqn (A.36)) in its form, that is the first term on the right is the deterministic potential felt by the system, the second term couples the system to the bath, and the third term originates from random properties of bath itself. Nevertheless, the two equations are not exactly the same, especially the second term in Eqn (A.59) does not look obvious. We might go head and equalize this term to the coupling term in Eqn (A.36) (that is with integration of velocity and memory kernel,  $\int d\tau Z(t - \tau)\dot{x}$ ), but that takes more work so here we choose a shortcut by focusing on random force only, which would give same but quicker answer (we show in the Appendix ??, that

the EOM of the stochastic part of the system can indeed be written sum of coupling and random forces, with exact same layout as expressed in Langevin equation).

Consider the random force in Eqn (A.56), the initial values satisfy

$$\langle z_k \rangle = \langle \dot{z}_k \rangle = 0 \quad (\text{A.60})$$

$$\langle |z_k|^2 \rangle = k_B T / M \omega_k^2 \quad (\text{A.61})$$

$$\langle |\dot{z}_k|^2 \rangle = k_B T / M, \quad (\text{A.62})$$

With all the mixed correlations go to zeros, the correlations for  $R_l(t)$  satisfies

$$\langle R_l(t) \rangle = 0 \quad (\text{A.63})$$

$$\langle R_l(t) R_l(0) \rangle = \sum_k |S_{kl}|^2 \langle |z_k(0)|^2 \rangle \cos(\omega_k t) \quad (\text{A.64})$$

$$= \frac{k_B T}{M} \sum_k |S_{kl}|^2 \frac{\cos(\omega_k t)}{\omega_k^2} \quad (\text{A.65})$$

$$= \frac{k_B T}{M} \int d\omega \frac{g(\omega)}{\omega^2} \cos(\omega t) \quad (\text{A.66})$$

with last equality uses same strategy as in Eqn (A.57). As we've chosen Debye density of state normalizes to unity,

$$g(\omega) = N \omega^2 \quad (\text{A.67})$$

we can get the normalization factor  $N$  by integrating till Debye cutoff  $\omega_D$ ,

$$\int_0^{\omega_D} g(\omega) d\omega = N \frac{\omega_D^3}{3} = 1 \quad (\text{A.68})$$



therefore  $N = \frac{3}{\omega_D^3}$  and

$$g(\omega) = \frac{3\omega^2}{\omega_D^3}. \quad (\text{A.69})$$

Plug Eqn (A.69) into Eqn(A.66) and do the integral, we have,

$$\begin{aligned} \langle R_l(t)R_l(0) \rangle &= \frac{k_B T}{M} \int d\omega \frac{g(\omega)}{\omega^2} \cos(\omega t) \\ &= \frac{3k_B T}{\omega_D^3 M} \int_0^{\omega_D} \cos(\omega t) d\omega \\ &= \frac{3k_B T}{\omega_D^3 M} \frac{\sin(\omega_D t)}{t}. \end{aligned} \quad (\text{A.70})$$

In order to make connection between Debye model and white noise, the quick approach here as we've mentioned earlier, is to equalize the random parts, that is making the Debye random process to be Markovian. Specifically, to have random forces in Eqn (A.59) the same property in Eqn (A.41)

$$C^2 \langle R_l(t)R_l(0) \rangle = \langle R(t)R(0) \rangle = mk_B T Z(t), \quad (\text{A.71})$$

We need to take long time limit ( $t \rightarrow \infty$ ) to get the constant coupling, that is,

$$mk_B T \int_0^\infty dt Z(t) = \int_0^\infty dt \langle R(t)R(0) \rangle = C^2 \int_0^\infty dt \langle R_l(t)R_l(0) \rangle \longrightarrow mk_B T \gamma \quad (\text{A.72})$$

Therefore the parameterized constant coupling for the Markovian limit of the Debye spectrum generator is,

$$\begin{aligned} \gamma &= \frac{3C^2}{mM\omega_D^3} \int_0^\infty \frac{\sin(\omega_D t)}{\omega_D t} d(\omega_D t) \\ &= \frac{3C^2 \pi}{2mM\omega_D^3}, \end{aligned} \quad (\text{A.73})$$

all the parameters of which has been defined in the above expressions.

### Debye simulator normalization factor and parameterization

In the process of incorporating Debye color bath model into heat conduction simulation, the spectral density function we take is not the actual quadratic discontinuous function, but a approximation function (Ref <sup>76</sup>)

$$g(\omega) = N \frac{(\omega/\omega_D)^2}{1 + (\omega/\omega_D)^{2n}}, \quad (\text{A.74})$$

where  $\omega_D$  is the Debye frequency and  $N$  is a normalization constant. The higher order  $n$  number the better approximation one will make, but with higher computational cost (normally  $n \geq 8$  makes a good approximation). Now we want to know how this normalization factor looks like, and confirm its expression converges to Debye at large  $n$  limit.

In Appendix B of Ref<sup>76</sup>, the authors show us  $N$  expression when normalizing to unity,

$$N = 2^{2(n-1)} 2 \sin\left(\frac{3\pi}{2n}\right) \prod_{l=1}^{n-1} \sin^2\left(\frac{\pi l}{2n}\right) / \pi \omega_D. \quad (\text{A.75})$$

In large  $n$  limit ( $n \rightarrow \infty$ ), Eqn (A.74) reduce to

$$N \frac{(\omega/\omega_D)^2}{1 + (\omega/\omega_D)^{2n}} \rightarrow N \left(\frac{\omega}{\omega_D}\right)^2. \quad (\text{A.76})$$

When we compare this expression to Eqn (A.69), we have under this limit,

$$N = \frac{3}{\omega_D}. \quad (\text{A.77})$$

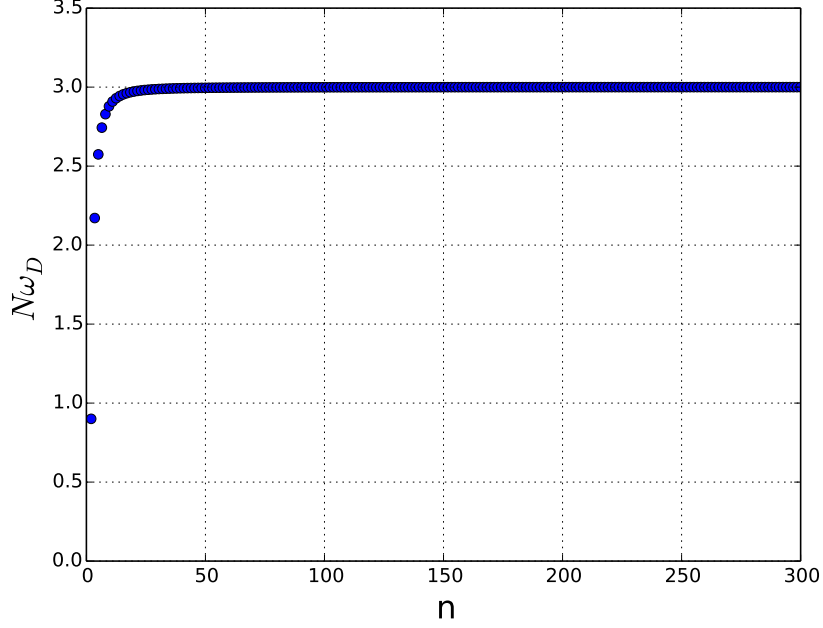


Figure A.14: Numerical plot for normalization factor with respect to the value of  $n$

Comparing to general expression for  $N$  (Eqn (A.75)), we have

$$N\omega_D \longrightarrow 3; \quad n \rightarrow \infty, \quad (\text{A.78})$$

and this exactly what we see (Fig A.14). Thus we confirm the accuracy of the normalization factor, which can be used to parameterize couplings in MD simulation.

To get the equivalent  $\gamma$  coupling under spectral density in Eqn (A.74), we need first calculate the correlation function of  $R_l$  like in Eqn (A.70),

$$\begin{aligned} \langle R_l(t)R_l(0) \rangle &= \frac{k_B T}{M} \int d\omega \frac{g(\omega)}{\omega^2} \cos(\omega t) \\ &= N \frac{k_B T}{2\omega_D^2 M} \int_{-\infty}^{\infty} d\omega \frac{1}{1 + (\omega/\omega_D)^{2n}} e^{i\omega t}, \end{aligned} \quad (\text{A.79})$$

replace  $\omega/\omega_D$  with  $x$  and  $t' = \omega_D t$ , and write the integral as

$$\begin{aligned}\langle R_l(t)R_l(0) \rangle &= N \frac{k_B T}{2\omega_D M} \int_{-\infty}^{\infty} dx \frac{1}{1+x^{2n}} e^{ixt'} \\ &= N \frac{k_B T}{2\omega_D M} \int_{-\infty}^{\infty} dx \frac{e^{ixt'}}{\prod_{m=0}^{2n-1} \left[ x - \exp\left(\frac{i\pi(2m+1)}{2n}\right) \right]}.\end{aligned}\quad (\text{A.80})$$

Eqn (A.80) can be evaluated with complex integration by closing a contour in the upper half complex plane.

$$\begin{aligned}\frac{k_B T}{M} B_n(t) &\equiv \langle R_l(t)R_l(0) \rangle \\ &= \frac{N k_B T \pi}{2^{2(n-1)} \omega_D M \prod_{l=1}^{n-1} \sin^2\left(\frac{\pi l}{2n}\right)} \times \\ &\quad \begin{cases} \sum_{m=0}^{n/2-1} e^{-b_m t'} [a_m \sin(a_m t') + b_m \cos(a_m t')], & (n \text{ even}) \\ \sum_{m=0}^{(n-3)/2} e^{-b_m t'} [a_m \sin(a_m t') + b_m \cos(a_m t')] + \frac{1}{2} e^{-t'}, & (n \text{ odd}), \end{cases}\end{aligned}\quad (\text{A.81})$$

where,

$$\begin{aligned}a_m &= \cos \frac{2m+1}{2n} \pi, \\ b_m &= \sin \frac{2m+1}{2n} \pi.\end{aligned}\quad (\text{A.82})$$

Recall the equality we make for the connection between Debye random forces and general dyanmics (Eqn (A.71)), we can make the same relation under Markovian limit.

$$\frac{C^2 k_B T}{M} B_n(t) = m k_B T Z(t)\quad (\text{A.83})$$

The difference between Langevin equation and its generalized form is the memory

kernel is integrated over a long period of time ( $t \rightarrow \infty$ ) to be a constant,

$$-\int_0^t d\tau Z(t-\tau)\dot{x} \longrightarrow -\gamma\dot{x}. \quad (\text{A.84})$$

Thus, integrate both sides of Eqn (A.83) we arrive

$$\gamma_n = \frac{C^2}{Mm} \int_0^\infty B_n(t)dt \quad (\text{A.85})$$

which is the counterpart of Eqn (A.73) for the spectral density form as chosen in Eqn (A.74).

Two cases are considered for the white noise, they are harmonic potential interaction and exponential repulsive potential for the system-bath interaction. The results are shown in Fig. A.15. We see from the heat current for the harmonic chain of the diatomic system increases as internal interaction increases until it reaches a plateau which equals to the center of mass heat conduction that does not depend on the internal structure. When the relative frequency goes to zero, the current also goes to zero, which is understandable as the two atoms of the diatomic system essentially become independent and the conduction channel is closed.

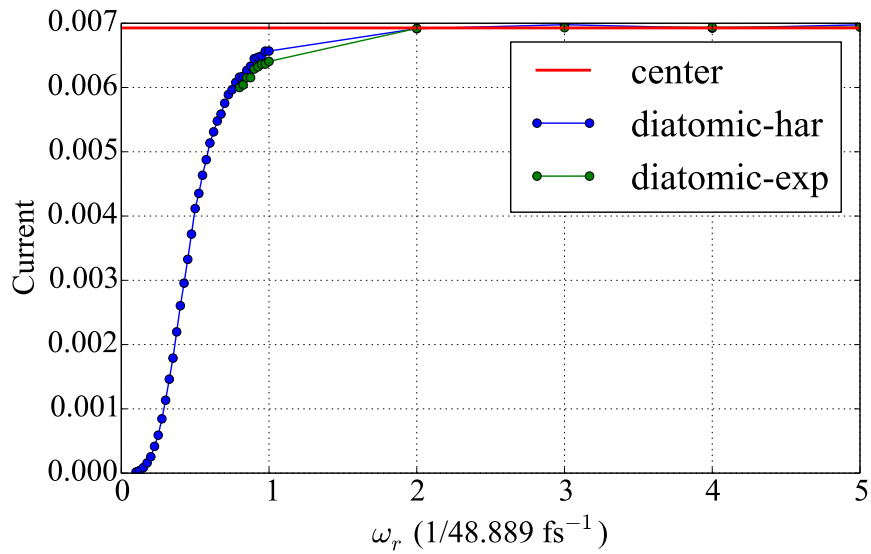


Figure A.15: Steady state heat current with regard to the change of relative interaction of diatomic molecule. the blue dot is harmonic link between system and bath, the green dot is exponential link, and the red solid line is for center of mass as a single particle of the diatomic system. The unit for the heat current is  $kcal \cdot mol^{-1} \cdot (48.889 fs)^{-1}$

## APPENDIX B

### Appendix of chapter 3

Here we provide details of computations data as supplementals to chapter 3. Though defining the microscopic concept of temperature is itself a challenging task<sup>11</sup>, it is straightforward to define such a characteristic quantity from our direct MD simulations of the molecular heat conduction. Specifically, we obtain temperature profiles for each atom in the molecules by calculating ensemble average of kinetic energies of the atoms. Figure B.2 shows a detailed temperature graph of Benzendithiols with para-, meta- and ortho- configurations. The main observation here is, regardless of the substitutions, the major temperature drops happen at the interfaces, that is the first layer of gold substrates. The center parts of the molecules, which consist of six carbons as backbones are essentially homogeneous in terms of temperature changes, which could be a sign of ballistic transport.

A simplified model is to consider a ring-bridged molecule, with only nearest-neighbour interactions<sup>193</sup>. As shown in Figure B.3, the system can be divided into four branches(the left, right, top and bottom), and the Hamiltonian is written as:

$$\mathcal{H} = \sum_{i \in n_l, n_t, n_b, n_r} \frac{1}{2} k [(u_{i+1} - u_i)^2 + (u_i - u_{i-1})^2], \quad \text{where}$$
$$\begin{aligned} -\infty &\leq n_l \leq 0 \\ 0 &\leq n_t \leq N_t \\ 0 &\leq n_b \leq N_b \\ 0 &\leq n_r \leq \infty, \end{aligned} \tag{B.1}$$

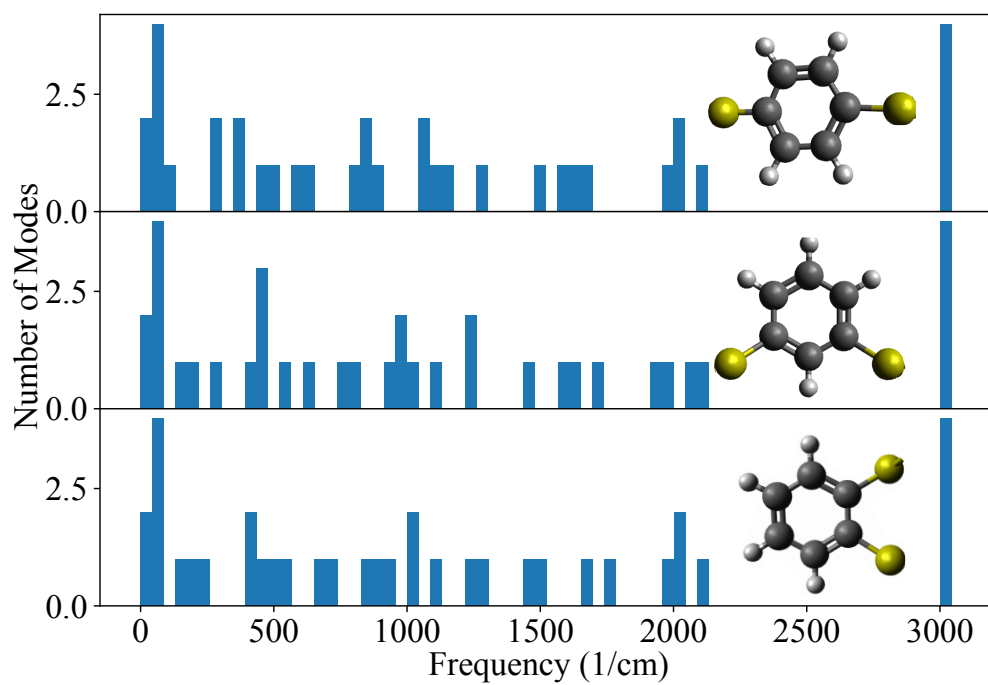


Figure B.1: Histogram of normal mode distributions of different substitutions of benzenedithiols.



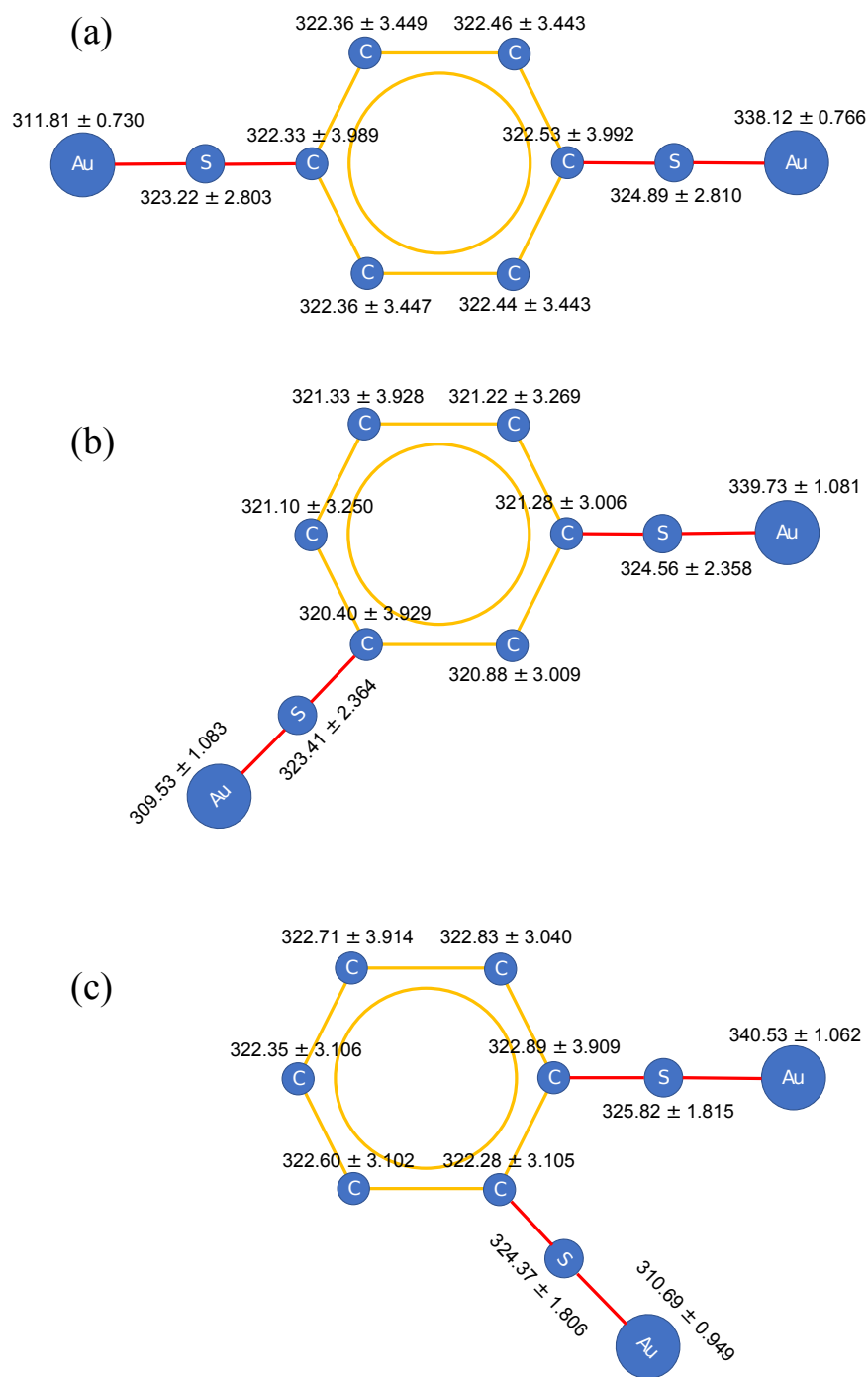


Figure B.2: Local temperature profiles of the atoms in benzenedithiol molecules with different substitution positions, measured from ensembles of kinetic energies of the atoms at steady states. The unit is in Kelvin. The temperatures of the cold and hot baths are 300K and 350K respectively. The errors represent standard error<sup>1,2</sup>.

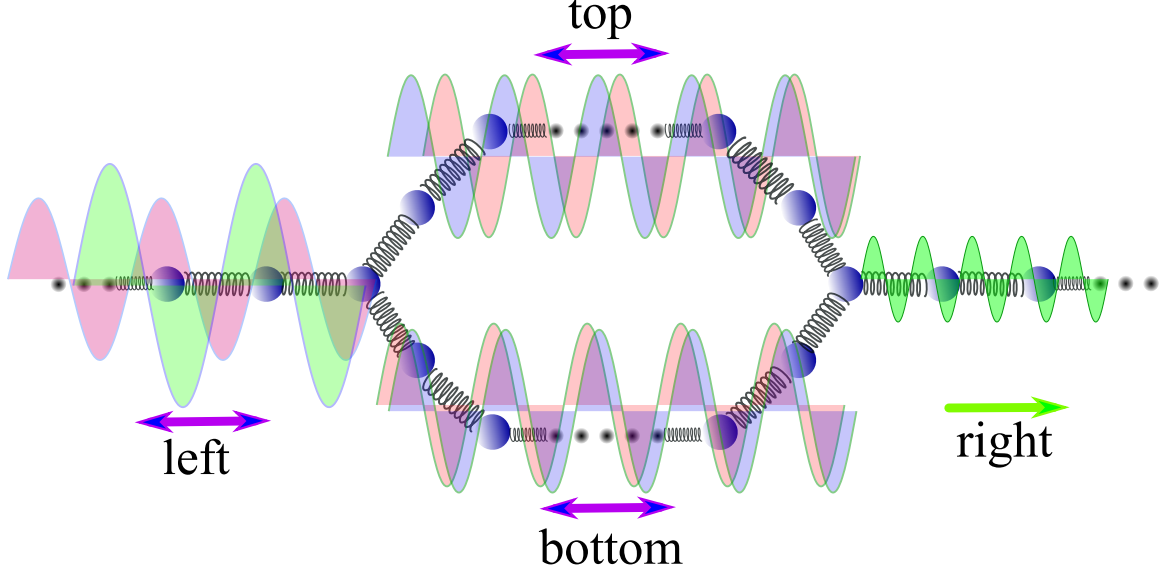


Figure B.3: Schematic graph of a ring molecule with only nearest-neighbour harmonic interactions, bridged by two linear chains. The circles are atoms in the molecule, and the dots represent the hidden numbers of atoms that are not shown. The molecule is segregated by four branches: left, top, bottom and right. The incident wave comes from the left (partly reflected), propagates (partially reflected) and leaves the system from the right.

where  $k$  is the force constant which we have made to be uniform (masses are also made the same) across the system.  $N_t$  is the number of atoms in the top branch, and  $N_b$  is the number of atoms in the bottom branch. Their relation is  $N_t + N_b = N$  which is the total number of atoms within the ring.

The solutions for the displacements have the following ansatz forms:

$$\begin{aligned}
 u_l &= (e^{i\theta n_l} + B_l e^{-i\theta n_l}) e^{-i\omega\tau}, \\
 u_t &= (A_t e^{i\theta n_t} + B_t e^{-i\theta n_t}) e^{-i\omega\tau}, \\
 u_b &= (A_b e^{i\theta n_b} + B_b e^{-i\theta n_b}) e^{-i\omega\tau}, \\
 u_r &= A_r e^{i\theta n_r} e^{-i\omega\tau},
 \end{aligned} \tag{B.2}$$

where the  $A$ 's and  $B$ 's are coefficients to be determined by boundary conditions, and

$\theta \in [0, \pi]$ . The dispersion relation gives the value for  $\omega = 2\sqrt{k/m} \sin(\theta/2)$  (which can be obtained by substituting  $u_r$  to the equation of motion). By solving the equations of motion at the junctions (i.e. when  $n_l = n_t = n_b = 0$  and  $n_t = N_t, n_b = N_b, n_r = 0$ ), the expressions for the coefficients can be found, and thus the transmission (and reflection) probabilities for the system.

The overall transmission is  $\mathcal{T} = |A_r|^2$ , where

$$A_r = \frac{(1 + e^{i\theta})(e^{i\theta N_t} + e^{i\theta N_b})(1 - e^{i\theta N})}{1 + 4e^{i\theta} + 4e^{i2\theta} - e^{i2\theta(1+N_t)} - e^{i2\theta(1+N_b)} - 2e^{i\theta N} + e^{i2\theta N} - 4e^{i\theta(N+1)} - 2e^{i\theta(N+2)}}. \quad (\text{B.3})$$

It is interesting to note the resultant transmissions do not depend on the lengths of the left and right branches, which indicates the interferences happen mainly in the ring parts of the system.

Now for our specific case of benzenes, without considering hydrogen atoms, the atomic numbers in the branches of the ring can be specified as Table B.1

Substituion	$N_t$	$N_b$	N
para-	3	3	6
meta-	4	2	6
ortho-	5	1	6

Table B.1: Table for different atom numbers in the top and bottom branches of the middle ring for benzene with different substitution positions.

Deriving from the general expressions above, we show the transmission probabilities for simplified benzene model under different substitutions (Figure B.4).

The x-axis for the transmissions is an index of wavenumber, which shows wavelength dependence of the transmission. For overall transmission (Figure B.4 the para-configuration shows smaller changes compared meta- and ortho-, both of which show deep decrease in probability at certain frequencies, where meta- has smaller magni-

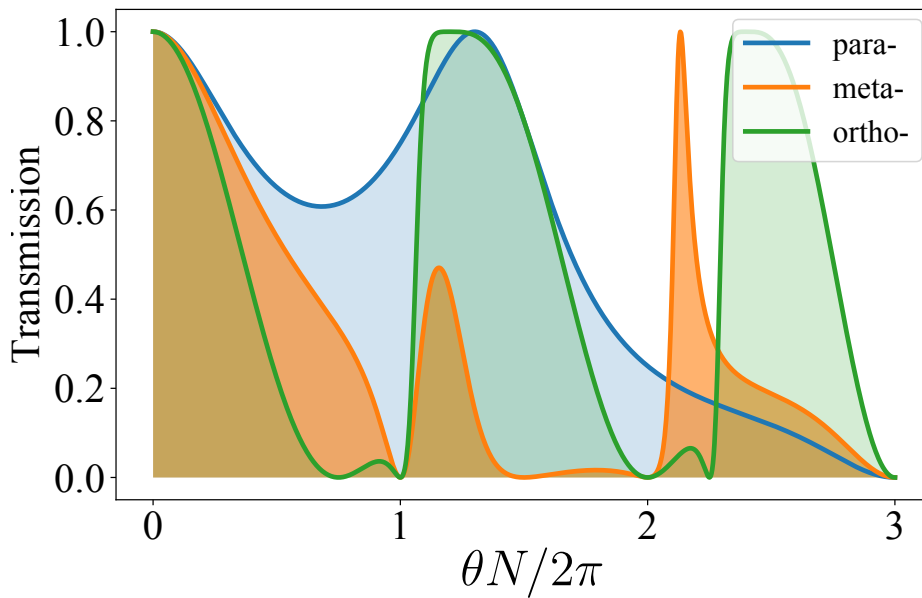


Figure B.4: Transmission probability for different substitutions of benzene-like (six atoms in the backbond) based on the harmonic ring model. (a) The overall transmission from the left side to the right side; If we define total transmission ratio over the period plot here as: The integrations of the corresponding functions divided by the square areas when the probability equals unity, we will have in the overall transmission figure (a) para: 34.8%, meta: 17.8%, ortho: 45.0%.

tudes for most range of the spectrum. This signature of destructive phonon interference explains in a simple fashion the decrease in conductance for meta-substitution in heat conduction. Therefore it is understandable, from such a simple model, phonon interference can be critical for heat conduction in ring structures like benzenedithiols.

One caveat here is that this over-simplified model only acts as an indicator to the interference effect, not to be taken as exact. For example, imagine in Figure B.4 we assume every frequency on the x-axis has the same weight on the conduction, and we simply integrate over the transmission, then we find the ortho- substitution has the highest percentage (see the description in the Caption) among three, which goes astray from our simulation results. Therefore, a elaborated calculation (e.g. Landauer or MD) to be taken among different vibrational channels, their interplay and their couplings to the bath spectra, to provide more accurate estimations.

Figure B.5 shows overall heat conductance for aromatic molecules with different ring numbers. Though Benzene(dithiol) and Naphthalene(dithiol) have similar conductance, the magnitude starts to decrease when the number increase to three (anthracene). Therefore, an initial rough conclusion might be made that increase of the ring number in the aromatic molecules may hinder the conduction overall, though only to an limited extend.

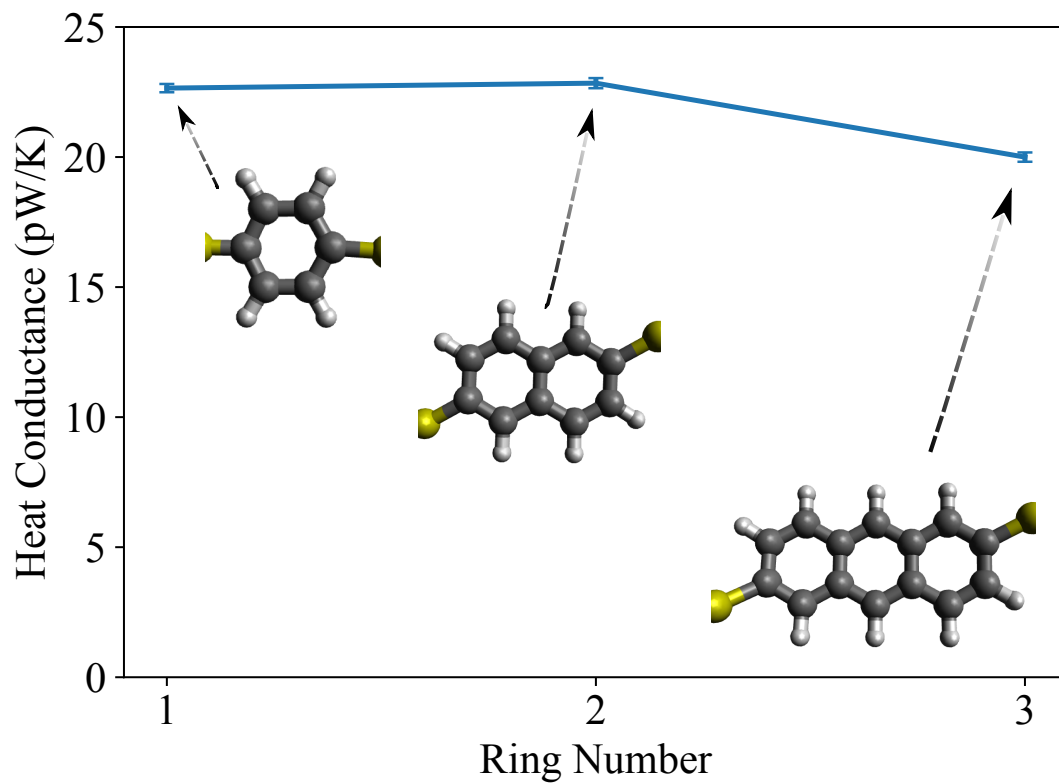


Figure B.5: Total heat conductance for Benzene-based ring molecules, that is, Benzene, Naphthalene and Anthracene. Simulation details (e.g. substrates, biases and couplings) are described in Chapter 2 and Section A.1. The error bars represent Standard Error<sup>1,2</sup>

## APPENDIX C

### Appendix of chapter 4

#### C.1 Explicit Debye bath simulation with two atomic layers

This appendix contains additional data for chapter 4. The Debye bath features shown here is specifically to the Debye bath simulation (versus mathematical filter Debye bath generator, which is detailed in Appendix A.6) using two explicit bath atoms in the main text (Chapter 4), showing characteristics of the spectrum density from the Fourier transform (Fig. C.2) of the correlation functions (Fig. C.1).

#### C.2 Anharmonic potential for the system-bath coupling in the toy model

The anharmonic interaction between the system molecule and the bath (the part represented by  $k_{01}$  in harmonic interaction sense in Fig. 4.4) is set to be Morse potential (consider 1-D case),

$$H_{pot} = D(e^{-\alpha(x-x_0)} - 1)^2, \quad (\text{C.1})$$

where  $D$  is the dissociation energy, and  $\alpha$  is the inverse of the characteristic length of the potential well. The second derivative with respect to the position is

$$\frac{\partial^2 H_{pot}}{\partial x^2} = -2\alpha^2 D e^{-\alpha(x-x_0)} (1 - 2e^{-\alpha(x-x_0)}). \quad (\text{C.2})$$

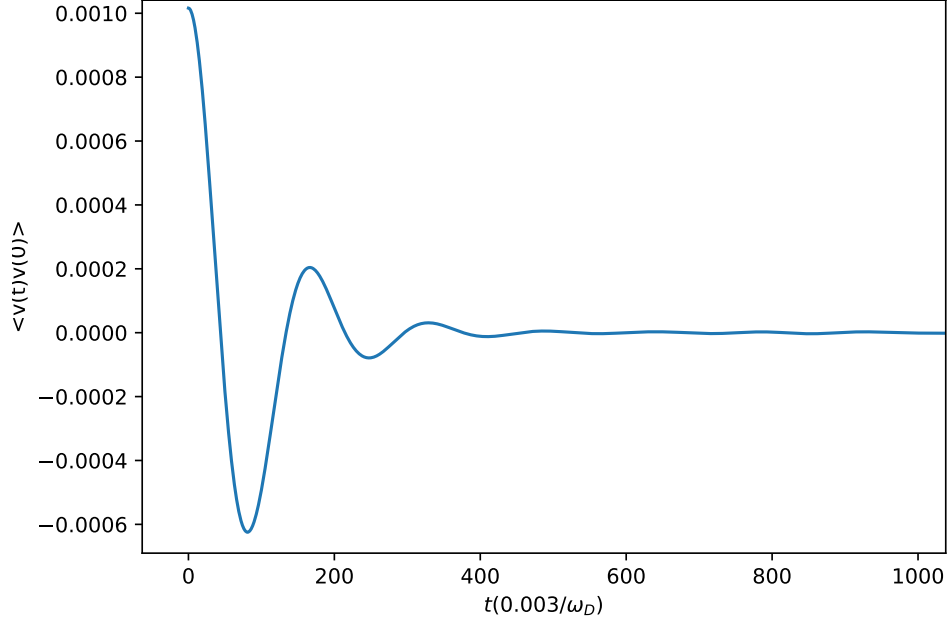


Figure C.1: velocity-velocity autocorrelation function of the atom 0 in Fig. 4.2

Taking the equilibrium position (i.e.  $x = x_0$ ), we have

$$\left. \frac{\partial^2 H_{pot}}{\partial x^2} \right|_{x=x_0} = 2\alpha^2 D. \quad (\text{C.3})$$

We might therefore define an “effective force constant” for such interaction, when the particle stays within the vicinity of the bottom of the potential surface and behave more like a harmonic oscillator.

$$k_{morse} = 2\alpha^2 D. \quad (\text{C.4})$$

In the simulations, the parameters are chosen so that  $k_{morse} = k_{01}$  (Fig. 4.4), meaning the harmonic potential is an approximation for the anharmonic potential when the displacement is small from the equilibrium.



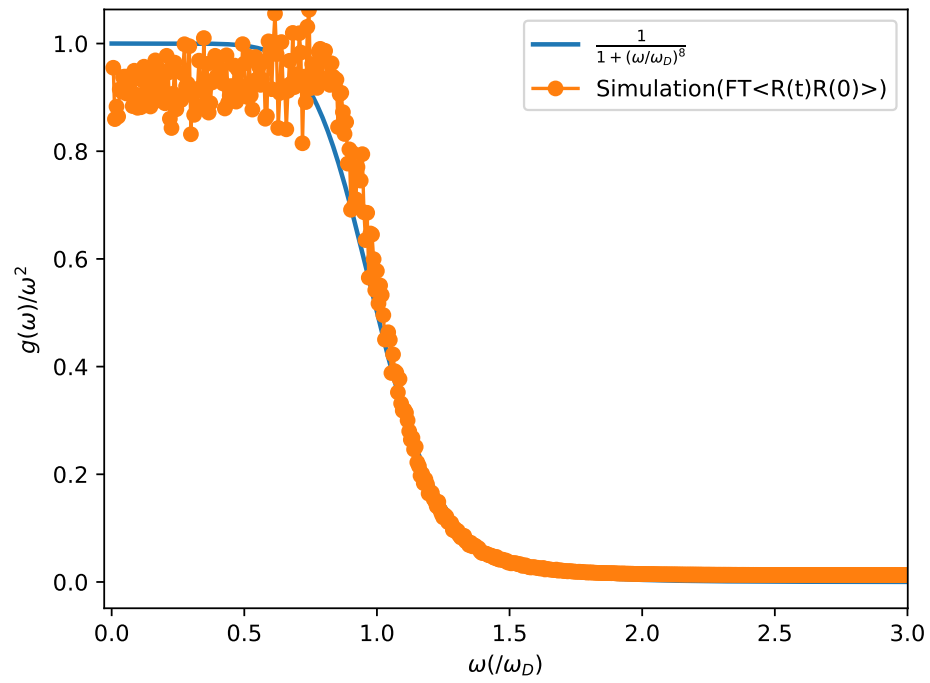


Figure C.2: Fourier transform of the position of the atom 0 in Fig. 4.2 autocorrelation function  $\langle R(t)R(0) \rangle$ . The circles are numerical implemented data points, and the solid line is analytical expression shown in the legend.

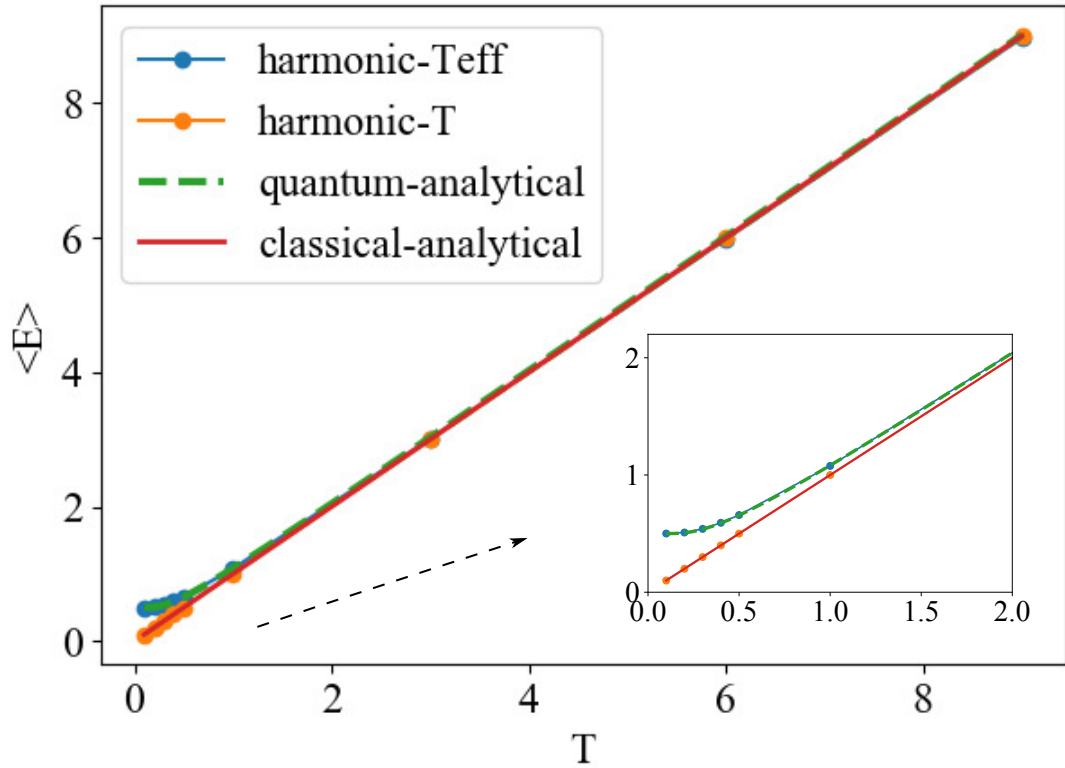


Figure C.3: Equilibrium energies of a single harmonic oscillator connected to thermal bath of different characteristic temperatures ( $T$  indicated on the x-axis). All dimensionless quantities are scale with respect to the oscillating frequency ( $\omega$ ) of the particle. Specifically, the unit for  $T$  is  $\hbar\omega/k_B$ , and the energy unit is  $\hbar\omega$ . The insert is a zoom-in of the full figure to the  $T$  range of 0 to 2.

### C.3 Dimensionless units

All the dimensionless variables are defined as follows in terms of harmonic oscillator frequency:

$$\begin{aligned}\bar{x} &= \frac{x}{\sqrt{\frac{\hbar}{m\omega}}} \\ \bar{v} &= \frac{v}{\sqrt{\frac{\hbar\omega}{m}}} \\ \bar{\omega}_n &= \frac{\omega_n}{\omega} \\ \bar{t} &= \omega t \\ \bar{\gamma} &= \frac{\gamma}{\omega} \\ \bar{T} &= \frac{\hbar\omega}{k_B T} \\ \bar{T}_{eff}^{(n)} &= \frac{\bar{\omega}_n}{e^{\bar{\omega}_n/\bar{T}} - 1} \\ \bar{D} &= \frac{D}{\hbar\omega} \\ \bar{\alpha} &= \alpha \sqrt{\frac{\hbar}{m\omega}}\end{aligned}\tag{C.5}$$

## BIBLIOGRAPHY

- (1) Standard error (SE) is defined as the Standard Deviation (SD) / square root of the sample size, is a statistical uncertainty indicator of the estimated mean value of the conducted measurements.
- (2) Altman, D. G.; Bland, J. M. Standard deviations and standard errors. *BMJ (Clinical research ed.)* **2005**, *331*, 903.
- (3) Chen, R.; Sharony, I.; Nitzan, A. Local Atomic Heat Currents and Classical Interference in Single-Molecule Heat Conduction. *J. Phys. Chem. Lett.* **2020**, *11*, 4261–4268.
- (4) Sharony, I.; Chen, R.; Nitzan, A. Stochastic simulation of nonequilibrium heat conduction in extended molecular junctions. *J. Chem. Phys.* **2020**, *153*, 144113.
- (5) Pop, E. Energy dissipation and transport in nanoscale devices. *Nano Res.* **2010**, *3*, 147–169.
- (6) Segal, D.; Agarwalla, B. K. Vibrational Heat Transport in Molecular Junctions. *Annu. Rev. Phys. Chem.* **2016**, *67*, 185–209.
- (7) Li, N.; Ren, J.; Wang, L.; Zhang, G.; Hänggi, P.; Li, B. *Colloquium* : Phononics: Manipulating heat flow with electronic analogs and beyond. *Rev. Mod. Phys.* **2012**, *84*, 1045–1066.
- (8) Cahill, D. G.; Ford, W. K.; Goodson, K. E.; Mahan, G. D.; Majumdar, A.; Maris, H. J.; Merlin, R.; Phillpot, S. R. Nanoscale thermal transport. *J. Appl. Phys.* **2003**, *93*, 793–818.

- (9) Cahill, D. G.; Braun, P. V.; Chen, G.; Clarke, D. R.; Fan, S.; Goodson, K. E.; Keblinski, P.; King, W. P.; Mahan, G. D.; Majumdar, A.; Maris, H. J.; Phillpot, S. R.; Pop, E.; Shi, L. Nanoscale thermal transport. II. 2003–2012. *Appl. Phys. Rev.* **2014**, *1*, 011305.
- (10) Leitner, D. M. Quantum ergodicity and energy flow in molecules. *Adv. Phys.* **2015**, *64*, 445–517.
- (11) Dubi, Y.; Di Ventra, M. *Colloquium* : Heat flow and thermoelectricity in atomic and molecular junctions. *Rev. Mod. Phys.* **2011**, *83*, 131–155.
- (12) Li, N.; Ren, J.; Wang, L.; Zhang, G.; Hänggi, P.; Li, B. *Colloquium* : Phononics: Manipulating heat flow with electronic analogs and beyond. *Rev. Mod. Phys.* **2012**, *84*, 1045–1066.
- (13) Rubtsova, N. I.; Rubtsov, I. V. Vibrational Energy Transport in Molecules Studied by Relaxation-Assisted Two-Dimensional Infrared Spectroscopy. *Annu. Rev. Phys. Chem.* **2015**, *66*, 717–738.
- (14) Cui, L.; Miao, R.; Jiang, C.; Meyhofer, E.; Reddy, P. Perspective: Thermal and thermoelectric transport in molecular junctions. *J. Chem. Phys.* **2017**, *146*, 092201.
- (15) Rubtsov, I. V.; Burin, A. L. Ballistic and diffusive vibrational energy transport in molecules. *J. Chem. Phys.* **2019**, *150*, 020901.
- (16) Cui, L.; Hur, S.; Akbar, Z. A.; Klöckner, J. C.; Jeong, W.; Pauly, F.; Jang, S.-Y.; Reddy, P.; Meyhofer, E. Thermal conductance of single-molecule junctions. *Nature* **2019**, *572*, 628–633.

- (17) Rieder, Z.; Lebowitz, J. L.; Lieb, E. Properties of a Harmonic Crystal in a Stationary Nonequilibrium State. *J. Chem. Phys.* **1967**, *8*, 1073–1078.
- (18) Cui, L.; Jeong, W.; Hur, S.; Matt, M.; Klöckner, J. C.; Pauly, F.; Nielaba, P.; Cuevas, J. C.; Meyhofer, E.; Reddy, P. Quantized thermal transport in single-atom junctions. *Science* **2017**,
- (19) Craven, G. T.; Nitzan, A. Electron transfer across a thermal gradient. *Proc. Natl. Acad. Sci.* **2016**, *113*, 9421–9429.
- (20) Craven, G. T.; Nitzan, A. Electrothermal Transistor Effect and Cyclic Electronic Currents in Multithermal Charge Transfer Networks. *Phys. Rev. Lett.* **2017**, *118*, 207201.
- (21) Craven, G. T.; Nitzan, A. Electron transfer at thermally heterogeneous molecule-metal interfaces. *J. Chem. Phys.* **2017**, *146*, 092305.
- (22) Schelling, P. K.; Phillpot, S. R.; Keblinski, P. Comparison of atomic-level simulation methods for computing thermal conductivity. *Physical Review B - Condensed Matter and Materials Physics* **2002**, *65*, 1–12.
- (23) Sellan, D. P.; Landry, E. S.; Turney, J. E.; McGaughey, A. J. H.; Amon, C. H. Size effects in molecular dynamics thermal conductivity predictions. *Phys. Rev. B* **2010**, *81*, 1–10.
- (24) McGaughey, A.; Kaviani, M. Thermal conductivity decomposition and analysis using molecular dynamics simulations. Part I. Lennard-Jones argon. *Int. J. Heat Mass Transf.* **2004**, *47*, 1783 – 1798.
- (25) McGaughey, A.; Kaviani, M. Thermal conductivity decomposition and analysis

- using molecular dynamics simulations: Part II. Complex silica structures. *Int. J. Heat Mass Transf.* **2004**, *47*, 1799 – 1816.
- (26) Chen, L.; Kumar, S. Thermal transport in graphene supported on copper. *J. Appl. Phys.* **2012**, *112*, 043502.
- (27) Zhang, M.; Lussetti, E.; de Souza, L. E. S.; Müller-Plathe, F. Thermal Conductivities of Molecular Liquids by Reverse Nonequilibrium Molecular Dynamics. *J. Phys. Chem. B* **2005**, *109*, 15060–15067.
- (28) Tang, S.; Kulkarni, Y. The interplay between strain and size effects on the thermal conductance of grain boundaries in graphene. *Appl. Phys. Lett.* **2013**, *103*, 213113.
- (29) Dong, H.; Wen, B.; Melnik, R. Relative importance of grain boundaries and size effects in thermal conductivity of nanocrystalline materials. *Sci. Rep.* **2014**, *4*, 7037.
- (30) Majumdar, S.; Malen, J. A.; McGaughey, A. J. H. Cooperative Molecular Behavior Enhances the Thermal Conductance of Binary Self-Assembled Monolayer Junctions. *Nano Letters* **2017**, *17*, 220–227.
- (31) Nguyen, P. H.; Park, S.-M.; Stock, G. Nonequilibrium molecular dynamics simulation of the energy transport through a peptide helix. *J. Chem. Phys.* **2010**, *132*, 025102.
- (32) Hung, S.-W.; Kikugawa, G.; Shiomi, J. Mechanism of Temperature Dependent Thermal Transport across the Interface between Self-Assembled Monolayer and Water. *J. Phys. Chem. C* **2016**, *120*, 26678–26685.

- (33) Segal, D.; Nitzan, A.; Hänggi, P. Thermal conductance through molecular wires. *J. Chem. Phys.* **2003**, *119*, 6840–6855.
- (34) Klöckner, J. C.; Bürkle, M.; Cuevas, J. C.; Pauly, F. Length dependence of the thermal conductance of alkane-based single-molecule junctions: An *ab initio* study. *Phys. Rev. B* **2016**, *94*, 205425–1–8.
- (35) Klöckner, J. C.; Cuevas, J. C.; Pauly, F. Tuning the thermal conductance of molecular junctions with interference effects. *Phys. Rev. B* **2017**, *96*, 205425–1–10.
- (36) Klöckner, J. C.; Cuevas, J. C.; Pauly, F. Transmission eigenchannels for coherent phonon transport. *Phys. Rev. B* **2018**, *97*, 155432.
- (37) Chen, R.; Craven, G. T.; Nitzan, A. Electron-transfer-induced and phononic heat transport in molecular environments. *The Journal of Chemical Physics* **2017**, *147*, 124101.
- (38) Marcus, R. A. On the Theory of Electron-Transfer Reactions. VI. Unified Treatment for Homogeneous and Electrode Reactions. *J. Chem. Phys.* **1965**, *43*, 679–701.
- (39) Richardson, J. O.; Thoss, M. Non-oscillatory flux correlation functions for efficient nonadiabatic rate theory. *J. Chem. Phys.* **2014**, *141*, 074106.
- (40) Nitzan, A. *Chemical Dynamics in Condensed Phases: Relaxation, Transfer and Reactions in Condensed Molecular Systems*; Oxford University Press, 2006.
- (41) Craven, G. T.; He, D.; Nitzan, A. Electron-Transfer-Induced Thermal and Thermoelectric Rectification. *Phys. Rev. Lett.* **2018**, *121*, 247704.



- (42) Craven, G. T.; Nitzan, A. Wiedemann–Franz Law for Molecular Hopping Transport. *Nano Lett.* **2020**, *20*, 989–993.
- (43) Leitner, D. M. Quantum ergodicity and energy flow in molecules. *Adv. Phys.* **2015**, *64*, 445–517.
- (44) Schwarzer, D.; Kutne, P.; Schröder, C.; Troe, J. Intramolecular vibrational energy redistribution in bridged azulene-anthracene compounds: Ballistic energy transport through molecular chains. *J. Chem. Phys.* **2004**, *121*, 1754–1764.
- (45) Rubtsova, N. I.; Qasim, L. N.; Kurnosov, A. A.; Burin, A. L.; Rubtsov, I. V. Ballistic Energy Transport in Oligomers. *Acc. Chem. Res.* **2015**, *48*, 2547–2555.
- (46) Wang, Z.; Carter, J. A.; Lagutchev, A.; Koh, Y. K.; Seong, N.-H.; Cahill, D. G.; Dlott, D. D. Ultrafast Flash Thermal Conductance of Molecular Chains. *Science* **2007**, *317*, 787–790.
- (47) Carter, J. A.; Wang, Z.; ; Dlott, D. D. Spatially Resolved Vibrational Energy Transfer in Molecular Monolayers. *J. Phys. Chem. A* **2008**, *112*, 3523–3529.
- (48) Wang, Z.; Cahill, D. G.; Carter, J. A.; Koh, Y. K.; Lagutchev, A.; Seong, N.-H.; Dlott, D. D. Ultrafast dynamics of heat flow across molecules. *Chem. Phys.* **2008**, *350*, 31 – 44, Femtochemistry and Femtobiology.
- (49) Berg, C. M.; Sun, Y.; Dlott, D. D. Temperature-Dependent Dynamic Response to Flash Heating of Molecular Monolayers on Metal Surfaces: Vibrational Energy Exchange. *J. Phys. Chem. B* **2014**, *118*, 7770–7776.
- (50) Wang, R. Y.; Segalman, R. A.; Majumdar, A. Room temperature thermal conductance of alkanedithiol self-assembled monolayers. *Appl. Phys. Lett.* **2006**, *89*, 173113.

- (51) Meier, T.; Menges, F.; Nirmalraj, P.; Hölscher, H.; Riel, H.; Gotsmann, B. Length-Dependent Thermal Transport along Molecular Chains. *Phys. Rev. Lett.* **2014**, *113*, 060801.
- (52) Gaskins, J. T.; Bulusu, A.; Giordano, A. J.; Duda, J. C.; Graham, S.; Hopkins, P. E. Thermal Conductance across Phosphonic Acid Molecules and Interfaces: Ballistic versus Diffusive Vibrational Transport in Molecular Monolayers. *J. Phys. Chem. C* **2015**, *119*, 20931–20939.
- (53) Mosso, N.; Sadeghi, H.; Gemma, A.; Sangtarash, S.; Drechsler, U.; Lambert, C.; Gotsmann, B. Thermal Transport through Single-Molecule Junctions. *Nano Lett.* **0**, *0*, null, PMID: 31560850.
- (54) Benenti, G.; Casati, G.; Saito, K.; Whitney, R. Fundamental aspects of steady-state conversion of heat to work at the nanoscale. *Phys. Rep.* **2017**, *694*, 1 – 124.
- (55) Kobus, M.; Nguyen, P. H.; Stock, G. Coherent vibrational energy transfer along a peptide helix. *J. Chem. Phys.* **2011**, *134*, 124518.
- (56) Manikandan, P.; Carter, J. A.; Dlott, D. D.; Hase, W. L. Effect of Carbon Chain Length on the Dynamics of Heat Transfer at a Gold/Hydrocarbon Interface: Comparison of Simulation with Experiment. *J. Phys. Chem. C* **2011**, *115*, 9622–9628.
- (57) Kikugawa, G.; Ohara, T.; Kawaguchi, T.; Kinefuchi, I.; Matsumoto, Y. A molecular dynamics study on heat conduction characteristics inside the alkanethiolate SAM and alkane liquid. *Int. J. Heat Mass Transf.* **2014**, *78*, 630 – 635.

- (58) Polanco, C. A.; Rastgarkafshgarkolaei, R.; Zhang, J.; Le, N. Q.; Norris, P. M.; Ghosh, A. W. Design rules for interfacial thermal conductance: Building better bridges. *Phys. Rev. B* **2017**, *95*, 195303.
- (59) Leitner, D. M.; Pandey, H. D. Asymmetric energy flow in liquid alkylbenzenes: A computational study. *J. Chem. Phys.* **2015**, *143*, 144301.
- (60) Pandey, H. D.; Leitner, D. M. Influence of thermalization on thermal conduction through molecular junctions: Computational study of PEG oligomers. *J. Chem. Phys.* **2017**, *147*, 084701.
- (61) Schade, M.; Hamm, P. Vibrational energy transport in the presence of intrasite vibrational energy redistribution. *J. Chem. Phys.* **2009**, *131*, 044511.
- (62) Ness, H.; Stella, L.; Lorenz, C. D.; Kantorovich, L. Nonequilibrium generalised Langevin equation for the calculation of heat transport properties in model 1D atomic chains coupled to two 3D thermal baths. *J. Chem. Phys.* **2017**, *146*, 164103.
- (63) Pandey, H. D.; Leitner, D. M. Vibrational energy transport in molecules and the statistical properties of vibrational modes. *Chem. Phys.* **2017**, *482*, 81 – 85, Electrons and nuclei in motion - correlation and dynamics in molecules (on the occasion of the 70th birthday of Lorenz S. Cederbaum).
- (64) Ladd, A. J. C.; Moran, B.; Hoover, W. G. Lattice thermal conductivity: A comparison of molecular dynamics and anharmonic lattice dynamics. *Phys. Rev. B* **1986**, *34*, 5058–5064.
- (65) Volz, S. G.; Chen, G. Molecular-dynamics simulation of thermal conductivity of silicon crystals. *Phys. Rev. B* **2000**, *61*, 2651–2656.

- (66) Che, J.; Çağın, T.; Deng, W.; Goddard, W. A. Thermal conductivity of diamond and related materials from molecular dynamics simulations. *J. Chem. Phys.* **2000**, *113*, 6888–6900.
- (67) Berber, S.; Kwon, Y.-k.; Tománek, D. Unusually high thermal conductivity of carbon nanotubes. *Phys. Rev. Lett.* **2000**, *84*, 4613–4616.
- (68) Jund, P.; Jullien, R. Molecular-dynamics calculation of the thermal conductivity of vitreous silica. *Phys. Rev. B* **1999**, *59*, 13707–13711.
- (69) Si, C.; Wang, X.-D.; Fan, Z.; Feng, Z.-H.; Cao, B.-Y. Impacts of potential models on calculating the thermal conductivity of graphene using non-equilibrium molecular dynamics simulations. *Int. J. Heat Mass Transf.* **2017**, *107*, 450 – 460.
- (70) Müller-Plathe, F.; Reith, D. Cause and effect reversed in non-equilibrium molecular dynamics: An easy route to transport coefficients. *Computational and Theoretical Polymer Science* **1999**, *9*, 203–209.
- (71) Müller-Plathe, F. A simple nonequilibrium molecular dynamics method for calculating the thermal conductivity. *J. Chem. Phys.* **1997**, *106*, 6082–6085.
- (72) Bagri, A.; Kim, S. P.; Ruoff, R. S.; Shenoy, V. B. Thermal transport across twin grain boundaries in polycrystalline graphene from nonequilibrium molecular dynamics simulations. *Nano Letters* **2011**, *11*, 3917–3921.
- (73) Shugard, M.; Tully, J. C.; Nitzan, A. Stochastic classical trajectory approach to relaxation phenomena. I. Vibrational relaxation of impurity molecules in solid matrices. *J. Chem. Phys.* **1978**, *69*, 336–345.

- (74) Nitzan, A.; Tully, J. C. Stochastic classical trajectory approach to relaxation phenomena. III. Comparison of trajectory results to quantum mechanical perturbation theory. *J. Chem. Phys.* **1983**, *78*, 3959–3963.
- (75) Zhou, Y.; Segal, D. Interface effects in thermal conduction through molecular junctions: Numerical simulations. *J. Chem. Phys.* **2010**, *133*, 094101.
- (76) Nitzan, A.; Shugard, M.; Tully, J. C. Stochastic classical trajectory approach to relaxation phenomena. II. Vibrational relaxation of impurity molecules in Debye solids. *J. Chem. Phys.* **1978**, *69*, 2525–2535.
- (77) Allen, P. B.; Kelner, J. Evolution of a vibrational wave packet on a disordered chain. *Am. J. Phys.* **1998**, *66*, 497–506.
- (78) Majumdar, S.; Sierra-Suarez, J. A.; Schiffres, S. N.; Ong, W.-L.; Higgs, C. F.; McGaughey, A. J. H.; Malen, J. A. Vibrational Mismatch of Metal Leads Controls Thermal Conductance of Self-Assembled Monolayer Junctions. *Nano Letters* **2015**, *15*, 2985–2991.
- (79) Crljen, Ž.; Baranović, G. Unusual conductance of polyynes-based molecular wires. *Phys. Rev. Lett.* **2007**, *98*, 1–4.
- (80) Garner, M. H.; Bro-Jørgensen, W.; Pedersen, P. D.; Solomon, G. C. Reverse Bond-Length Alternation in Cumulenes: Candidates for Increasing Electronic Transmission with Length. *J. Phys. Chem. C* **2018**, acs.jpcc.8b05661.
- (81) Rappe, A. K.; Casewit, C. J.; Colwell, K. S.; Goddard, W. A.; Skiff, W. M. UFF, a full periodic table force field for molecular mechanics and molecular dynamics simulations. *Journal of the American Chemical Society* **1992**, *114*, 10024–10035.

- (82) Inon Sharony, Renai Chen, Abraham Nitzan, "Heat Conduction in Molecular Junctions" software package, <https://bitbucket.org/heat-conduction-molecular-junctions/workspace/projects/HCMJ>, 2020.
- (83) Goga, N.; Rzepiela, A. J.; de Vries, A. H.; Marrink, S. J.; Berendsen, H. J. C. Efficient Algorithms for Langevin and DPD Dynamics. *J. Chem. Theory Comput.* **2012**, *8*, 3637–3649.
- (84) O’Boyle, N. M.; Banck, M.; James, C. A.; Morley, C.; Vandermeersch, T.; Hutchison, G. R. Open Babel: An open chemical toolbox. *J. Cheminformatics* **2011**, *3*, 33.
- (85) Hanwell, M. D.; Curtis, D. E.; Lonie, D. C.; Vandermeersch, T.; Zurek, E.; Hutchison, G. R. Avogadro: an advanced semantic chemical editor, visualization, and analysis platform. *Journal of Cheminformatics* **2012**, *4*, 17.
- (86) Torii, D.; Nakano, T.; Ohara, T. Contribution of inter- and intramolecular energy transfers to heat conduction in liquids. *J. Chem. Phys.* **2008**, *128*.
- (87) Dhar, A.; Roy, D. Heat Transport in Harmonic Lattices. *J. Stat. Phys.* **2006**, *125*, 801–820.
- (88) Dhar, A. Heat transport in low-dimensional systems. *Adv. Phys.* **2008**, *57*, 457–537.
- (89) Wang, J.-S.; Wang, J.; Zeng, N. Nonequilibrium Green’s function approach to mesoscopic thermal transport. *Phys. Rev. B* **2006**, *74*, 033408.
- (90) Yamamoto, T.; Watanabe, K. Nonequilibrium Green’s Function Approach to Phonon Transport in Defective Carbon Nanotubes. *Phys. Rev. Lett.* **2006**, *96*, 255503.

- (91) Meir, Y.; Wingreen, N. S. Landauer formula for the current through an interacting electron region. *Phys. Rev. Lett.* **1992**, *68*, 2512–2515.
- (92) More generally, we may consider  $K_{ij}(t) = \sum_k C_{Lk}^{(i)} C_{kR}^{(j)} \frac{1}{\omega_k} \sin[\omega_k t]$  that connect between motion in the i direction at one end and j direction at the other.
- (93) Roy, D. Crossover from ballistic to diffusive thermal transport in quantum Langevin dynamics study of a harmonic chain connected to self-consistent reservoirs. *Phys. Rev. E* **2008**, *77*, 062102–3.
- (94) Luckyanova, M. N. et al. Phonon localization in heat conduction. *Sci. Adv.* **2018**, *4*.
- (95) Qasim, L. N.; Atuk, E. B.; Maksymov, A. O.; Jayawickramarajah, J.; Burin, A. L.; Rubtsov, I. V. Ballistic Transport of Vibrational Energy through an Amide Group Bridging Alkyl Chains. *J. Phys. Chem. C* **2019**, *123*, 3381–3392.
- (96) Dhar, A. Heat conduction in the disordered harmonic chain revisited. *Phys. Rev. Lett.* **2001**, *86*, 5882–5885.
- (97) Dhar, A.; Lebowitz, J. L. Effect of phonon-phonon interactions on localization. *Phys. Rev. Lett.* **2008**, *100*, 134301–4.
- (98) Zhai, J.; Zhang, Q.; Cheng, Z.; Ren, J.; Ke, Y.; Li, B. Anomalous transparency induced by cooperative disorders in phonon transport. *Phys. Rev. B* **2019**, *99*, 195429.
- (99) Casher, A.; Lebowitz, J. L. Heat Flow in Regular and Disordered Harmonic Chains. *J. Math. Phys.* **1971**, *12*, 1701–1711.

- (100) Rubin, R. J.; Greer, W. L. Abnormal lattice thermal conductivity of a one-dimensional, harmonic, isotopically disordered crystal. *J. Math. Phys.* **1971**, *12*, 1686–1701.
- (101) Matsuda, H.; Ishii, K. Localization of Normal Modes and Energy Transport in the Disordered Harmonic Chain. *Prog. Theor. Phys. Suppl.* **1970**, *45*, 56–86.
- (102) Hansen, T.; Solomon, G. C. When Conductance Is Less than the Sum of Its Parts: Exploring Interference in Multiconnected Molecules. *J. Phys. Chem. C* **2016**, *120*, 6295–6301.
- (103) Hansen, T.; Solomon, G. C.; Andrews, D. Q.; Ratner, M. A. Interfering pathways in benzene: An analytical treatment. *J. Chem. Phys.* **2009**, *131*.
- (104) Solomon, G. C.; Andrews, D. Q.; Duyne, R. P. V.; Ratner, M. A. When Things Are Not as They Seem: Quantum Interference Turns Molecular Electron Transfer “Rules” Upside Down. *J. Am. Chem. Soc.* **2008**, *130*, 7788–7789.
- (105) Solomon, G. C.; Andrews, D. Q.; Hansen, T.; Goldsmith, R. H.; Wasielewski, M. R.; Van Duyne, R. P.; Ratner, M. A. Understanding quantum interference in coherent molecular conduction. *J. Chem. Phys.* **2008**, *129*, 054701.
- (106) Solomon, G. C.; Herrmann, C.; Hansen, T.; Mujica, V.; Ratner, M. A. Exploring local currents in molecular junctions. *Nature Chem.* **2010**, *2*, 223–228.
- (107) Garner, M. H.; Li, H.; Chen, Y.; Su, T. A.; Shanguan, Z.; Paley, D. W.; Liu, T.; Ng, F.; Li, H.; Xiao, S.; Nuckolls, C.; Venkataraman, L.; Solomon, G. C. Comprehensive suppression of single-molecule conductance using destructive  $\sigma$ -interference. *Nature* **2018**, *558*, 416–419.



- (108) Garner, M. H.; Solomon, G. C.; Strange, M. Tuning conductance in aromatic molecules: Constructive and counteractive substituent effects. *J. Phys. Chem. C* **2016**, *120*, 9097–9103.
- (109) Manrique, D. Z.; Huang, C.; Baghernejad, M.; Zhao, X.; Al-Owaedi, O. A.; Sadeghi, H.; Kaliginedi, V.; Hong, W.; Gulcur, M.; Wandlowski, T.; Bryce, M. R.; Lambert, C. J. A quantum circuit rule for interference effects in single-molecule electrical junctions. *Nature Communications* **2015**, *6*, 6389.
- (110) Markussen, T.; Stadler, R.; Thygesen, K. S. The relation between structure and quantum interference in single molecule junctions. *Nano Lett.* **2010**, *10*, 4260–4265.
- (111) Medrano Sandonas, L.; Rodríguez Méndez, Á.; Gutierrez, R.; Ugalde, J. M.; Mujica, V.; Cuniberti, G. Selective Transmission of Phonons in Molecular Junctions with Nanoscopic Thermal Baths. *J. Phys. Chem. C* **2019**, *123*, 9680–9687.
- (112) Hu, S.; Zhang, Z.; Jiang, P.; Chen, J.; Volz, S.; Nomura, M.; Li, B. Randomness-Induced Phonon Localization in Graphene Heat Conduction. *J. Phys. Chem. Lett.* **2018**, *9*, 3959–3968.
- (113) VanGessel, F.; Peng, J.; Chung, P. W. A review of computational phononics: the bulk, interfaces, and surfaces. *J. Mater. Sci.* **2018**, *53*, 5641–5683.
- (114) Moghaddasi Fereidani, R.; Segal, D. Phononic heat transport in molecular junctions: Quantum effects and vibrational mismatch. *J. Chem. Phys.* **2019**, *150*, 024105.
- (115) Li, Q.; Strange, M.; Duchemin, I.; Donadio, D.; Solomon, G. C. A strategy to

- Suppress Phonon Transport in Molecular Junctions Using  $\pi$ -Stacked System. *J. Phys. Chem. C* **2017**, *121*, 7175–7182.
- (116) Markussen, T. Phonon interference effects in molecular junctions. *J. Chem. Phys.* **2013**, *139*, 244101.
- (117) Pronk, S.; Páll, S.; Schulz, R.; Larsson, P.; Bjelkmar, P.; Apostolov, R.; Shirts, M. R.; Smith, J. C.; Kasson, P. M.; van der Spoel, D.; Hess, B.; Lindahl, E. GROMACS 4.5: a high-throughput and highly parallel open source molecular simulation toolkit. *Bioinformatics* **2013**, *29*, 845–854.
- (118) YALIRAKI, S. N.; RATNER, M. A. Interplay of Topology and Chemical Stability on the Electronic Transport of Molecular Junctions. *Ann. N.Y. Acad. Sci.* **2002**, *960*, 153–162.
- (119) Rai, D.; Hod, O.; Nitzan, A. Circular Currents in Molecular Wires. *J. Phys. Chem. C* **2010**, *114*, 20583–20594.
- (120) Kalantar, N.; Agarwalla, B. K.; Segal, D. Harmonic chains and the thermal diode effect. *Phys. Rev. E* **2021**, *103*, 052130.
- (121) Dahl, J. P.; Springborg, M. The Morse oscillator in position space, momentum space, and phase space. *J. Chem. Phys.* **1988**, *88*, 4535–4547.
- (122) Reddy, P.; Jang, S.-Y.; Segalman, R. A.; Majumdar, A. Thermoelectricity in Molecular Junctions. *Science* **2007**, *315*, 1568–1571.
- (123) Walczak, K. Thermoelectric properties of vibrating molecule asymmetrically connected to the electrodes. *Physica B* **2007**, *392*, 173 – 179.

- (124) Malen, J. A.; Doak, P.; Baheti, K.; Tilley, T. D.; Majumdar, A.; Segalman, R. A. The Nature of Transport Variations in Molecular Heterojunction Electronics. *Nano Lett.* **2009**, *9*, 3406–3412.
- (125) Malen, J. A.; Yee, S. K.; Majumdar, A.; Segalman, R. A. Fundamentals of energy transport, energy conversion, and thermal properties in organic-inorganic heterojunctions. *Chem. Phys. Lett.* **2010**, *491*, 109–122.
- (126) Tan, A.; Balachandran, J.; Sadat, S.; Gavini, V.; Dunietz, B. D.; Jang, S.-Y.; Reddy, P. Effect of Length and Contact Chemistry on the Electronic Structure and Thermoelectric Properties of Molecular Junctions. *J. Am. Chem. Soc.* **2011**, *133*, 8838–8841.
- (127) Ren, J.; Zhu, J.-X.; Gubernatis, J. E.; Wang, C.; Li, B. Thermoelectric transport with electron-phonon coupling and electron-electron interaction in molecular junctions. *Phys. Rev. B* **2012**, *85*, 155443.
- (128) Kim, Y.; Jeong, W.; Kim, K.; Lee, W.; Reddy, P. Electrostatic control of thermoelectricity in molecular junctions. *Nature Nanotech.* **2014**, *9*, 881–885.
- (129) Koch, T.; Loos, J.; Fehske, H. Thermoelectric effects in molecular quantum dots with contacts. *Phys. Rev. B* **2014**, *89*, 155133.
- (130) Perroni, C. A.; Ninno, D.; Cataudella, V. Electron-vibration effects on the thermoelectric efficiency of molecular junctions. *Phys. Rev. B* **2014**, *90*, 125421.
- (131) Zimbovskaya, N. A. The effect of dephasing on the thermoelectric efficiency of molecular junctions. *J. Phys.: Condens. Matter* **2014**, *26*, 275303.
- (132) Marcus, R. A. On the Theory of Oxidation-Reduction Reactions Involving Electron Transfer. I. *J. Chem. Phys.* **1956**, *24*, 966–978.

- (133) Marcus, R. A. Chemical and Electrochemical Electron-Transfer Theory. *Annu. Rev. Phys. Chem.* **1964**, *15*, 155–196.
- (134) Marcus, R. A.; Sutin, N. Electron transfers in chemistry and biology. *Biochim. Biophys. Acta* **1985**, *811*, 265 – 322.
- (135) Marcus, R. A. Electron transfer reactions in chemistry. Theory and experiment. *Rev. Mod. Phys.* **1993**, *65*, 599–610.
- (136) Tachiya, M. Generalization of the Marcus equation for the electron-transfer rate. *J. Phys. Chem.* **1993**, *97*, 5911–5916.
- (137) Peters, B. Common Features of Extraordinary Rate Theories. *J. Phys. Chem. B* **2015**, *119*, 6349–6356.
- (138) Kuznetsov, A. M.; Ulstrup, J. *Electron Transfer in Chemistry and Biology: An Introduction to the Theory*; John Wiley & Sons, Ltd., 1999.
- (139) Hush, N. Adiabatic Rate Processes at Electrodes. I. Energy-Charge Relationships. *J. Chem. Phys.* **1958**, *28*, 962–972.
- (140) Hush, N. Adiabatic theory of outer sphere electron-transfer reactions in solution. *Trans. Faraday Soc.* **1961**, *57*, 557–580.
- (141) Hush, N. Homogeneous and heterogeneous optical and thermal electron transfer. *Electrochim. Acta* **1968**, *13*, 1005–1023.
- (142) Truhlar, D. G.; Garrett, B. C.; Klippenstein, S. J. Current Status of Transition-State Theory. *J. Phys. Chem.* **1996**, *100*, 12771–12800.
- (143) Komatsuzaki, T.; Berry, R. S. Dynamical hierarchy in transition states: Why and how does a system climb over the mountain? *Proc. Natl. Acad. Sci.* **2001**, *98*, 7666–7671.

- (144) Bartsch, T.; Hernandez, R.; Uzer, T. Transition state in a noisy environment. *Phys. Rev. Lett.* **2005**, *95*, 058301(1)–058301(4).
- (145) Hernandez, R.; Bartsch, T.; Uzer, T. Transition State Theory in Liquids Beyond Planar Dividing Surfaces. *Chem. Phys.* **2010**, *370*, 270–276.
- (146) Craven, G. T.; Bartsch, T.; Hernandez, R. Persistence of transition state structure in chemical reactions driven by fields oscillating in time. *Phys. Rev. E* **2014**, *89*, 040801(R).
- (147) Craven, G. T.; Hernandez, R. Lagrangian descriptors of thermalized transition states on time-varying energy surfaces. *Phys. Rev. Lett.* **2015**, *115*, 148301.
- (148) Tachiya, M. Relation between the electron-transfer rate and the free energy change of reaction. *J. Phys. Chem.* **1989**, *93*, 7050–7052.
- (149) Steeger, M.; Griesbeck, S.; Schmiedel, A.; Holzapfel, M.; Krummenacher, I.; Braunschweig, H.; Lambert, C. On the relation of energy and electron transfer in multidimensional chromophores based on polychlorinated triphenylmethyl radicals and triarylaminines. *Phys. Chem. Chem. Phys.* **2015**, *17*, 11848–11867.
- (150) Soudackov, A. V.; Hazra, A.; Hammes-Schiffer, S. Multidimensional treatment of stochastic solvent dynamics in photoinduced proton-coupled electron transfer processes: Sequential, concerted, and complex branching mechanisms. *J. Chem. Phys.* **2011**, *135*, 144115.
- (151) Hammes-Schiffer, S. Proton-Coupled Electron Transfer: Moving Together and Charging Forward. *J. Am. Chem. Soc.* **2015**, *137*, 8860–8871.
- (152) Harshan, A. K.; Yu, T.; Soudackov, A. V.; Hammes-Schiffer, S. Dependence of Vibronic Coupling on Molecular Geometry and Environment: Bridging Hydro-

- gen Atom Transfer and Electron-Proton Transfer. *J. Am. Chem. Soc.* **2015**, *137*, 13545–13555.
- (153) Grunwald, E. Structure-energy relations, reaction mechanism, and disparity of progress of concerted reaction events. *J. Am. Chem. Soc.* **1985**, *107*, 125–133.
- (154) Guthrie, J. P. Multidimensional Marcus Theory: An Analysis of Concerted Reactions. *J. Am. Chem. Soc.* **1996**, *118*, 12878–12885.
- (155) Lambert, C.; Nöll, G.; Hampel, F. Multidimensional Electron Transfer Pathways in a Tetrahedral Tetrakis Phosphonium Salt: One-Step vs Two-Step Mechanism. *J. Phys. Chem. A* **2001**, *105*, 7751–7758.
- (156) Zwickl, J.; Shenvi, N.; Schmidt, J. R.; Tully, J. C. Transition State Barriers in Multidimensional Marcus Theory. *J. Phys. Chem. A* **2008**, *112*, 10570–10579.
- (157) Rubtsov, I. V. State-specific electron transfer: Shake it off. *Nature Chem.* **2015**, *7*, 683–684.
- (158) Lebowitz, J. L. Stationary Nonequilibrium Gibbsian Ensembles. *Phys. Rev.* **1959**, *114*, 1192–1202.
- (159) Rieder, Z.; Lebowitz, J. L.; Lieb, E. Properties of a Harmonic Crystal in a Stationary Nonequilibrium State. *J. Math. Phys.* **1967**, *8*, 1073–1078.
- (160) Sekimoto, K. Langevin Equation and Thermodynamics. *Prog. Theor. Phys. Supp.* **1998**, *130*, 17–27.
- (161) Segal, D.; Nitzan, A.; Hänggi, P. Thermal conductance through molecular wires. *J. Chem. Phys.* **2003**, *119*, 6840–6855.

- (162) Segal, D.; Nitzan, A. Spin-Boson Thermal Rectifier. *Phys. Rev. Lett.* **2005**, *94*, 034301.
- (163) Dhar, A.; Lebowitz, J. L. Effect of Phonon-Phonon Interactions on Localization. *Phys. Rev. Lett.* **2008**, *100*, 134301.
- (164) Kannan, V.; Dhar, A.; Lebowitz, J. L. Nonequilibrium stationary state of a harmonic crystal with alternating masses. *Phys. Rev. E* **2012**, *85*, 041118.
- (165) Sabhapandit, S. Heat and work fluctuations for a harmonic oscillator. *Phys. Rev. E* **2012**, *85*, 021108.
- (166) Dhar, A.; Dandekar, R. Heat transport and current fluctuations in harmonic crystals. *Physica A* **2015**, *418*, 49 – 64.
- (167) Velizhanin, K. A.; Sahu, S.; Chien, C.-C.; Dubi, Y.; Zwolak, M. Crossover behavior of the thermal conductance and Kramers' transition rate theory. *Sci. Rep.* **2015**, *5*.
- (168) Murashita, Y.; Esposito, M. Overdamped stochastic thermodynamics with multiple reservoirs. *Phys. Rev. E* **2016**, *94*, 062148.
- (169) Cahill, D. G.; Goodson, K.; Majumdar, A. Thermometry and thermal transport in micro/nanoscale solid-state devices and structures. *J. Heat Transfer* **2002**, *124*, 223–241.
- (170) Galperin, M.; Nitzan, A.; Ratner, M. A. Heat conduction in molecular transport junctions. *Phys. Rev. B* **2007**, *75*, 155312.
- (171) Leitner, D. M. Energy Flow in Proteins. *Annu. Rev. Phys. Chem.* **2008**, *59*, 233–259.

- (172) Li, Q.; Duchemin, I.; Xiong, S.; Solomon, G. C.; Donadio, D. Mechanical Tuning of Thermal Transport in a Molecular Junction. *J. Phys. Chem. C* **2015**, *119*, 24636–24642.
- (173) Yang, N.; Xu, X.; Zhang, G.; Li, B. Thermal transport in nanostructures. *AIP Adv.* **2012**, *2*, 041410.
- (174) Luo, T.; Chen, G. Nanoscale heat transfer - from computation to experiment. *Phys. Chem. Chem. Phys.* **2013**, *15*, 3389–3412.
- (175) Rubtsova, N. I.; Nyby, C. M.; Zhang, H.; Zhang, B.; Zhou, X.; Jayawickramarajah, J.; Burin, A. L.; Rubtsov, I. V. Room-temperature ballistic energy transport in molecules with repeating units. *J. Chem. Phys.* **2015**, *142*, 212412.
- (176) Li, B.; Wang, L.; Casati, G. Negative differential thermal resistance and thermal transistor. *Appl. Phys. Lett.* **2006**, *88*, 143501.
- (177) Ben-Abdallah, P.; Biehs, S.-A. Near-Field Thermal Transistor. *Phys. Rev. Lett.* **2014**, *112*, 044301.
- (178) Joulain, K.; Drevillon, J.; Ezzahri, Y.; Ordonez-Miranda, J. Quantum Thermal Transistor. *Phys. Rev. Lett.* **2016**, *116*, 200601.
- (179) Terraneo, M.; Peyrard, M.; Casati, G. Controlling the Energy Flow in Nonlinear Lattices: A Model for a Thermal Rectifier. *Phys. Rev. Lett.* **2002**, *88*, 094302.
- (180) Chang, C.; Okawa, D.; Majumdar, A.; Zettl, A. Solid-state thermal rectifier. *Science* **2006**, *314*, 1121–1124.
- (181) Newton, M. D.; Sutin, N. Electron Transfer Reactions in Condensed Phases. *Annu. Rev. Phys. Chem.* **1984**, *35*, 437–480.



- (182) Hartmann, C.; Latorre, J. C.; Ciccotti, G. On two possible definitions of the free energy for collective variables. *Eur. Phys. J. Spec. Top.* **2011**, *200*, 73–89.
- (183) Esposito, M.; Ochoa, M. A.; Galperin, M. Efficiency fluctuations in quantum thermoelectric devices. *Phys. Rev. B* **2015**, *91*, 115417.
- (184) Lim, J. S.; López, R.; Sánchez, D. Dynamic thermoelectric and heat transport in mesoscopic capacitors. *Phys. Rev. B* **2013**, *88*, 201304.
- (185) Craven, G. T.; Nitzan, A. Upside/Downside statistical mechanics of nonequilibrium Brownian motion. I. Distributions, moments, and correlation functions of a free particle. *The Journal of Chemical Physics* **2018**, *148*, 044101.
- (186) Craven, G. T.; Chen, R.; Nitzan, A. Upside/Downside statistical mechanics of nonequilibrium Brownian motion. II. Heat transfer and energy partitioning of a free particle. *The Journal of Chemical Physics* **2018**, *149*, 104103.
- (187) Cui, B.; Craven, G. T.; Nitzan, A. Heat transport induced by electron transfer: A general temperature quantum calculation. *J. Chem. Phys.* **2021**, *in press*.
- (188) Zhang, Y.; Barnes, G. L.; Yan, T.; Hase, W. L. Model non-equilibrium molecular dynamics simulations of heat transfer from a hot gold surface to an alkylthiolate self-assembled monolayer. *Phys. Chem. Chem. Phys.* **2010**, *12*, 4435–4445.
- (189) Carles, R.; Benzo, P.; Pécassou, B.; Bonafos, C. Vibrational density of states and thermodynamics at the nanoscale: the 3D-2D transition in gold nanostructures. *Sci. Rep.* **2016**, *6*, 39164.
- (190) Akkerman, H. B.; Naber, R. C. G.; Jongbloed, B.; van Hal, P. A.; Blom, P. W. M.; de Leeuw, D. M.; de Boer, B. Electron tunneling through alkanedithiol

self-assembled monolayers in large-area molecular junctions. *Proc. Natl. Acad. Sci.* **2007**, *104*, 11161–11166.

- (191) Love, J. C.; Estroff, L. A.; Kriebel, J. K.; Nuzzo, R. G.; Whitesides, G. M. *Self-Assembled Monolayers of Thiolates on Metals as a Form of Nanotechnology*; 2005; Vol. 105; pp 1103–1170.
- (192) Renai Chen, "The-Spectrum-Generator-source", Software Package, <https://github.com/renaichen/The-Spectrum-Generator-source.git>, 2019.
- (193) Yan, Y.; Zhao, H. Phonon interference and its effect on thermal conductance in ring-type structures. *J. Appl. Phys.* **2012**, *111*, 113531.